

Broadband Liquid Dampers to Stabilize Flexible Spacecraft Structures

PROEFSCHRIFT

ter verkrijging van de graad van doctor
aan de Technische Universiteit Delft,
op gezag van de Rector Magnificus prof. ir. K.C.A.M. Luyben,
voorzitter van het College voor Promoties,
in het openbaar te verdedigen op 26 november 2012 om 10:00 uur

door

Johannes Maria KUIPER

natuurkundig ingenieur

geboren te Zaandam

Dit proefschrift is goedgekeurd door de promotor:

Prof. dr. E.K.A. Gill

Samenstelling promotiecommissie:

Rector Magnificus	voorzitter
Prof. dr. E.K.A. Gill	Technische Universiteit Delft, promotor
Prof. ir. B.A.C. Ambrosius	Technische Universiteit Delft
Prof. dr. H.C.W. Beijerinck	Technische Universiteit Eindhoven
Prof. dr. K. Bri�	Technische Universit�t Berlin
Prof. dr. J. van der Ha	Kyushu University Japan
Dr. M.H.M. Ellenbroek	Dutch Space / Technische Universiteit Twente
Prof. dr. ir. J.A. Mulder	Technische Universiteit Delft, reservelid

Science is organized knowledge.
Wisdom is organized life.

Immanuel Kant
German philosopher (1724 - 1804)

Aan mijn ouders Jaap en Agaath

Dankwoord

Family

Aan Jacqueline, Jolien en Floris voor alle tijd die zij mij gunden.

Eberhard Gill

Voor zijn accelerated course in scientific writing.

Herman Beijerinck

Voor zijn inhoudelijk enthousiasme en steun.

Ed Bongers

Voor zijn collegiale steun ook al werk ik niet meer bij Dutch Space sinds 2001.

Rene Olie

For all “muti-culti” talks throughout the many years.

Jasper Bouwmeester

Voor zijn steun en open collegialiteit.

Contents

Samenvatting.....	v
Summary.....	vii
Symbols.....	ix
Abbreviations.....	xii
1 Introduction	1
1.1 Background.....	1
1.2 Thesis Motivation.....	2
1.3 Scope and Research Questions.....	3
1.4 Structure of Thesis.....	4
1.5 Objectives	5
1.6 Classification of Dampers	6
1.7 Terrestrial Applications of Mass and Liquid Dampers.....	7
1.8 Space Applications of Passive Liquid Dampers	13
1.9 Conclusions.....	23
2 Theory of Spacecraft Nutation Damping	25
2.1 Introduction.....	25
2.2 Attitude and Orbit Control Systems	26
2.3 Spin-Stabilized S/C	27
2.4 Spacecraft Nutation.....	30
2.5 Quasi-rigid Spacecraft Configuration	33
2.6 Stability of a Spinning Spacecraft.....	34
2.7 Forcing Acceleration, Power Dissipation and Time Constant.....	36
2.8 Velocity Profile and Dissipation.....	38
2.8.1 Introduction.....	38
2.8.2 Laminar and Turbulent Performance	40
2.8.3 Effective Damping Length.....	43
2.8.4 Hagen-Poiseuille Model.....	48
2.8.5 Refined Hagen-Poiseuille Models.....	51
2.8.6 Navier-Stokes Solution.....	53
2.8.7 Model Results	55
2.9 Multiple Excitations	57
2.10 Residual Nutation Angle	60
2.11 Scaling Space to Terrestrial Test Conditions	65
2.12 Design Tuning.....	68

2.13	System Engineering Considerations.....	69
2.14	Conclusions.....	71
3	Verification & Validation	73
3.1	Introduction.....	73
3.2	Verification and Validation data.....	74
3.2.1	Ulysses.....	74
3.2.2	Cluster	74
3.2.3	Feng Yun 2	74
3.2.4	Meteosat	74
3.2.5	EQUATOR-S.....	78
3.2.6	COS-B	79
3.2.7	Selected Cases	79
3.3	Airbearing Pendulum Tests.....	80
3.3.1	Vertical Pendulum.....	80
3.3.2	Horizontal Pendulum.....	80
3.4	EQUATOR-S and COS-B Data Analysis	84
3.4.1	Design Data	84
3.4.2	Applicable Models.....	84
3.4.3	EQUATOR-S S/C Nutation.....	85
3.4.4	COS-B S/C Nutation	86
3.5	Conclusions.....	89
4	Stabilizing the FY-2 Spacecraft	91
4.1	Introduction.....	91
4.2	Spacecraft and Mission Description.....	92
4.3	FY-2 ND Design	93
4.3.1	Requirements.....	93
4.3.2	Functional Design.....	93
4.3.3	Structural Design.....	97
4.4	Verification, Qualification and Flight Acceptance.....	97
4.4.1	Test Plans PTM-DM-QM-FM	98
4.5	PTM Design and Test Matrix	101
4.6	PTM Experiments.....	103
4.7	Recursive PTM Tuning.....	108
4.8	Final FM ND Design	110
4.9	Qualification and Acceptance Tests	110
4.10	Radiation Analysis.....	115
4.11	Verification and Validation.....	119

4.12	Conclusions.....	121
5	Ulysses Spacecraft: Feedback from Space.....	123
5.1	Introduction.....	123
5.2	Mission Operations.....	126
5.3	Ulysses AOCS Anomaly and its Control	127
5.4	Early Nutation Anomaly Investigation	130
5.4.1	ND Design Recovery and Recalibration.....	131
5.4.2	Transient ND Flow Phenomena	134
5.4.3	Enlarged ND Bandwidth.....	136
5.4.4	Antenna Deployments and Invoked Nutation Instabilities	137
5.4.5	In-orbit S/C Data Analysis	139
5.5	Conclusions	141
6	Spacecraft with Extended Wire-Booms: A New Challenge.....	143
6.1	Introduction.....	143
6.2	Cluster Mission.....	144
6.3	Wire Boom Sensor Designs.....	145
6.4	Mission Data	147
6.5	Wire Boom Oscillation Modes	151
6.6	Stability Considerations	153
6.7	Wire Boom Cable Composition	154
6.8	Multi-mode Analysis	155
6.9	Conclusions	161
7	Multi-mode Liquid Damper for the Cluster ADCS	163
7.1	Introduction.....	163
7.2	Trade-off towards a Multi-mode Damper Design.....	164
7.3	Redundancy and Enlarged Bandwidth	164
7.4	Design Implementation	165
7.5	Early Assessments	166
7.6	Recursive Bottom-up Approach	168
7.7	Implementation of the Multi-mode Damping Principle	169
7.8	Spacecraft Stability Analysis	176
7.9	Bandwidth Considerations and Design Options.....	180
7.10	Tuning Sensitivity of the Final Design.....	181
7.11	PTM Experiments	181
7.12	Normal Operation	183
7.13	Summary and Conclusions	184
8	Conclusions and discussion.....	187

8.1	Introduction.....	187
8.2	Objectives and Results	187
9	Outlook.....	197
9.1	Future Research Topics.....	197
9.2	Valorization Opportunities	198
9.3	Application Scenarios.....	198
9.4	Final Remarks.....	198
	Bibliography.....	199
	Authors Background and Motivation.....	209
	Curriculum Vitae	211

Samenvatting

Massa-veer en vloeistof dempers faciliteren structurele vibratie controle om enkele, gekoppelde laterale en torsie vibraties te dempen. De passief ge-tune-de vloeistof demper genaamd Tuned Liquid Damper (TLD) klasse hieruit is gewild vanwege de brede toepasbaarheid, extreme betrouwbaarheid, robuustheid, lange levensduur en eenvoud in productie. In dit PhD onderzoek werden de theorie, ontwerp, verificatie en validatie van multi-mode TLDs in aardse en voornamelijk ruimtevaartuig (S/C) toepassingen bestudeerd.

Het meest uitdagende TLD ontwerp van het type “buis-met eindpotten” was de Chinese FY-2 S/C nutatie demper in de jaren 90. De extreme performance eisen zoals de 0.5° residuele nutatie dempingshoek legden een uitgebreid test programma op welke leidden tot verfijnde inzichten in de recursieve kalibratie methode en de beperkingen in het dempingsgedrag. De testanalyse resultaten en de betrokkenheid in de vluchtanalyse van de Ulysses S/C nutatie anomalie in dezelfde periode, bracht de auteur op het idee van een multi-mode TLD systeem. Het concept werd voorgesteld en succesvol toegepast in de Cluster S/C voor het effectief dempen van zowel nutatie als gekoppelde draadantenne oscillatie modes.

Om zover te komen, moest de essentie van S/C dynamica en controle worden uitgebreid op het gebied van vloeistof stromingsmodellen en een geschikte TLD ontwerp methodologie met inbegrip van multi-mode excitaties. De TLD sleutel performance parameters zijn het dissipatie tempo, de residuele dempingshoek en de resonantie frequentie die direct gerelateerd is aan de effectieve dempingslengte. Deze parameter werd aanvankelijk verkregen door een pragmatische schatting op basis van eerdere testgegevens. De bestaande praktische ontwerpregels werden echter overtroefd door inzichten die werden verkregen vanuit de jongste wetenschappelijke resultaten uit de vloeistofmechanica. Deze kennis en de uitgebreide analyse van alle beschikbare TLD dempingstesten resulteerden in een nieuwe verfijnde methodologie om de effectieve dempingslengte goed te kunnen schatten. De uiteindelijke waarde moet echter nog steeds worden bepaald via recursieve kalibratie cycli maar betere beginschattingen verminderen de vereiste testtijden aanzienlijk.

De residuele dempingshoek wordt gelimiteerd door het TLD eindpot gedrag en is bepaald door de fysica van de interactie van de vloeistof meniscus met de wand. Hoewel het TLD ontwerp is gekarakteriseerd door een zeer lage residuele hoek met een bijna nul dode band, is de uiterste limiet niet duidelijk. Deze kwestie werd onderzocht met gebruik van diverse modellen en experimenten terwijl de state-of-the-art in de wetenschappelijke literatuur van nano-tribologie en de overgangsverschijnselen van het nat maken van biomimetische oppervlakken werd verkend. Testverfijningen worden voorgesteld ter beperking van de dempingsfluctuaties en het uitbreiden van het lage test hoekbereik. Hoewel de limiterende hoek niet bekend is, is er krachtig bewijs dat de limiet kan worden verzet naar een ruimtewaarde lager dan 0.1°.

De eerste ontwerp fase van de breedband Cluster TLDs in 1991 en de TLD ontwikkelingen tot 2012 werden bestudeerd. Bovendien werden de spin gestabiliseerde S/C Bepi-Colombo, Cluster, RBSP, DICE, Themis en FAST onderzocht, die de brede toepasbaarheid van het multi-mode TLD concept laten zien. De studie van de generieke theorie van draad antenne oscillaties, gyroscopisch gekoppeld aan de S/C hub spin en nutatie modes, resulteerde in een nieuwe geharmoniseerde parametrische voorstelling met afgeleide vergelijkingen. Het Cluster TLD systeem met daaraan toegevoegd de interne antenne demping maken de draadantenne uitwijkhoek en zijn tijdsconstante tot additionele ontwerp parameters. Op basis van deze kennis werd een recursieve TLD ontwerp methodologie ontwikkeld. De stabiliteitsstudie met inbegrip van de draad antenne compositie maakte duidelijk waar de limiet van het multi-mode model wordt bereikt en bread-board experimenten en praktische

engineering afwegingen vereist worden. De draad antenne ontplooiingsstrategie werd behandeld gebruik makend van het multi-mode dampingsprincipe en vergeleken met een literatuur voorbeeld. Bij kleine antenne uitwijkingen domineren echter verscheidene materiaal artefacten en niet-elastische buigingen dus alleen gerichte engineering testen kunnen deze issues verhelderen.

De huidige status van het TLD ontwerp werd onderzocht door het vergelijken van het RBSP S/C [2012] ring TLD en het Cluster S/C [2000] eindpot TLD ontwerp. De combinatie van de Cluster TLD bottom-up ontwerp methodologie met het 9 vrijheidsgraden tellende RBSP top-down model maakte de model basis compleet voor het ontwerp van multi-mode TLDs in flexibele S/C. De RBSP TLD is behept met aanzienlijke hoek afwijkingen en aanloop tijdsconstanten die niet worden verdisconteerd in het RBSP model. Het Cluster TLD ontwerp heeft echter van beide artefacten geen last. RBSP S/C vluchtdata zijn echter nog niet beschikbaar. De nutatie gerelateerde Cluster vlucht data valideren de TLD model voorspellingen ruim binnen de eisen. Dit levert indirect maar onvolledig bewijs van de effectiviteit van het TLD system ontwerp. Het is echter moeilijk om het ontworpen multi-mode gedrag zelf te traceren en valideren. Het is daarom van groot wetenschappelijk belang om Attitude Determination en Control Systeem vlucht data te verkrijgen.

Een succesvolle TLD ontwikkeling vereist risico verlichting als essentieel onderdeel van systems engineering (SE). Een inventarisatie van de bepalende randvoorwaarden werd gemaakt vooruitdenkend aan productie en project escalaties. In de high-tech industrie is echter weinig focus op een wetenschappelijk benadering van SE terwijl dit wel dit loont. Het was een van de uitdagingen van dit onderzoek de toegevoegde waarde aan te tonen van zo'n investering. Als resultaat is aan te geven dat de ontwikkelde methodieken inderdaad bijdragen aan een gedegen SE benadering in de ontwikkeling van multi-mode TLDs.

Het ruimtevaart gekwalificeerd breedbandig TLD ontwerp met eindpotten is een excellente keuze voor gebruik in toekomstige spin-gestabiliseerde ruimtevaarttuigen met draadantenne configuraties. De resultaten van het PhD onderzoek maken het mogelijk het gegeven damper concept in extreme zin te verfijnen. Marktonderzoek en het aanreiken van toegewijde oplossingen zijn een weg naar valorisatie. Aardse afgeleide ontwerpen in de engineering gebieden van verfijnde (ultra) centrifuges, pulserende industriële pijpsystemen, windmolens, aardbevingscontrole van bouwstructuren, scheepsbouw en stabilisatie van bruggen bieden de beste valorisatie mogelijkheden op korte termijn.

Summary

Mass-spring and liquid dampers enable structural vibration control to attenuate single, coupled lateral and torsional vibrations in diverse structures. Out of these, the passively tuned liquid damper (TLD) class is wanted due to its broad applicability, extreme reliability, robustness, long life time and ease of manufacturability. In this PhD thesis, the theory, design, verification and validation of multi-mode TLDs in terrestrial and mainly spacecraft (S/C) applications have been studied.

The most challenging TLD design of the type “tube-with-endpots” was the Chinese meteorological FY-2 S/C nutation damper in the 90s. The extreme performance requirements like the 0.5° residual nutation damping angle implied an extended test program which led to refined insights in the recursive calibration method and limiting damping performance. The test analysis results and the involvement in the in-orbit analysis of the Ulysses S/C nutation anomaly in the same period, led the author to the idea of a multi-mode TLD system. The concept was proposed and successfully applied in the Cluster S/C for the effective damping of both nutation and coupled wire boom (antenna) oscillation modes.

To come that far, the essentials of spacecraft dynamics and its control required an extension of the liquid flow models and an appropriate TLD design methodology to include multi-mode excitations. The TLD key performance parameters are the dissipation rate, residual damping angle and the resonance frequency which is directly related to the effective damping length. This parameter used to be obtained by an educated guess on basis of test heritage. The existing practical design rules, however, were overruled by new insights which are based on the latest scientific results from fluid mechanics. This knowledge and the extensive analysis of all available TLD damping performance tests resulted in a new refined methodology to estimate the effective damping length properly. The eventual value, however, must still be determined via recursive calibration cycles but better initial estimates reduce the required test times significantly.

The residual damping angle is limited by the TLD endpoint behavior which is determined by the physics of the liquid meniscus interaction with the endpoint wall. Though the TLD design is characterized by a very low residual angle with almost zero dead-band, the very limit is not clear. This issue was investigated using multiple models and experiments whilst the state-of-the-art in the scientific literature from nano-tribology and wetting transitions on biomimetic surfaces was explored. Test refinements are proposed to decrease damping fluctuations and extend the low angular test range. Although, the limiting angle is not known, there is strong evidence that the limits can be extended beyond the 0.1° flight value.

The early design phase of the broadband Cluster TLDs in 1991 and the TLD developments up to 2012 were studied. Moreover, the spin-stabilized magneto-spherical S/C Bepi-Colombo, Cluster, RBSP, DICE, Themis and FAST are compared which confirm the applicability of the multi-mode TLD concept. The study of the generic theory of wire boom oscillations, gyroscopically coupled to the S/C hub spin and nutation modes, resulted in a new harmonized parameterization and derived equations. The Cluster TLD system with in addition the internal wire boom damping enable the boom deflection limit and its damping time constant to be design parameters. On basis of this knowledge, a recursive bottom-up TLD design methodology was developed. The stability study including the wire boom composition made clear where the limit of multi-mode modeling is reached and breadboard experiments and practical engineering trade-offs are required. The optimal wire boom deployment strategy using the multi-mode damping principle was analyzed. At small angular deflections, however, material artifacts and anelastic flexure dominate and only dedicated engineering tests can clarify these issues.

The current status of the TLD design was investigated by comparing the RBSP S/C [2012] ring TLD and the Cluster S/C [2000] endpoint TLD designs. The combination of the Cluster

TLD bottom-up design methodology with the 9 degrees of freedom RBSP top-down model completed the model base for the design of multi-mode TLDs in flexible S/C. The RBSP TLD suffers with considerable angular off-sets and inrush time constants which are not accounted for in the RBSP model. The Cluster TLD design, however, lacks these artifacts. RBSP S/C flight validation data, however, are not yet available. The nutation related Cluster flight data validate the TLD model predictions firmly within the requirements. This renders an indirect but incomplete prove of the effectiveness of the TLD system design. It is hard, however, to trace and validate the designed multi-mode performance itself. It is, therefore, of great scientific value to obtain Attitude Determination and Control System flight data.

A successful TLD development requires risk mitigation as an essential part of systems engineering (SE). An inventory of boundary conditions was made thinking ahead for production and project cost escalations. In the high-tech industry, however, there is little focus on a scientifically based bottom-up SE approach though such effort does pay off. It was one of the quests of this thesis to prove the added value of such an investment. As a result, the developed methodologies do contribute to a profound SE approach in the development of multi-mode TLDs.

The space qualified broadband TLD design with endpots is an excellent choice for use in future spin-stabilized S/C with wire boom configurations. The results of the PhD thesis enable the extreme refinement of the given damper concept. Market research and the allocation of dedicated solutions are a way towards valorization. Terrestrial spin-offs in the engineering fields of refined (ultra) centrifuges, pulsating industrial piping systems, windmills, earthquake control of building structures, shipbuilding and bridge stabilization offer the best valorization opportunities in short terms.

Symbols

a	Liquid tube radius of the nutation damper (ND)	[m]
a_0	Amplitude of forcing acceleration of a single excitation	[m/s ²]
$a_0(t)$	Amplitude of forcing acceleration for multiple excitations $a_{0,i}$	[m/s ²]
\mathbf{a}_f	Forcing (e.g. nutation push-up) acceleration vector	[m/s ²]
$a_{0,max}$	Forcing acceleration along the fluid tube at the start of a (test)run	[m/s ²]
$a_{0,min}$	Forcing acceleration along the fluid tube at the end of a (test)run	[m/s ²]
a_z	Forcing acceleration in the Z direction	[m/s ²]
A_x	X amplitude of the harmonic Euler solution of ω_X	[rad/s]
A_y	Y amplitude of the harmonic Euler solution of ω_Y	[rad/s]
A_r	Enlarged surface area due to roughness	[m ²]
A_g	Geometric surface of a perfect flat area	[m ²]
b	Endpot radius of the nutation damper (ND)	[m]
Bo	Bond number	[-]
b_{eff}	Effective endpot entrance radius towards the fluid tube	[m]
C_d	Drag coefficient	[-]
d	Distance or (end pot wall) thickness	[m]
\mathbf{e}	Body Reference Frame vector $\mathbf{e} = (e_1, e_2, e_3) = (e_x, e_y, e_z)$	[m]
\mathbf{E}	Inertial Reference Frame (IRF) vector $\mathbf{E} = (E_1, E_2, E_3)$	[m]
E	Spacecraft rotational (kinetic) energy	[J]
$E(t)$	Kinetic energy of the liquid flow in the liquid tube and endpots	[J]
E_f	Spacecraft final rotational (kinetic) energy after extinction of nutation	[J]
f	Friction factor in head losses	[-]
f	Additional factor in natural damper frequency equation in RHP-2 model	[-]
f_i	Surface fraction area of the i -th component	[-]
f_0	Lowest structural resonance frequency	[Hz]
F	Oppositional force in the endpots due to damping liquid surface tension	[N]
$F(r)$	Radius dependent fluid velocity	[m/s]
F_a	Amplitude of the fluid velocity at the tube-wall with $r=a$	[m/s]
F_m	Meridian ND geometry factor	[-]
Fr	Froude number	[-]
F_{vx}	Frictional force along the liquid tube wall	[N]
F_{vy}	Frictional force along the endpot wall	[N]
F_v	Total frictional force along the liquid tube and endpot walls	[N]
g	Earth gravity	[m/s ²]
G	Torsional stiffness of the rotor of the testing apparatus	[m/s ²]
$G_{e,m}$	Equatorial (e) or Meridian (m) factor in residual angle equation	[-]
$G(t)$	Lagrangian, i.e. $G(t) = E(t) - V(t)$	[J]
h	Inner endpot height	[m]
h	Endpot sticking height or droplet height	[m]
h_f	Head loss factor	[m]
h_{in}	Tube inlet head loss factor	[m]
h_{out}	Tube outlet head loss factor	[m]
\mathbf{h}	Angular momentum vector $\mathbf{h} = (h_1, h_2, h_1)$	[Nm.s]
H_c	Capillary end pot height	[m]
I_o	Moment of inertia of the rotor, i.e. the airbearing test arm	[kg/s ²]
I_B	Moment of inertia of the wire boom(s)	[kg/s ²]
I_{eq}	Equivalent moment of inertia of a symmetrical spacecraft	[kg/s ²]
I_i	Moment of inertia with respect to i -axis (X, Y or Z)	[kg/s ²]
I_T	Total moment of inertia with respect to the Z-axis including wire booms	[kg/s ²]

$I(x)$	Radiation intensity at mass effective cross-section $x = \rho d$	[1/s]
I_0	Radiation intensity at $x=0$	[1/s]
J_0	Bessel function of zero order	[-]
J_1	Bessel function of first order	[-]
k_s	effective (RMS) surface roughness	[m]
k_0	Effective viscous damping mass ratio in RHP-1 model	[-]
K_{in}	Tube inlet flow loss factor	[-]
K_{out}	Tube exit flow loss factor	[-]
L	Tube length of the damper	[m]
L_{eff}	Effective tube length of damper	[m]
L_{AB}	Axial boom length (Ulysses)	[m]
L_0	Nominal (constant) effective liquid tube length at small angles	[-]
L_r	Scale factor	[-]
m	Mass	[kg]
M	S/C hub mass without wire booms	[kg]
n	Match factor for fluid surface tilt	[-]
n_i	Gas amount type i	[mole]
p	Pressure	[Pa]
p_0	Nominal equilibrium pressure above the endpots	[Pa]
P	Dissipation per nutation cycle	[J/s]
$P(t)$	Time dependent dissipation for multiple ($i=1...N$) excitations $a_{0,i}$	[J/s]
r	Radius	[m]
r_{SC}	Ulysses S/C effective radius	[m]
R	Gas constant $R = 8.3$	[J/mole/K]
Re	Reynolds number of a laminar flow	[-]
Re_A	Reynolds number of an oscillatory flow (I)	[-]
Re_R	Reynolds number of an oscillatory flow (II)	[-]
Re_δ	Reynolds number with respect to the boundary layer thickness δ	[-]
R_0	Hub radius	[m]
R_m	Mounting radius of damper (distance from spin-axis to center fluid tube)	[m]
R_a	Mounting radius of PTM on rotor of the air-bearing	[m]
s	Fluid displacement in the endpoint	[m]
s_0	Effective fluid displacement in endpoint in case of testing a flight model	[m]
S_0	Wire boom stiffness	[kg·m ² /s ²]
St	Strouhal number	[-]
t	Time	[s]
$u(r)$	Hagen-Poiseuille velocity in the fluid tube at radius r	[m/s]
T	External torque	[N.m]
T	Pendulum time	[s]
T	Temperature	[K]
T_0	Operational temperature (or nominal pendulum time)	[K]
T_{test}	Estimated duration of an air-bearing test run	[s]
$u_z(r, t)$	Radius and time-dependent fluid velocity in the Navier-Stokes model	[m/s]
V	Velocity	[m/s]
V	Volume	[m ³]
$V(t)$	Potential energy of displaced endpoint liquid against the centrifugal force	[J]
$w(r)$	Hagen-Poiseuille velocity in the endpoint tube at radius r	[m/s]
X_0	X-position of mounted nutation damper in $Z=Z_0$ plane	[m]
Y_0	Y-position of mounted nutation damper in $Z=Z_0$ plane	[m]
Z_0	Height of equatorial nutation damper mounting plane above COG plane	[m]
Z_m	Bessel function m-th order	[-]
α	Match factor for effective tube length	[-]
α	Tilt angle of the flight model	[rad]

α	ND mounting angle with respect to the X-axis	[rad]
β	Effective “mouth” ratio a/b_{eff}	[-]
β	Factor in the Navier-Stokes solution of ND liquid flow	[-]
γ	Mass heat ratio $\gamma = c_p/c_v = 1.66$ as exponent in the isentropic gas law	[-]
γ_0	ND design tuning factor Ω_0/ω_0	[-]
γ_0	Surface tension of the damping liquid	[N/m]
δ	Stokes boundary layer thickness at the tube wall	[rad]
ε_r	Womersley parameter at radius r	[-]
ζ	Top angle of body cone of satellite	[rad]
θ	Nutation angle or equivalent Euler angle	[rad]
θ_i	Intrinsic equilibrium contact angle for the i -th surface component	[rad]
θ_C	Cassie contact angle for a heterogeneous surface	[rad]
θ_a	Endpot advancing (a) liquid (flow) to wall angle	[rad]
θ_e	Endpot equilibrium (e) liquid to wall angle	[rad]
θ_r	Endpot receding (r) liquid (flow) to wall angle	[rad]
θ_0	Initial or nominal nutation angle	[rad]
θ_{res}	Residual nutation angle	[rad]
θ_W	Wenzel (true) contact angle	[rad]
κ	Damping factor	[1/s]
λ_0	Nominal (X,Y) lateral inertia ratio	[-]
λ_x	Inertia X ratio I_z / I_x	[-]
λ_y	Inertia Y ratio I_z / I_y	[-]
λ_{max}	Maximum (X,Y) inertia ratio	[-]
λ_{min}	Minimum (X,Y) inertia ratio	[-]
μ	Dynamic viscosity of damping fluid	[Pa.s]
μ	Absorption factor (nuclear)	[m ² /g]
ν	Kinematic viscosity of damping fluid	[m ² /s]
ξ	Stability time constant of a spin-axis	[s]
ρ	Density	[kg/m ³]
σ_B	Breakage strain	[N/m ²]
$\sigma_{0.2}$	Strain at 0.2% linear offset	[N/m ²]
σ_{VM}	Von-Mises maximum tension	[N/m ²]
τ	Time constant	[s]
φ	Euler (nutation) angle	[rad]
φ	Liquid flow phase angle at $t = 0$	[rad]
φ_i	Wire boom i in-plane angular deviation	[rad]
Φ	Angular deviation of the air-bearing rotor	[rad]
Φ_i	Wire boom i in-plane angular deviation	[rad]
Φ_{max}	Angular deviation of the rotor at the start of a test run	[rad]
Φ_{min}	Angular deviation of the rotor at the end of a test run	[rad]
χ	Educated guess factor to estimate the effective damping length	[-]
ω_0	Natural damper frequency without damping	[rad/s]
ω_p	Natural damper frequency with damping	[rad/s]
ω_Z	Spin (angle) frequency	[rad/s]
ψ	Euler angle	[rad]
ψ_i	Wire boom i out-of-plane angular deviation	[rad]
$\psi_{EA,i}$	EA mode wire boom i in-plane angular deviation	[rad]
$\psi_{MA,i}$	MA mode wire boom i out-of-plane angular deviation	[rad]
Ω_{EA}	EA mode oscillation angular frequency	[rad/s]
Ω_{MA}	MA mode oscillation angular frequency	[rad/s]
Ω_N	Nutation mode oscillation angular frequency	[rad/s]
Ω_o	Nominal nutation mode oscillation angular frequency	[rad/s]

Abbreviations

AC	Alternating Current
ACS	Attitude Control System
ADC(S)	Attitude Determination and Control (System)
ADS	Attitude Determination System
AOCE	Attitude and Orbit Control Electronics
AOC(S)	Attitude and Orbit Control (System)
AIAA	American Institute of Aeronautics and Astronautics
AMO	Atmospheric Mass Zero
AMPTE-IRM	Active Magnetospheric Particle Tracer Explorers - Ion Release Module (German S/C)
AND(s)	Active Nutation Damper(s)
AOCS	Attitude and Orbit Control System
ATR	Acceptance Test Review
BICE	Beijing Institute of Control Engineering
BLM	Boundary Layer Model
BOL	Begin-Of-Life
BRF	Body Reference Frame
CAD	Computer Aided Design
CSA	Canadian Space Agency
CCD	Charge Couple Device
CDR	Critical Design Review
CMA	China Meteorological Administration
COG	Center-Of-Gravity
COM	Center- Of- Mass
CONSCAN	Conical Scanning system
COSPAR	Committee on Space Research
COS-B	Cosmic ray S/C ('option B')
CTE	Coefficient of Thermal Expansion
CTM	Collapsible Tube Mast
CTMD(s)	Coupled Tuned Mass Damper(s)
CTMLD(s)	Coupled Tuned Mass Liquid Damper(s)
CZ-3	ChangZheng-3 (Chinese launcher)
DARA	Deutsche Agentur Fuer Raumfahrtangelegenheiten
DC	Direct Current
DE	Differential Equation
DICE	Dynamic Ionospheric Cubesat Experiment S/C
D/L	Down-Link
DM	Dummy Model
DSN	Deep Space Network
DW	Diffusion Welding
EA	Equatorial Anti-symmetric mode
EAA	Earth Aspect Angle
EBW	Electron Beam Welding
ECS-MARECS	European Communications Satellite-Maritime European Communication S/C
ECT	Energetic particle, Composition, and Thermal Plasma instrument
EFW	Electric Field and Wave sensor
EM	Electro-Magnetic
EMFISIS	Electric and Magnetic Field Instrument Suite and Integrated Science instrument

EO	Earth Observation
EOL	End-Of-Life
ES	Equatorial Symmetric mode
ESA	European Space Agency
ESTEC	European Space Technology Center
ESU	Earth Sensor Unit
FAST	Fast Auroral SnapshoT S/C
FDS	Fokker Dutch Space (file record)
FGM	Field Gate Magnetometer
FLEVO	Dutch Sloshsat mission S/C
FOV	Field-Of-View
FM	Flight Model
FRW	FRiction Welding
FSW	Friction Stir Welding
FW	Flash Welding
FWHM	Full Width at Half Maximum
FY-2(A)	Feng-Yun 2(A) means Cloud-Wind 2(A) Chinese meteorological S/C series
GEO	Geostationary Earth Orbit
GEOS	Geo-Stationary S/C
GMAW	Gas Metal Arc Welding
GPS	Global Position Satellite
GMS	Japan S/C
GNC	Guidance, Navigation and Control
GOES	Geostationary Satellite System (US)
GTAW	Gas Tungsten Arc Welding
GTO	Geostationary Transfer Orbit
GWIC	Great Wall Industry China
HAZ	Heat Affected Zone
HEO	Highly Elliptical Orbit
HGA	High Gain Antenna
HP(E)	Hagen-Poiseuille (Equation)
HR	Heliocentric Range
HST	Hubble Space Telescope
HVA	Homogeneous Vortex Approach
ISAS	Institute of Space and Astronomical Science
IADC	Interagency Space Debris Coordination Committee
IAA	International Academy of Astronautics
IAF	International Astronautical Federation
I/F	Interface
IISL	International Institute of Space Law
IMAGE	Imager for Magnetopause to Aurora Global Exploration
INTELSAT	International Telecommunications Satellite
IRF	Inertial Reference Frame
ISEE-B	International Sun-Earth Explorer S/C
ISPM	International Solar Polar Mission (later mentioned Ulysses) by ESA/NASA
ISS	International Space Station
ISTP	International Solar Terrestrial Physics Program
IUS	Inertial Upper Stage
JPL	Jet Propulsion Laboratory
LBW	Laser Beam Welding
LCD	Liquid Column Damper
LDV	Laminar Delamination Velocity
LEO	Low Earth Orbit

LRD	Liquid Ring Damper
LSS	Least Squares Sum
MA	Meridian Anti-symmetric mode
MagEIS	Magnetic Electron Ion Spectrometer
MEO	Medium Earth Orbit
NFF	Nutation Forcing Function
MMO	Magneto-Spheric-Orbiter as part of the Bepi-Colombo Mercury mission
MOI	Moment Of Inertia
MS	Meridian Symmetric mode
MS	Margin of Safety
MSG	Meteosat Second Generation
MTLCD	Multiple Tuned Liquid Column Damper
MTLRD	Multiple Tuned Liquid Ring Damper
N	Nutation mode
NASA	National Aeronautics and Space Administration
NASDA	National Space Development Agency of Japan
ND(s)	Nutation Damper(s)
NMSC	National Meteorological Satellite Center
NOAA	National Oceanic and Atmospheric Administration
NS(E)	Navier-Stokes (Equation)
OBDH	Onboard Data Handling system
OGO-III, IV	Spinning S/C in the 60s
OOSA	Office for Outer Space Applications
PAM	Payload Assist Module
PDR	Preliminary Design Review
PND(s)	Passive Nutation Damper(s)
P-POD	NASA's Poly Picosatellite Orbital Deployer
PSD	Power Spectral Density
PRA	Probabilistic Risk Assessments
PTM	Performance Test Model
Q	Resonance quality factor: Tuned frequency normalized by its FWHM
QM	Qualification Model
QTR	Qualification Test Review
RA	Roughness Amplitude
RAMS	Reliability, Availability, Maintainability and Serviceability
RANS	Reynolds Averaged Navier-Stokes equations method
RBSP	Radiation Belt Storm Probe S/C
RF	Radio Frequency
RHP-1	Adapted HP model used in the EQUATOR-S mission
RHP-2	Adapted HP model used to model active damping by using the isentropic gas law
ROM	Rough-Order-of-Magnitude
RPM	Rounds Per Minute
RPW	Radio and Plasma Wave instrument
RSS	Root Sum Square
RSW	Resistance Spot Welding
RTG	Radioisotope Thermoelectric Generator
SAR	Synthetic Aperture Radar
S/C	Spacecraft
SE	System(s) Engineering
SED	Storm Enhanced Density magnetic Earth plasma
SEVIRI	Spinning Enhanced Visible and Infra-Red Imager
SMART	Small Missions for Advanced Research and Technology

SPB	Spin Plane Boom
SPF	Single Point of Failure
SSA	Sun Aspect Angle
SSP	Spacecraft Synchronization Pulse
SSU	Sun Sensor Unit
STAFF	Spatio Temporal Analysis Field Fluctuation
STEM	Storable Extendible Member
S/W	Software
THEMIS	“Time History of Events and Macro-scale Interactions during Substorms” S/C
TLD	Tuned Liquid Damper
TMLD	Tuned Mass Liquid Damper
TLCD	Tuned Liquid Column Damper
TLRD	Tuned Liquid Ring Damper
TMD	Tuned Mass Damper
TUD	Delft University of Technology
TUE	Eindhoven University of Technology
TUT	Twente University of Technology
UCBSSL	University of California Berkeley Space Sciences Laboratory
UCN	Ultra Centrifuge Netherlands
USA	United States of America
V&V	Verification and Validation
VIS	Visible
VISSR	Visible and Infrared Spin Scan Radiometer
VP-PAW	Variable Polarity - Plasma Arc Welding

1 Introduction

The beginning is the most important part of the work.

Plato, *The Republic*

Greek philosopher in Athens (427 BC - 347 BC)

1.1 Background

The need to control the dynamics of flexible systems is widespread. Harmonic and broad-band motions which appear, for example in ocean waves or Earthquake spectra, can be passively but also actively damped. In this PhD thesis the class of passively controlled systems will be studied in terrestrial and space applications. The basic damper concept to be dealt with provides structural vibration control to attenuate single, coupled lateral and torsional vibrations of diverse structures.

The focus will be on the special class of (multiple) tuned liquid column dampers applied in the structures of buildings, bridges, ships, windmills and spin stabilized spacecraft. Viscous fluid dampers reduce the stress of a specified mode, its higher modes and the deflection in structures subjected to dynamic excitations [Kassalanati et al., 1999]. The dampers can be small in size and are easy to incorporate in a mechanical structure. Another advantage is their excellent Reliability, Availability, Maintainability and Serviceability (RAMS) status. The liquid damper as passive device, provides a transfer of vibrational energy into a dissipative form (viscous dissipation) being the accumulated heat in the liquid. This type is used in a broad range of engineering disciplines and may be just a single sloshing liquid vessel.

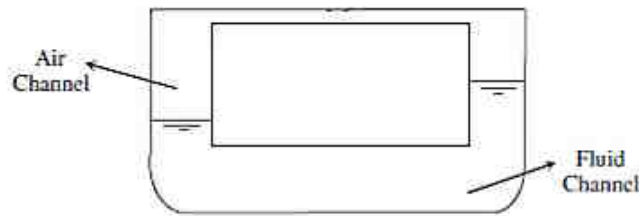


Fig-1.1 A tube-with-end-pots liquid damper after [Bell and Walker, 1996].

The so-called tube-with-endpots damper, shown in Fig-1.1, is a closed system of two communicating vessels connected by a liquid and a vapor tube. The open endpot vessel geometry without a vapor tube is shown in the configuration of a tuned liquid column damper (TLCD) in Fig-1.4. In a closed configuration, however, the vapor tube provides an instantaneous equal pressure above both endpots. This specific class is used for many decades now to dampen out the nutation of spinning spacecraft, an irregular movement of the spin-axis. This aspect of space rotational mechanics will be dealt with in section 1.8 (light version) and in full detail in Chapter 2.

The design and qualification of broadband tube-with-endpots liquid dampers is the main topic of this thesis. The work confines to the development of this liquid damper class which was produced by Fokker (Dutch) Space and UCN Aerospace in the past decades. The application of the damper type is still wanted due to its extreme reliability, robustness, life time and ease of manufacturability.

1.2 Thesis Motivation

The effects of structural flexibility on spacecraft (S/C) attitude and orbit control systems (AOCS) have been investigated from the early stages of S/C engineering. In a NASA report dated April 1969 [NASA, 1969], just a few months before the launch of the first moon mission, a number of guidelines was given. These were based on the experience from the following S/C series: Explorer-I, ATS D and E, Ranger, Nimbus, Alouette-I, 1963-22A, Dodge, OGO-III and IV and Gemini/Agena. In the introduction the following statement is made:

“Thus the control system engineer must be aware of the numerous and subtle ways in which a control system and flexible structure may interact.”

This statement proves to be a perpetual truth regarding the history of S/C engineering. Alouette-I, launched 1957, showed an increasing de-spin which was explained by asymmetric thermal boom bending caused by solar radiation. In the following decades diverse other S/C showed similar problems. After the launch of Ulysses, 33 years later, the axial hinge antenna proved to be the root cause of the nutation anomaly for the same reason. This makes clear that the straightforward implementation of lessons learned is far from obvious.

The author was involved in the early Ulysses anomaly study at ESTEC in November and December 1990. In the same time he was appointed as Design Leader of the Chinese FY-2 spacecraft nutation dampers at Dutch Space. The synergy of both projects created an innovative concept for multi-mode damping by liquid dampers [Kuiper, 1991] and 20 years later the motivation to write this PhD thesis. The motivation evolved mainly from scientific curiosity (and partly displeasure) because of the lack of a scientific and

consequent Systems Engineering (SE) approach in the development of space nutation (liquid) dampers in the early 90s. The implementation of a dedicated SE approach, however, necessitates the following:

- A compliance in top-down driven SE by the prime contractor with the bottom-up SE approach at the sub-contractor being essential for a controllable and successful project. It also requires an active attitude to look beyond the SE border (i.e. insights and interfaces) of the customer by verifying his top level documents, required interfaces and derived requirements.
- The application of tailored bottom-up SE tools in the interactive field between (mathematical) physics and realization of qualified flight hardware. Such tools have to be developed from prior knowledge (engineering heritage) and a survey of scientific literature. In parallel stepwise bread-boarding is required in compliance with the project specific test and qualification philosophy within time delivery constraints.

In the high-tech industry, however, there is little focus on a scientifically driven SE approach and publications due to intellectual property restrictions and as a rule the purely market driven development. The same holds for the available time to explore pertinent recurring and therefore costly issues enough in scientific depth. On the other hand this is a *contradictio in terminis* since in the end such effort does pay off. It was the quest of the author to prove the added value of such an investment. This will be shown by the methodologies and insights being developed throughout this thesis. The effort will include theory, engineering applications, verification and validation, leading to overall conclusions on liquid dampers for space application and beyond.

1.3 Scope and Research Questions

The extended use of (broadband) liquid dampers with endpots applied in space systems engineering (SE) will be studied in this thesis. Though a liquid damper looks like a simple communicating vessels design, the fluid mechanics to describe its performance is far from easy, not known in detail, and differs considerably for every new design. Moreover, endpot hysteresis phenomena at extreme small liquid displacements play a critical role. The fluid damper performance is key and predictable up to an extent to be investigated. Therefore, the following research questions were formulated:

- Investigate and extend the theory of liquid dampers and their design methodology. Prove the added value of a scientific approach to support a dedicated SE methodology.
- Extract insights from the in-depth analysis of test records and flight data. Study the verification and validation data of a series of missions.
- Study and extend the application areas of liquid dampers. Investigate the scope of cross-fertilization between space and terrestrial applications of liquid dampers.

One of the key items in the design of liquid dampers is the uncertainty in the effective damping length whilst its determination is very time consuming. The effective length is directly related to the accuracy of tuning the nutation damper (ND) design towards its required frequency in relation to the effective bandwidth. On basis of many performance tests it was evident that the effective length (L_{eff}) exceeds the physical tube length by a factor α times its diameter $D=2\cdot a$ [mm] with a typical range $1 < \alpha < 3$.

A new ND design has to be qualified, therefore, by study and analysis of multiple scaled verification experiments in a recursive cycle.

The ND development during the last decades up to its present status and the residual limiting damping angle will be traced and examined. The study focusses on the lessons learnt from the FY-2A and Ulysses ND development and qualification and will confine to the modern scope of applications. The acquired system engineering knowledge is dedicated to the design and qualification of broadband liquid dampers for passive multi-mode spacecraft (S/C) Attitude and Orbit Control Systems (AOCS) beyond the scope of nutation.

1.4 Structure of Thesis

Chapter 1 will confine to the terrestrial application of mass and liquid dampers. The cross-fertilization of space and terrestrial applications is explored whilst space nutation dampers are introduced.

Chapter 2 investigates the scope of applicable ND models and their validation, ranging from the integration of physics-based models to model-based Systems Engineering (SE). The terrestrial experiments (ground tests) are governed by fluid mechanics scaling rules which are defined in section 2.11. Finally design tuning and SE considerations will be dealt with in section 2.13.

Chapter 3 deals with the ND verification and validation (V&V) status of a series of missions: Ulysses, Cluster, FY2, MSG, COS-B and EQUATOR-S. The COS-B and EQUATOR-S missions are analyzed in-depth on basis of their rich amount of available V&V data.

Chapter 4 describes the development and qualification of the Chinese FY2 ND which tracks the ultimate possible damping range of liquid NDs. The large record of experiments is fully analysed and yields the basic ND design rules to supply the multi-mode design methodologies in Chapter 6.

Chapter 5 deals with the Ulysses [launch 1990] nutation anomaly with in particular the role of the three NDs. In the scope of the root cause analysis the nutation anomalies of the Alouette-I [launch 1960] and S3-2 S/C [launch 1971] are explored. The lessons learned, in terms of ND artefacts, complete the scope of Chapter 4.

Chapter 6 and 7 deal with the broadband damper design of the Cluster S/C [Kuiper, 1991] to complete the flow from the previous chapters. The potentials of multimode damping with specially designed NDs will be shown. A series of similar spacecraft (S/C) configurations equipped with wire booms are considered for reference. These are the following S/C which serve planetary magneto-spherical research missions:

- FAST [launch 1996]
- Cluster [launch 2000]
- THEMIS [launch 2007]
- DICE [launch 2011]
- RBSP [launch 2012]
- Mercury Magneto-spheric Orbiter (MMO) as part of the Bepi-Colombo mission [launch 2015]

At the end the circle is closed: The developed bottom-up design methodology is compared with the top down approach given by the RBSP modal and stability model. Finally the Cluster V&V record will be considered.

Chapter 8 and 9 summarize the overall conclusions: objectives and results and outlook: future research topics, valorisation opportunities and application scenarios.

1.5 Objectives

The following six categories of objectives reflect the overall research methodology in this thesis. The applicable chapters and sections are indicated between brackets. In Chapter 8 an inventory of the achievements will be made and the objectives are referred to by e.g. M-1 or SE-2.

Methodology (M)

1. Make an inventory of passive dampers both in terrestrial and space applications. Allocate and investigate cross-fertilization items between both application domains (1, 2).
2. Make an inventory of the Dutch tube-with-endpot liquid nutation dampers and summarize their characteristics, limitations and key design drivers. Formulate the research scope towards the extended use of liquid dampers beyond nutation (1).
3. Classify the terrestrial performance tests and identify the specific test limitations (3).

Theory (T)

1. Investigate the nutation damping theory from a broad range of sources. Study the diverse models and their differences on basis of model calibration (2).
2. Derive the required theory to support the design of multi-mode liquid dampers (2.9).
3. Investigate the theory, modeling and engineering of ND performance at the linear limit (2.10).
4. Derive the required fluid dynamics scaling theory (2.8).
5. Derive fluid dynamics theory to enable the scaling of space to terrestrial tests results (2.11).

Systems Engineering (SE)

1. Derive a profound SE approach for the development of NDs on basis of an inventory and research of the scientific literature and accessible documents from space industry (2, 3, 4, 5 and 6).
2. Find a method to estimate the effective damping length by an investigation of the latest fluid mechanics literature dealing with the entrance and exit phenomena in oscillatory tube flows and all available ND test results (2, 4, 5 and 7).
3. Investigate the development records of the FY-2A ND including its qualification, acceptance and V&V record. Extract the SE lessons learned and make them part of the theory chapter (4).
4. Investigate the Ulysses anomaly record with a detailed ND study. Extract the SE lessons learned and make them part of the theory chapter (5).

Verification and Validation (V&V)

1. Investigate the available ND related flight records, i.e. those from the Ulysses, Cluster, FY-2, MSG, EQUATOR-S and COSB missions (3, 4, 5 and 7).
2. Make a complete study of the COSB and EQUATOR-S meridian ND designs on basis of their open records of model, test and flight results by using the different models explored in Chapter 2 (3).
3. Analyze all the performance tests from the accessible FY-2, Ulysses and Cluster sources (4, 5 and 7).
4. Analyze and test the limits of extreme small nutation angle damping (4).

Design (D)

1. Introduce the scientific S/C class with antenna wire boom morphology to study a planetary magnetosphere (Bepi-Colombo, Cluster, RBSP, DICE, Themis and FAST

- missions) and investigate the applicability of the multi-mode liquid damper concept (6).
2. Investigate the stability theory of wire boom constellations from classical sources up to the current multi-mode analysis models. Gain insights, trace differences, derive methodologies, compliant parameterization and equation formats to deal with the Cluster liquid damper design (2, 3, 4, 5 and 6).
 3. Investigate the crucial stability role of the cable boom composition and the wire boom attachment to the S/C hub for a series of S/C from the early development (1960s) to the state-of-the-art (5, 6 and 7).
 4. Deal with the phase-A trade-offs towards the final design of the Cluster multi-mode liquid dampers and the implementation methodology on basis of insights gathered from the previous bullets (7).
 5. Derive an optimization approach to attenuate both in-plane and out-of-plane oscillation modes (2, 7).
 6. Analyze optimal deployment scenarios and compare them with results from literature (7).
 7. Use the multi-mode dynamics stability model of the RBSP S/C to analyze and compare the differences with the dynamics of the Cluster. Use the results to uncover the hidden Cluster ADCS C/D trade-offs. Generate stability conclusions by comparing the RBSP and Cluster S/C multi-mode damper concepts (7).
 8. Derive an alternative multi-mode liquid damper design on basis of bandwidth considerations (7.9).
 9. Deal with the tuning sensitivity of the Cluster Flight Model (FM) ND design (7.10).
 10. Characterize the impact of the combined action on the Performance Test Model (PTM) test requirements using the two different PTM_{EA} and PTM_{MA} models (7.11).
 11. Investigate the Cluster ADCS flight operation record and the V&V status of the damper performance (7.12).

Future (F)

1. Derive the main thesis conclusions, identify future research topics and extended applications (8 and 9).

The following chapters of this thesis will focus to the heritage of spacecraft (S/C) nutation dampers (NDs) and at the end its multi-mode extension in Chapter 7. The following parts of this chapter will consider terrestrial damper designs and the cross-fertilization between space and terrestrial applications. Finally S/C nutation is introduced and the Dutch ND heritage will be explored. To start the study, the generic classification of dampers will be dealt with first.

1.6 Classification of Dampers

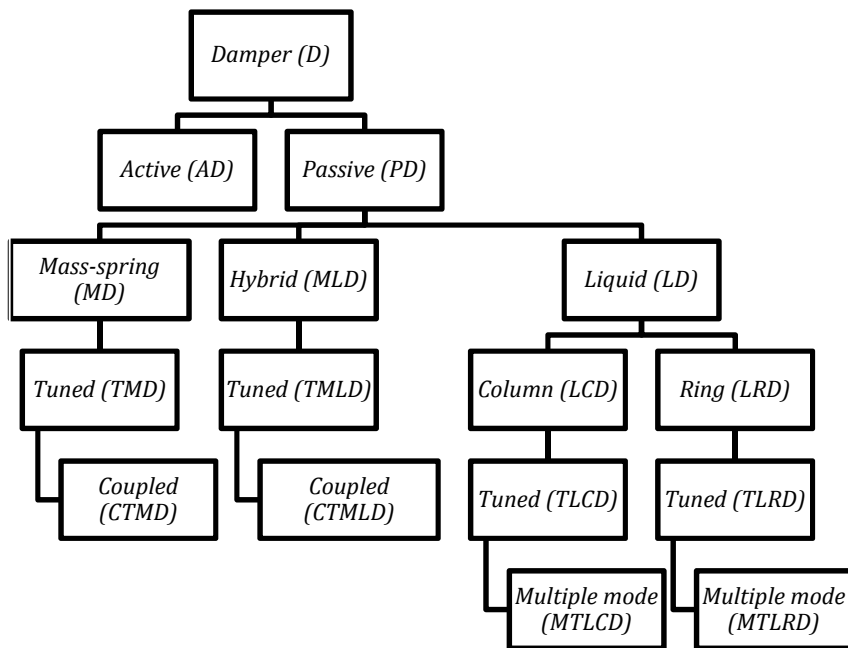
The classification of passive and active dampers is shown in Table-1.1. The flowchart was made to comprise the diverse abbreviations found in the scientific literature and to introduce consistency in the nomenclature. A consequent extension was made to cover the damper concepts throughout this thesis. The table is self-explaining whilst the abbreviations are applied in the following sections.

The active part of Table-1.1 is limited but will be considered for a single concept in the evaluation of an Active Nutation Damper (AND) design in section 2.8.5.

The hybrid Mass-spring Liquid Damper (MLD) branch represents a combination of a mass-spring (MD) and a liquid damper (LD) concept.

In this thesis the focus will be on the right LD branch which separates in a Liquid Ring Damper (LRD) and a Liquid Column Damper (LCD) branch. Both types are applied in terrestrial and space applications. The LRD is named an annular or torus damper as well. The LCD is also known as the tube-with-endpots (communicating vessels) damper design and will play a major role throughout this study. A LRD, half-filled with a damping liquid, can be regarded as a closed symmetric version of a LCD with two endpots, a liquid tube and a vapor tube. This will become clear in the following sections. The feasibility study of multiple mode LD concepts applied in spacecraft engineering at the bottom of the LD branch, is the final goal of the study in Chapter 7. The MTLRD concept is applied in the RBSP S/C (launch 2012) whilst the MTLCD concept was applied [Kuiper, 1991] in the Cluster S/C formation (launch 2000).

Table-1.1 The nomenclature and classification of passive and active dampers.



1.7 Terrestrial Applications of Mass and Liquid Dampers

In this subchapter the broad terrestrial application field of mass and liquid dampers is explored. At the end an active damper concept from shipbuilding engineering is highlighted. This selected design will be further examined in Chapter 2 to regard its potentials for space applications.

Bridges

The engineering field studying the interaction of humans and structures in case of dynamic motions is named bio-dynamics. The London Millennium footbridge (UK) is today a classic example of this discipline. It showed large vibrations of the bridge deck once subjected to pedestrian loads right after its first use in June, 2000.



Fig-1.2 *The London Millennium bridge(UK) [Dallard, 2001].*

The successful retrofit method of this bridge by the application of fluid viscous dampers [Dallard, 2001] shows a spin-off from space engineering. A frictionless hermetic damper (Taylor Devices) based on hydrodynamic bushes was selected whilst the design was scaled from its space qualified example. The original space design was applied in solar array panel systems of over 70 satellites. The complicated multi-mode random bridge excitation problem was tackled with a number of differently sized dampers. The implementation was successful and qualified by dynamic load tests with groups of people and random tests free from Mother Nature: severe wind storms.

Some of the applied System Engineering trade-off criteria are interesting in the scope of this thesis:

1. Increase of the structure (bridge) stiffness
2. Limiting the number of people on the bridge (load)
3. Active control
4. Passive damping.

An increase of mass is unacceptable in space engineering or tightly restricted. The structural stiffness is optimized compliant to mass constraints whilst the load is specified. The last two items 3 and 4 are relevant for the space ND trade-offs to follow and will be regarded in Chapter 2.

A 3D mathematical model, based on a modified Bernoulli equation, dealing with the excessive lateral vibrations of pedestrian bridges like the London Millennium Bridge and the Toda Park Bridge in Japan, is given by [Reiterer and Hochrainer, 2004]. Their TLCD model results comply well with scaled experiments. The advantages of tuned liquid column dampers (TLCD) compared to conventional tuned mass dampers (TMD) and tuned liquid dampers (TLD) are:

- Simple construction
- Low cost of design and maintainability
- Easy tunable.

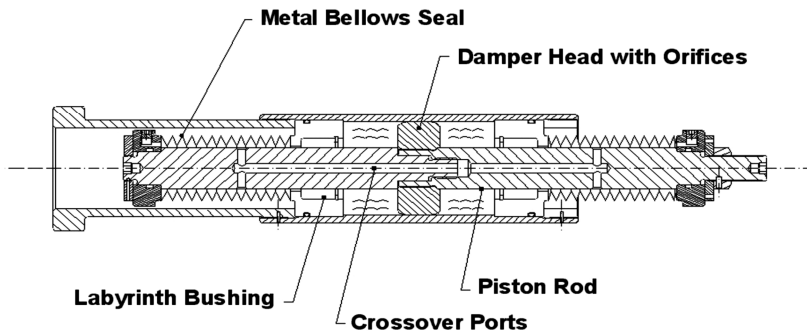


Fig-1.3 London Millennium bridge damper scaled from space engineering example [Dallard, 2001].

The performance of a multiple tuned liquid column damper (MTLCD) in a long span bridge construction is modeled by [Shum and Xu, 2004]. The two water filled MTLCDs, one shown in Fig-1.4, contain an orifice. In the modeling head losses and the interaction between damper and structure are taken into account. The use of MTLCDs to reduce coupled torsional and lateral vibrations was studied for white noise, harmonic and wind (random) excitation.

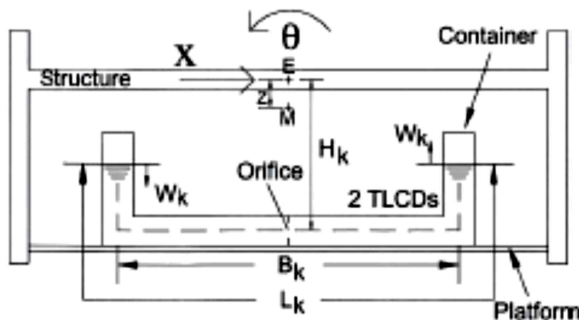


Fig-1.4 A single damper (out of two) of the MTLCD bridge system [Shum and Xu, 2004].

An optimal liquid mass distribution exists between the two dampers which depends on the required relative damping of the torsional and lateral mode.

Aircrafts

The author of this thesis used a comparable aeronautical MTLCD design [Kuiper, 1996] without orifice to attenuate the stablilo tail oscillations of the Fokker F-100 passenger airplane. He concluded that the endpoints play an essential role in the specific design. An exotic design on basis of an array of glycerine and water dampers was made using an extended Lagrange approach (dealt in Chapter) to include endpoint friction. The concept was healthy but rejected since its mass was too high.

Buildings

A recent new concept dealing with the passive control of vibrations in buildings is dealt by [Samanta and Banerji, 2010] and shown in Fig-1.5. The modified TLD for structural vibration control is placed on an elevated platform and coupled to the top of a building through a rigid rod with a flexible rotational spring at its bottom. At specific values of the spring constant, the rotational acceleration is in phase with the structure (building) top acceleration. The spring constant can be chosen optimally to make the design more

effective than a standard TLD design. The given model is refined with respect to earlier ones in literature and complies well with scaled experiments. The shallow water model of liquid sloshing was used to investigate the response to both harmonic and broadband earthquake excitations.

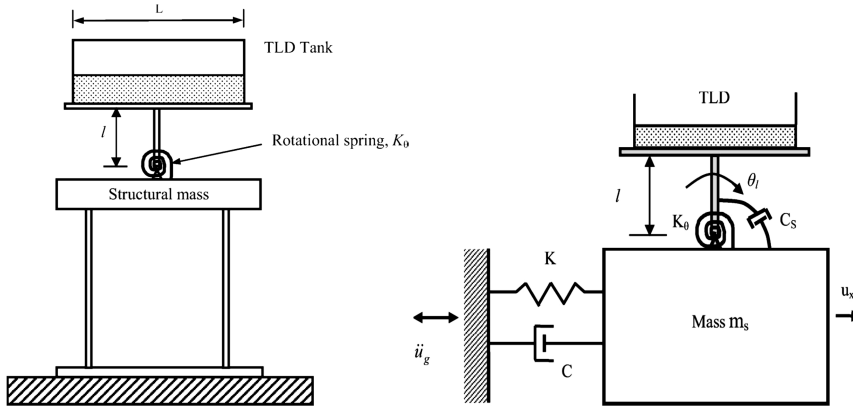


Fig-1.5 Modified TLD design for structural vibration control [Samanta and Banerji, 2010].

A system of tuned mass dampers (TMD) for seismic response control of torsional building structures was investigated by [Singh et al., 2002]. Active and passive control schemes are considered but the latter are more commonly accepted and therefore implemented in practical applications. The principle design composed of four TMDs, shown in Fig-1.6, provides for bi-directional damping of coupled lateral and torsional ground motions. The multi (14) parameter design optimization input is the seismic response spectrum or a stationary random model.

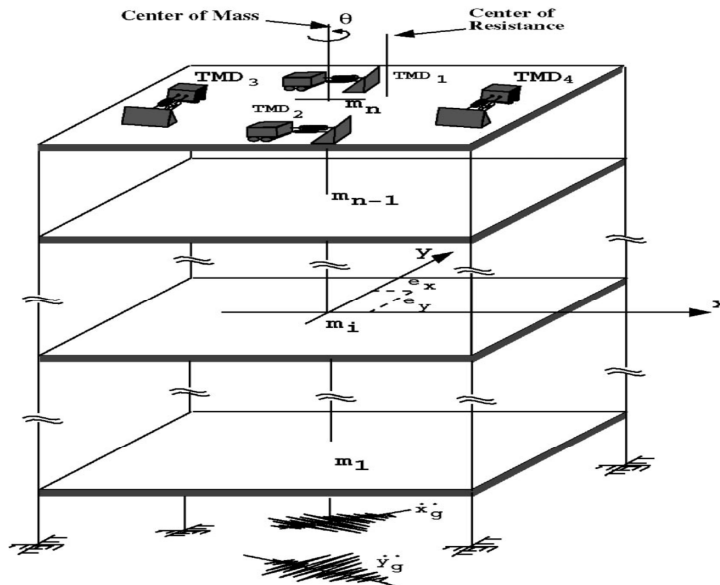


Fig-1.6 A four TMD design used for structural bi-directional vibration control [Singh et al., 2002].

The use of coupled TMDs (CTMDs) is considered by [Desu et al., 2005] who solve the multi-objective optimization problem. Comparing the performance of the CTMDs with

the conventional and bi-directional TMD proves that the first one is more effective and robust to control coupled lateral and torsional vibrations of asymmetric buildings. The CTMD arrangement is shown in Fig-1.7.

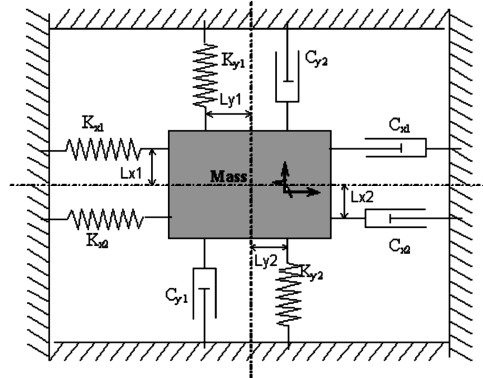


Fig-1.7 The CTMD arrangement [Desu et al., 2005].

Windmills

An early thorough investigation, driven by S/C engineering applications, Earthquake control and ship attitude engineering, was given by [Modi et al., 1990]. The authors deal with toroid (annular) passive liquid dampers, shown in Fig-1.8, to attenuate low frequency vibrations in the industrial aerodynamics of windmills. Due to the increasing impact of the sustainable energy revolution this is a still a vivid field of development in wind energy applications. Modeling and tests with 2D and 3D scale models indicate that both in laminar and turbulent flows, these dampers can successfully attenuate vortex resonance and self-excited oscillations.

In S/C engineering these torus-shaped liquid dampers are used to dampen the very long period libration modes in gravity gradient stabilized S/C and the nutation of spinning S/C. The models of S/C nutation ring dampers given by [Ancher et al., 1977], [Hong, 1989] and [Reynolds, 2002] comply with [Modi et al., 1990].

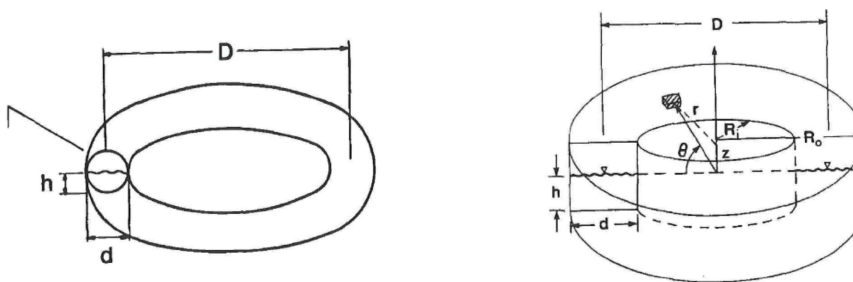


Fig-1.8 Toroid liquid ring damper (TLRD) concept applied in windmills and S/C [Modi et al., 1990].

Ships

The exuberant field of shipbuilding engineering literature was explored with as a result Fig-1.9 up to Fig-1.12 showing the application of liquid dampers to control (quasi) harmonic roll movements of ship vessels induced by sea waves. The frequency and amplitude spectrum of these are very diverse and, as a consequence, many concepts have been developed in the past. Passive and active anti-roll liquid tube constructions, called U-tanks in marine engineering, have been modeled, e.g., by [Moaleji and Greig,

2007] and [Gawad et al., 2001]. These constructions control the most severe roll motions at resonance frequencies.

In Fig-1.9 the upper pictures show (left) a C-shape endpot design interconnected by a liquid tube without a vapor tube and (right) a rectangular tank with baffles. The third picture shows diverse baffle configurations tested by [Lee and Vasalos, 1996]. Fig-1.10 shows the Frahm tank liquid damper configuration used on the SS Ypiranga [Vasta et al., 1961] with an air connection (damp) tube and air throttling valves.

A design with a control valve in the vapor tube may provide a refined Tuned U-tube Liquid Column Damper (TLCD) for active attenuation of broadband vibrations. Trade-offs between passive and active design options will be given in Chapter 2 in the scope of space systems engineering.

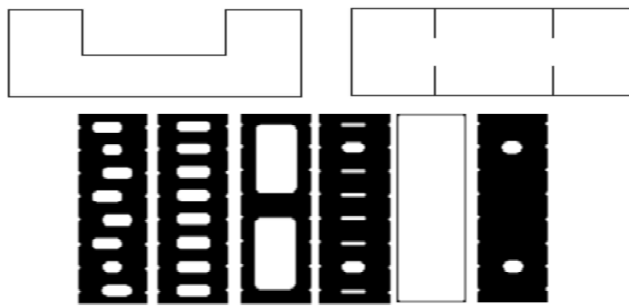


Fig-1.9 Liquid dampers used in shipbuilding engineering [Lee and Vasalos, 1996].

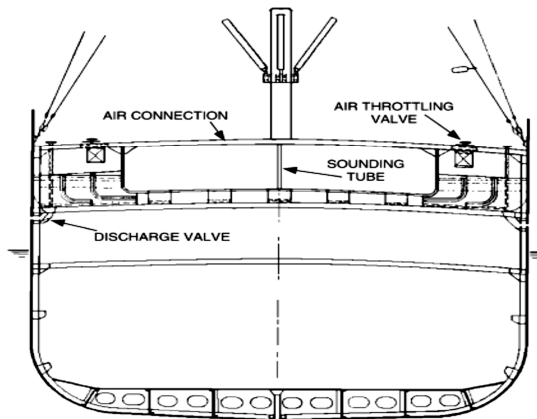


Fig-1.10 The Frahm tank liquid damper configuration used on the SS Ypiranga [Vasta et al., 1961].

In Fig-1.11 an air controlled passive tank liquid damper [Bell and Walker, 1996] was shown. The tunable U-tank liquid damper in shipbuilding engineering constructions [Shyu and Kuo, 1996] shown in Fig-1.12, will be further explored for possible space applications in Chapter 2. In this design, the active control of the nominal endpot pressure p_0 enables a dynamic control of induced structural vibrations.

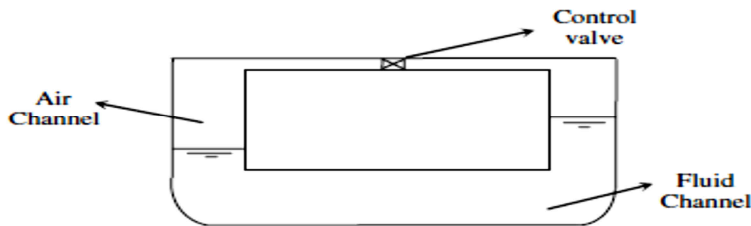


Fig-1.11 An air controlled passive tank liquid damper [Bell and Walker, 1996].

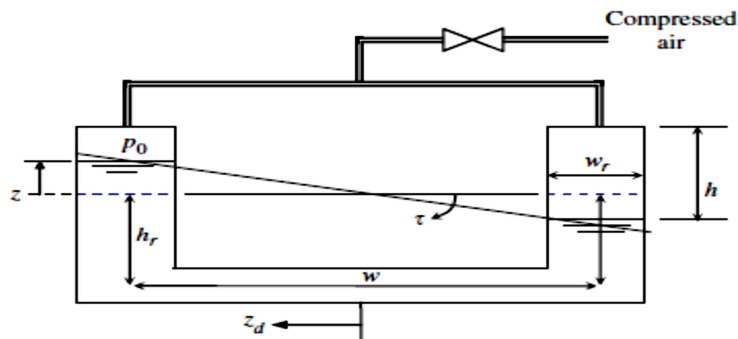


Fig-1.12 Tuneable U-tank liquid dampers in shipbuilding engineering [Shyu and Kuo, 1996].

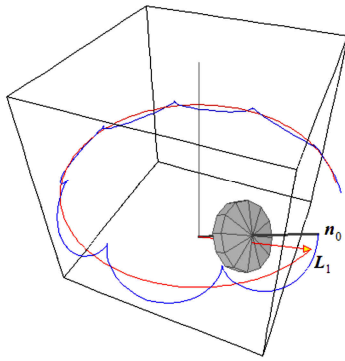
1.8 Space Applications of Passive Liquid Dampers

After the broad exploration of dampers for terrestrial applications the focus will now be their usage in space applications. A spacecraft (S/C) can be stabilized by a rotation around a spin-axis providing it with so-called gyroscopic stiffness. The inertial stability of the spin-axis can be accurately controlled by applying NDs to attenuate S/C nutation. First a glimpse in to the essentials of rotational mechanics, i.e. nutation, is given. An extensive introduction into the theoretical aspects of S/C nutation is provided by [Goldstein, 1980] and [Wertz, 2003] and Chapter 2.

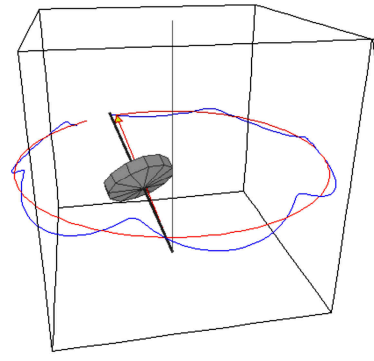
Nutation basics

Rotational mechanics and especially spacecraft (S/C) rotational mechanics is far from intuitive. The phenomenon nutation refers to an unwanted component of rotational instability of a gyroscope, a spinning S/C, a bicycle wheel, a planet or a top. Nutation is an irregular motion in the axis of rotation of an axially symmetric object. Nutation is also the name of the Euler rotations that characterize the change in angle due to the "nodding". In popular as well as in scientific literature nutation is sometimes mentioned erroneously mutation. This confusion is understandable since nutation may be described as a mutation of a stabilized precession since not any nutation is the same. Every nutation, however, is deterministically defined by the precession start conditions on basis of the solution of the Euler-Lagrange equations given by [Goldstein, 1980] and [Wertz, 2003].

An instructive three dimensional (3D) MathLab® model, given by [Butikov, 2006], facilitates the simulation of a spinning top at different start and boundary conditions. Some precession cases accompanied by nutation are shown in Fig-1.13.



The precession L_1 occurring after the axis n_0 of a spinning top is released with initial velocity zero is accompanied by nutation.



Damping out of nutation due to friction, and smoothing of the axis trajectory during transition to steady precession.

Fig-1.13 Precession and nutation induced by a gravity torque on a spinning top [Butikov, 2006]

The steady state top precession Ω [rad/sec], given by the circle in Fig-1.13, is related to the directional temporal change in angular momentum $d\mathbf{H}/dt$ by [Goldstein, 1980]:

$$\frac{d\mathbf{H}}{dt} = \Omega \times \mathbf{H}. \quad (1.1)$$

The change in $d\mathbf{H}/dt$ itself is caused by an external torque \mathbf{T} which may arise from many sources

$$\frac{d\mathbf{H}}{dt} = \mathbf{T} = M \cdot \mathbf{g} \times \mathbf{r}. \quad (1.2)$$

In the second term of Eqn. (1.2) the external torque is due to the gravitational acceleration vector \mathbf{g} . The top mass equals M and \mathbf{r} is the vector from the frictional rotation point to the center of mass (COM) of the top.

In the space environment, S/C precession is hardly present but only nutation due to the fact that the external torque resultant is negligible. This seems in contradiction with the precession of the Earth. The Earth's precession, however, is the result of its highly flattened asymmetrical shape. This shape causes a net external torque due to the Earth-Sun gravitational forces which differ for the upper and lower half of the globe. For the S/C series dealt with in this thesis only nutation is present. The nutation is described by the torque free Euler-Lagrange equations, to be introduced in Chapter 2.

Spacecraft passive nutation dampers

For most non-spinning S/C active 3-axis stabilization is a prerequisite. This can only be accomplished at the expense of a complex AOCs to control the six degrees of freedom. The Attitude Determination and Control System (ADCS) is therefore typically equipped with three sets of thruster pairs in (feedback) loop control.

For a spinning S/C, however, an elegant and relative simple way to obtain a passive spin stabilized spacecraft beside the use of an ADCS is the application of passive Nutation Dampers (PNDs). There are several classes of this ND category based on pendulum, magnetic or liquid sloshing [Ancher et al., 1977]. A liquid ND is a passive device providing a transfer of nutational energy into a dissipative form. The latter is the accumulated heat in the liquid which is radiated e.g. to deep space (at 4 K) or the inner S/C structure.

Nutation Dampers (ND) applied for passive spacecraft (S/C) Attitude and Orbit Control Systems (AOCS), are used now for over 50 years. The first ND ever used in the Pioneer-1 in 1958, was an annular equatorial tube type, shown in Fig-1.8, with sloshing Mercury to dampen out the nutation energy. This damping liquid and the annular ND type, however, have serious drawbacks and are overruled by alternatives as will be explained in Chapter 2 and the following chapters.

A series of space-qualified liquid NDs was built in the Netherlands with a zero failure record. These were developed for the ECS-Marecs, Giotto, COS-B, Ulysses, FY2A, MSG and Cluster S/C. The Ulysses ND was developed at Fokker Space in the early eighties and the Chinese FY-2 design in the years 1990-1992. Afterwards the intellectual heritage was taken over by the UCN Aero-Space Division (now Aeronamic) in Almelo, the Netherlands. The Cluster ND development started in December 1991 in close cooperation during phase-A and B with Fokker Space. The author was a consultant in the knowledge transfer.

The geometrical definition of the endpot geometry and the ND mounting plane choice comprises several options as can be seen in Fig-1.14 [Hong, 1987] and Fig-1.15 [Ancher et al., 1977]. The NDs can be mounted in an equatorial or meridian plane as a result of a damping performance trade-off to be explored in Chapter 2. In the context of the study in this thesis the Ulysses, FY2 and Cluster ND designs are all of the equatorial type whilst in Chapter 3 the meridian NDs of the COS-B and EQUATOR-S S/C are taken into account. In addition, Chapter 3 deals with the verification and validation of ND performance of the limited number of missions with available flight data.

The Fokker Nutation Damper

The Fokker ND uses the viscous dissipation of a fluid in a special tube construction, called the energy sink method. The construction comprises two connection tubes: a liquid tube and a vapor tube to create a set of communicating end pot vessels. The basics of ND performance were revealed in several Fokker documents [FDS, 1992]. An extended treatise of liquid NDs theory is given in Chapter 2. The ND design is given by the damping fluid type and the following four geometrical parameters which determine its performance:

- a Inner radius of the liquid tube
- b Inner radius of the liquid endpots
- h Inner height of the endpot with nominal equilibrium liquid height $h/2$
- L Length of the liquid and vapor tube.

The damper and its dimensions, shown in Figs-1.14 and 1.15, comprise two half-filled endpots interconnected by two tubes. The endpot cross-section area equals πb^2 in the YZ cross-section in the left picture of Fig-1.14 or the XZ cross-section in Fig-1.15. The "upper" vapor tube (see Fig-1.17 and 1.18) as well as half of the volume of the end pots is filled with Helium at 1 bar pressure. This supplies an undisturbed fluid motion at damp equilibrium. The fluid motion in the "lower" liquid tube (see Fig-1.17) in the equatorial (or meridian) plane "picks up" the axial acceleration component of the nutation. In an equatorial design, the ND pair is positioned in the equatorial plane at $(0, \pm Y_o, Z_o)$ with respect to the S/C center whilst the Z-axis is coaxial with the S/C spin axis.

Key design drivers

The ND acts like a damped harmonic oscillator with resonance frequency ω_0 given by Eqn. (2.59). The bandwidth, given by the Full Width at Half Maximum (FWHM) of the resonance curve, equals $\Delta\omega_0$ whilst the resonance quality factor $Q = \omega_0/\Delta\omega_0$.

The resonance frequency needs to be tuned towards the nutation excitation frequency. This is achieved on basis of modeling by the choice of the structural design geometry parameters and damping liquid properties: $\langle a, b, h, L, \eta, \rho, \sigma \rangle$. The selected damping fluid, a fluoro-carbon (a Freon) owns a high density (ρ) and appropriate dynamic viscosity (η). Due to its very low surface tension (σ), disturbance effects in the end pots (possibly causing an unwanted second time-constant) are minimized. The choice of the liquid type also influences the resonance bandwidth.

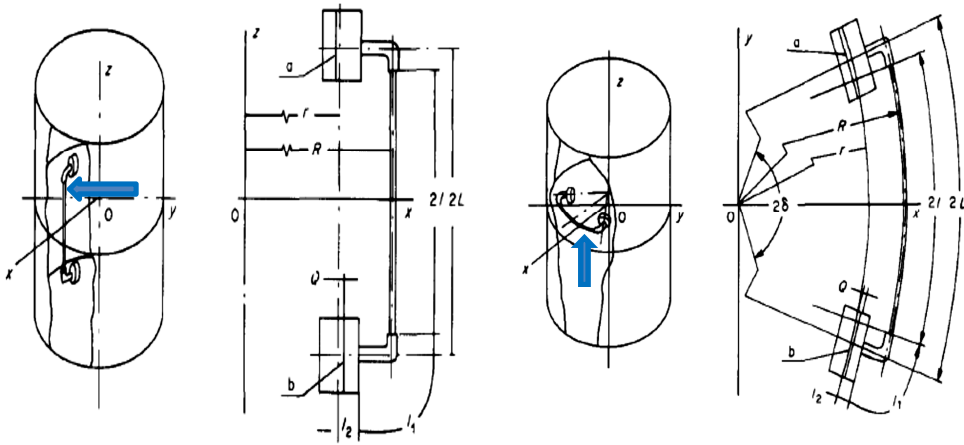


Fig-1.14 Endpot geometry defined by [Hong, 1987]. The left picture shows a meridian mounting parallel to the Z spin-axis. The right picture shows an equatorial mounting in the X-Y plane. The enlarged parts are indicated by arrows. The symbols differ from the nomenclature in the thesis.

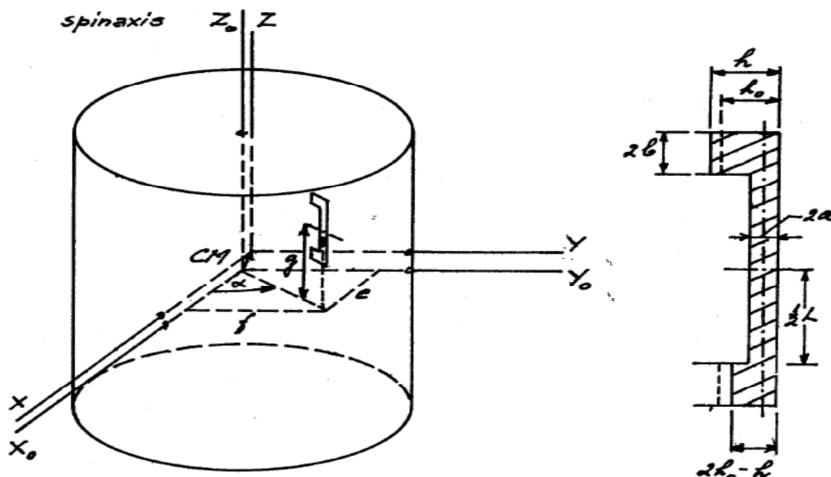
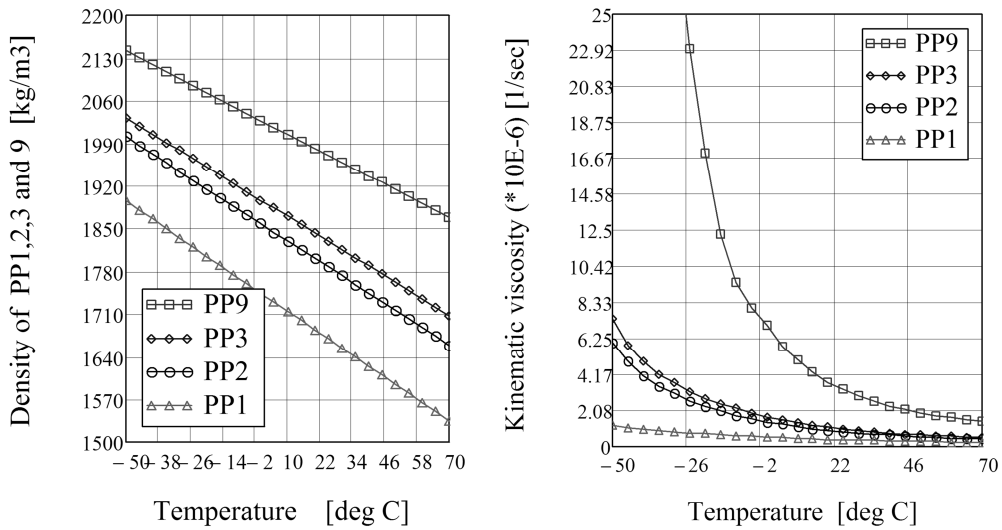


Fig-1.15 Another end-pot geometry defined by [Ancher et al., 1977]. Only the meridian mounting is shown for a tube-with-endpots damper installed parallel to the Z spin-axis.

Fig-1.16 shows the design freedom resulting from the density and kinematic viscosity of the regular four Fluoro-Carbon damping liquid choices with commercial name Flutec (types PP1, PP2, PP3 and PP9) which are qualified for radiation hardness.

**Fig-1.16**

Density range of the Flutec series PP1, 2, 3 and 9

Kinematic viscosity range of the Flutec series PP1, 2, 3 and 9

The modeling yields a first order design compliant with Eqn. (2.59). The initial design length of the liquid tube, interpreted as the tube length with in addition a factor times the radius of the endpot or liquid tube diameter, is called the effective length. From former programs this proved to be a realistic and pragmatic design rule. In terms of physics it is clear that the fluid flow is not immediately distorted after entering and leaving the end pots. This means that the effective length is as a rule larger than the physical length. Chapter 2 comprises a study of these effects and describes how to quantify them analytically. Chapter 8 will present a refined method to estimate the effective length on basis of the overall thesis results.

The two driving Ulysses and FY-2 ND designs within this thesis will be briefly introduced here. The Ulysses ND was part of the very successful Ulysses S/C mission that lasted almost two decades from its launch in November 1990 up to its de-commissioning phase in December 2008. The FY-2 ND design and qualification will be dealt extensively in Chapter 4. The development of the FY2 ND started at the same time as the analysis of the Ulysses nutation anomaly. This analysis, dealt in Chapter 5, was the backbone of the multi-mode Cluster ND design to be presented in Chapter 6 and 7.

The Ulysses nutation damper design

The Ulysses ND design, shown in Fig-1.17, is driven by the low spin-rate $\omega_z = 5$ rpm and the nutation angle damping requirement $\theta < 72'' (= 0.02^\circ)$. Though showing a regular straight ND in Fig-1.17, the design is remarkable since:

- The relative large liquid tube radius $a = 8$ mm implies sweep-up phenomena to be dealt in Chapter 5
- Three equatorial NDs are applied to comply with damping requirements over diverse operational phases.

In a regular equatorial design two redundant NDs are placed on the opposite positions of the equatorial mounting plane. Due to volumetric constraints, however, the Ulysses NDs were placed at one side of the equatorial platform at $Z = 326$ mm above the S/C equatorial Center-Of-Mass (COM) plane. The NDs are mounted at the clockwise angles 69° , 90° and 111° with respect to the +X axis (see Fig-5.10).



Fig-1.17 Mechanical drawing of the straight Ulysses nutation damper. The upper tube is the vapor tube whilst the lower one with the largest diameter is the liquid tube [courtesy Dutch Space].

The FY2 nutation damper design

The Chinese Feng-Yun 2 (Weather and Wind) meteorological S/C ND design is shown in Fig-1.18. The FY2 ND design was driven by its high spin-rate $\omega_z = 100$ rpm and the extreme required nutation angle $\theta < 0.5^\circ$. The project was gained on basis of the Fokker ND heritage although such an extreme damping range was never qualified before. The air-bearing test equipment, however, had the potential to reach the required scaled damping range. This is one of the major issues of Chapter 4.

The tubes of the FY2 ND were required to be bent, to coincide with the mounting radius $R_0 = 900$ mm as iso-centrifugal line although analysis showed that this hardly served any purpose. The outer (lowest) tube in Fig-1.18 is the fluid tube whilst the inner (upper) tube provides the vapor equilibrium above the endpots. The X-axis is the centrifugal (or in ground tests the 1-g) direction. The Y-axis coincides with the S/C fluid nutation main forcing acceleration direction. The Z-axis coincides with the S/C spin-axis and with the vertical axis of the terrestrial air bearing test setup to be dealt in Chapter 3. The drawing comprises also a mechanical support bracket (with holes in it) which boosts the lowest vibrational resonance frequency above the required 200 Hz.

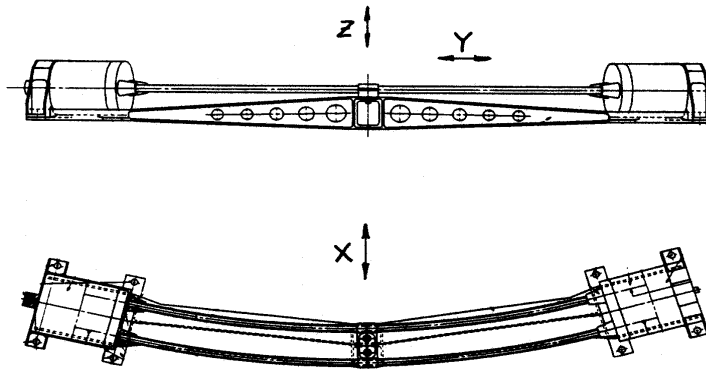


Fig-1.18 The FY-2 Flight Model ND geometry CAD parameter set $\langle a, b, h, L \rangle$ with liquid tube length $L = 515$ mm, radius $a = 3.8$ mm, end pot radius $b = 40$ mm and inner height $h = 40$ mm [courtesy Dutch Space]. The CAD geometry and dimensions are shown in Fig-4.6 whilst the definition of b for the rectangular (non-cylindrical) endpot is given in Fig-4.3.

Characteristics of Fokker nutation dampers

The radiation compatibility parameters and the damping performance of most of the liquid NDs built in the Netherlands are given in Table-1.2 and 1.3. The inertia data and (single unit) requirements of Dutch ND series are given in Table-1.3.

The dissociation of the damping liquid due to radiation is a potential threat of degraded performance as will be studied in full detail in the reliability analysis of the FY2 ND in Chapter 4 and the following section 1.8. The endpots contain most of the damper liquid since b is up to ten times the liquid damper tube radius a in a regular ND design. Therefore, to first order, the thickness of the liquid tube wall plays a minor role compared to the endpot wall thickness. The End-Of-Life (EOL) radiation compatibility for a series of NDs is given by the parameters in Table-1.2. This table includes the selected damping liquid (a Fluoro-Carbon with commercial name Flutec) as well as the thickness of the endpot wall.

Table-1.2 ND design parameters to comply with EOL radiation hardness requirements.

S/C ND project	Damping liquid [Flutec type]	Endpot wall thickness [mm]
ECS-MARECS	PP9	1.0
Giotto	PP9	1.0
ISEE-B / COSB	PP1	1.0
Ulysses / ISPM	PP1	1.0
FY2	PP1	1.5
Cluster	PP3	1.0

Normally the radiation hardness compliance record, given by Table-1.2, is sufficient for a new customer. An exception was the Chinese FY2 ND where additional analysis was asked to qualify the ND in terms of EOL radiation hardness. This extended analytical evidence is given in the last section of Chapter 4.

The following section deals with the reliability analysis of a ND design which is related to the maximum pressure build-up towards EOL by radiation degradation of the damping fluid. The requirements: no Single Point of Failure and reliability of a ND are different ones but both related to the quality of the endpot welding.

Table- 1.3 Traceable inertia data and (single) ND damper requirements for the series built in the Netherland [courtesy Dutch Space].

<i>S/C</i>		<i>GEOS</i>	<i>ECS/MARECS</i>	<i>ISEE-B/COSB</i>	<i>ISPM / Ulysses</i>			<i>FY-2</i>	<i>Cluster</i>
Orbit phase		Transfer	Transfer	Operational	Launch	Booms deployed	Operational	Operational	Operational
Spin inertia									
I_z	[kg·m ²]	110	300	54.53	314	468	572	265±12%	439.0
I_x									210.0
I_y									240.0
Spin rate	[rpm]	90 nom	60 nom	10 nom	60 (c)	5 (c)	4.9 (c)	100±10%	15±10%
Inertia ratio λ_o	[-]	1.3	1.2	1.232	1.72 1.88	1.729 1.891	1.6860 1.1841	1.125±5.0% (a) 1.166±2.2% (b)	1.95±0.04
Inertia ratio λ_x	-	-	-	-	1.388 1.505	1.193 1.266	1.258 1.349	-	-
Nutation frequency range	[Hz]	0.25 0.65	0.07 0.33	0.0387	0.72 1.17	-	0.056 0.071	0.208	0.243
Nutation amplitude									
– initial	[deg]	3	5	3.8	10	-	2	10	
– ultimate		< 0.1	< 0.035	-	< 0.1		< 0.02	< 1/7200 (0.5")	< 0.05
Temperature range	[°C]	-20 +40	-10 +55	-20 +30	-20 +40	-20 +40	-20 +40	-25 +50	-40 +30
Damping time constant	[min]	20	120		13	-	120	30 sec (a) 21 sec (b)	600
ND mass	[g]	560	700	136	560	-	560	1400 / 1500(c)	300
Z_o	[cm]	-	-	0	33	33	32.6	60-63	30
R_o	[cm]	-	-	66.8	94	86	86	90±5%	90±5

a) Preliminary values at the start of the project.

b) Definite values in the final stage of the project.

c) Worst Case

Single Point of Failure and Reliability

The requirement to avoid a single point of failure (SPF) is a strict ESA S/C design rule. Therefore the NDs are applied as a redundant pair so a single ND weld failure will never be fatal. The critical parts of the NDs are the welds at the top and bottom (lids on both cylinders) of the end-pots and the four interconnections of the damp and liquid tubes through flanges at the end-pots. This yields a total weld length

$$L_{tot} = 2 \cdot 2 \cdot (2\pi a + 2\pi b) = 8\pi(a + b) \quad (1.3)$$

with a [mm] the liquid and vapor tube radius (taken equal for convenience) and b [mm] the endpot radius.

The determination of the weld reliability requires basic some knowledge from the vivid field of weld engineering. Therefore the actual art of welding will be briefly explored first.

New discoveries and the availability of electric energy in the nineteenth century accelerated the development of modern welding techniques like friction welding (FRW), friction stir welding (FSW), flash welding (FW), resistance spot welding (RSW), gas metal arc welding (GMAW), gas tungsten arc welding (GTAW), variable polarity plasma arc welding (VP-PAW), laser beam welding (LBW), electron beam welding (EBW), and diffusion welding (DW) [Lancaster, 1997]. Welds did replace rivets rapidly in a variety of components in the space and aeronautics industry, to improve cost and structural integrity [Mendez and Eagar, 2002]. DW and EBW are preferred in commercial aircraft whilst the application of EBW for the joining of titanium components expands. In Fig-1.19 the difference between EBW and the classical GTAW is shown. The high heat intensity of EBW generates a much smaller fusion zone, Heat Affected Zone (HAZ) and little distortion. EBW has the advantage over LBW that it has no problems with beam reflection on the molten metal but has to be operated in a vacuum. This characteristic makes EBW especially suitable for the welding of titanium alloys that cannot be welded in an open atmosphere. Titanium alloys are widely applied in military aircraft (A/C) and S/C because of their light weight, high strength, and performance at elevated temperatures.

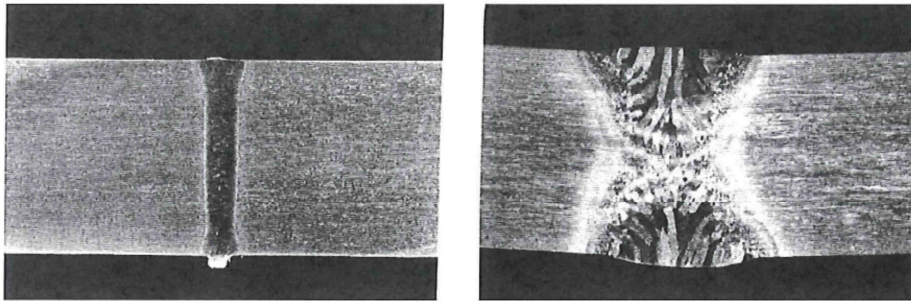


Fig-1.19 The cross sections of EBW (left) and GTAW (right) [Mendez and Eagar, 2002].

LBW and EBW comprise the most concentrated heat sources for welding, with the advantages of higher accuracy and weld quality and smaller distortions. The ND reliability assessment uses an EBW failure rate $\lambda = 2.4 \times 10^{-8} \text{ m}^{-1}\text{hr}^{-1}$ applicable to pressure bottles [FDS, 1992]. This value complies with failure rates from fusion reactor safety plans applicable to the design of the US Tokamak Fusion Test Reactor or the Joint European Torus (JET), given by [Cadwallader, 1998] and [UCLA, 2000]. An EBW failure rate of $1.8 \times 10^{-7} \text{ m}^{-1}\text{hr}^{-1}$ is given for small leaks whilst for large leaks this is a factor of 10 lower and for weld ruptures a factor of 100 lower. The upper bound failure rate for small weld leaks is set at $2.0 \times 10^{-6} \text{ m}^{-1}\text{hr}^{-1}$. If the welds are double welded with two complete welds per joint, the failure rate can be reduced by a factor of 10 as applies to double wall piping as well.

The conditional estimates of failure rates for nuclear power plant piping systems as key input to a Probabilistic Risk Assessments (PRA) are dealt with by [Fleminga and Lydellb, 2004]. A critical issue in the estimation of these parameters is the treatment of uncertainties, which can exceed an order of magnitude deviation from failure rate point estimates.

Reliability Assessment

In the earlier Fokker Space ND projects an empirical welding failure rate $\lambda = 2.4 \times 10^{-9} \text{ m}^{-1} \cdot \text{hr}^{-1}$ was taken. Table-1.4 comprises the applicable EBW failure rates of the ND reliability assessment. The ND reliability R is the chance of specification compliant EOL ND performance without welding failure given by

$$R(t, L_{tot}, \lambda) = \prod_i e^{-\lambda t L_i} = e^{-\lambda t \sum L_i} = e^{-\lambda t L_{tot}} \quad (1.4)$$

with L_{tot} total length of the weldings in one ND [m], L_i the individual weld length in a ND [m] and t the mission (EOL) duration [hr].

The typical 5 years GEO FY2 mission ($a = 3.8 \text{ mm}$ and $b = 40 \text{ mm}$) is considered with a reliability requirement of 0.999. The (bold) worst case (small leaks upper bound) with double welding failure rate 2.0×10^{-7} from Table-1.4 is taken. The application of Eqn. (1.3) and (1.4) yields a single ND reliability $R = 0.990403$. The redundancy of a ND pair increases this value to $R_p = 1 - (1 - R)^2 = 0.999908$. In case less extreme failure rates are taken into account from Table-1.4, the reliability over-classes the requirement even more.

In addition the Aluminium (type 5xxx) shielding and thicknesses are chosen such that not any specified radiation shall lead to any significant performance degradation and pressure increase beyond qualification levels. This was analysed in length for the FY2 ND qualification at the end of Chapter 4.

Table-1.4 Typical EBW failure rates applicable to the Fokker ND reliability assessment.

Origin	Failure rate [$\text{m}^{-1} \cdot \text{hr}^{-1}$]	Double welded or walled piping	Comment
Fokker [FDS, 1992]	2.4×10^{-8}		Conservative GTAW
	2.4×10^{-9}		EBW update
Tokamak fusion reactor [Cadwallader, 1998]	1.8×10^{-7}	1.8×10^{-8}	Small leaks
	2.0×10^{-6}	2.0×10^{-7}	Small leaks upper bound
	1.8×10^{-8}	1.8×10^{-9}	Large leaks
	1.8×10^{-9}	1.8×10^{-10}	Weld ruptures

1.9 Conclusions

This introduction chapter has summarized the thesis motivation, objectives, scope and the broad field of both terrestrial and space applications of liquid dampers. The cross-fertilization between these fields has been shown. One selected terrestrial liquid damper design (see Fig-1.12) will be considered in the theory Chapter 2 (section 2.8.5, called RHP-2) because of its potential to function as an active broadband space nutation damper.

The Dutch heritage with zero failure record on the design and application of space liquid NDs was discussed. The key design requirements have been explored and summarized. The basics of nutation have been briefly explained restricted to S/C nutation and will be explored in depth in Chapter 2. The reliability of a liquid damper was dealt with in the scope of the newest welding technologies.

The study in the following chapters will be confined towards S/C applications. Chapter 3 will deal with the validation and verification of the ND performance of a selected number of S/C on basis of available flight data.

The Ulysses and FY2 ND design have been highlighted as the driving design cases of this thesis. The insights gathered in the FY2 ND project (Chapter 4) and the in-orbit analysis of the Ulysses S/C AOCS anomaly (Chapter 5) led the author to the idea of a combined (multi-mode) passive damping of antenna oscillation modes and nutation. A phase-A design concept [Kuiper, 1991] was accepted and incorporated in the Cluster S/C ADCS and will be explored stepwise in Chapter 6 and 7. Chapter 8 contains the overall conclusions of the work presented in this thesis whilst Chapter 9 finally deals with the Outlook.

2 Theory of Spacecraft Nutation Damping

If the facts don't fit the theory, change the facts.

Albert Einstein, (attributed)
US (German-born) physicist (1879 - 1955)

2.1 *Introduction*

The famous picture Fig-2.1 was taken at the opening of the institute of physics at the University of Lund in Sweden in 1951, where Wolfgang Pauli and Niels Bohr are looking in wonder at a Tippe Top. This is a spinning top, which will automatically lift its center of mass while it starts to turn in the opposite direction. The interesting thing is that when the Tippe Top inverts, it also changes the direction of the rotation. At some point during the inversion, the top stops spinning around the axis through the stem and then starts to rotate the other way. At the same time, the center of mass is lifted, and the top is thus a quite interesting problem concerning conservation of energy and angular momentum [Bohr and Pauli, 1951]. The same inversion effect can be achieved by spinning a hardboiled egg [Mitsui et al., 2006], an American football, or a round (oval) smooth stone. If a hard-boiled egg is spun sufficiently rapidly on a table with its axis of symmetry horizontal, this axis will rise from the horizontal to the vertical. A raw egg, oppositely, when similarly spun, will not rise. This shows that rotational dynamics is far from intuitive and rather complex.



Fig-2.1 Wolfgang Pauli (left) and Niels Bohr (right) studying a Tippe Top (right hand picture). The picture was taken at the opening of the new institute of physics at the University of Lund on May 31 1951 [Bohr and Pauli, 1951].

In this chapter the theory of spin-stabilized spacecraft will be stepwise explored as the follow up of section 1.8 of the previous chapter. First the rotational mechanics will be dealt followed by the theory of nutation damping by liquid dampers. The latter will be extended to multiple excitations beyond the scope of nutation only. After this the ultimate residual nutation angle will be discussed and the scaling theory to deal with terrestrial scale tests. Finally the liquid damper design rules and system engineering considerations are given.

The generic theory of passive S/C attitude control by liquid nutation dampers (ND) is introduced and developed. The theory will be applied in the subsequent chapters: in Chapter 3 for the verification and validation of the applied models in a series of S/C with passive attitude control, in Chapter 4 for the design and space qualification of the Chinese FY-2 damper and in Chapter 5 for the Ulysses flight anomaly analysis. In Chapter 6 and 7 the theory is extended further and applied to the innovative design of the Cluster NDs. At first, a stepwise introduction of the applicable Attitude and Orbit Control Systems (AOCS) will be given in the following section.

2.2 Attitude and Orbit Control Systems

Spacecraft attitude control comprises the art of keeping the S/C pointed with the desired orientation. A number of applicable abbreviations and definitions are used as given by [Paluszek et al., 2008], [Chobotov, 1991], [Fortescue et al., 2003], [Ginsberg, 1998] and [Hughes, 1986]:

AOCS	Attitude and Orbit Control System
ADS	Attitude Determination System
ACS	Attitude Control Systems
ADC(S)	Attitude Determination and Control (System).

The ADCS is specified by the pointing and attitude (high) accuracy requirements which depend on the mission requirements. Nowadays most S/C are actively 3-axis stabilized with typical examples Eutelsat, Envisat and the Hubble Space Telescope (HST) given in Table-2.1.

Table-2.1 Typical pointing accuracy and stability of three key 3-axis stabilized S/C.

S/C	Mission	Pointing accuracy		Stability	
Eutelsat	Telecommunications	0.1 ⁰	360"	-	-
Envisat	Environmental monitoring	0.01 ⁰	36"	0.001 ⁰	3.6"
HST	Scientific (planetary)		0.1"		0.01"

A number of characteristic S/C configurations with 3-axis or (dual) spin-stabilization are given in Table-2.2 after [Wertz and Larson, 1999], [Wertz, 2003] and [Fortescue et al., 2003]. The combination of very rapid and accurate sensing requires the use of both gyroscopes and star sensors in the $< 0.1^0$ domain.

Table-2.2 Typical spin-stabilized and 3-axis controlled S/C platform configurations.

AOCS type	Pointing accuracy	AOCS configuration
Gravity gradient	$> 5^0$	Extended boom and additional liquid or magnetic dampers to suppress disturbances (librations). The principal moments of inertia comply with $I_z \ll (I_x, I_y)$
Spin-stabilization or 3-axis control	$1^0 - 5^0$	Sun and horizon sensors, reaction wheels or magnetorquers, thrusters for spin stabilization.
3-axis or dual spin-stabilized	$0.1^0 - 1^0$	Sun and horizon sensors, reaction wheels and thrusters, flexible modes not taken in to account.
3-axis stabilized	$< 0.1^0$	Gyros, star sensors, reaction wheels and thrusters, flexible modes modeled in controller, vibration isolated payload platform (option).

The AOCS design can be subdivided into: attitude and orbit determination, the control of both and control distribution. Attitude- and Orbit determination require sensor data acquisition to obtain an estimate of the S/C pointing and position. The control of these items requires the design and implementation of control loops and therefore the intake of control demands and subsequent conversion into actuator demands.

The S/C AOCS comprises several areas like control system design, dynamics and modeling of systems, software (S/W) design, user interface (I/F) design, close orbit control, spacecraft operations, automatic rendez-vous and docking, formation flying and close maneuvers. The dynamics of systems control can be split up into modeling and simulation to replicate the physical behavior of the S/C system [Auslander et al., 2008 and McGee et al., 2009]. In orbit S/C operations may be of critical importance for AOCS fall back scenarios. This will become explicitly clear in Chapter 5 dealing with the Ulysses S/C nutation anomaly.

The following sections will focus on passive attitude control and especially to the (extended) damping of nutation and flexible S/C structures by liquid dampers. The extended theory in the subsequent chapters in the scope of liquid damping will prove to be applicable to the combined tuned damping of S/C nutation and vibrations of antenna's or flexible parts.

2.3 Spin-Stabilized S/C

A spinning body can be passively stable about the principal axis with the largest principal moment of inertia. The intrinsic gyroscopic stiffness of the spinning S/C is used to maintain its spatial orientation in inertial space. In the absence of an external torque the S/C nutation

has to be controlled by passive damping. This is a direct consequence of the law on conservation of angular momentum \mathbf{H} in the absence of external torques acting on the spacecraft (S/C). In addition body-flexing parts and sloshing liquids (propulsion tanks and dampers) dissipate energy to a rotational energy minimum [Meirovitch, 1972]. A thorough treatise on the theory of spinning rigid bodies is given by [Chobotov, 1991], [Fortescue et al., 2003], [Ginsberg, 1998], [Goldstein, 1980] and [Hughes, 1986].

A spin stabilized platform has a number of overruling advantages for certain mission classes. To be competitive with a 3-axis stabilized AOCS its nutation control has to be very tight. The two classes to be dealt in this thesis are the high and the low rate spin-rate stabilized S/C both equipped with equatorial NDs. The intermediate class equipped with meridian NDs is dealt in Chapter 3.

High Spin-rate S/C

The 100 rpm Meteosat Second Generation (MSG) meteorological S/C, shown in Fig-2.2, requires a nutation damping value down to 2" whilst the 100 rpm Chinese FY-2 S/C to be dealt in Chapter 4 requires an ultimate value of 0.5". The MSG main AOCS requirements and its performance budget is given in Table-2.3.

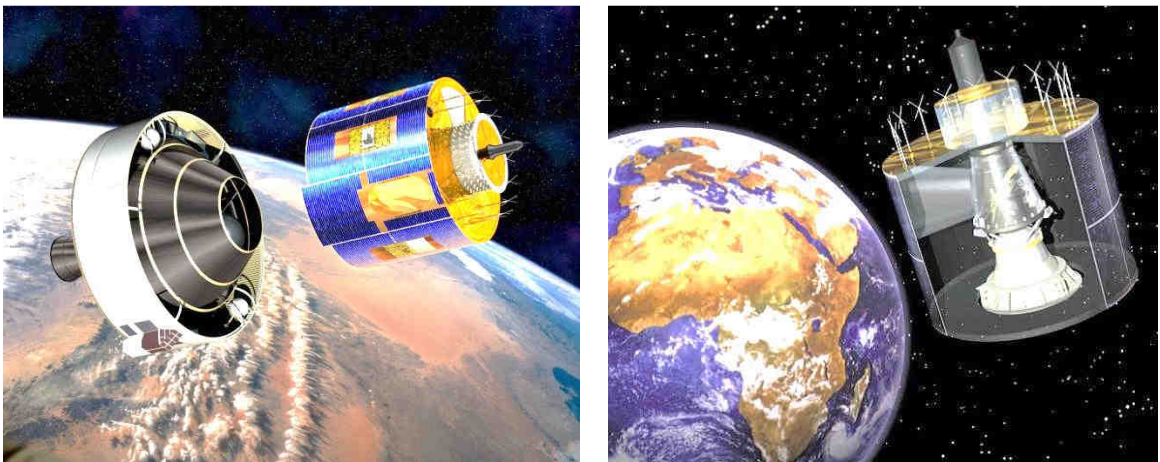


Fig-2.2 The MSG S/C right after release from the Ariane-V payload adaptor (left) and once in operational mode in Geostationary orbit with visible SEVIRI instrument (right).

The Meteosat First Generation series contains Meteosat 1 up to 7 (1977-1997) whilst the MSG comprises Meteosat 8 (MSG-1) (2002) up to Meteosat 11 (MSG-4) (launch 2013). The Meteosat Third Generation (MTG) launch is scheduled in 2015 [Weymiers et al, 1999]. After an intensive trade-off study by European industry, considering a three-axis versus a spin-stabilized platform for MSG, the decision in 1994 was made to continue with the spinning S/C concept. The clear advantages are:

1. Improved geometric image quality
2. Better spectral and geometric image resolution
3. Better mission availability
4. Moderate operational complexity
5. Equal radiometric performance though at a slightly larger instrument aperture.

The disadvantages of triple axis stabilization are: a higher S/C launch mass raising the launch costs and a very high satellite attitude control complexity with a potential degraded reliability. The latter is undesirable for an operational system [ESA, 1999].

Table-2.3 *The main MSG AOCS requirements and performance [ESA, 1999].*

Function	Requirement	Result	Remark
Sun, SSP1 ¹	< 0.05 ⁰	0.046 ⁰	outside central SAA under common mode noise and AOCS jitter with 1 rpm spin rate variation into Eclipse excluding Earth radiance error.
Eclipse, SSP2 ¹	< 200 ns, jitter < 0.18 ⁰	< 136 ns < 0.175 ⁰	
Active and Passive Nutation Damping (AND & PND)			
AND in GTO	to 0.15 ⁰ in < 10 min	5.2 < τ < 10 min	at 55 rpm and inertia ratio 1.20 < λ < 1.35
PND in GEO	0.01 ⁰ to 2 arcsec	τ < 4 min	50% margin for λ = 1.1 at 40°C and λ = 1.25 at 5°C
Spin –Rate Measurement [rpm]			
GTO	< 1 at 5-30	< 0.001	no nutation, no eclipse
5-100	< 0.1 at 30-100	< 0.002	
GEO	< 0.01	< 0.0002	
99-101 rpm	< 0.1 at 30-100	< 0.05	
Spin-Axis-Orientation Measurement			
GTO	< 0.03 ⁰	< 0.273 ⁰	all ESUs ² with on ground ESU calibration
GEO	< 0.1 ⁰	< 0.05 ⁰	no nutation, no wobble no nutation, including wobble error
Nutation Determination			
GTO	< 0.01 ⁰ resolution	0.001-0.0023 ⁰	for 0.01-5 ⁰ at 55 rpm
GEO	< 0.003 ⁰	< 0.0023 ⁰	for 0.003-0.12 ⁰ at 100 rpm

¹S/C Synch Pulse (SSP) Generation: SSP 1= Sun Synch Pulse, SSP 2= Earth Synch Pulse and spin-rate.

²ESU=Earth Sensor Unit

Low Spin-rate S/C

The low-frequency (5 rpm) class of spin-stabilized S/C is used to study Electric Fields in the Magneto-Sphere and Interplanetary Space like the 5 rpm Ulysses or Cluster S/C. The most pronounced examples are the THEMIS S/C [Auslander et al., 2008] and RBSP S/C [McGee et al., 2009]. The ADCS of this S/C class, typically applying long (tethered) antennas, is the main topic of Chapter 5, 6 and 7.

The Cluster S/C pointing performance and accuracy budget, the most relevant case in the context of this thesis and especially Chapter 7, is given in Table-2.4 [ESA, 2009]. The Cluster ND design was extended by the author [Kuiper, 1991] to dampen orthogonal modes of the wire boom antenna as well.

Table-2.4 *Spin (phase) pointing performance and accuracy budget for the Cluster S/C [ESA, 2009].*

Attitude Reconstruction Accuracy [deg]		
1. Ground Processing	0.060	
2. Spacecraft Wobble	0.060	
3. Structure Distortions	0.100	
4. Star Mapper inaccuracy	0.197	Required
Total RSS	0.24	0.25
Attitude Pointing Accuracy [deg]		
1. Minimum Precession Increment	0.050	
2. Attitude Reconstruction Accuracy	0.240	Required
Total worst case (linear)	0.29	0.50
Experiment Spin Phase Accuracy [deg]		
1. Sun Sensor Misalignment	0.023	
2. Spin Phase Error	0.028	
3. Experiment Misalignment	0.070	
4. Wobble Effect	0.013	
5. Residual Nutation	0.011	
6. Attitude Uncertainty	0.020	
7. Ground Processing Inaccuracies	0.060	
8. Structure Distortion	0.010	
9. Other effects	0.050	Required
Total RSS	0.11	0.20

2.4 Spacecraft Nutation

The torque free motion of an axis symmetrical rigid body with angular momentum \mathbf{h} is visualized in the following Fig-2.3 and 2.4. Two key reference systems are indicated:

1. Inertial Reference Frame (IRF) with $\mathbf{E} = (E_1, E_2, E_3)$. The E_3 direction through the S/C Center-Of-Mass (COM) coincides with \mathbf{h} .
2. Body Reference Frame (BRF) with $(e_1, e_2, e_3) = (e_x, e_y, e_z)$ used in this thesis. The BRF is arbitrarily tight to the S/C geometrical structure of the S/C body. In this study the BRF angular velocity $\boldsymbol{\omega} = (\omega_1, \omega_2, \omega_3)$ and BRF angular momentum $\mathbf{h} = (h_1, h_2, h_3)$.

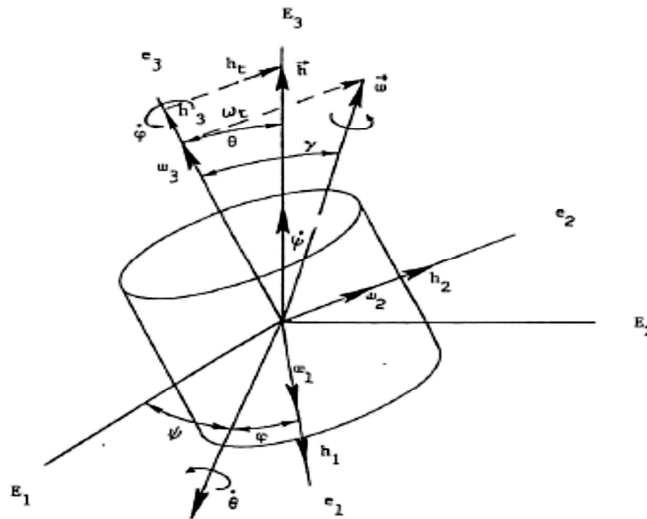


Fig-2.3 Torque free motion of a cylindrical body within the Inertial Reference Frame (IRF) denoted by $\mathbf{E} = (E_1, E_2, E_3)$ and Body Reference Frame (BRF) by $(e_1, e_2, e_3) = (e_x, e_y, e_z)$ [Chobotov, 1991].

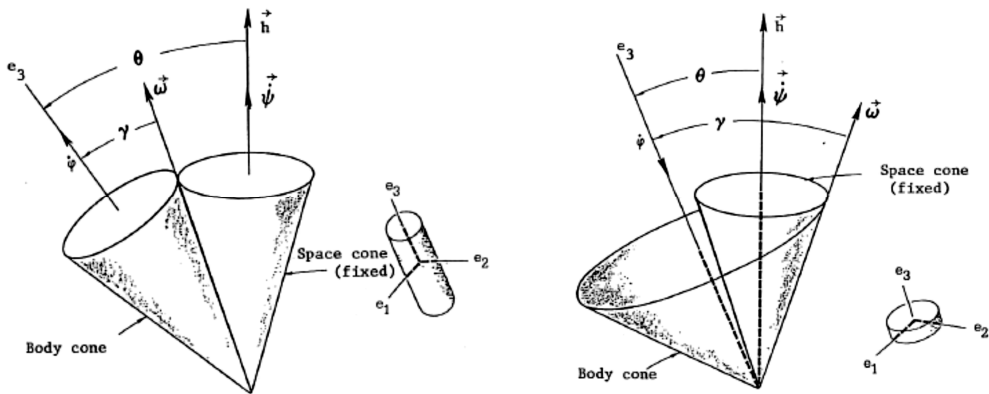


Fig-2.4 Visualization of precession and nutation of a prolate (left picture) and oblate (right picture) rotating body. The body cone rolls on the space cone. The space cone (IRF) is fixed in space while the body cone (BRF) is fixed to the S/C body cone [Wertz, 2003].

The transition between these frames is defined by three orthogonal rotations with the Euler angles ψ , θ and φ about the axis \mathbf{e}_3 , \mathbf{e}_1 and \mathbf{e}_3 again by successive matrix operations [Wertz, 1993]. The nowadays regular quaternion approach which avoids a singularity in the transition is not required or used in this thesis.

The principle axis \mathbf{e}_3 and the instantaneous rotation vector $\boldsymbol{\omega}$ are both rotating around the axis of the spatially fixed angular momentum vector \mathbf{h} in the space Inertial Reference Frame (IRF). Precession is the rotation of the S/C body \mathbf{e}_3 vector about the \mathbf{h} vector. This motion is accompanied by a rotation of the \mathbf{e}_3 vector about an axis perpendicular to the \mathbf{h} axis called nutation. The nutation angle θ is compliant to the Euler angle with purpose and defined by the angle between the principal body axis \mathbf{e}_3 and angular momentum vector \mathbf{h} . Precession and nutation, a one-egg twin of counter-intuitive motion of a spinning body, are simultaneously shown as the spatial directional variation of the \mathbf{e}_3 BRF vector on the unit sphere in Fig-2.5. The unit vector nods up and down on the unit sphere between the extremes θ_1 and θ_2 and is therefore nutating around the precession. In the picture the (residual) nutation is defined by $\Delta\theta_{nut} = \theta_1 - \theta_2$. This was elaborated mathematically by [Goldstein, 1980] using the Lagrange approach rather than the Euler equations. The derived results are valid for a child's top as well as for the complex physical behavior of any gyroscope.

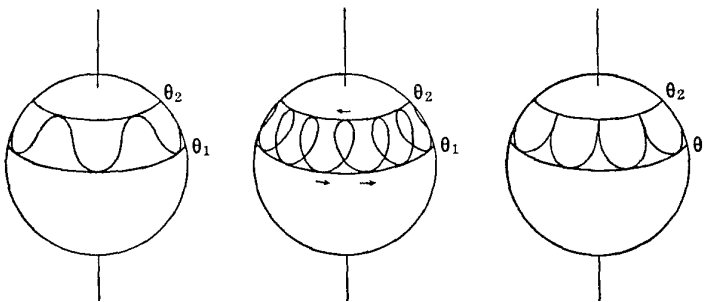


Fig-2.5 Nutation defined as the spatial directional variation of the BRF Z-axis unit vector \mathbf{e}_3 on the unit sphere [Goldstein, 1980].

In this chapter the expression for the nutation angle, forcing acceleration, power dissipation rate and damping time constant are derived. It is assumed that the body fixed axes $\langle X, Y, Z \rangle$ are the BRF principle axes of the spacecraft (S/C). This makes the principal inertia-tensor \mathbf{I} diagonal since

$$\mathbf{I} = \begin{bmatrix} I_{xx} & -I_{xy} & -I_{zx} \\ -I_{xy} & I_{yy} & -I_{yz} \\ -I_{zx} & -I_{yz} & I_{zz} \end{bmatrix} = \begin{bmatrix} I_x & 0 & 0 \\ 0 & I_y & 0 \\ 0 & 0 & I_z \end{bmatrix} \quad (2.1)$$

with $I_x = I_{xx} = \int_M (y^2 + z^2) dm$ and $I_{xy} = \int_M xy dm$.

The other moments of inertia follow by cyclic permutation. The stable S/C spin-axis is defined as the Z -axis which means that the moment of inertia I_z is the largest. This will be made clear in section 2.6.

The dynamic Euler equations of motion [Goldstein, 1980] for a rigid S/C, taking body-fixed axes, at a steady inertia \mathbf{I} are derived from the S/C momentum equation.

The general solution with total exerted torque $\mathbf{T} = \mathbf{T}_{disturb} + \mathbf{T}_{control} \neq \mathbf{0}$ [N·m] on the S/C is dealt with by [Wertz, 2003]. The differential mass dm in the inertia integral is taken over the full S/C mass (M) at (internal S/C body reference) positions \mathbf{r} . In the presence of a negligible external torque \mathbf{T} the equation becomes in the BRF

$$\mathbf{T} = \frac{d\mathbf{h}}{dt} + \boldsymbol{\omega} \times \mathbf{h} = \mathbf{I} \frac{d\boldsymbol{\omega}}{dt} + \boldsymbol{\omega} \times \mathbf{h} = \mathbf{0} \quad (2.2)$$

with

$$\mathbf{h} = \int_M \mathbf{r} \times (\boldsymbol{\omega} \times \mathbf{r}) dm = \mathbf{I} \cdot \boldsymbol{\omega} \quad \text{angular momentum vector [kg·m}^2\text{/s]}$$

$$\boldsymbol{\omega} = (\omega_x, \omega_y, \omega_z)^T \quad \text{S/C body fixed angular rotation vector [rad/s]}$$

$$E = \boldsymbol{\omega}^T \mathbf{I} \boldsymbol{\omega} \quad \text{kinetic rotation energy of the S/C [J].}$$

With these assumptions the Euler equations in component form reduce to:

$$I_x \frac{d\omega_x}{dt} = (I_y - I_z) \omega_y \omega_z \quad I_y \frac{d\omega_y}{dt} = (I_z - I_x) \omega_z \omega_x \quad I_z \frac{d\omega_z}{dt} = (I_x - I_y) \omega_x \omega_y \quad (2.3)$$

The torque-free solution of Eqn. (2.2) is described by Jacobian elliptic functions given by [Abramowitz, 1965] and [Ginsberg, 1998]. Rearranging Eqn. (2.3) into $\ddot{\omega}_x + \Omega^2 \omega_x = 0$ at small nutation angles with consequently $(\omega_x, \omega_y) \ll \omega_z$ (constant), the solutions of the Euler equations simplify to:

$$\omega_x = -A_x \sin \Omega t \quad \omega_y = A_y \cos \Omega t \quad \omega_z = \omega_{z0} \text{ (constant)} \quad (2.4)$$

with

$$\Omega = (\lambda - 1) \omega_z \quad \text{nutation frequency [rad/sec]} \quad (2.5)$$

$$\lambda = \sqrt{(\lambda_x - 1)(\lambda_y - 1)} \quad \text{lateral (RMS) inertia ratio [-]} \quad (2.6)$$

$$\lambda_x = \frac{I_z}{I_x} \text{ and } \lambda_y = \frac{I_z}{I_y} \quad \text{X, Y normalized inertia ratios [-]} \quad (2.7)$$

$$\frac{A_y}{A_x} = \frac{\lambda_y}{\lambda_x} \sqrt{\frac{\lambda_x - 1}{\lambda_y - 1}} \quad \text{nutation (lateral) amplitude ratio [-].} \quad (2.8)$$

In the course of a S/C design project the nominal inertia λ_0 is specified within the range $\lambda_{min} < \lambda_0 < \lambda_{max}$. Starting from phase A towards phase C/D the range confines and the inertia value λ_0 maturizes towards its final value. This has a huge impact on the ADCS design as will become clear in Chapter 4 and beyond.

The S/C kinetic energy E and its final value E_f after dissipation of the nutational energy at constant angular momentum H are related by

$$E = E_f + \Delta E \quad (2.9)$$

with

$$\Delta E = \frac{I_z \lambda_x - 1}{2 \lambda_x^2} A_x^2 \quad \text{and} \quad E_f = \frac{\mathbf{h} \cdot \mathbf{h}}{2 I_z} = \frac{L_z^2}{2 I_z} = \frac{1}{2} I_z \omega_z^2.$$

Moreover for further analysis the following equations apply

$$h = (I_x^2 \omega_x^2 + I_y^2 \omega_y^2 + I_z^2 \omega_z^2)^{\frac{1}{2}} \quad E = \frac{1}{2} (I_x \omega_x^2 + I_y \omega_y^2 + I_z \omega_z^2) \quad \text{with} \quad I_{total} = \frac{h^2}{2E} \text{ converging to } I_z \text{ when the nutation thus } \Delta E \text{ decreases.} \quad (2.10)$$

The nutation angle θ is defined by the angle between the nominal spin Z-axis and \mathbf{h} so

$$\sin^2 \theta = \frac{(I_x \omega_x)^2 + (I_y \omega_y)^2}{(I_x \omega_x)^2 + (I_y \omega_y)^2 + (I_z \omega_z)^2} \cong \tan^2 \theta = \frac{(I_x \omega_x)^2 + (I_y \omega_y)^2}{(I_z \omega_z)^2}. \quad (2.11)$$

The latter part of Eqn. (2.11) is valid at small nutation angles. Combining this part with Eqns. (2.2) until (2.6), the equation of the time dependent nutation angle is obtained:

$$\theta(t) = \frac{A_x}{\omega_z \lambda_x} \sqrt{1 + \frac{\lambda_x - \lambda_y}{\lambda_y - 1} \cos^2 \Omega t} \approx \frac{A_x}{\omega_z \lambda_x}. \quad (2.12)$$

In case of (lateral) symmetry the transverse inertia components and nutation amplitudes become $\lambda = \lambda_x = \lambda_y$ and $A_x = A_y$ so

$$\theta = \frac{A_x}{\omega_z \lambda_x}. \quad (2.13)$$

So far nutation has been dealt as a phenomenon in the absence of precession which is valid for the S/C passive ADCS systems to be dealt with in the scope of this thesis. In reality there are always slight external (gravitational) torques causing both phenomena with nutation being a (major) side effect.

2.5 Quasi-rigid Spacecraft Configuration

A rigid S/C body does not exist. Internal inertial force fields vary with time and may induce time-dependent deformations in case of flexible parts and the presence of (sloshing) fluids. In our case the existence of a quasi-rigid condition is needed to deal with the dissipative action of the nutation dampers (NDs) independently from the S/C equations of motion.

This desired condition, analytically described by [Hughes, 1986], is called the ‘major-axis rule’ (Z-axis) for a spinning S/C being fulfilled if $\Delta E \ll E_f$ whilst the ratio of ND liquid mass m versus S/C mass obeys $m/M \ll 1$. The latter condition determines that the damper acts uncoupled from the S/C dynamics whilst the coupling factor is given by $(1 - m/M)^{-1}$ [Ancher et al., 1977]. A more detailed analysis of the quasi-rigid S/C condition requires

$$\frac{dI_{total}}{dt} = -\frac{I_{total}}{E} \dot{E} \geq 0 \quad (2.14)$$

and to ensure that the time derivatives are small enough to define the quasi-rigidity

$$\left| \frac{\dot{I}_{total}}{\omega I_{total}} \right| = \left| \frac{\dot{E}}{\omega E} \right| \ll 1 \quad \text{with } \omega = |\boldsymbol{\omega}|. \quad (2.15)$$

These conditions are essential for the S/C nutation cases to be dealt in the following chapters.

2.6 Stability of a Spinning Spacecraft

The stability of the spin-axis is the key issue for a spin stabilized S/C ADCS. Using perturbation theory [Ginsberg, 1998] proves that the following characteristic parameter ξ determines if a transient in the orientation is stable

$$\xi = \frac{h}{I_y} \sqrt{\frac{(I_z - I_x)(I_y - I_x)}{I_y I_z}}. \quad (2.16)$$

This equation refers to time evolutions in the order of $\exp(-\xi t)$ with small initial disturbances. The stability of a free S/C rotation solution is defined by $(I_z - I_x)(I_y - I_x) > 0$ as given by Eqn. (2.16). The motion is therefore stable for either $I_z > I_x$ and $I_y > I_x$ or $I_z < I_x$ and $I_y < I_x$. This proves that a stable motion is only possible about a minor or major axis but not about an intermediate axis. For these cases the nutation angle θ will never exceed its bounded value determined by the initial conditions. As a consequence the S/C inertias are normally classified by the relation $I_z > I_y > I_x$.

The condition applies to the spinning S/C cases in this thesis since their inertia values comply with the spin stability rule $\lambda > 1$. This becomes clear by using a comparable approach, referring to the energy sink method to be dealt in section 2.7. The rule is obtained by expressing the nutation angle θ in the angular momentum h and the kinetic energy E of the S/C using Eqns. (2.10) and (2.11). Taking for simplicity (not violating the general principle) a symmetrical S/C by applying the $\lambda = \lambda_x = \lambda_y$ relationship, the nutation angle time derivative is expressed by the following equation

$$\frac{d\theta}{dt} = \frac{2I_x I_z}{(I_z - I_x) h^2 \sin 2\theta} \frac{dE}{dt} \quad (2.17)$$

A dissipation of S/C kinetic energy, indicating $dE/dt < 0$, may be induced by flexible spacecraft parts or sloshing of propellants. In that case Eqn. (2.17) proves that only if $I_z > I_x$ is valid the nutation will decrease. A stable spinning condition therefore only exists about the Z-axis. The spin stability requirement can therefore be defined by the relation $\lambda > 1$ and consequently also by the spin stability margin of safety $MS = \lambda - 1 > 0$. Practically spoken this favors a disk shape and not a rod shape.

Scientifically spoken the S/C is called oblate and stable when the nominal spin-axis is coaxial with the maximum moment of inertia (MOI) axis and prolate and unstable otherwise. The nowadays classical example of a prolate S/C was the Explorer-1 (1958) where this basic rule was violated in the design. This first US S/C became unstable since it

started spinning on an inertia axis perpendicular to its rotation (long) axis. This was due to energy dissipation in the 22-inch flexible antennas shown in Fig-2.6 and 2.7. This meant a hard lesson learnt in terms of rotational space mechanics.

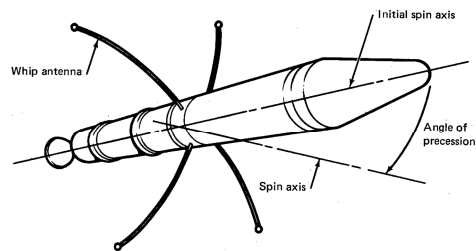


Fig-2.6 The Explorer-1 S/C model, held by JPL's Director William Pickering, scientist James Van Allen and rocket pioneer Werner von Braun (left). The right picture shows clearly the four 22-inch flexible antennas which caused the nutation instability [NASA, 1969].

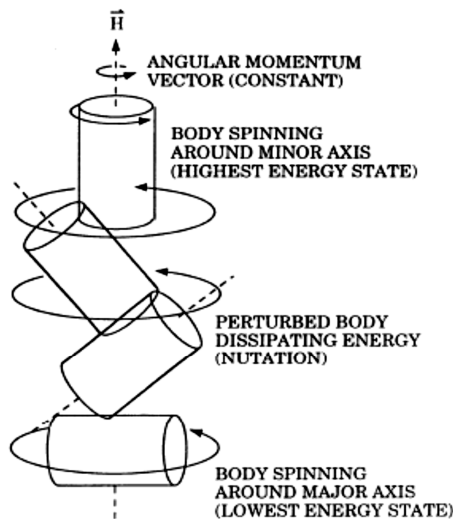


Fig-2.7 Example of a system that evolves from an unstable maximum-energy state of a body spinning along a minor axis to the stable minimum-energy state, invoking nutation by energy dissipation [Bryson, 1994].

Even in the decennia after the 1960s diverse nutation anomalies occurred due to internal dissipation or solar thermal deformation of flexible antennas. In the 60s these were Explorer-1, Alouette, Explorer XX and AT-5 [NASA, 1969]. In the 70s, 80s and 90s others followed like the Ulysses S/C (launch 6 BOL October 1990 and EOL 30 June 2008) which showed shortly after launch a considerable nutation anomaly. The Ulysses case is the main topic of Chapter 5.

2.7 Forcing Acceleration, Power Dissipation and Time Constant

In the space fixed (IRF) system using $\mathbf{r}(E_1, E_2, E_3)$ and $\boldsymbol{\omega}(E_1, E_2, E_3)$ the acceleration vector $\mathbf{a}_s(E_1, E_2, E_3)$ equals

$$\mathbf{a}_s = \frac{d^2\mathbf{r}}{dt^2} + \frac{d\boldsymbol{\omega}}{dt} \times \mathbf{r} + 2\boldsymbol{\omega} \times \frac{d\mathbf{r}}{dt} + \boldsymbol{\omega} \times (\boldsymbol{\omega} \times \mathbf{r}). \quad (2.18)$$

The acceleration $\mathbf{a}(e_1, e_2, e_3)$ at $\mathbf{r}(e_1, e_2, e_3)$ with $\boldsymbol{\omega}(e_1, e_2, e_3)$ in the satellite body-fixed (BRF) coordinates simplifies to a tangential and a centrifugal contribution given by

$$\mathbf{a} = \frac{d\boldsymbol{\omega}}{dt} \times \mathbf{r} + \boldsymbol{\omega} \times (\boldsymbol{\omega} \times \mathbf{r}). \quad (2.19)$$

In the following $\dot{\omega}_z = 0$ is assumed and the lateral velocities are neglected so $\omega_x, \omega_y \ll \omega_z$.

Nutation Dampers

Expressions for equatorial and meridian dampers and trade-offs between the two options are found in [Hong, 1987], [Bongers, 1984] and [Ancher et al., 1977]. The latter derives the damping equations of diverse damper types (rigid active mass, pendulum type, annular, tube with endpots) using the Lagrange principle. Diverse dampers for terrestrial and space engineering applications were shown in Chapter-1.

Equatorial mounting

An equatorial configuration with two NDs (one extra redundancy) mounted at $(\pm R_m \cos \alpha, \pm R_m \sin \alpha, Z_0)$ is considered. Taking the angle with the X-axis $\alpha = 90^\circ$ the mounting position is $(0, \pm R_0, Z_0)$ and the axial acceleration $\mathbf{a}_{1,2}$ in the liquid tubes results by combining Eqn. (2.3) and (2.19) with the superscript T denoting the transposed vector

$$\mathbf{a}_{1,2} = \pm Z_0 \left(\frac{d\omega_y}{dt} + \omega_x \omega_z, 0, 0 \right)^T. \quad (2.20)$$

Using the approximate Euler solution Eqn. (2.13) the X component equals

$$a_x = \theta \omega_z^2 Z_0 (\lambda^2 - 2\lambda + 2\lambda_x) \sin \Omega t$$

with

$$a_0 = \theta \omega_z^2 Z_0 (\lambda^2 - 2\lambda + 2\lambda_x) \text{ the amplitude in the X direction and} \quad (2.21)$$

$$a_0 = \theta \omega_z^2 Z_0 \lambda^2 \text{ for a laterally symmetrical S/C.} \quad (2.22)$$

The latter Eqns. (2.21) and (2.22) prove that the nutation acceleration is in good approximation harmonic and linear dependent to Z_0 . Displacing the ND from the 0° to the 90° position (from the X-axis to the Y-axis) the liquid forcing acceleration changes from the e_y to e_x direction (e_2 to e_1).

Meridian mounting

The meridian assembly contains two NDs mounted with the liquid tubes parallel to the Z-axis at the positions $(\pm R_m \cos \alpha, \pm R_m \sin \alpha, 0)$. This yields the Z acceleration by combining Eqn.(2.3) and (2.19) so

$$\mathbf{a}_{1,2} = \pm R_m \left[0, 0, \left(\frac{d\omega_x}{dt} + \omega_y \omega_z \right) \sin \alpha + \left(-\frac{d\omega_y}{dt} + \omega_x \omega_z \right) \cos \alpha \right]^T. \quad (2.23)$$

The Energy Sink Principle

The various types of dampers, based on the so-called energy heat-sink principle, are dealt by [Ancher, 1977], [Chobotov, 1991] and [Hughes, 1986]. The specific liquid damper design ('tube-with-endpots') to be regarded here, was described in Chapter 1 already. Due to the nutation driving force the ND liquid mass in this damper type will oscillate harmonically whilst the nutation will dampen out exponentially by viscous dissipation. The heat-sink principle, shown in Fig-2.8, will be elaborated in this section but is only valid for a single excitation since the dissipation is averaged over one nutation cycle. In section 2.9 the theory will be extended to multi-mode excitation cases. After extinction of the nutational rotation energy, given by Eqn. (2.9), the final kinetic energy E_f is the S/C spin energy only. At the end the difference $(E - E_f)$ has been dissipated by the (liquid) nutation dampers as a heat sink. In a steady state the damping force is equal to the nutation driving force. This means that the amount of nutation energy delivered to the ND equals the amount of dissipated energy. Before extinction the average dissipation per unit of time \bar{P} is given by

$\bar{P} = \bar{P}(a, b, L, \omega_z, \lambda, \nu, T, R_0)$ and using Eqn. (2.9) this equation becomes

$$\bar{P} = -\frac{d(E - E_f)}{dt} = -I_z \frac{\lambda_x - 1}{\lambda_x^2} A_x^2 \frac{dA_x}{A_x dt} = I_z \frac{\lambda_x - 1}{\lambda_x^2} A_x^2 \frac{1}{\tau} \quad (2.24)$$

with

τ	average damping time constant	[s]
$\mu(T)$	dynamic viscosity	[kg/m/s]
$\rho(T)$	density	[kg/m ³]
$\nu(T) = \mu(T)/\rho(T)$	kinematic viscosity	[m ² /s]
a	nutation damper tube radius	[m]
b	nutation damper endpot radius	[m]
L	effective damping length	[m]
T	temperature of the damping liquid	[K]
R_m	ND mounting radius from the spin-axis	[m].

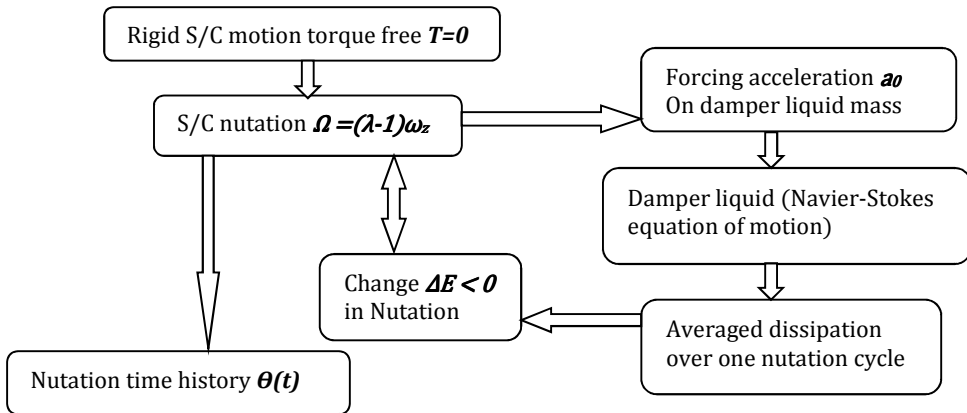


Fig-2.8 The “heat energy sink” principle adapted after [Ancher, 1977] and [Chobotov, 1991]

Eqn. (2.24) implies that an exponential time constant exists if \bar{P}/A_x^2 is a constant since

$$\frac{1}{\tau} = -\frac{1}{A_x} \frac{dA_x}{dt} = \frac{\lambda_x^2}{(\lambda_x - 1)I_z} \frac{\bar{P}}{A_x^2}. \quad (2.25)$$

This can be proved if $\bar{P}/a_0^2 = \text{constant}$ which is clear from $A_x(t) \cong \omega_z \lambda_x \theta(t)$ given by Eqn. (2.13) and Eqn. (2.21) with $a_0(t) = \theta(t) \omega_z^2 Z_0 (\lambda^2 - 2\lambda + 2\lambda_x)$ showing that A_x and a_0 as well as $\theta(t)$ are linearly related.

The desired relation $\bar{P}/a_0^2 = \text{constant}$ is indeed valid for the tube-with-endpots damper at fixed temperature and nutation rate as will be proved in section 2.8.2. Re-arranging terms finally yields Eqn. (2.26) and (2.27) for the a_0^2 normalized average nutation dissipation \bar{P} in related to the damping factor κ [s⁻¹] and nominal exponential damping time constant τ [s]:

$$\kappa = \frac{1}{\tau} = F_e(\alpha, \lambda_x, \lambda_y) \frac{(\omega_z Z_0)^2}{I_z} \frac{\bar{P}}{a_0^2} \quad (2.26)$$

with the equatorial geometry factor F_e at the regular $\alpha = 90^\circ$ position

$$F_e(\alpha = 90^\circ, \lambda_x, \lambda_y) = \frac{(\lambda^2 - 2\lambda + 2\lambda_x)^2}{\lambda_x - 1}. \quad (2.27)$$

The same derivation for a meridian ND starting at Eqn. (2.23) yields the following equation for the time constant of a meridian ND

$$\kappa = \frac{1}{\tau} = F_m(\alpha, \lambda_x, \lambda_y) \frac{(\omega_z R_m)^2}{I_z} \frac{\bar{P}}{a_0^2} \quad (2.28)$$

with the meridian geometry factor F_m at arbitrary angle

$$F_m(\alpha, \lambda_x, \lambda_y) = \frac{1}{\lambda_x - 1} [\lambda_x + \lambda_y(1 - \lambda_x)]^2 \left[1 + \frac{\lambda_x - \lambda_y}{\lambda_y - 1} \sin^2 \alpha \right]. \quad (2.29)$$

The subsequent step is to derive a mathematical expression for the a_0^2 normalized dissipation \bar{P}/a_0^2 . This is done in section 2.8.4 to 2.8.6 starting with a Hagen-Poiseuille (HP) liquid flow model yielding Eqn. (2.64) and secondly by solving the Navier-Stokes Equation (NSE) with result Eqn. (2.82). Though the HP model is a special case of the NSE this sequence was chosen, in the following section, to be in line with the historical development of the ND models at (Fokker) Dutch Space from COSB up to the Cluster S/C.

2.8 Velocity Profile and Dissipation

2.8.1 Introduction

The impact of fluid dynamics on the TLD performance and its design is vast. The practical way of dealing with this complicated topic, to be dealt with in section 2.12, has nevertheless led to a series of successful NDs. In this section, however, a systematic study of scientific fluid dynamics literature is presented. The results initiated a refined method to estimate the effective damping length.

As a first order approximation of the liquid flow in the ND tube, the HP model is regarded which assumes a parabolic laminar velocity profile. The model is able to quantify both the damping performance at small angles and the resonance behavior at sweep-up moments of nutation. The sweep-up phenomenon (“beat-up”) was indeed observed during the Performance Test Model (PTM) tests of the Ulysses ND given in Chapter 5. The HP

approach is only valid when the flow can fully develop which is generally not the case due to the harmonic nutation sweep-up force in the liquid tube. Therefore the model will be refined by deriving the NS solution which contains the Bessel functions J_0 and J_1 as a natural consequence of the cylindrical symmetry. The NS solution allows for cylindrical reverse flow layers whilst the reduction of the nutation frequency shows that a HP flow solution emerges. The NS solution was derived using diverse sources [Batchelor, 1980], [Muto and Nakane, 1996], [Papanastasiou et al., 1999], [Loitsyanskii, 1966] and [FDS, 1992]. The NS model is the backbone of refined tube flow modeling as expressed by [Sato and Kanki, 2008]. They verified their extended theoretical models for compression waves and oscillating flows in a circular pipe on the experimental work of [Muto and Nakane, 1980] with excellent agreement. The relevant results are shown in Fig-2.9 whilst the nature of the indicated Womersley parameter $\varepsilon_a = a\sqrt{\Omega/\nu}$ is explained in Table-2.5. Along the horizontal axis the normalized fluid velocity is given whilst the vertical axis shows the normalized diameter.

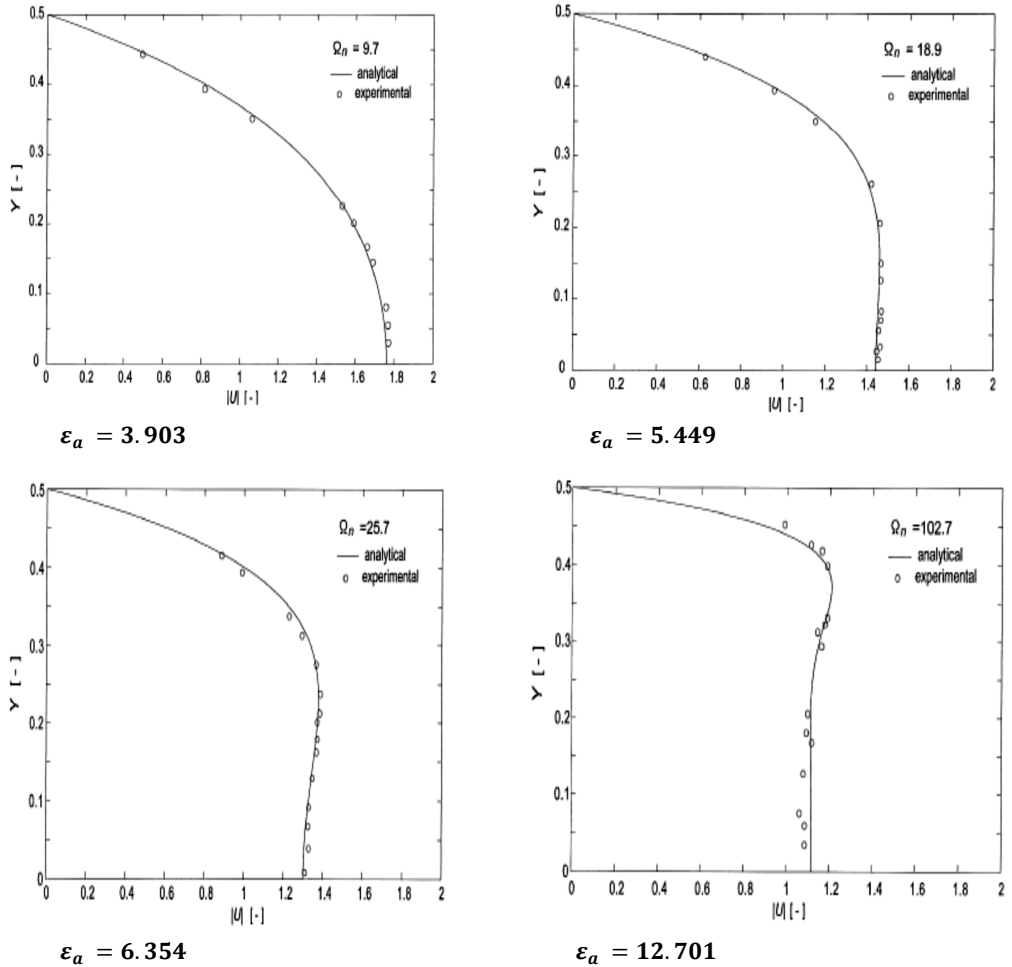


Fig-2.9 The NS solution verified for compression waves and oscillating flow in a cylindrical pipe with $\Omega_n = \frac{2}{\pi} \varepsilon_a^2$ as parameter, showing the flow velocity (horizontal) as function of the normalized radial coordinate. The parameter ε_a is the non-dimensional Womersley number [Sato and Kanki, 2008].

At small ε_a values the viscous forces apply to the full velocity profile whilst at large values they restrict to the (Stokes) boundary layer with a center core performing like an irrotational plug flow.

An intermediate HP model (RHP-1) was derived by [Häusler and Eidel, 2001] as an extension of the generic HP model from [Truckenbrodt, 1986]. This model will be explored, right after the HP model, to enable the analysis of the different results (flight and test data) from literature in Chapter 3.

A second HP (RHP-2) model, describing a tunable liquid damper (TLD) design, will be analyzed from the scientific field of shipbuilding engineering [Moaleji and Greig, 2007]. The goal was to evaluate the possibility to implement such a design in the scope of space engineering applications and especially the broadband damping of vibrations.

Before these models will be discussed, we will first investigate the impact of turbulent flow behavior and the tube inlet effects. The latter is related to the key design parameter, i.e., the definition of the effective damping length.

2.8.2 Laminar and Turbulent Performance

The liquid flow in a ND liquid tube acts with a sudden contraction in the streamlines at one side and a sudden enlargement at the other endpoint side. The liquid tube is regarded to be smooth whilst the infinite length definition $2 \cdot a \ll L$ holds. The nutation damping towards small angles copes with the transition from turbulent to laminar flows. The impact of the following items will be stepwise regarded: unidirectional versus oscillatory flows, limited tube length, rough surfaces and sharp transition areas from the endpots to the liquid tube as initiators of turbulence, additional (eddy) losses and the effective damping length.

The unidirectional flow losses at the entrance and exits of pipe flows, shown in Fig-2.10, are well described by diverse sources like [Duckworth, 1977] and [Batchelor, 1980]. The practical value in the application and efficiency of (industrial) hydraulic systems has been a strong driver for this knowledge.

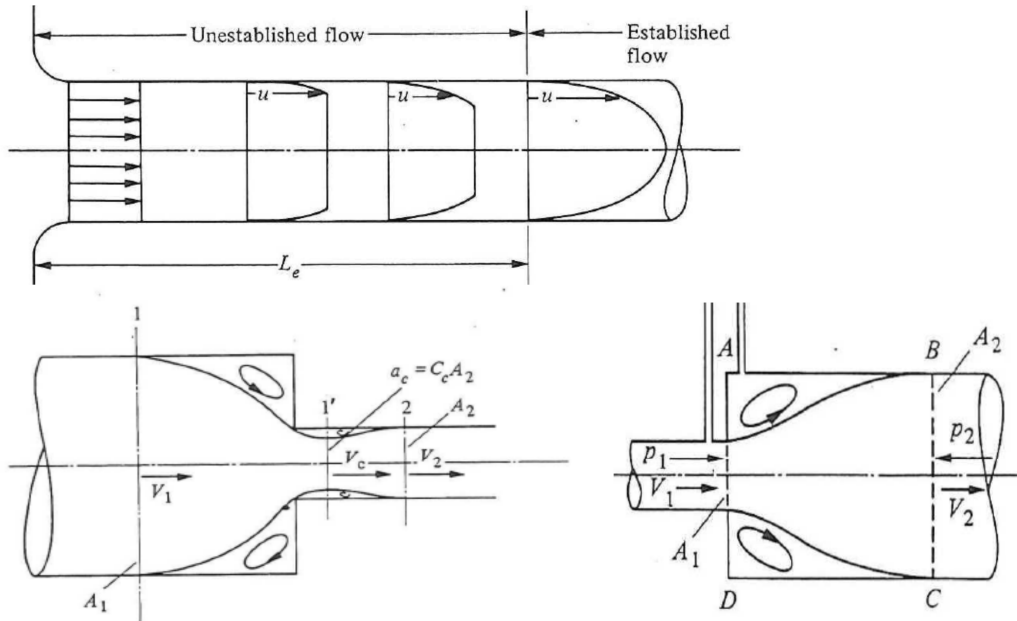


Fig-2.10 Unidirectional tube flow conditions at the inlet and exit [Duckworth, 1977].

The tube flow inlet length L_e up to the region where the HP established flow results is indicated whilst the lower pictures depict the conditions at the inlet and exit of the tube. The latter show the dissipation through eddy losses and the so-called vena contracta at the **1'** indicated position in the second picture. This is the cross-section in the inlet fluid stream where the diameter of the stream is the least and fluid velocity at its maximum.

Bernoulli's equation Eqn. (2.30a) applies at an arbitrary point along a streamline.

$$\frac{V^2}{2g} + z + \frac{p}{\rho g} = \text{constant} \quad (2.30a)$$

with

V	fluid flow velocity at a chosen point on a streamline in the liquid tube [m/s]
$g = \omega_Z^2 R$	centrifugal acceleration in the ND due to the S/C spin-rate [m/s ²]
z	elevation of the chosen point above the endpot equilibrium level as reference plane in the direction opposite to the g [m/s ²] acceleration [m]
p	pressure at the chosen streamline point

At different cross-sections of the flow in a tube the pressure difference between these positions can be solved by using Eqn. (2.30a). In addition, the so-called head loss h_f in circular tubes, given by Eqn. (2.30b) accounts for the frictional pressures losses along a tube with length L . Its format is compliant with Eqn. (2.30a) using $\Delta p = \rho g h_f$ as the pressure loss and the following Darcy-Weisbach equation

$$h_f = 4f \frac{L}{D} \frac{V^2}{2g} \quad (2.30b)$$

With

$D=2a$	tube diameter [m]	
$f = \frac{16}{Re}$	Hagen-Poiseuille friction factor [-] in the laminar $Re < 2300$ range and	(2.31)

$\frac{1}{\sqrt{f}} = -4^{10} \log \left[\frac{k_s}{3.71D} + \frac{1.26}{Re\sqrt{f}} \right]$	Colebrook-White recursive semi-empirical equation for f in the turbulent region $4000 < Re < 10^6$	(2.32)
--	--	--------

k_s	effective (RMS) roughness factor [m] obtained experimentally
-------	--

$Re = \frac{VD}{\nu}$	Reynolds number equals the ratio of momentum (inertia) to viscous forces and ν the kinematic viscosity [m ² /s].	(2.33)
-----------------------	---	--------

where the following approximate ranges of the Reynolds number apply:

$0 < Re < 10^0$	Highly viscous motion
$1 < Re < 10^2$	Laminar with strong Re dependence
$10^2 < Re < 10^3$	Laminar with applicable boundary layer theory
$10^3 < Re < 10^4$	Transition to turbulence
$10^4 < Re < 10^6$	Turbulent with moderate Re dependence
$Re > 10^6$	Turbulent with slight Re dependence.

The typical value $Re = 2300$ applies for the transition of turbulent (fluctuating) to laminar (steady) flows and vice versa in cylindrical tubes. The transition is primarily driven by Re but depends also on the wall roughness and fluctuations in the inlet flow (entrance effects).

The given straightforward definition of pressure losses based on Bernoulli's Eqn. (2.30a) for an inviscid liquid tube flow will be extended by the introduction of additional loss factors K_{in} and K_{exit} to account for the (ND) inlet and exit pressure losses. These enable a first assessment of the effective ND tube length. Before this is investigated, the stability of the applicable flow types will be addressed first.

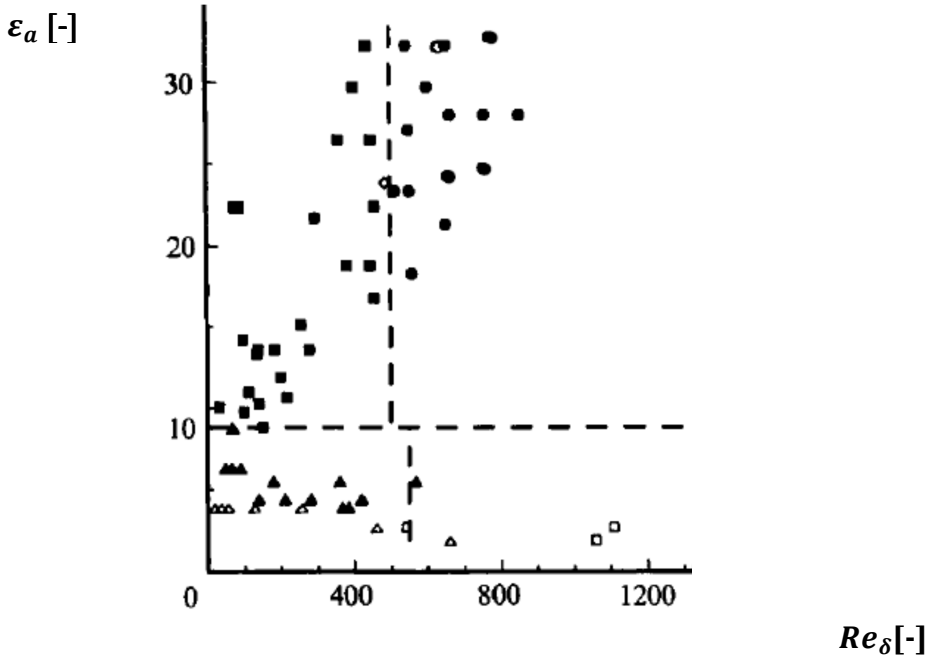
Flow stability

The characteristic parameters given in Table-2.5 are an integral part of fluid dynamics to describe the oscillating liquid flow in a ND. At large values of the Womersley parameter (see Fig-2.9) compliant to small nutation angles (typically less than 0.1°), the viscous forces are restricted to the boundary (Stokes) layer with the adapted Reynolds stability parameter Eqn. (2.34) and thickness given by Eqn. (2.35). This layer imposes the stability of the stacked laminar layers resulting from the NS solution [Eckman and Grotberg, 1991]. In the oscillatory flow caused by the nutation acceleration, however, turbulence is induced at large Reynolds (Re) numbers in the deceleration phase of the cycle [Hino et al., 1976].

In a specific ND test or flight operational case the Womersley and Reynolds Re_δ parameters enable the initial assessment of the flow stability on basis of a diagram given by [Eckman and Grotberg, 1991]. The four regions, given in the diagram Fig-2.11, result from Laminar Delamination Velocity (LDV) measurements. The ND performance was verified to be typically in the upper left LDV laminar (■) region without turbulence. In addition the ND design qualification tests have to verify the real performance which account for surface roughness, inlet effects, finite tube length and (possibly) multiple excitations (section 2.9).

Table-2.5 Description of the relevant characteristic fluid dynamics parameters in a ND design after [Batchelor, 1980] and [Prandtl and Tietjens, 1934].

Parameter	Name	Description	
$Re_\delta = \frac{V\delta}{\nu}$	Reynolds	Refers to the stability of the wall boundary layer with $V = \bar{u}$ the average fluid velocity over the tube cross-section of a creeping flow with $Re \ll 1$.	(2.34)
$\delta = \sqrt{\nu/\Omega}$	Stokes	Stokes boundary layer at the tube wall	(2.35)
$St = \frac{L}{VT}$	Strouhal	Describes oscillating flow mechanisms. At large numbers ~ 1 , the viscosity dominates the full flow yielding a collective oscillating movement of the fluid called plug flow. At low values $\sim 10^{-4}$ and below, the high-speed, quasi steady state portion of the movement dominates the oscillation. Oscillation at intermediate Strouhal numbers is characterized by the buildup and rapidly subsequent shedding of vortices with period T [s].	(2.36)
$Fr = \frac{V^2}{a_0 L}$	Froude	Defines the similarity (transfer, resistance) in inertia acceleration versus gravity (or nutation a_0) as driving acceleration.	(2.37)
$\varepsilon_a = a\sqrt{\Omega/\nu}$	Womersley	Applies to oscillatory tube flows and describes the NS imposed laminar character of the velocity profile with typical values indicated in Fig-2.9 and $\Omega_n = \frac{2}{\pi} \varepsilon_a^2$ as derived parameter.	(2.38)



■ = Laminar; ● LDV turbulent boundary layer; ◇ = hot-film laminar; ○ = hot-film turbulent boundary;
Hino et al. (1976): ▲ = laminar; Δ = weakly turbulent; □ = turbulent.

Fig-2.11 Assessment of flow stability on basis of a diagram from [Eckman and Grotberg, 1991]. The four regions result from Laminar Delamination Velocity (LDV) measurements. The ND performance was verified to be typically in the upper left LDV laminar ■ region without turbulence.

The stability of oscillatory and pulsatile flows in tubes is analyzed by [Nebauer and Blackburn, 2009] as an extension of [Yang and Yih, 1977] whilst both are based on the original article of [Womersley, 1955]. The authors validate that all laminar oscillatory (and as an extension pulsatile) flows in tubes are linearly stable.

The linear damping behavior of the Fokker damper type is valid at small nutation angles. In Chapter 4 the refined FY2 ND performance test model experiments show that at large angles (see Fig-4.10) the dissipation of nutation energy still takes place but the performance is no longer analytically predictable. In case of turbulence at large Reynolds (Re) values the damping becomes \dot{s}^2 dependent with s the tube liquid profile displacement. Therefore, the adapted NS differential equation (DE) yields no longer a closed solution and has to be solved numerically. As a rule, however, nutation damping requirements apply to the laminar ND range and the following effective damping length.

2.8.3 Effective Damping Length

Knowledge of the effective damping length is crucial to tune the ND design towards its desired frequency. The heritage of ND performance tests made clear that the effective length, in terms of viscous dissipation, extends the physical liquid tube length L . As a rule the additional length ΔL equals a few times the tube radius. The Ulysses (Chapter 5) ND calibration and the recursive FY2 PTM tests in Chapter 4 will make this explicitly clear. This empirical issue is obviously caused by the fact that both the combination of entrance flow from the endpot and inlet length in the tube and the outlet flow into the other endpot add additional damping. This important issue will be studied in depth. The following analysis of

literature will start with unidirectional flows to gather basic insights and is finally confined to the oscillatory flows which apply to the ND behavior.

Unidirectional flows

At the ultimate nutation angle range Reynolds numbers down to $Re \ll 1$ are valid. The resulting pressure driven unidirectional Stokes flow is dominated by viscous forces and characterized by Eqn. (2.34). This flow type was studied by [Wang et al., 2009] on basis of a Hamiltonian systematic method. Their analysis shows that a minimum entrance length is obtained by a pinch-off of the inlet radius from $r = a$ to $r_{inlet} = 0.76 \cdot a$ as depicted in the Figs-2.12 and 2.13.

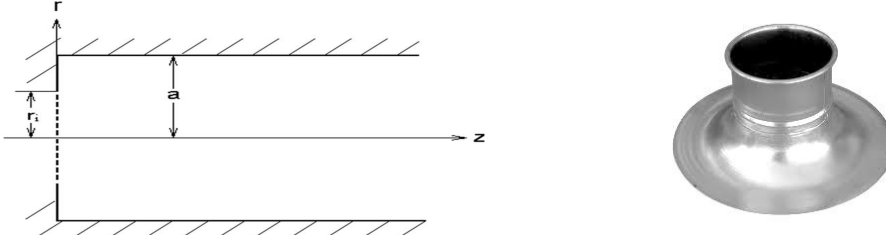


Fig-2.12 The left picture shows the square edged entry ratio $r/a=0.67$ [Wang et al., 2009] whilst the right picture shows a bell mouth duct.

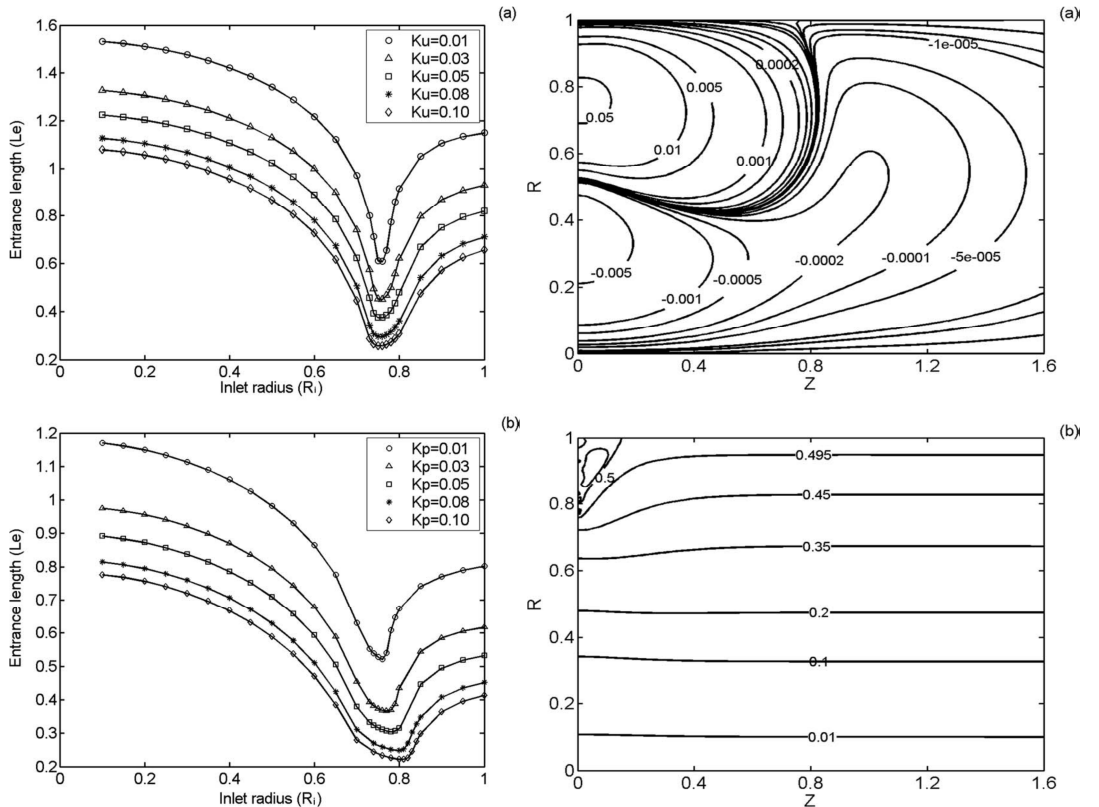


Fig-2.13 Tube inlet length in a uni-directional Stokes flow with the inlet radius R [-] and entrance length Le [-] both normalized by the tube radius $r = a$. The right pictures show the streamline patterns of the 0.76 minimum entrance solution with (a) the velocity increment streamlines corresponding to non-zero eigen-solution and (b) the real velocity streamlines solution of the same problem. The corner vortex flow in the last picture refers to inlet turbulence dissipation ("eddy") losses [Wang et al., 2009].

Such a choice could help in fixing the effective lengths in a design. The oscillatory nutation flow, however, obstructs this solution because of its different behavior and the fact that the mirrored geometry is present at the other side of the tube. Nevertheless, the impact of the optimum inlet ratio choice is shown in Fig-2.13. The left picture shows the impact of the choice on basis of a normalized velocity (Ku) or normalized pressure (Kp) criterion. An inlet ratio of 100% ($R_i = 1$) is applicable in a regular ND design. Using the **O** marked curves with the $Kp = 0.01$ or $Ku = 0.01$ criterion, the entrance (inlet) length becomes about $0.8 \cdot a$ ($Kp = 0.01$) to $1.2 \cdot a$ ($Ku = 0.01$). This range is close to the values from [Wu and Richard, 1983] who showed earlier that Stokes theory applies to moderate Reynolds numbers (in a typical ND range $< 0.1^0$) whilst evaluation of Fourier integrals yields entrance lengths of $1.2 \cdot a$ to $1.3 \cdot a$ and smaller outlet flow lengths [Lubbers et al., 2006]. These results yield an educated guess (inclined by ND test heritage) at low Ω on basis of quasi-steady non-oscillatory behavior: The additional effective length ΔL from inlet and outlet behavior is estimated to be in the range $2a < \Delta L < 3a$. This result is close to the experience from the oscillatory ND experiments at small angles and high Ω as well. The rationale for this non-obvious fact is investigated further as a key SE issue.

The classical unidirectional flow approach to define the effective length, regards the dissipation losses from the inlet and exit flows which are usually minor [Cox and Gerlando, 1947] but do contribute according to

$$L_{eff} = L + \Delta L \quad (2.39)$$

The losses in the tube at the inlet and outlet are described in analogy with Eqn. (2.30) by

$$h_{in} = K_{in} \frac{V^2}{2g} \quad \text{inlet head loss} \quad (2.40)$$

$$h_{exit} = K_{exit} \frac{V^2}{2g} \quad \text{exit head loss} \quad (2.41)$$

with

$$K_{in} = 0.5(1 - \beta^2) \quad (2.42)$$

$$K_{exit} = (1 - \beta^2)^2$$

$$\beta = \frac{a}{b_{eff}} \quad \text{damping tube inlet ratio} \quad (2.43)$$

b_{eff} effective ND endpoint “mouth” radius endpoint towards the tube.

The value of b_{eff} depends on the endpoint design of the specific ND. The endpoint design geometry of the FY-2 and the Ulysses ND is similar and shown in Fig-5.9. The depth of the bottom plate and half the inner endpoint height $h/2$ lead to an educated guess of b_{eff} .

Finally, the additional length ΔL in Eqn. (2.39) follows by combining Eqn. (2.30) and (2.31) with (2.39) to (2.43) by

$$(K_{in} + K_{exit}) \frac{V^2}{2g} = 4f \frac{\Delta L}{2a} \cdot \frac{V^2}{2g}$$

whilst the evaluation of this equation yields

$$\Delta L = \alpha Re \cdot 2a \quad (2.44)$$

with

$$\alpha = \frac{1}{64} \left(\beta^4 - \frac{3}{2} \beta^2 - \beta + \frac{1}{2} \right) \quad (2.45)$$

The Ulysses and FY2A ND design data yield $\alpha_{\max} = 0.02$ (2% “rule”) on basis of Eqn. (2.45).

This unidirectional flow result indicates that the additional effective length disappears with decreasing average velocity thus low Re value. This is not observed in scale tests for the oscillatory flow within a ND. In contrary, it is found in the limit of very small nutation angles that the additional effective length becomes a constant. [Knott and Flower, 1980] concluded already that oscillatory flows lead to a quite different behavior. [Patience and Mehrota, 1989] show that the inlet length settle time due to an instantaneously imposed pressure in a one-way flow differs for a short tube compared to a long tube. Applying their results to typical ND tube sizes yields at typical small Re values a settle time in the order of 100 s. This makes clear that the oscillatory ND flows with much shorter typical flight nutation periods $T = 10$ to 20 s impose a different behavior.

Optional inlet and outlet adapter

A method to define a distinct damping length might be the following. The pressure and dissipation loss of a bell mouth entrance (Fig-2.12, right) or exit duct is minimal and $< 10\%$ of the square edged entry applied in the Fokker ND design. The fluid is directed gradually into the liquid tube without turbulence which is the principle cause of non-viscous dissipation loss. The effective damping length may be obtained by the use of complex conformal flow mapping [Batchelor, 1980], a regular method in fluid dynamics. This idea is not worked out further here but popped up since a precise effective length determination could avoid recursive calibration efforts thus time and money. A refined method to estimate ΔL based on the following theory, will finally be derived in Chapter 8.

Oscillatory flows

Many sources throughout the years dealt with the analysis of tube entrance effects due to (non)oscillatory flows both in the laminar and turbulent range, like [Prandtl, 1934], [Cox et al., 1947], [Fargie and Martin, 1971], [Duckworth, 1977], [Bauer and Eidel, 1997] and [Nebauer and Blackburn, 2009]. They comply all in assessing a worst case tube inlet length given by

$$L_{inlet} = \alpha Re \cdot 2a \quad \text{Boussinesq's inlet length equation at constant } \alpha=6.5\%. \quad (2.46)$$

In case of an oscillatory flow the factor α becomes [Iguchi et al., 1992] in terms of the Womersley factor ε_a

$$\alpha = \frac{k(\varepsilon_a)}{2\varepsilon_a^2}. \quad (2.47)$$

The value of $k(\varepsilon_a)$ can be found in diagrams based on the model from [Iguchi et al., 1992] and [Uchida et al., 1987] by using the Womersley, Strouhal and Reynolds characteristic numbers. Their refined Three Subregion Model regards the effective particle flows at the inlets and accounts for the velocity distributions in the axial and radial direction. It was applied by [van Bakel, 1993] to the Cluster ND. The approach delivers better, i.e. smaller less conservative [as given by Eqn. (2.46)] estimates of the inlet lengths but the conclusion remains the same: In a ND relevant damping range starting at about $Re=5000$, the inlet length is of the same magnitude as the tube length itself. At low Reynolds values, however, decreased forcing accelerations and nutation angles apply whilst on basis of the given results a linear relation between L_{inlet} and ΔL is expected. The effective damping length decreases and finally exceeds the physical length with a ND specific constant amount ΔL in Eqn. (2.39). This is in line with the ND heritage and the detailed analysis of the FY2 PTM experiments. The results, given in Chapter 4 (Fig-4.11), made clear that the (additional) effective length becomes a constant at less than 0.01° flight nutation angle in the moderate

Stokes flow range $Re < 430$. This is an issue of utmost importance as will become clear by the exploration of the following theory from recent literature.

A sound analysis which reflects the latest insights in the numerical investigation of oscillatory flows in tubes is given by [Su et al., 2012]. Their analysis, validated by experiments from [Gerhard and Hughes, 1971] and [Yamanaka et al., 2002], uses the characteristic parameters Re_R and Re_A to discriminate between the diverse oscillatory flow types. The stability of the Stokes layer is related to the tube radius (a) and the amplitude p_0 of the harmonic (nutation) pressure by defining

$$Re_A = \frac{p_0^2}{\Omega^4 \delta^2} \quad \text{and} \quad Re_R = \frac{a^2}{\delta^2} \quad (2.48)$$

whilst adapting the format to comply with the ND Navier-Stokes (NS) solution (using section 2.8.3) yields

$$Re_A = \frac{1}{\nu \Omega^3} \left(\frac{a_o \beta}{\gamma^2 + \beta} \right)^2 \quad \text{and} \quad Re_R = \varepsilon_a^2 = \frac{a^2 \Omega}{\nu} \quad (2.49)$$

with a_o the nutation push-up acceleration in the ND liquid tube and constants γ and β given by Eqn. (2.79).

The authors [Su et al., 2012] solve the Reynolds Averaged Navier-Stokes equations (RANS method) with the [Saffman, 1970] turbulence model over wide parameter ranges to reveal the full structures of the fluid flow in oscillating pipe flows. At low Re_A the flows are laminar and the computed results are in excellent agreement with those predicted from the analytical solution. The laminar flow characteristics depend solely on Re_R with $Re_R \gg 1$ corresponding to the Stokes layer flow limit and $Re_R \ll 1$ to the quasi-steady laminar flow limit. At increasing Re_A the high Re_R Stokes layer flow becomes unstable at approximately 8000 and progresses through a turbulent boundary layer flow regime before reaching a quasi-steady turbulent flow regime at Re_A going to infinity. The low Re_R quasi-steady laminar flow transits directly to the quasi-steady turbulent flow with the critical value $Re_R^{3/2} Re_A^{1/2} = 2300$ as the skew dashed line in Fig-2.14. All these numerical results comply well with experiments.

The application of this theory to the ND performance analysis delivers interesting results. At $Re_A = 8000$ the critical nutation transition angle θ_A applies. This value can be obtained by a NS model sensitivity analysis using Eqn. (2.49) and successively Re can be determined on basis of the NS model as well. The ND performance typically follows a horizontal line at constant $Re_R = 50$ to 60 in Fig-2.14 going from right to left. The FY-2 ND and Ulysses ND flight performance trajectory (Re_R, Re_R) is characterized by Table-2.6 and starts at 1° (right). The Ulysses ND trajectory starts at 1° already in the Stokes laminar range whilst the FY-2 ND starts in the turbulent boundary layer flow range and enters the Stokes range only at about 72° . The reason is the high nutation acceleration in the FY-2 liquid as expressed by Eqn. (2.22) with its quadratic spin-rate dependence.

A very important result with respect to the design and tuning of NDs is derived in the experimental studies of [Yamanaka, 2002] and [Gerhard and Hughes, 1971]. In oscillating tube flows the vorticity diffuses in the entrance region only across the oscillatory boundary layer with thickness δ . This implies that the inlet length is smaller compared to a unidirectional steady flow with a factor close to δ^2/a^2 as evidenced experimentally by the authors. The dimensionless entrance length of an oscillating pipe flow can therefore be obtained from the steady case by adapting Eqn. (2.46) into

$$L_{inlet} = \alpha Re_R^{-1} Re \cdot 2a \quad (2.50)$$

This equation beside Eqn. (2.46) yields educated guesses for the additional effective damping length as will be made clear in Chapter 7 after the extended analysis of the Ulysses, FY-2 and Cluster NDs performance tests in Chapter 4, 5 and 7.

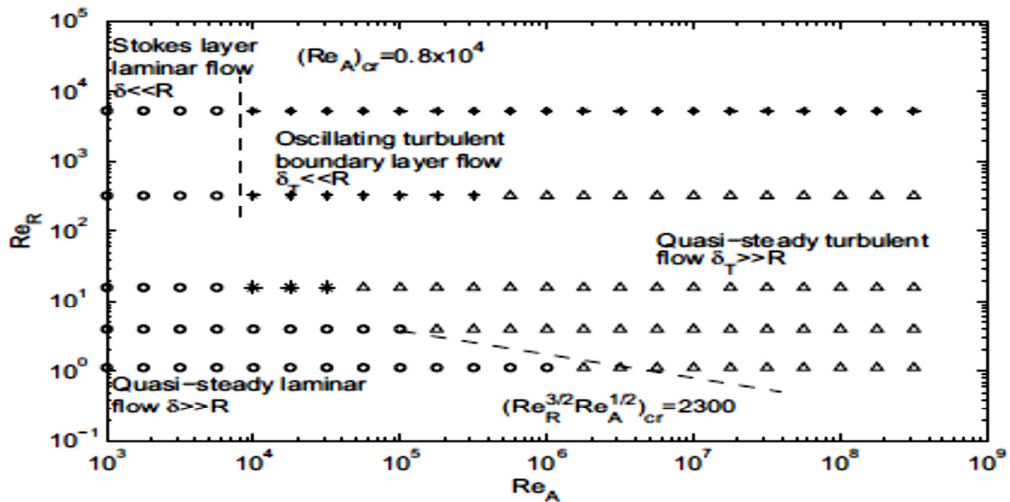


Fig-2.14 The diverse regimes of oscillating tube flows using the coordinates (Re_A, Re_R) with o : laminar flow; $*$: oscillating turbulent boundary layer flow; Δ : quasi-steady turbulent flow; dashed lines: flow transition lines at the two extremes corresponding to boundary layer flows and quasi-steady viscous flows [Su et al., 2012].

Table-2.6 Flight liquid flow trajectory (Re_R, Re_A) of the 5 RPM Ulysses and 100 RPM FY-2 ND. The nutation angles $0.5''$ (FY-2) and 0.02° (Ulysses) are the specified maximum values.

	ω_z [rpm]	Re_R [-]	δ [mm]	a [mm]
FY-2	100	60	0.492	3.8
Ulysses	5	51	1.121	8.0

← Decreasing nutation

	θ	0.5'' (FY-2)	3.6''	36''	0.02 ^o (Ulysses)	360''=0.1 ^o	1 ^o
FY-2	Re_A [-]	0	23	2.2x10 ³	9.1x10 ³	2.3x10 ⁵	2.3x10 ⁷
Ulysses		0	0	1	2	62	6.2x10 ³

In the following sections the four applicable models (HP, RHP-1, RHP-2 and NS) with common NS basis are dealt with. They cover the full scope of nutation modeling and its verification and validation in Chapter 3, 4, 5, 6 and 7.

2.8.4 Hagen-Poiseuille Model

The HP model yields the first assessment of the liquid tube dissipation. Its derivation comprises the Lagrange principle and includes the friction in both the liquid tube and the endpot walls. Applying the Poiseuille parabolic velocity profiles $u(r)$ in the liquid tube and $w(r)$ in the endpots yields the following equations and derived parameters

$$u(r) = 2\bar{u} \left(1 - \frac{r^2}{a^2} \right) \quad \text{and} \quad w(r) = 2\bar{w} \left(1 - \frac{r^2}{b^2} \right) \quad \text{velocity profile in tube and endpot}$$

$$s \text{ and } s_0 = \Delta h = \frac{a^2}{b^2} s \quad \text{tube and endpot liquid level displacement} \quad (2.51)$$

$$\dot{s} = \bar{u} \text{ and } \dot{s}_0 = \bar{w} = \frac{a^2}{b^2} \dot{s} \quad \text{tube and endpot average liquid velocity.} \quad (2.52)$$

In the following equations the kinetic energy in the liquid tube E_a and endpots E_b as well as the total energy $E(t)$ are derived. The potential energy to displace the endpot liquid levels against the centrifugal force equals $V(t)$ and balances $E(t)$ by the Lagrange energy equilibrium principle:

$$E(t) = E_a + E_b = \frac{1}{2} \rho L \int_0^a 2\pi r u(r)^2 dr + \frac{1}{2} \rho s_0 \int_0^b 2\pi r w(r)^2 dr = (a_1 + b_1 s) \dot{s}^2 \quad (2.53)$$

$$V(t) = -\omega_z^2 R_o \rho \pi b^2 s_0 s_0 = c_1 s^2 \quad (2.54)$$

with

$$a_1 = \frac{2}{3} \pi \rho a^2 L \quad b_1 = \frac{2}{3} \pi \rho \frac{a^6}{b^4} \quad c_1 = -\pi \rho \frac{a^4}{b^2} \omega_z^2 R_o.$$

The nutation force in the liquid tube equals $F_x(t) = \pi a^2 L \rho a_0 \cos(\Omega t - \varphi)$ as caused by a single harmonic excitation. The sum of the frictional force F_{vx} in the liquid tube and F_{vy} in the endpot equals

$$F_v = F_{vx} + F_{vy} = 2\pi a L \mu \left(\frac{\partial u}{\partial r} \right)_{r=a} + 2s_0 2\pi b \mu \left(\frac{\partial w}{\partial r} \right)_{r=b} = (d_1 + e_1 s) \dot{s} \quad (2.55)$$

$$\text{with } d_1 = -8\pi \mu L \quad \text{and} \quad e_1 = -16\pi \mu \frac{a^5}{b^5}.$$

The endpot effects with 4th and higher order terms are neglected by taking $b_l = e_l = 0$. This means that only small endpot fluid level displacements and velocities are regarded since as a rule $b \gg a$. Therefore the kinetic energy and the frictional force in the endpots are negligible. The inclusion of these terms provides a higher order non-linear differential equation which enables the analysis of the damping of the endpots.

Applying the Lagrange variation principle to the Lagrangian $G(t) = E(t) - V(t)$ results in

$$\frac{d}{dt} \left(\frac{\partial G}{\partial \dot{s}} \right) - \frac{\partial G}{\partial s} = F_v(t) + F_x(t)$$

whilst elaboration yields the Lagrange imposed linear differential equation (DE)

$$\ddot{s} + \frac{6\nu}{a^2} \dot{s} + \omega_o^2 s = \dot{s}^2 + 2\kappa \dot{s} + \omega_o^2 s = -\frac{3}{4} a_o \cos(\Omega t - \varphi) \quad (2.56)$$

with

$$\tau = \frac{a^2}{3\nu} = \kappa^{-1} \quad \text{HP transient damping time constant} \quad (2.57)$$

$$\omega_o^2 = \frac{3ga^2}{2Lb^2} = \frac{3\omega_z^2 R_o a^2}{2L b^2} \quad \text{squared HP damper resonance frequency.} \quad (2.58)$$

This HP frequency differs from the following equation

$$\omega_o^2 = \frac{2ga^2}{Lb^2} = \frac{2\omega_z^2 R_o a^2}{L b^2} \quad \text{obtained by solving the Navier-Stokes equation.} \quad (2.59)$$

The $s(t)$ solution of the well know DE given by Eqn. (2.56) is found by using [Inman, 2001]. In the applicable weak damping case with $\kappa < \omega_0$ the following solution is obtained by taking $s(0) = 0$ as arbitrarily boundary condition at $t=0$

$$s(t) = \frac{\frac{3}{4}a_0}{\sqrt{(\omega_0^2 - \Omega^2)^2 + 4\kappa^2\Omega^2}} [e^{-\kappa t} \cos(\omega_p t - \varphi) - \cos(\Omega t - \varphi)] \quad (2.60)$$

with

$$\tan \varphi = \frac{2\kappa\Omega}{\Omega^2 - \omega_0^2} \quad \text{phase equation and} \quad (2.61)$$

$$\omega_p = \sqrt{\omega_0^2 - \kappa^2} \quad \text{enforced vibration frequency.} \quad (2.62)$$

The homogeneous solution, given by the first part between the brackets in Eqn. (2.60), describes the natural resonance behavior at moments of sweep-up of nutation or airbearing oscillations. This behavior can be evaluated by rewriting the two cosine terms between the brackets at $t = 0$. The resulting angular frequencies $(\Omega - \omega_p)/2$ and $(\Omega + \omega_p)/2$ are essential to discern anomalies in the ND test and flight behavior. As a rule the nutation or airbearing angular frequency Ω is about ω_p indicating that the “beating” pendulum time may become small enough to be significantly present since $T_{beat} = 4\pi/(\Omega + \omega_p)$.

The a_0^2 normalized average HP model damping is obtained by using Eqn. (2.55) and the time derivate of Eqn. (2.60) which yields the average viscous dissipation equation $\bar{P} = \bar{F}_{vx}\dot{s}$ and finally

$$\frac{\bar{P}}{a_0^2} = \frac{\frac{9}{4}\pi\mu L\Omega^2}{(\omega_0^2 - \Omega^2)^2 + 4\kappa^2\Omega^2} \quad (2.63)$$

with

$$\left(\frac{\bar{P}}{a_0^2}\right)_{max} = \frac{\rho\pi L a^4}{16\nu} \quad \text{its maximum at } \Omega = \omega_0. \quad (2.64)$$

These equations, however, do not match at high spin-rates as shown in Fig-2.15.

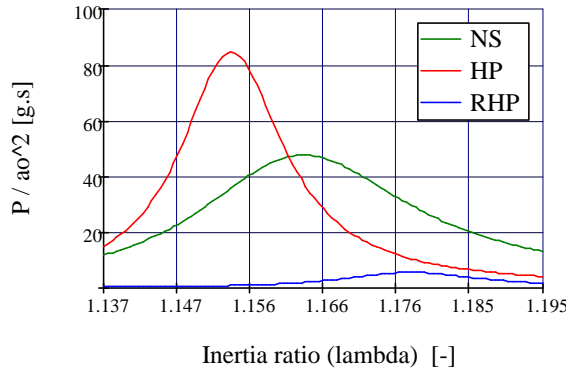


Fig-2.15 HP and NS model results of the 100 RPM FY-2 ND performance at $\lambda_0 = 1.166$ and $T = +20^\circ\text{C}$. The third RHP curve refers to a Refined HP model to be dealt with in section 2.8.5.

The nutation frequency offset of the HP model versus the NS model at high spin-rates (as for the FY-2 damper to be dealt in Chapter-4) is about -6% and the damping about 80% larger. This is shown in Fig-2.15 below and is caused by the fact that the HP model does not account for the presence of reverse flows at high spin-rates. The refined NS solution is derived in the following section. The ND test and qualification knowledge base [Dutch

Space], based on the NS solution, proved that the design resonance value normally agrees within 2% with experimentally found values. This range is acceptable to most customers. The NS model became the backbone for the design of NDs. Before deriving this model the two refined HP models (RHP-1 and RHP-2) are considered.

2.8.5 Refined Hagen-Poiseuille Models

RHP-1 model

The RHP-1 model [Häusler and Eidel, 2001] was used to verify and analyze the nutation flight data of the spin stabilized EQUATOR-S spacecraft. The technology of building the spacecraft NDs and its workmanship was based on the AMPTE S/C series heritage [Truckenbrodt et al., 1982].

The model is interesting since the amount of EQUATOR-S damping liquid 14% is relatively high making it a case of provoking the issue of quasi-rigidity described in section 2.5. To account for this a static (s) and dynamic (d) part of the inertia tensor is applied so $I = I_s + I_d$.

The application of the RHP-1 model to the heritage of Dutch Space NDs results revealed considerable differences between the diverse models. These will be further analyzed to enable the analysis of the diverse model validation ranges in Chapter 3. The RHP-1 model is based on the fluid mechanics theory from [Truckenbrodt, 1996]. The author treats the stationary case of communicating vessels starting with the Bernoulli energy conservation along a streamline applying an incompressible liquid without damping. The extended case includes damping and oscillatory flows with the following restrictions

1. Negligible dissipation losses in the endpots and transition parts of the liquid tubes
2. Turbulence magnitude at entrance and exit of the endpots is about the same
3. Instantaneous damp pressure equilibrium above the endpots.

The solution of the homogeneous DE resembles Eqn. (2.56) but the damping constant and resonance frequency differ slightly since the RHP-1 solution is given by

$$\ddot{s} + 2\kappa\dot{s} + \omega_0^2 s = 0 \quad (2.65)$$

with

$$\kappa = \frac{4\nu}{\left(1 + \frac{h}{L} \frac{a^2}{b^2}\right) a^2} \cong \frac{4\nu}{a^2} \quad \text{RHP-1 damping factor}$$

$$\omega_0^2 = \frac{2\omega_z^2 R_0}{h \left(1 + \frac{L}{h} \frac{b^2}{a^2}\right)} \cong \frac{2\omega_z^2 R_0}{L} \frac{a^2}{b^2} \quad \text{RHP-1 resonance frequency.} \quad (2.66)$$

The above equations show that:

1. The impact of the internal endpot height h diminishes since for regular ND designs the conditions $h \ll L$ and $b \gg a$ apply yielding less than 0.2% impact.
2. The RHP-1 damping factor is a factor 4/3 higher compared to the HP value.

In addition an inertia correction factor k_θ is added to the RHP-1 model. It quantifies the fraction of effective viscous mass based on the HP velocity profile and becomes significant at small a/b and ω_z since

$$k_\theta = \frac{4\nu L (\lambda - 1) b^2}{R_0 \omega_z a^4}. \quad (2.67)$$

The model results are reported to be in good agreement with both EQUATOR-S ground test results and in orbit flight data. The factor k_0 and the parameter m/M (see section 2.5) are used in Chapter 3 to categorize the ND design and classify the applicable ND model.

RHP-2 model

The second (RHP-2) model originating from the field of shipbuilding engineering literature is given by [Shyu and Kuo, 2000] and [Gawad et al., 2001]. It describes the performance of a tuneable U-type liquid damper (TLD) coupled to the structure of a naval ship. It was studied because of the broadband attenuation design trade-offs to follow in Chapter 5, 6 and 7. A systematic elaboration of theory dealing with the TLD development since 1880 is given by [Moaleji and Greig, 2007].

Normally a vapor tube is an essential part of a Passive liquid ND (PND) since it provides an instantaneous equal pressure above both endpots. The active U-type design, however, is not equipped with an open vapor tube but incorporates a non-communicating vessel design. Its TLD concept, shown in Fig-1.12, is applied for the active attenuation of broadband vibrations.

The nominal damp pressure p_0 is the equilibrium endpot pressure at equal liquid levels. At unequal endpot levels the pressure difference is found by applying the isentropic gas law. This law is valid for an reversible adiabatic process with constant entropy at constant total endpot volumes. Taking $s_0 \ll h$ and applying a typical damper liquid type PP1 (specified in section 2.10 and 2.11), the following equation results

$$\frac{\Delta p}{p_0} = \left[1 - \left(\frac{2s_0}{h} \right) \right]^{-\gamma} - \left[1 + \left(\frac{2s_0}{h} \right) \right]^{-\gamma} \cong 4\gamma \frac{s_0}{h} \quad (2.68)$$

with

- γ mass heat ratio $\gamma = c_p/c_v = 1.66$ of Helium gas at $T = 20^\circ\text{C}$
- ρ damper liquid PP1 density ρ_{PP1} about 1700 kg/m^3 at $T = 20^\circ\text{C}$
- h typical passive ND inner endpot height $h = 40 \text{ mm}$.

By including this term in the Lagrangian, the resonance Eqn. (2.66) is extended by the factor

$$f = \frac{2\gamma p_0}{\rho gh} \quad \text{and by substitution of } g = \omega_z^2 R_0^2 \quad \text{Eqn. (2.63) becomes}$$

$$\omega_0^2 = \frac{2R_0 a^2}{L b^2} \omega_z^2 (1 + f) = \frac{2ga^2}{Lb^2} \left(1 + \frac{2\gamma p_0}{\rho gh} \right). \quad (2.68a)$$

From this equation it is concluded that active pressure control enlarges the design freedom considerably. Disadvantages are the complication of the damper system and the introduction of resonance error contributors since:

1. The condition $s_0 \ll h$ is not fulfilled at initial nutation angles. In the case that s_0 is about $h/4$ the deviation in Eqn. (2.68) is already about 40%. This means that the resonance frequency decreases towards the smaller nutation amplitude range.
2. Pressure control requires active parts like valves and bellows which introduce thermo-mechanical complications like hysteresis, drift and non-linearity's.

Considering a space qualified TLD, active endpot pressure control is out of the question since the elegance of robustness, reliability and ease of design and manufacturability is lost. However, by applying Eqn. (2.68a) to a potential space ND design an indication of the tuning capability and applicability of such an exotic design can be obtained. The vapor tube and half endpots of passive dampers are filled (common practice) with Helium gas at 1 bar.

Taking this value as the equilibrium pressure p_0 in a realistic spin-rate range $\omega_z = 100$ down to 10 rpm, the multiplication factor $\sqrt{(1+f)}$ in Eqn. (2.68a) varies from 1.2 up to 60. This indicates an offset in resonance frequency of almost two orders compared to the passive ND design. This means that either the ratio a/b has to be reduced or the nominal fill pressure p_0 of the endpots (with considerable accuracy) to get in the regular nutation frequency range. It is concluded that the application of this unconventional design in space engineering is far from obvious. It is therefore disregarded in the broadband attenuation design trade-offs to follow in Chapter 5, 6 and 7. In these chapters a passive multi-mode damping solution will be dealt with. The required additional theory, which is capable to deal with multiple excitations, is derived in section 2.9.

2.8.6 Navier-Stokes Solution

The resonance Eqn. (2.59) is derived by applying the Navier-Stokes Equation (NSE) to the flow in the liquid tube. This flow is not restricted to a Poiseuille flow profile since also allows for reverse flow layers. The NS model incorporates the detailed interaction of the fluid particles. The only assumption made is that the fluid flow be laminar. The following NSE describes the fluid velocity $\mathbf{u} = (u, v, w)^T$ for an incompressible medium with $\nabla \cdot \mathbf{u} = 0$ in the liquid tube

$$\frac{d\mathbf{u}}{dt} = -\frac{\nabla p}{\rho} + \mathbf{a}_f + \nu \Delta \mathbf{u} \quad \text{which equals} \quad \frac{\partial \mathbf{u}}{\partial t} + (\mathbf{u} \cdot \nabla) \mathbf{u} = -\frac{\nabla p}{\rho} + \mathbf{a}_f + \nu \nabla^2 \mathbf{u}.$$

The laminar flow equation in the X-axis direction without convective term becomes

$$\frac{\partial u}{\partial t} = -\frac{1}{\rho} \frac{\partial p}{\partial x} + a_0 + \nu \left(\frac{1}{r} \frac{\partial u}{\partial r} + \frac{\partial^2 u}{\partial r^2} \right) \quad (2.69)$$

with

$$\begin{aligned} p &= p(x, t) && \text{pressure gradient over the liquid tube length } L \\ \mathbf{a}_f &= (a_0 e^{-i\Omega t}, 0, 0)^T && \text{nutation pushup acceleration in the liquid tube.} \end{aligned}$$

In the following cylindrical coordinates (r, x) and the developed laminar coaxial flow are taken in phase. As a result the velocity in the X direction can be described by a separation of variables in a radial velocity $F(r)$ distribution and harmonically in time by

$$u(x, r, t) = u(r, t) = \text{Re}[F(r)e^{i\Omega t}]. \quad (2.70)$$

The average velocities in the liquid tube \bar{u} and endpot \bar{w} become using Eqn. (2.52)

$$\bar{u} = \frac{e^{-i\Omega t}}{\pi a^2} \int_0^a F(r) 2\pi r dr = e^{-i\Omega t} \bar{F} \quad \bar{w} = \frac{a^2}{b^2} e^{-i\Omega t} \bar{F} \quad (2.71)$$

and the related (imaginary) pressure gradient at time t using

$$s_0 = \int_0^t \bar{w} dt = \int_0^t \bar{u} \frac{a^2}{b^2} dt \quad \text{becomes} \quad (2.72)$$

$$\frac{1}{\rho} \frac{\partial p}{\partial x} = \frac{2s_0 g}{L} \quad \text{whilst further elaboration yields} \quad \frac{1}{\rho} \frac{\partial p}{\partial x} = -\frac{e^{-i\Omega t}}{i\Omega} \bar{F} \omega_0^2. \quad (2.73)$$

In the last equation the incompressible fluid resonance frequency ω_0 given by Eqn. (2.59) is introduced. Substitution of Eqn. (2.70) and (2.73) in the NSE Eqn. (2.69) yields

$$-i\Omega F = \frac{\omega_0^2}{i\Omega} \bar{F} + a_0 + \nu \Delta F \quad \text{and with elaboration}$$

$$\frac{d^2 F}{dr^2} + \frac{1}{r} \frac{dF}{dr} + \frac{i\Omega}{\nu} F + \frac{\omega_0^2}{i\Omega\nu} \bar{F} + \frac{a_0}{\nu} = 0. \quad (2.74)$$

The Womersley parameter change $x = \epsilon_r = r\sqrt{i\Omega/\nu}$ is introduced (see Fig-2.9) with $\epsilon_a = a\sqrt{i\Omega/\nu}$ and the updated Eqn. (2.74) is compared with the m -th order Bessel DE which equals

$$\frac{1}{x} \frac{d}{dx} \left(x \frac{dZ_m}{dx} \right) + \left(1 - \frac{m^2}{x^2} \right) Z_m = 0 \quad (2.75)$$

with

$$Z_m(x) = C_0 J_m(x) + C_1 Y_m(x) \quad Y_m(x) = \frac{J_m(x) \cos(m\pi) - J_{-m}(x)}{\sin(m\pi)}$$

$$J_m(x) = \sum_{n=0}^{\infty} \frac{(-1)^n (x/2)^{2n+m}}{n! (n+m)!} \quad \text{and} \quad \frac{dJ_0(x)}{dx} = -J_1(x). \quad (2.76)$$

Taking $m=0$ and $C_1=0$ since $Y_m(x)$ is singular at $x=0$ Eqn. (2.75) becomes

$$\frac{d^2 Z_0}{dx^2} + \frac{1}{x} \frac{dZ_0}{dx} + Z_0 = 0 \quad \text{whilst Eqn. (2.74) becomes}$$

$$\frac{d^2 F(x)}{dx^2} + \frac{1}{x} \frac{dF(x)}{dx} + F(x) - \frac{\omega_0^2 \bar{F}}{\Omega^2} + \frac{a_0}{i\Omega} = 0$$

Comparing these two equations yields the solution

$$Z_0(\epsilon_r) = F(\epsilon_r) - \frac{\omega_0^2 \bar{F}}{\Omega^2} + \frac{a_0}{i\Omega} = C_0 J_0(\epsilon_r)$$

and with the boundary condition at the tube wall $F(\epsilon_a) = 0$ this determines

$$C_0 = \frac{1}{J_0(\epsilon_a)} \left[\frac{a_0}{i\Omega} - \frac{\omega_0^2 \bar{F}}{\Omega^2} \right] \quad \text{and} \quad \frac{dF(\epsilon_r)}{d\epsilon_r} = \left[\frac{J_0(\epsilon_r)}{J_0(\epsilon_a)} - 1 \right] \left[\frac{a_0}{i\Omega} - \frac{\omega_0^2 \bar{F}}{\Omega^2} \right]. \quad (2.77)$$

The average viscous dissipation power per nutation cycle \bar{P} can now be evaluated with

$$\bar{P} = \frac{2}{a^2} \int_0^a r F(r) dr \quad (2.78)$$

and using the recurrent relation from Eqn. (2.76) the substitution of Eqn. (2.77) in (2.78) delivers

$$\bar{P} = \frac{a_0 \beta \Omega}{i \omega_0^2 (\gamma^2 + \beta)} \quad (2.79)$$

with

$$\beta = \frac{2J_1(\epsilon_a)}{x_a J_0(\epsilon_a)} - 1 \quad \text{and} \quad \gamma = \frac{\Omega}{\omega_0} \quad \text{the ND design tuning factor.}$$

On basis of Eqn. (2.79) the factor $F(r)$ becomes

$$F(r) = \frac{\gamma^2}{\gamma^2 + \beta} \left(\frac{J_0(x)}{J_0(x_a)} - 1 \right) \frac{a_0}{i\Omega}. \quad (2.80)$$

The last step to define the dissipation is the derivation the dissipation density

$$p(r, t) \Delta r = 2\pi r L \mu \frac{du}{dr} \Delta u = 2\pi r L \mu \left(\frac{du}{dr} \right)^2 \quad \text{whilst the average dissipation power is}$$

$$\bar{P} = \frac{\Omega}{2\pi} \int_0^{\frac{2\pi}{\Omega}} \int_0^a p(r, t) dr dt. \quad (2.81)$$

Elaboration of \bar{P} using Eqns. (2.70), (2.80) and (2.81) finally delivers the normalized average power dissipation over one nutation cycle [QED]

$$\frac{\bar{P}}{a_0^2} = \frac{L\pi\rho}{\Omega} \frac{\gamma^4}{(\gamma^2 + \beta)^2} \frac{\int_0^a \left| J_1\left(r\sqrt{\frac{i\Omega}{v}}\right) \right|^2 r dr}{\left| J_0\left(a\sqrt{\frac{i\Omega}{v}}\right) \right|^2} \quad (2.82)$$

This proves that the Eqns. (2.25) until (2.28) indeed represent an exponential constant. Eqn. (2.82) is further condensed by introducing $\xi = r/a$ and the flow characteristic Womersley parameter $|\varepsilon_a|$ yielding

$$\frac{\bar{P}}{a_0^2} = \frac{L\pi a^2 \rho}{\Omega} \frac{\gamma^4}{(\gamma^2 + \beta)^2 |J_0(\varepsilon_a)|^2} \int_0^1 |J_1(\xi \varepsilon_a)|^2 \xi d\xi \quad (2.83)$$

The NS model, enabling the design of both meridian and equatorial NDs, was originally (1990) implemented in Fortran-77 requiring about 1200 lines of software code including a user-friendly interface. Nowadays two sheets of MathCad® 14.0 code are sufficient to do the essential analysis. Taking the Bessel functions up to 11 terms creates a sufficient 10^{-9} absolute accuracy in Eqn.(2.83). Modeling and post-processing results are given in the following section.

2.8.7 Model Results

The MathCad 14.0 modeling results in Fig-2.16 show the liquid velocity profiles of the Chinese F2 ND. The design and testing of this damper will be dealt extensively in Chapter 4. The principle parameter to describe oscillating flows is the earlier defined Womersley parameter $|\varepsilon_a|$. The parameter enables the distinction in which coaxial liquid layers the viscous dissipation takes place. At large values [Muto et al., 1980] typically beyond 5 the viscous dissipation gets restricted to the boundary (Stokes) layer at the walls. This effect can be clearly seen in the $T = 50^\circ\text{C}$ case of the following Fig-2.16 with conditions:

- The extreme operational temperatures -25°C and 50°C were chosen as model input to express clearly the more or less independent behavior of reverse flow layers
- Nutation range and Reynolds number - The pictures are valid at nutation angle $\theta_0 = 62^\circ$ which is 124 times the required $\theta = 0.5^\circ$ and chosen to be just within the laminar flow conditions as defined by $Re < 2300$ and $T = 50^\circ\text{C}$
- Forcing acceleration $a_0 = \theta_0 \omega_Z^2 \lambda_0 Z_0 = 0.2168 \text{ mm/s}^2$.

The first six pictures show the liquid flow at $T = +50^\circ\text{C}$ and the last three at $T = -25^\circ\text{C}$ as a movie sequence during one nutation cycle with $\Omega_0 = 1.738 \text{ rad/sec}$. The cycle steps is $\Delta t = T/6 = 602.5 \text{ ms}$ whilst the Reynolds number and the average flow velocity are given for each step. Comparing the second half cycles shows that due to a decrease in operational temperature of $\Delta T = -75^\circ\text{C}$ the viscosity profile gets more sluggish and rounded. As expected the viscosity being the resistance to flow increases significantly. This means that the normalized dissipation decreases and the time constant increases. On the other hand the damping bandwidth (FWHM) increases. The impact of the latter will be regarded in more detail in the study of the nutation anomaly of the Ulysses S/C in Chapter-5.

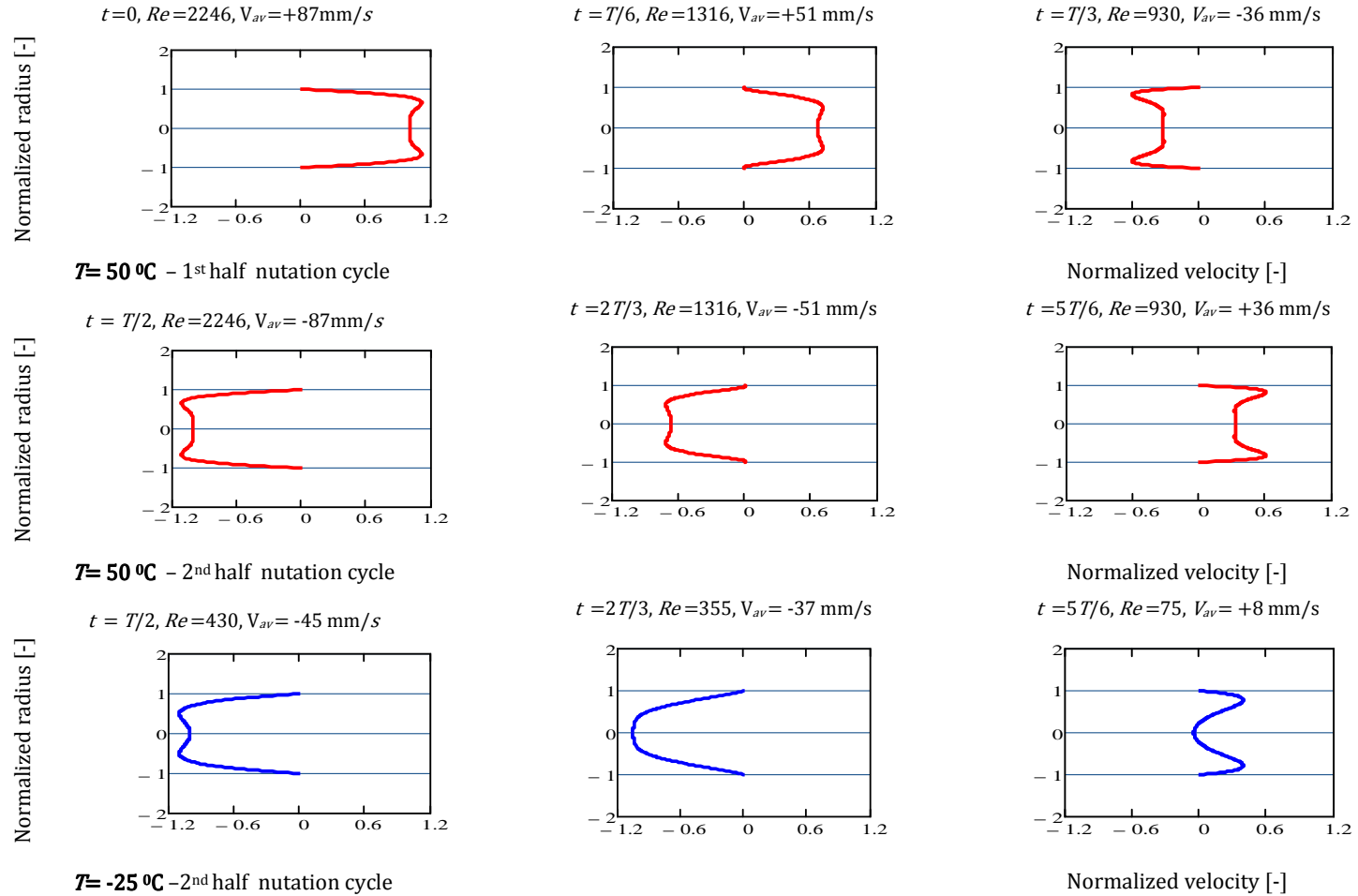


Fig-2.16 NS solution with nutation cycle steps $\Delta t = T/6 = 602.5\text{ ms}$ at the extreme operational temperatures 50°C and -25°C (bottom row).

2.9 Multiple Excitations

In reality single mode excitations do not exist. Flexible space structures, sloshing propellants, antennas, ground test air-bearing arms, etc., all provide contributions to the diverse vibration modes of other susceptible S/C subsystems. Multi-modal models for tuned liquid dampers of an arbitrary damper or tank geometry are nowadays a hot item in diverse scientific fields as reflected by the range of applications given in Chapter 1. [Love and Tait, 2011] show the latest modeling potentials for a TLD.

The simplest multiple extension, taking two modes with a slight difference in frequency, shows that the energy sink principle is no longer valid: Two excitations yield the angular frequencies $(\Omega_1 - \Omega_2)/2$ and $(\Omega_1 + \Omega_2)/2$ which shows that long oscillation periods may be present exceeding the natural nutation period multiple times in magnitude. Therefore the average dissipation definition Eqn. (2.83), defined for the limited single nutation cycle, loses its value and becomes time dependent with $P = P(t)$.

Significant multi-mode excitations may result from long flexible parts like wire antennas. These play an important role in the design and stability of S/C for magneto-spherical planetary research. The wire booms include tip masses carrying dedicated sensors for magneto-spherical research. The S/C is modeled as a rigid body with pendulum attachments to a central hub in the spin plane using joints with two degrees of freedom. This S/C class gets special attention in the frame of this thesis in Chapter 5 and 6 which deal with the Ulysses and Cluster S/C stability. The oscillation modes of four S/C wire boom antennas (two pairs) are illustrated in Fig-2.17 taken from [Auslander et al., 2008].

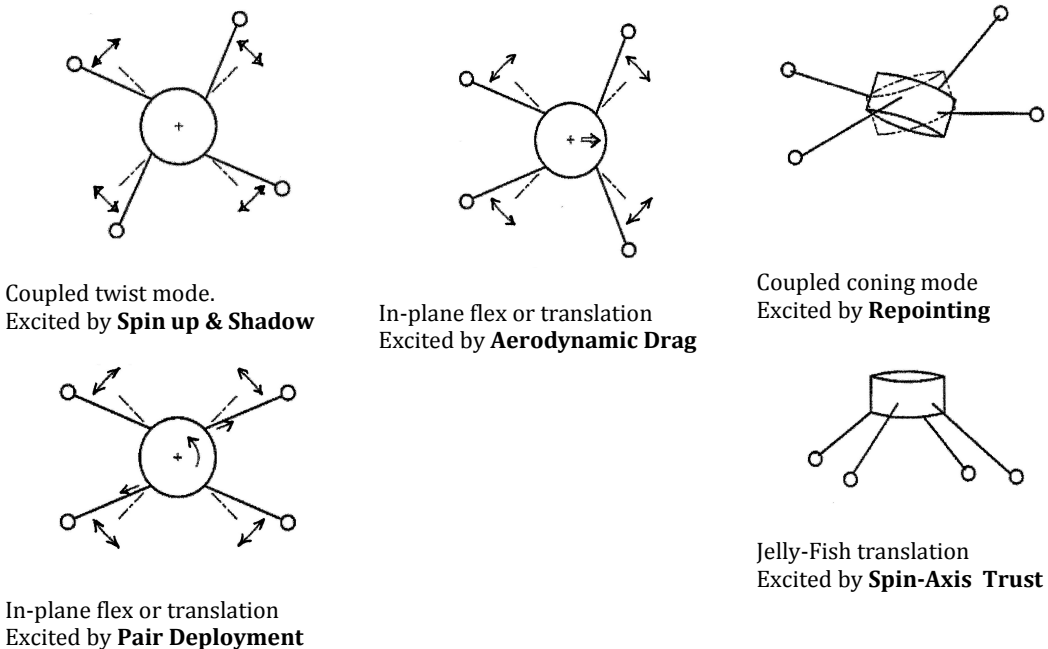


Fig-2.17 Coupled and uncoupled antenna planar oscillation modes. The main excitation modes of a spin stabilized S/C with pendulum attachments to a central hub are shown [Auslander et al., 2008] after [Lai et al., part I and II, 1979] and [Longman and Fedor, 1974].

The full Lagrangian theory to describe the linear resonant modes of a spinning S/C with wire boom configurations was explored by [Lai et al., part I and II, 1979] based on [Lai and Bhavnani, 1975]. [Longman and Fedorf, 1974] explore the quadratic approximation to the Lagrangian for the IMP-J S/C employing four radial wire antennas for the first time in space.

A spinning S/C hub with two wire pairs (four wire booms) can be modeled as a 14 degree of freedom (DOF) system. The linearized equations of motion define the lowest order vibrational modes and natural frequencies of the gyroscopically coupled system. The multi-body movements can be computed from the Lagrangian equations of motion and studied by mode visualization tools like SimuLink. The simulated resonant modes can be extracted via Fast Fourier Transforms. Thruster firings can be simulated which induce in-plane and out-of-plane boom oscillations whereas the results serve the verification of analytical predictions. Identified thruster firing frequencies and spin-rate operational constraints for the THEMIS S/C as well as system design and mission planning considerations are dealt in [Auslander et al., 2008]. The THEMIS S/C multi-mode model contains eight antennas in total with six tip mounted sensors. An analytical approach for the comparable RBSP S/C is given by [McGee et al., 2009]. The main excitation modes in Fig-2.17 serve the cases of the Ulysses and Cluster spacecraft, to be dealt in the following chapters, as well.

The resonant modes are characterized by the abbreviations EA (Equatorial Anti-symmetric), MA (Meridian Anti-symmetric) and N (Nutation) whereas ES and MS account for the symmetric modes. Their impact on the S/C ADCS design is specified in an equal format as used for nutation damping e.g. by $\lambda_{MA-1} = \Omega_{MA} / \omega_Z$. Only the anti-symmetric antenna modes induce satellite spin-axis oscillations. In the specification of the required Cluster ADCS antenna and nutation performance, the frequencies ratios of the diverse modes are input parameters. These parameters drive the extended (innovative) ND design as will be clarified Chapter 6.

Multi-mode dissipation theory

The existence of multi-mode excitations in a liquid tube requires a theory to model the simultaneous internal energy dissipation. This is especially required in a design with different liquid dampers. A multi-mode model supports the subsequent design and engineering of NDs tuned at different frequencies. In this section, the basis of such a model is derived as a spin-off from the single ND excitation model described in section 2.8.6. The aim is to model the broadband simultaneous damping behavior of a specific (MA, N, EA) damper combination as will be dealt in Chapter 6 and 7.

The total squared multiple mode acceleration in a liquid tube is given by its Fourier format Eqn. (2.84). This equation follows from the sum of N push-up accelerations which differ in amplitude, frequency and phase by

$$a_o(t) = \sum_{i=1}^N a_{oi} \cos(\Omega_i t - \varphi_i) = \sum_{i=1}^N a_i \cos \Omega_i t + b_i \sin \Omega_i t.$$

with $a_i^2 + b_i^2 = a_{oi}^2$ and $\tan \varphi_i = b_i / a_i$.

The following orthonormal Fourier format of a_o^2 results as a consequence since

$$a_0^2 = \sum_{i=1}^N \sum_{j=1}^N a_i a_j \cos(\Omega_i t) \cos(\Omega_j t) + b_i b_j \sin(\Omega_i t) \sin(\Omega_j t) + a_i b_j \cos(\Omega_i t) \sin(\Omega_j t) + b_i a_j \sin(\Omega_i t) \cos(\Omega_j t). \quad (2.84)$$

Regarding the factor $F(r)$ of the single excitation velocity profile given by Eqn. (2.80), its derivative for the multiple excitation becomes with $\varepsilon_{ri} = r\sqrt{i\Omega_i/\nu}$ and $\varepsilon_{ai} = a\sqrt{i\Omega_i/\nu}$

$$\sum_{i=1}^N \frac{dF_i(r)}{dr} = \sum_{i=1}^N \frac{\gamma_i^2}{(\gamma_i^2 + \beta_i)} \frac{-J_1\left(r\sqrt{\frac{i\Omega_i}{\nu}}\right)}{J_0\left(a\sqrt{\frac{i\Omega_i}{\nu}}\right)} \frac{a_{oi}}{i\Omega_i} \sqrt{\frac{i\Omega_i}{\nu}} = \sum_{i=1}^N \frac{\gamma_i^2}{(\gamma_i^2 + \beta_i)} \frac{-J_1(\xi\varepsilon_{ri})}{J_0(\varepsilon_{ai})} \frac{a_{oi}}{i\Omega_i} \sqrt{\frac{i\Omega_i}{\nu}}.$$

Consequently the factor $(dF/dr)^2$ becomes

$$\sum_{i=1}^N \sum_{j=1}^N \frac{dF_i(r)}{dr} \frac{dF_j(r)}{dr} = \frac{1}{\nu} \sum_{i=1}^N \sum_{j=1}^N \frac{i\gamma_i^2}{(\gamma_i^2 + \beta_i)} \frac{J_1(\xi\varepsilon_{ai})}{J_0(\varepsilon_{ai})} \frac{a_{oi}}{\sqrt{i\Omega_i}} \frac{\gamma_j^2}{(\gamma_j^2 + \beta_j)} \frac{J_1(\xi\varepsilon_{aj})}{J_0(\varepsilon_{aj})} \frac{a_{oj}}{\sqrt{j\Omega_j}} = \sum_{i=1}^N \sum_{j=1}^N \alpha_{ij}(\xi).$$

Incorporation of the four basic orthonormal coupled vibration modes on basis of Eqn. (2.83) with equal phase contributions yields the (simultaneous i and j excitation) dissipation summation elements

$$P_{ij}(\xi, t) = \frac{\alpha_{ij}(\xi)}{2} [\cos(\Omega_i t) \cos(\Omega_j t) + \sin(\Omega_i t) \sin(\Omega_j t) + \cos(\Omega_i t) \sin(\Omega_j t) + \sin(\Omega_i t) \cos(\Omega_j t)].$$

The factor $1/2$ yields compliance with Eqn. (2.83) using the fact that in general there is no a priori information with respect to the different phases of the diverse excitation modes. This means that $\overline{a_i a_j} = \overline{a_i} \overline{a_j} = \overline{b_i} \overline{b_j} = \overline{b_i} \overline{b_i}$ is taken in Eqn. (2.84). The selection of other phase distributions at the same $\alpha_{ij}(\xi)/2$ Root Sum Square (RSS) value provides means to investigate the sensitivity of the design to this issue.

In the derivation of Eqn. (2.83) the following dissipation density function was elaborated

$$p(r, t) = 2\pi r L \rho \nu (dF/dr)^2 e^{-i\Omega t}.$$

The same holds for the multi-mode excitation compliant to Eqn. (2.84) by including the total time dependent dissipation

$$P(t) = \int_0^a p(r, t) dr = 2L\pi a^2 \rho \sum_{i=1}^N \sum_{j=1}^N \int_0^1 P_{ij}(\xi, t) \xi d\xi. \quad (2.85)$$

Finally the following equation enables the comparison of the multiple and the single mode excitation in terms of effective damping on basis of the multi-mode equivalence

$$\frac{P(t)}{a_0^2} = \frac{L\pi a^2 \rho}{a_0^2} \sum_{i=1}^N \sum_{j=1}^N \int_0^1 P_{ij}(\xi, t) \xi d\xi \quad (2.86)$$

with

$$a_0^2 \equiv \sum_{i=1}^N \sum_{j=1}^N a_{oi} a_{oj} = \left(\sum_{i=1}^N a_{oi} \right)^2.$$

Taking $N = 1$ as a trivial check (single excitation) and applying a time average over the limited nutation cycle shows indeed that Eqn. (2.83) re-appears. A comparable equation

(without derivation) given by [van Bakel, 1993] is based on the prior developed models at Fokker Space in the period 1980-1992 and was used as part of the qualification of the Cluster ND design.

2.10 Residual Nutation Angle

The residual nutation restriction by the end pot walls is explored in to depth in this section because of its high relevance to the cases to be dealt in the following chapters. An equation for the residual nutation angle θ_{res} of equatorial and meridian nutation dampers is derived by [Hong, 1987]. The derivation, compliant with [Truckenbrodt, 1996] and [Häusler and Eidel, 2002], is based on applying Bernoulli's equation along a streamline and the HP model. The approach, however, is not valid at high spin-rates and nutation frequencies due to the presence of reverse flow layers. The following forces apply:

1. End pot resistance due to wall sticking hysteresis phenomena
2. Viscous damping
3. Centrifugal inertia force
4. Excitation force due to nutation.

The latter three forces are all accounted for in the derivation of the HP and NS models in section 2.8 and 2.9. Thus the ND performance is dominated by the first item below a critical nutation angle [Hubert and Swanson, 2000] and [FDS, 1992]. The ND behavior locks once the sum of the centrifugal inertia force, push-up force by nutation and the viscous damping force becomes smaller than the resistant force. This condition causes the so-called dead band in the damping performance. The residual nutation angle Eqn. (2.87) was adapted from [Hong, 1987]. The derivation is based on the Coulomb alike resistance of the endpot friction line. The equations were adapted to comply with the specific design geometry of the tube-with-endpots ND with result

$$\theta_{res} = \frac{4\gamma_0}{G\rho\lambda_0^2bhR_0\omega_z^2} \left(1 - \frac{a^2 L}{b^2 h} \right) \quad (2.87)$$

with γ_0 the liquid surface tension, h the inner endpot height and G either the equatorial G_e or the meridian G_m factor given by

$$G_e = Z_0 (R_0 \delta)^{-1} \sin \delta \quad G_m = 1 - 2 \frac{R_0(\lambda_0 - 1)}{\lambda_0(R_0 - h)} \quad \text{and} \quad \delta = \frac{L + 2b}{2R_0}.$$

This equation will be applied to estimate the ultimate nutation damping both in flight and in the terrestrial test in the following chapters. They enable as well trade-offs on the use of either meridian or equatorial NDs and the limits of damping on basis of the design parameters given in the above equation.

The part between brackets in Eqn. (2.87) suggests that a particular combination of the ND design parameters $\langle a, b, h, L \rangle$ can create a zero residual angle. Analysis, however, learns that this refers to a non-feasible design since the required endpot height h is in the order of 5 mm.

The limiting endpot phenomena will now be dealt with.

Endpot phenomena and Bond number

The residual nutation angle for fluid dampers is restricted by endpot surface tension phenomena, from intermolecular forces, making it act like a membrane under tension. For a circular tube, the net force F with θ the endpot liquid wall angle, is given by

$$F = 2\pi b\gamma_0 \cos \theta \quad (2.88)$$

At low spin rates the liquid free surface can be immobilized by surface tension down to a level fully obstructing the nutation damping. The dual spinning IMAGE (Imager for Magnetopause to Aurora Global Exploration) S/C was spin-stabilized with a single magnetic torque rod and PNDs of the tubular ring type partly filled with Hg, attached to the spinning upper stage. The IMAGE inner magnetosphere science mission lasted from 1999 to December 2005. The S/C initial nutation showed an unpredicted decay. Detailed analysis of the dynamics by [Hubert and Swanson, 2000] and [Hubert and Swanson, 2002] showed that this happened in an early operational phase at low 2-3 rpm spin-rates. The nutation damping problem was successfully resolved by a work around being a ground-commanded open loop control damper using the magnetic torque rod. A comparable solution was chosen to solve the Ulysses S/C ADCS anomaly to be dealt in Chapter-5.

Figure 2.18 shows the so-called wetting condition of the tube wall. The three phase's liquid, gas, and solid all meet up to free energy equilibrium. The liquid surface tension force F_S applied to the wall is opposed by an equal and opposite wall force F_W to the liquid. The contact angle θ is a function of the materials (liquid, solid, and gas) and of physical parameters such as temperature and pressure. The so-called wetting liquids have contact angles less than 90° whilst non-wetting liquids have contact angles greater than 90° . In the case the adhesive force exceeds the cohesive force, the liquid tends to spread outward and is said to “wet” the surface. A non-wetting liquid tends to retreat.

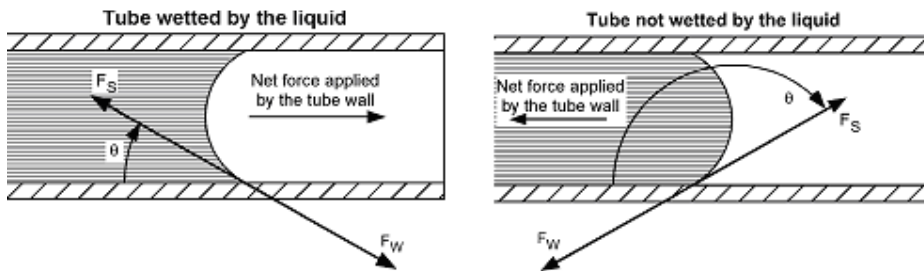


Fig-2.18 Contact angle and net force for wetting and non-wetting liquids [Hubert & Swanson, 2000].

In case of contact angle hysteresis a membrane action of the end pot liquid meniscus may be present. This is caused by “sticking” of the meniscus to the end pot walls which in its turn is related to the specific surface roughness and the so-called wetting speed [Ibrahim, 2005]. The resulting retarding force is similar to Coulomb friction because it is essentially independent of the velocity of the liquid slug through the tube. The effect is shown in Fig. 2.19 with typical angles:

- θ_e end pot equilibrium angle condition without nutation acceleration
- θ_r receding meniscus angle with nutation acceleration
- θ_a advancing meniscus angle with nutation acceleration.

From this picture it is seen that the fluid column in the ND end pots meets an extra resistance due to this effect. Since the static contact angle depends on the free energy equilibrium of the contact media it is essentially a constant. A worst case sticking angle condition is shown in Fig. 2.19 due to a relative large surface tension representative for Mercury with typical values of the contact angle hysteresis 124-146 degree and for the surface tension $\gamma = 0.475 \text{ N/m}$ at 25°C . On basis of Eqn. (2.88) the effect is small if the angle θ_e and consequently θ_r and θ_a are close to 90° . The contact angle can be verified by a dedicated experiment with droplets of the selected damping liquid (possibly volatile) and H_2O (for cross-reference checks) on an Aluminium plate. This approach was used during the FY-2 ND development at Dutch Space [FDS, 1992] and will be explored in Chapter-4.

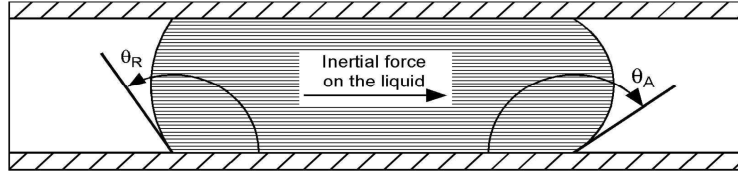


Fig-2.19 Advancing and receding contact angles for a stationary Hg slug subject to an inertial force [Hubert & Swanson, 2000].

A typical fluid mechanics characteristic number to define the condition whether the hydrostatical force overrules the (endpot) surface tension is the Bond number Bo .

$$Bo = \frac{\rho \pi b^2 \omega_z^2 R_0 \Delta h}{2\pi b \gamma_0 (\cos\theta_a - \cos\theta_r)} = \frac{\rho b \omega_z^2 R_0 \Delta h}{2\gamma_0 (\cos\theta_a - \cos\theta_r)} \quad (2.89)$$

The “sticking” phenomena to the end pot walls may be neglected at Bond number values $Bo \gg 1$. In the NS model derivations of Eqns. (2.59) and (2.83) the end pot effects were already neglected since $b \gg a$ as a rule which supports a relative large Bo number in the design. The selection of an appropriate damping liquid is essential.

Fluoro-Carbons as ideal ND liquids

The very low surface tensions of Perfluorocarbons [Simons, 1950] make them the ideal ND damping liquids. These liquids with commercial names Flutec PP1, PP2, PP3 and PP9 are selected for the low surface tension as well as for their appropriate density, dynamic viscosity and temperature dependency. These fluorinated alkanes are characterized by strong C–F bonds with typical characteristics [O’Hagan, 2008]:

1. High thermal stability
2. Very low surface tension
3. High bond energies, i.e. 486 kJ/mol in the C–F bond within CF_4
4. Strong chemical resistance and thus stability
5. Low polarizability
6. Physiological inert
7. Good electric properties (low dielectric constant, high insulation value).

The Fowler process to produce fluorocarbons was born as a spinoff of the World War II Manhattan Project. This project required the production and handling of uranium hexafluoride to enrich uranium. Uranium hexafluoride is very corrosive, oxidizing and volatile solid (with sublimation point at $T = 56^\circ C$). Therefore novel materials were required like coolant liquids, to survive contact with uranium hexafluoride. Perfluorocarbons were identified as ideal materials, but at that time no methods were at hand to produce them in sufficient quantities. After World War II the technology was released and commercialized by ISC Chemicals (UK) with trade name Flutec, a name which still persists. The Flutec business went into a decline, due to a drop in its main application, vapor phase reflow soldering. The latest applications are in the medical field and the production is today at F2 Chemicals Ltd since 1998. Small amounts of Flutec to supply NDs are thus still available on the commercial market [Simons, 1950].

An additional advantage of the Flutec series is the radiation hardness, as part of the ND qualification. This will be proved explicitly in Chapter 4 in detail as part of the qualification of the FY2 ND.

At small Bond numbers the damping liquid properties γ and ρ are part of the triple phase (He, Al, Flutec) equilibrium. Beside these the following end pot wall properties determine the contact angle [Lemal, 2004].

1. Aluminum material type
2. Surface RMS roughness amplitude (RA)
3. Material finishing treatment
4. Scale of surface inhomogeneity.

Items 1 and 3 refer to the choice of the Aluminum type prescribed by the build standard of the ND whilst the same applies for the Alodine finishing treatment as corrosion inhibitor. In the following sections items 2 and 4 are dealt with in more detail to analyze their impact. The goal is to distinguish the main contributors in a pragmatically engineering sense.

Surface roughness

It was [Wenzel, 1948] who first incorporated the surface roughness by

$$\cos \theta_w = \frac{A_r}{A_g} \cos \theta_e \quad (2.90)$$

with

θ_w	True (Wenzel) contact angle at rough surface
θ_e	Equilibrium contact angle for a perfectly smooth solid surface
A_r	Enlarged surface area due to roughness and
A_g	Geometric surface of a perfect flat area.

This shows that a polished surface is best to avoid contact angle variations and thus hysteresis effects. An increasing effective surface roughness factor k_s (given in Eqn. 2.32) at a homogeneous interface leads to increasing contact angle hysteresis [Bhushan, 2008].

Inhomogeneous surface

The impact of chemical remnants on a surface was described by [Cassie, 1948]. The following equation applies for an inhomogeneous but perfectly smooth surface, based on the free energy equilibrium at the surface of the solid-liquid interface

$$\cos \theta_c = \sum_i f_i \cos \theta_i \quad (2.91)$$

with

θ_c	(Cassie) contact angle for the heterogeneous surface
θ_i	Intrinsic equilibrium contact angle for the i -th surface component
f_i	Surface fraction area of the i -th component

The amount of chemical remnants and their degree of inhomogeneity is hard to control. The same applies for the combined impact of the four dealt items on the contact angle hysteresis. A reliable analysis is also not possible. A droplet experiment, to be dealt in the following section, was chosen to prove in practical sense the limited overall impact of these potential nutation damping limitations.

Droplet verification

The experiment can be carried out using a light microscope, imaging the droplet and measuring the contact angle θ as indicated in Fig-2.20 [Schetz, 1999]. The wetting condition with $\theta < 90^\circ$ is shown in the left picture and refers to the Flutec ND liquids with extreme low surface tension. The minimization of the surface tension leads to the preferred wetting condition which results in a non-scattering film instead of single droplets. A water example is the anti-fog treatment which results by application of a surfactant film, or by creating a hydrophilic surface structure.

The right picture shows the non-wetting condition for liquids with high surface tension like Mercury. An example from Mother Nature is the Lotus flower surface which exhibits a very high water repellence (super hydrophobicity) with a contact angle θ of about 33° .

A complete (customer convincing) wetting proof is obtained by observing the droplets on the Aluminum plate with the same surface properties and finish as the ND materials. Subsequently a link can be made between CAD figures, measured contact angles θ and the theory. Two semi-infinite related cases are considered: the end pot wall case and the liquid drop case.



Fig-2.20 Wetting (left) and non-wetting conditions of a droplet on a plate [Schetz, 1999].

The following equations [Batchelor, 1980] apply with temperature dependent input parameter $\gamma_0 = \gamma_0(T)$. The endpot case is taken semi-infinite thus non-capillary since its radius b is large compared to the sticking height h . The droplet height h on a horizontal plate (equivalent of the end-pot wall case) is given by

$$h(\gamma_0, \rho, \theta) = \sqrt{\frac{2\gamma_0}{\rho g} (1 - \cos \theta)} \quad \text{and the end-pot wall the sticking height equals}$$

$$h(\gamma_0, \rho, \theta) = \sqrt{\frac{2\gamma_0}{\rho g} (1 - \sin \theta)}. \quad (2.92)$$

In both cases θ equals the smallest angle (up to 90°) between the liquid surface and the end-pot wall. In addition the capillary end-pot height H_c which does not apply for the semi-infinite case is

$$H_c(\gamma_0, \rho, \theta) = \frac{2\gamma_0 \cos \theta}{\rho g b}. \quad (2.93)$$

The end-pot meniscus time dependence obtained by the derivate of Eqn. (2.92) becomes

$$\frac{dh}{dt} = \frac{d\gamma_0}{dt} \sqrt{\frac{1 - \sin \theta}{2\rho g \gamma_0}} - \cos \theta \frac{d\theta}{dt} \sqrt{\frac{\gamma_0}{2\rho g (1 - \sin \theta)}}. \quad (2.94)$$

The impact of surface roughness and surface inhomogeneity was briefly described but these issues do not offer an explanation for a possible contact angle meniscus hysteresis. A large value (close to 90°) of the end-pot equilibrium wall angle θ_e is a hard indicator for a minimum presence. Eqns. (2.92) and (2.94) show (as for PP1) that this condition and a small surface tension γ_0 minimize in best possible sense the contact angle hysteresis $\Delta\theta = \theta_a - \theta_r$. In the end an independent measurement of the real contact angle provides the ultimate convincing evidence. In chapter 5 dealing with the FY-2 ND it will be shown that the Fokker ND ultimate damping performance has almost a zero dead band.

State of the art

An exploration of recent scientific literature in the field of nano-tribology [Bhushan, 2008] and wetting transitions on biomimetic surfaces [Bormashenko, 2010] showed

- The need for fundamental knowledge development of adhesion, friction, stiction and wetting
- A broad applicability in the field of micro-electronics, NEMS/MEMS, green technologies, coating technology, joining processes, design of hydrophobic materials, self-cleaning properties, etc
- The general theory of contact angle hysteresis has still not been formulated.

Well defined microscopic surface treatments are the experimental way forward. Refined surface treatment of the endpot materials in combination with dedicated coatings offers a way to reduce the ND ultimate angle and dead band even further.

2.11 *Scaling Space to Terrestrial Test Conditions*

An essential part of the space qualification of a ND design is the verification of the predicted dissipation performance. Therefore a refined terrestrial experiment with a scale model is required in the presence of the 1-g gravity condition. To enable these conditions three regular 0-g performance tests setups are the:

1. Horizontal iso-gravity pendulum in the 1-g plane with two degrees of freedom [Dutch Space]
2. Vertical pendulum as reported by [Häusler and Eidel, 2001]
3. Zero gravity parabolic airplane flight (airborne test) like the drop test developed by [Harrison, 1987].

The first two options will be compared extensively in Chapter 3 while the relevant theory of scaling essentials is given here [FDS, 1992]. Considering the design of the scale model and its ground equipment, the scaling theory reflects that the liquid motion caused by nutation in space can be exactly reproduced. Prerequisite is that all the non-dimensional fluid dynamics key parameters are equal. In this section these parameters are explored in detail. Starting from the NSE for an incompressible fluid given by Eqn. (2.69), the scaling conditions for flight to terrestrial conditions will be derived. The flow direction coincides with the X-axis and the radial (tube cross-sectional) position is given by r as parameter. Due to the rotational symmetry (section 2.8.4 to 2.8.6) the angular dependence is absent. The NSE followed by (r, x) evaluation yields

$$\frac{\partial u}{\partial t} + u_r \frac{\partial u}{\partial r} + u \frac{\partial u}{\partial x} = -\frac{1}{\rho} \frac{dp}{dx} + a_0 + \nu \left(\frac{\partial^2 u}{\partial r^2} + \frac{1}{r} \frac{\partial u}{\partial r} + \frac{\partial^2 u}{\partial x^2} \right). \quad (2.95)$$

Neglecting the axial position dependency x for a well-developed tube flow, the radial velocity u_r and convection reduce the NSE to the following dimensionless format

$$\frac{L}{VT} \frac{\partial u^*}{\partial t^*} = -\frac{\partial p^*}{\partial x^*} + \frac{La_0}{V^2} + \frac{\nu}{VL} \left(\frac{\partial^2 u^*}{\partial r^{*2}} + \frac{1}{r^*} \frac{\partial u^*}{\partial r^*} \right) \quad (2.96)$$

whilst all the key non-dimensional parameters are defined by

$$\begin{aligned} u^* &:= \frac{u}{V} & \text{Velocity} & & t^* &:= \frac{t}{T} & \text{Time} \\ x^* &:= \frac{x}{L} & \text{Length} & & p^* &:= \frac{p}{\rho V^2} & \text{Pressure.} \end{aligned}$$

The last equation transforms with use of the fluid dynamics characteristic numbers into

$$St \frac{\partial u}{\partial t} = -\frac{\partial p}{\partial x} + \frac{1}{Fr} + \frac{1}{Re} \left(\frac{\partial^2 u}{\partial r^2} + \frac{1}{r} \frac{\partial u}{\partial r} \right). \quad (2.97)$$

From Eqn. (2.97) it is seen that for fixed values of St , Fr and Re the flow described by the NSE in flight and test will be identical. Since the NSE effectively incorporates the physics of

the damping behavior of the nutation damper this holds the rules to scale space-to-terrestrial test conditions with V , T , L , ν and a_0 being controlled parameters. However for the ND the velocity V is not known at forehand and cannot be controlled. In this case V will be eliminated from the triplet $\langle St, Fr, Re \rangle$ and this approach will be further elaborated. The NSE does not describe surface tension effects in the end-pots. This was done separately in the previous section by the dimensionless Bo number. Finally the scaling conditions are found by defining the following constants with index r to distinguish the following relative terrestrial-to-space parameters:

$$\begin{aligned} V_r &= \frac{V_{test}}{V_{flight}} \quad \text{velocity,} & L_r &= \frac{L_{test}}{L_{flight}} \quad \text{length,} & \nu_r &= \frac{\nu_{test}}{\nu_{flight}} \quad \text{kinematic viscosity,} \\ t_r &= \frac{t_{test}}{t_{flight}} \quad \text{time constant and} & a_{or} &= \frac{a_{o,test}}{a_{o,flight}} \quad \text{acceleration scaling.} \end{aligned} \quad (2.98)$$

Flow similarity in flight (FM) and performance test model dampers (PTM) requires

$$\frac{St_{test}}{St_{flight}} = \frac{Re_{test}}{Re_{flight}} = \frac{Fr_{test}}{Fr_{flight}} = 1$$

resulting in

$$\frac{V_r L_r}{\nu_r} = 1 \quad \frac{V_r^2}{L_r a_{or}} = 1 \quad \text{and} \quad \frac{L_r}{V_r T_r} = 1 \quad \text{with} \quad \rho_r = \frac{\rho_{test}}{\rho_{flight}}. \quad (2.99)$$

Finally the elimination of V_r yields the following two key scaling equations

$$L_r^2 \nu_r^{-1} T_r^{-1} = 1 \quad \text{and} \quad L_r a_{or}^{-1} T_r^{-2} = 1. \quad (2.100)$$

These two equations enable the derivation of all other scaling relations by subsequent dimensional analysis. Starting with n the ratio space-centrifugal to terrestrial 1-g acceleration with $g=9.81 \text{ m/s}^2$ at the 52° northern latitude (Amsterdam):

$$n = \frac{R \omega_z^2}{g} \quad \text{and consequently} \quad a_{or} = n^{-1} \quad (2.101)$$

and by using n the further elaboration of (the first) Eqn. (2.97) yields

$$\nu_r = \frac{\nu_{test}}{\nu_{flight}} = \frac{L_r^{3/2}}{\sqrt{n}} \quad \text{and therefore} \quad \nu_{test} = \sqrt{\frac{g}{R_m}} \frac{L_r^{3/2}}{\omega_z} \nu_{flight}. \quad (2.102)$$

Taking the relative kinematic viscosity $\nu_r=1$ in Eqn. (2.102) the dimensional scaling $n = L_r^3$ is valid if the flight damper uses the same damping liquid as the test damper. Elaboration of Eqns. (2.100) up to (2.102) delivers the following three key equations for the test parameters of a ND performance test model (PTM).

1. Test frequency Ω_{test}

The test frequency Ω_{test} is defined by its scaling Ω_r and inversely proportional to the time scaling T_r so

$$\frac{\Omega_{test}}{\Omega_{flight}} = \Omega_r = \frac{1}{T_r} \quad \text{and by applying Eqn. (2.100) and (2.101)}$$

$$\Omega_r = \frac{1}{T_r} = \frac{1}{\sqrt{n} L_r} \quad \text{and finally using Eqns. (2.5) and (2.101)}$$

$$\Omega_{test} = \frac{\lambda - 1}{\sqrt{L_r}} \sqrt{\frac{g}{R}}. \quad (2.103)$$

2. Air bearing arm amplitude

The terrestrial tests are performed by a test-setup with an airbearing pendulum in the horizontal iso-gravity 1-g plane with two degrees of freedom. The test acceleration is derived from the flight nutation acceleration Eqn. (2.21) and elaborated the related test parameters:

$$a_{\theta, test} = \Phi R_a \Omega_{test}^2 \quad \text{test acceleration value,}$$

$$\Phi \quad \text{air-bearing angle amplitude and}$$

$$R_a \quad \text{air bearing test arm length.}$$

By combining Eqn. (2.5) and (2.21) it follows

$$a_{\theta, flight} = \theta_0 Z_0 \frac{(\lambda - 2\lambda + 2\lambda_x)}{(\lambda - 1)^2} \Omega_{flight}^2 \quad \text{whilst further elaboration in to}$$

$$a_{\theta r} = \frac{\Phi_a R}{\theta_0 Z_0} \frac{(\lambda - 1)^2}{(\lambda - 2\lambda + 2\lambda_x)} \Omega_r^2 \quad \text{finally yields the air bearing arm amplitude}$$

$$\Phi_a R = L_r \theta_0 Z_0 \frac{\lambda - 2\lambda + 2\lambda_x}{(\lambda - 1)^2}. \quad (2.104)$$

This equation enables the definition of the angular test range related to the S/C nutation angle range.

3. Dissipation rate

Dimensional analysis of the relative (test to space) dissipation rate in the liquid tube shows

$$\left[\frac{\bar{P}}{a_\theta^2} \right]_r = \rho_r L_r^3 T_r$$

This gets clear by a dimensional analysis of the first factor at the right hand side of Eqn. (2.83) and therefore

$$\left[\frac{\bar{P}}{a_\theta^2} \right]_{test} = \rho_r L_r^3 T_r \left[\frac{\bar{P}}{a_\theta^2} \right]_{flight} \quad (2.105)$$

This equation enables the verification of flight damping performance by its model prediction and PTM tests. Eqns. (2.103) until (2.105) are the key to define the test setup to be dealt with in Chapter-3.

The following sections of this Chapter 2 will confine to the systems engineering considerations in a ND development project. The derived rules are gathered insights mainly from the FY2 ND project to be dealt in Chapter 4.

2.12 Design Tuning

Thinking ahead for time, production and project cost escalations, risk mitigation is an essential part of systems engineering. In this section and the following one, an inventory of mitigation issues will be made. Starting with the description of design tuning and its boundary conditions, the key SE rules for a controllable ND project will follow. At first three design tuning effects will be discussed playing a key role in the design and verification. The first two are implemented in the model to calibrate the design towards the air-bearing test results. The experiments are described in Chapter 3 and 4. The third is a design driver for the end pot height.

The first TLD design step is the implementation of the flight (inertia) parameter using Eqns. (2.6) and (2.7). Tuning of the resonance frequency ω_0 towards the nutation frequency Ω is achieved by the choice of the geometry parameter set $\langle a, b, h, L \rangle$ and the damping liquid. These parameters offer a first order guess of the Flight Model (FM) ND design dimensions and its scaled Performance Test Model (PTM). The time constant τ and damping performance of the nominal design has to comply with the extreme operational cases.

The practical rule was used to choose the resonance frequency ω_0 roughly 10% ‘faster’ to tune it with the nominal nutation frequency Ω_0 . This design rule was based on ‘healthy’ engineering (back of the envelope calculation) knowledge from the COSB and Ulysses ND design heritage at Dutch Space implying

$$\gamma_0 = \frac{\Omega_0}{\omega_0} \cong 10/11 \quad \text{and therefore as design rule}$$

$$\frac{a}{b\sqrt{L}} = \frac{110\%\Omega_0}{\omega_z\sqrt{2R_0}} = \frac{11\lambda_0 - 1}{10\sqrt{2R_0}}. \quad (2.106)$$

The 10% rule can be understood by regarding the oscillatory in- and outlet flow effects which enlarge the effective tube damping length. From Eqns. (2.58) and (2.59) it can be seen that this effect increases the effective tube length and decreases the resonance frequency. However this practical approach lacks a rigorous scientific treatment and justification. The development of the latter was one of the quests of this thesis and resulted in a refined approach [2012] based on the use of either Eqn. (2.46) or (2.50) using a specific value of Re . The methodology of this specific choice will be clear in Chapter 7 after the refined processing of the test results in Chapter 4 and 5. This approach, however, was not applied in the design and development of the FY-2, Ulysses and Cluster TLDs which are successively dealt with in Chapter 4 up to 7.

The final calibrated FM design results after a recursive cycle of design by analysis and verification by refined testing. The new method yields educated guesses (first shot almost right) of the effective length and will therefore decrease the test and analysis time significantly.

Effective Damping Length and Fluid Level Tilt

The endpot level is not parallel to the liquid tube axis since in the NS Eqn. (2.69) both the nutation a_0 and the centrifugal acceleration $g = \omega^2 R$ act simultaneously. This yields a fluid level tilt $\tan(\varphi) = a_0/g$ and as a consequence the pressure gradient in the NS equation must to be corrected. Regard a tilt length $\delta = b \tan(\varphi)$ in the endpot which corresponds to an acceleration difference $2g\delta/L$ since both sides of the liquid tube counteract. The maximum change in the normalized pressure gradient in the NS equation Eqn. (2.73) becomes

$$\Delta \left(\frac{1}{\rho} \frac{\partial p}{\partial x} \right) = a_0 \frac{2b}{L} \quad \text{whilst } \bar{P}/a_0^2 \text{ is enlarged by the square tilt factor}$$

$$\left(1 + \frac{2b}{L} \right)^2. \quad (2.107)$$

The recursive FY-2 ND calibration approach (Chapter 4) was implemented in the Cluster S/C ND program by [van Bakel, 1993]. This changed the quadratic format of Eqn. (2.107) by introducing a power n and results in

$$\left[1 + \frac{2b}{L_{eff}} \right]^n. \quad (2.108)$$

The effective length is consequently written compliant to Eqns. (2.39) and (2.44) in the format

$$L_{eff} = L + \Delta L = L + \alpha \cdot 2b \quad (2.109)$$

This was required to obtain a methodology based on a convergent PTM tuning cycle during the Cluster ND phase B development. Consequently the PTM experiments are repeated in successive steps such that the design is fine-tuned and the parameters α and n get stable.

Endpot Geometry

For the curved FM ND design in a 1-g terrestrial performance verification test, the circular endpot liquid cross section gets ellipsoidal whilst an endpot level tilt is induced. The FY2 ND being the sole example of a curved ND in the Fokker-Dutch Space heritage. For a straight ND the reverse applies since in space the circular end pot liquid cross section gets ellipsoidal. This effect plays an important role in the design of straight and curved dampers and requires the end pot height h has to be chosen with care. The vapor tube shall not be filled with liquid in space operation or in terrestrial performance tests meanwhile the overall ND mass has to comply with its requirements.

2.13 System Engineering Considerations

The following considerations are the Systems Engineering rules of a successful ND project in terms of risk mitigation as well as technical and project control.

The Release of Changing Inertia Values

The development of a spinning S/C requires flexible recalibrations of the ND design. As a rule, due to I/F restrictions, the mass and thermal-mechanical requirements are fixed. The redesign may be made with just a change in the value of the liquid tube radius. This means, however, a change in the mechanical resonance spectrum of the damper which has to be acceptable. If not, the design of the structural support bracket of the damper has to be altered also. Taking the tube radius a to re-tune the design the following equation applies

$$\frac{\Delta a}{a} = \frac{\Delta \Omega}{\Omega} = \frac{\lambda}{\lambda - 1} \frac{\Delta \lambda}{\lambda}. \quad (2.110)$$

This equation may indicate a high sensitivity for a change in the inertia ratio λ in an early phase of a ND project. This was indeed the case for the Cluster phase-A ND design to be dealt in Chapter 6. A key negotiation issue between prime (customer) and ND subcontractor is therefore the inertia ratio contingency allowance.

The changes in the Mass-Of-Inertia (MOI) and Center-Of-Mass (COM) of the S/C are the result of the maturation of the S/C system design going from phase A to C/D. The impact can be made clear in terms of project risks towards the customer on basis of Eqns. (2.106)

up to (2.110). Re-tuning the ND design by applying these equations clarifies a number of restrictions and requirements like:

1. Only discrete values of the tube radius are procured according to space engineering standards.
2. The endpot radius b and tube length L can be varied continuously. However, as a rule, this has undesirable structural interface (I/F) consequences. The mechanical strength- and stiffness requirements are imposed by the launcher choice and or by customer derived requirements like the S/C mechanical I/F restrictions.
3. An endpot radius requirement $b > b_0$ to make the Bond number large enough.

Required Bandwidth (FWHM)

The existence of a nutation bandwidth allows for a limited frequency offset from the optimum ND resonance frequency. This may be acquired by a discrete (re)design by application of another damping liquid. This option does not change the geometrical design but results in a mass and structural stability penalty. The effects on the scaling relations are dealt with in Chapter 2.11. The ND bandwidth consequences are explored in detail for the Ulysses S/C NDs in Chapter-5 and for the Cluster S/C in Chapter 6.

Amount of Damping Fluid

The damping liquid is a substantial part of the mass budget. The mass contingency allowance is another key negotiable issue towards the customer with impact on the re-design flexibility. The ratio m/M is an important design driver of the ND as well as the factor k_0 .

Effective Tube Length and Required Curvature

A curved liquid tube coincides in the ideal case with the R defined iso-gravitational line. A straight tube yields some loss in damping performance compared to a curved one but is preferable in terms of less mechanical and test complexity.

Cultural Aspects

This is the last but not the least issue. A different attitude (philosophy) in development, verification and qualification priorities may exist between the S/C prime and the subsystem developers. This issue covers the hidden agenda in engineering interests. The subcontractor uses limited or extended shadow engineering efforts (up to S/C system performance) depending on the degree of common interests.

In the following chapter 3 the Verification and Validation of the ND performance of a number of spin stabilized spacecraft will be explored.

2.14 Conclusions

This chapter dealt with the theory of passive stabilization of spinning S/C by refined tuned liquid dampers of the Fokker tube-with end-pots type. Beside the essentials of spacecraft nutation and its control, the scope of applicable liquid flow models was extended towards multi-mode excitations.

The given literature investigation has shown that the ND operates linearly and stable in the laminar range and follows a traceable trajectory through a flow characterization diagram.

The key performance parameter of a liquid damper - beside the dissipation rate - is its tuned resonance frequency. The latter is directly related to the effective length which can be estimated by an educated guess on basis of test heritage. This serves as an initial value to start the recursive frequency calibration process of a ND design. The (old) practical rule to choose the resonance frequency ω_0 roughly 10% 'faster' to tune it with the nominal nutation frequency Ω_0 is overruled by insights on basis of the latest scientific literature in fluid mechanics. The merit of the new insights is verified in the following chapters dealing with the design and operation of the COS-B, Ulysses, FY-2 and Cluster nutation dampers. The eventual effective length must be determined from a recursive calibration cycle as will be shown in Chapter 4 for the FY-2 ND. A better initial estimate may reduce project test time and costs considerably. The methodology to derive a sound estimate for the additional effective length (in addition to the physical tube length) will be given in the Chapter 8 as an overall result of the thesis work in the following chapters.

The ultimate nutation damping angle is limited by endpot behavior, i.e., contact angle hysteresis (dead band performance) due to the physics of the interaction of the liquid meniscus with the wall. Though the Fokker ND design is characterized by a very low residual angle with almost zero dead-band the ultimate limit is not clear. Recent publications show no limits either. Refined surface treatment of the endpot materials in combination with dedicated coatings offers a way to reduce the ND ultimate angle and dead band even further. Therefore, well defined microscopic surface treatments are the experimental way forward. The given theory is used to explore this item in Chapter 4 at the limits of air-bearing test performance.

The system engineering rules derived from the processing of acquired insights were given. These facilitate the successful control of a liquid damper design, development and qualification project.

3 Verification & Validation

By far the best proof is experience.

Sir Francis Bacon

*English author, courtier, & philosopher
(1561 - 1626)*

3.1 Introduction

In the exploration of the applicable nutation damping theory in Chapter 2 different models were distinguished and compared. This chapter is dedicated to the verification and validation (V&V) of these models. The first step is the verification of the model predictions by scaled ground tests using a Performance Test Model (PTM). This typically happens during the phase B of a Nutation Damper (ND) project and is essential to convince the customer (prime contractor) of the health of the design. After the Preliminary Design Review (PDR) milestone is successful the go ahead is given for the extended test and production phase C/D of the qualification (QM) and the flight models (FM).

The ground test equipment will be discussed as primary instrument for verification of the ND model predictions. The validation of the ND performance can only be obtained when flight data becomes available. Dedicated space nutation tests, e.g. in a decommissioning phase, are required to enable a systematic evaluation of model, ground test and space performance results. Space nutation flight data, however, are sparsely available.

The six spinning S/C with passive ADCS candidates, given in Table-3.1, were selected for reasons of availability of ND design heritage, flight and ground test as well as qualification data. The S/C refer to different mission classes: meteorological (3, 4) in GEO and purely scientific (1, 2, 5, 6). From the latter class 2, 5 and 6 are in high elliptical Earth orbits whilst

1 is in a Solar elliptical orbit. The AOCS of S/C 5 and 6 incorporate meridian type NDs. The potential V&V data from these six missions will be discussed in the scope of ND performance here.

Table-3.1 *The selection of nutation damping V&V missions.*

V&V candidate	S/C	Prime contractor and/or Principal Investigator	ND type ¹	Spin-rate [rpm]	Lifetime
1	Ulysses	ESA/NASA	E	5	1990-2008
2	Cluster	ESA/NASA	E	5	2001-
3	FY-2	Chinese GWIC	E	100	1994-
4	MSG	ESA/Eumetsat	E	100	2002-
5	EQUATOR-S	Max Planck	M	48	1997
6	COS-B	ESA	M	10	1975-1982

¹ E=equatorial, M= Meridian

3.2 Verification and Validation data

3.2.1 Ulysses

The Ulysses S/C 5 rpm spin-stabilized mission studied the sun during the years 1990-2008 from solar polar latitudes. The S/C with some of its instruments and subsystem parts is shown in Fig-5.1. The BOL anomalous AOCS nutation behavior of the Ulysses S/C is dealt in Chapter-5. The cause of this behavior was outside the scope of the three NDs as will be shown in Chapter 5. The quasi nutation behavior was caused by solar heating of the axial boom shown in Fig-5.1. Beside this anomaly diverse sources mention the nominal nutation behavior of Ulysses [ESA, 2012].

3.2.2 Cluster

The Cluster mission is currently investigating the Earth's magnetic environment and interaction with the solar wind in three dimensions. Science output from Cluster greatly advances the knowledge of space plasma physics, space weather and the Sun-Earth connection and has been key in improving the modeling of the magnetosphere and understanding its various physical processes. The design and qualification of the extended Cluster NDs towards a multi-spectral wobble damper is dealt in Chapter 6. The four Cluster S/C are part of a very successful ESA mission and show a better than nominal AOCS behavior up to now [ESA, 2012].

3.2.3 Feng Yun 2

The Chinese meteorological Feng Yun 2 (FY-2) spacecraft and especially its ND design and qualification is extensively dealt in Chapter 4. The valuable refined PTM data, the QM qualification and the FM acceptance data were the backbone of the Cluster wobble damper design to be dealt in Chapter 6. Indirect V&V evidence of the FY-2 AOCS and its nominal ND performance was found and will be dealt in section 4.11.

3.2.4 Meteosat

The MSG S/C and the FY-2 S/C are both 100 rpm spin-stabilized. The sophisticated Meteosat mission and its limited nutation V&V data is dealt here briefly since it serves as the supreme mirror version (for comparence) of the FY-2 mission. The relevance of the Meteosat Second Generation (MSG) S/C within the scope of this thesis was already explained in Chapter 2.3. The MSG ND of the equatorial 'Fokker' type was designed and built by URENCO since Dutch Space transferred the ND knowledge to UCN/URENCO in the

early 90s. The author was involved independently in the pre-phase A study questions from Marconi Space Systems as subcontractor of Aerospatiale Cannes [Crowden, 1990], i.e., to supply a basic ND design and a Rough Order of Magnitude (ROM) costs estimate.

The 100 rpm AOCS space flight validation data from the Meteosat Second Generation (MSG) program is given by [Weymiens et al., 1999], [Luengo, 2004] and [Ebert and Reger, 1994]. The relevant parts are dealt here after an introduction of the MSG mission.

Mission and S/C Composition

The MSG is part of the family of geostationary spin stabilized spacecraft. The MSG S/C incorporates the imaging instrument SEVIRI (Spinning Enhanced Visible and Infra-Red Imager) which is capable to provide measurements of stars, Earth horizon and landmarks, apart from meteorological images. The author was involved as system engineer in the design team of the SEVIRI passive radiant cooler [Boyd and Kuiper, 1996].

The MSG concept, shown in Figs-2.2 and 3.1, is based on the same design principles as the Meteosat 1st generation S/C and also spin-stabilized at 100 rpm. A cylindrical-shaped solar drum, 3.2 m in diameter, includes in the center the radiometer (SEVIRI), and on top the antenna farm. The S/C height, including the antenna assembly, is 3.74 m. The MSG ensures continuity of atmospheric observation from the geostationary orbit at 0.0° longitude and inclination, as part of a worldwide, operational meteorological satellite system consisting of four polar-orbiting and five geostationary satellites (the World Weather Watch program of the World Meteorological Organization). The Meteosat users declared the SEVIRI instrument the benchmark in the field of geostationary imaging [ESA, 1999].

The MSG satellites benefit from several major improvements with respect to the first Meteosat generation (items in brackets) in terms of performance: 12 imaging channels (3), an image every 15 minutes (30), improved spatial resolution, and extra services such as a Search and Rescue Mission, an experimental Radiation Budget measurement instrument and improved communications services. MSG is a joint project between the ESA and Eumetsat (European organization for the exploitation of Meteorological Satellites). It consists of a ground segment and three satellites with the first launched in summer 2002 and the second in December 2005. These MSG satellites have been renamed Meteosat-8 and Meteosat-9. Some key differences between the Meteosat 1st and 2nd generation are shown in Fig-3.1.

Attitude and Orbit Control System

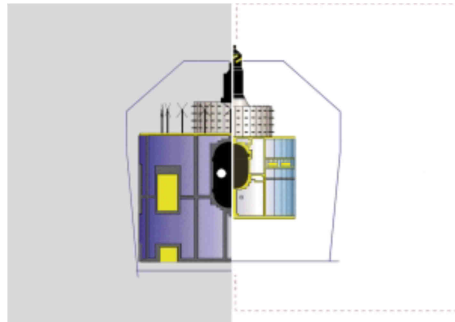
The MSG AOCS [ESA, 1999] is equipped with a subsystem with attitude, nutation, spin-rate and reference pulse to be generated by specific Sun, Earth and acceleration sensors. The main processing unit of the Attitude and Orbit Control Electronics (AOCE) and the Passive Nutation Damper (PND) are MSG-specific developments. The Active Nutation Damping (AND) in GEO Transfer Orbit (GTO) is primarily required in case a liquid apogee boost motor fails. The utilization of the AND is restricted to GTO whilst the PNDs are tuned for the GEO inertia ratios, to achieve optimum SEVIRI instrument performance. The AOCS is equipped with one internally redundant Sun Sensor Unit (SSU) and one Earth Sensor Unit (ESU). The major AOCS tasks are:

- **Attitude Measurement:** Sun/Earth Aspect Angle (SAA/EAA), nutation angle, frequency (in GTO)
- **S/C Synch Pulse Generation:** SSP 1=Sun Synch Pulse, SSP 2=Earth Synch Pulse and spin-rate.

The MSG S/C main AOCS requirements and performance were given in Table-2.3

Nutation due to SEVIRI scan mirror movements

The SEVIRI instrument contains a 20 kg mirror that rotates around an axis parallel to the S/C X-axis (SEVIRI FOV) with the Z-axis being the S/C spin-axis. The NDs are mounted on the Y-axis. The SEVIRI mirror rotation can be described as an initial stage in which the mirror is repositioned (retraced) in the starting point to obtain the meteorological data, a second Black-Body calibration stage at fixed position and a final scanning stage to acquire the image.



Meteosat Second Generation (MSG)

12 channel enhanced imaging
Bi-propellant unified propulsion system
500 W power
2000 kg total mass in GTO

First generation Meteosat

3 channel imaging radiometer
Solid apogee boost motor
200 W
720 kg in GTO

Fig-3.1 Main differences between the 1st Meteosat and MSG S/C series [Weymiens et al, 1999].

This mirror movement induces a variation in the S/C inertia matrix and as a consequence modified rotations thus S/C nutation during the scanning and retracing phases. A dynamical model, including the NDs, is given by [Luengo, 2004]. Using a simple model with only viscous damping compliant to the ND data, the results comply very well with the results extracted from the telemetry data. This is beside a confirmation of the correctness of the applied model also a proof of the ND nominal performance. The worst case yields a time constant $\tau = 2$ min compliant with the requirement $\tau < 4$ min [Weymiens et al., 1999]. The maximum impact in between two nominal cycles equals $\Delta\omega_y = 0.5$ [mrad/s].

Nutation damping and tank sloshing

The nutational damping may reveal sharp resonance effects at particular propellant tank fillings. This effect was studied for MSG by [Ebert and Reger, 1997]. The authors state that liquid inertial modes and S/C nutation are strongly resonance related and may explain the strong variations in in-orbit tests on INTELSAT V and in airbearing tests given by [Agrawal, 1993]. The MSG liquid tank configuration and the equivalent pendulum model are shown in Fig-3.2. Incompressible liquids and rigid tanks are taken as modeling assumptions. Two models are regarded:

1. The Homogeneous Vortex Approach (HVA) replaces the internal rotational degrees of the liquid by a single vortex mode. The dynamics of the tank surface modes allows for an equivalent pendulum model.
2. The Boundary Layer Model (BLM) uses a rigorous liquid motion model. This model is well suited to account for the coupling of liquid inertial modes and S/C nutation.

The BLM results are given by Fig-3.3 [Ebert and Reger, 1997]. An optimal interaction appears to be present in the tank filling range 50-60% where the sharp resonance peaks in Fig-3.4 fluctuate between a few minutes to hundreds of minutes. The overall damping nutation effect is a function of the tank filling and sloshing history as well as the PNDs damping.

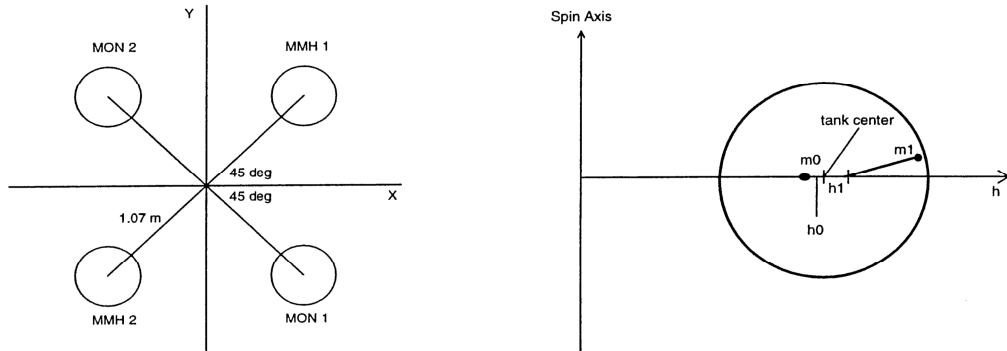


Fig-3.2 MSG tank configuration in the body frame (left) and equivalent pendulum model (right). The Z-axis is the S/C spin-axis [Ebert and Reger, 1997].

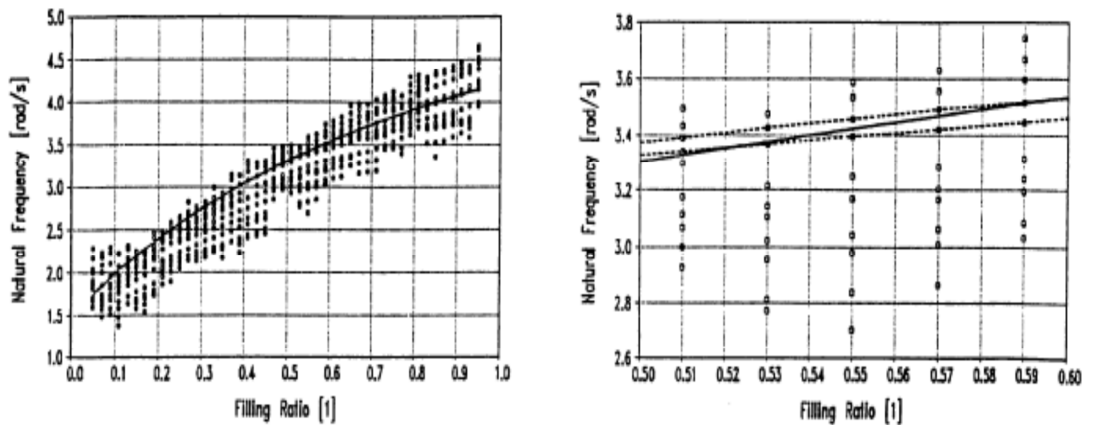


Fig-3.3 Nutation and natural resonance-frequencies of internal tank rotational modes derived from the BLM for different tank filling ratios: left picture 0-100% and right one (enlarged range) 50-60% in the tank filling ratio at 100 rpm spin-rate. The continuous line is the nutation frequency whilst dots and dashed line are the rotational modes [Ebert and Reger, 1997].

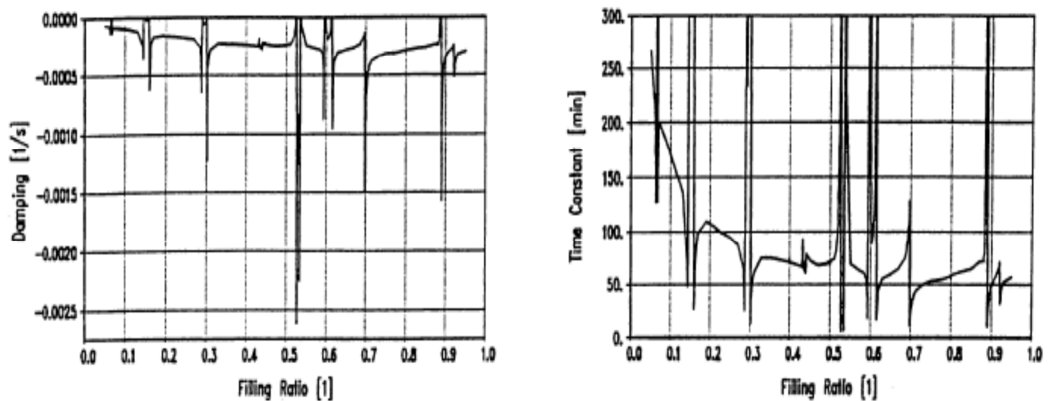


Fig-3.4 Nutation damping [1/s] (real part of system eigenvalue, left picture) and time constant (right) versus tank filling ratio. The results are derived from the boundary layer model at 100 RPM S/C [Ebert and Reger, 1997].

Many authors have worked on tank sloshing phenomena. [Vreeburg, 2009] deals with the key importance of a validated model of liquid momentum transfer during S/C manoeuvres. The availability of such a model enables liquid management and can make missions more efficient and less costly. The Dutch Sloshsat FLEVO mission (the author was system engineer of the electrical power S/S) was flown to deliver data to support such a model. The comparison of numerical solutions with space flight data is given by [Veldman et al, 2007].

3.2.5 EQUATOR-S

The EQUATOR-S S/C mission was designed and developed at the Max-Planck Institute in Garching with some supplementary items from agencies and industry. The S/C was launched the 2nd of December 1997 into an elliptical Earth orbit (perigee 479 km, apogee 67,275 km, inclination 3.9° and $T=22.3$ hour). The science mission included magnetospheric plasma and field measurements in the frame of ISTP (International Solar Terrestrial Physics Program).

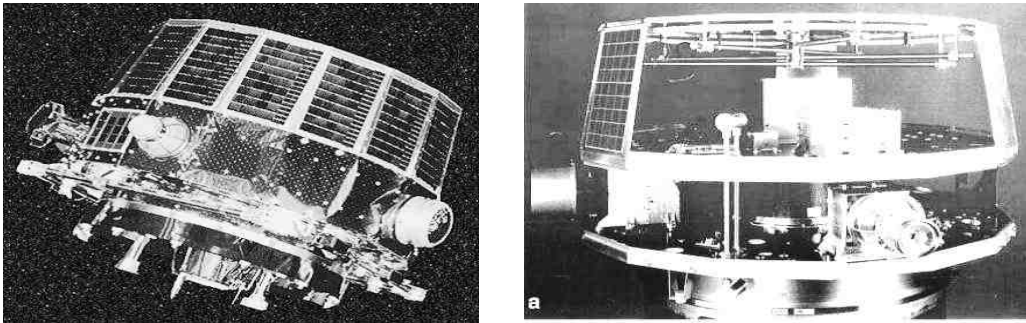


Fig-3.5 he EQUATOR-S S/C (left picture) [Haerendel et al, 1999] and (right picture) the interior of the S/C showing one of the two meridian NDs vertically mounted [Häusler et al, 2002].

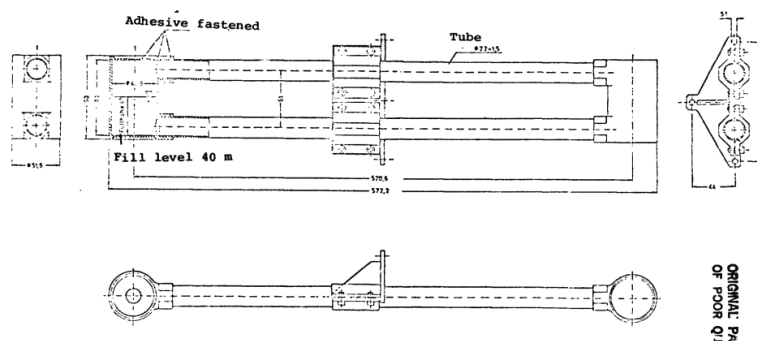


Fig-3.6 AMPTE ND build standard [Truckenbrodt et al, 1982].

The meridian EQUATOR-S ND is shown in the right picture of Fig-3.5. Its build standard is derived from the AMPTE-IRM S/C meridian ND [Truckenbrodt et al, 1982] and shown in Fig-3.6. The endpoints are adhesive fastened whilst the Fokker NDs are electron beam welded. Space validation data for the EQUATOR-S operational case are given by [Häusler and Eidel, 2001] and [Häusler et al, 2002].

3.2.6 COS-B

The COS-B scientific mission [Willmore, 1970] was to study in detail the sources of extra-terrestrial gamma radiation at energies above about 30 MeV. The successful COS-B space missions had no optical telescopes or complicated scientific instrumentation. Its only function was to point in the direction of a star or other object and measuring its gamma-ray emissions. COS-B was an ESA mission, built and equipped by European scientists and launched by NASA. It was ESA's first satellite dedicated to a single experiment enabling an extensive survey of the galaxy in the energy range 50 MeV to 5 GeV. The spacecraft overall mass equals 278 kg and the attitude measurement accuracy 1° . Its cylindrical sizes are a height 1.2 m and a diameter 1.4 m. The 37-hour orbit of Cos-B was an eccentric orbit (launch 1975-08-09, perigee 350 km, apogee 100,000 km, inclination 90°) that ensured that the satellite was outside the Earth's radiation belts for most of the time [COS-B, 1975]. The end of the mission coincided with the end of its propellant supply, which had been conserved by careful choice of maneuvers. The originally foreseen duration of the mission was two years, but COS-B was finally switched off on 25th April 1982, having functioned successfully for more than 6.5 years. In spring 1982 a dedicated series of space nutation experiments were executed at different frequencies and initial nutation angles induced by thruster firing. The rich amount of COS-B nutation modeling, ground verification and space operational validation data is given by [Bongers, 1984]. The original design of the meridian ND was made on basis of HP modeling dealt in Chapter 2. The position of the NDs in the S/C is shown in Fig-3.7 (top right).

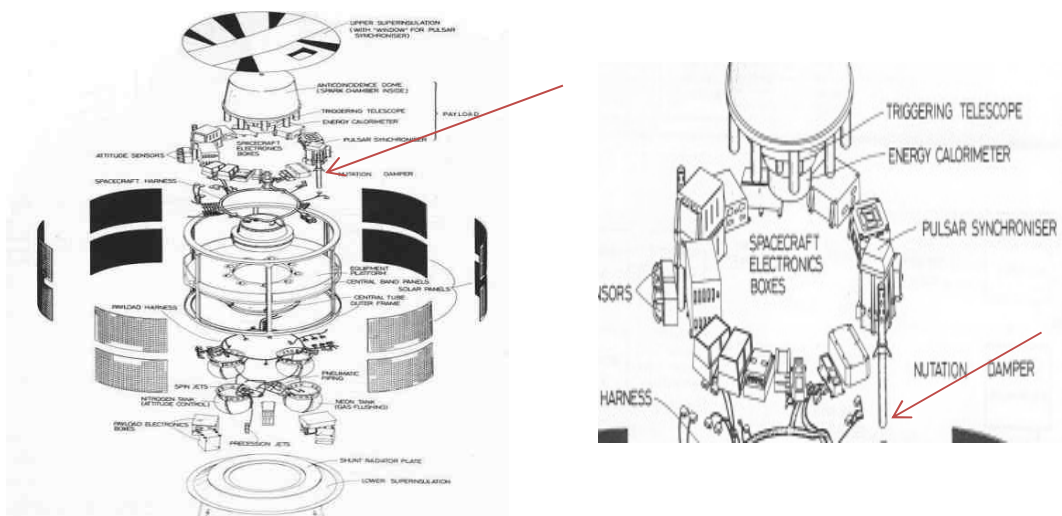


Fig-3.7 The COS-B S/C exploded view (left) and the upper stage zoomed-in to show the position of the meridian NDs (top right) [COS-B, 1975].

3.2.7 Selected Cases

The only traceable useful space test validation data are from the COS-B S/C [Bongers, 1984] and the EQUATOR-S S/C [Häusler et al., 2002] mission. The applied NDs are both of the meridian type with comparable design driving requirements as becomes clear from Table-3.2. A cross verification of models using experimental results on ground and in space is therefore the key to analyze the differences systematically.

The ultimate ground test system, to verify and validate flight ND damping performance, is either a horizontal pendulum arrangement like the air bearing test setup at Dutch Space

[FDS, 1992] or a vertical pendulum [Häusler and Eidel, 2001]. These will be dealt in the following section.

3.3 Airbearing Pendulum Tests

3.3.1 Vertical Pendulum

The vertical air-bearing pendulum used by [Häusler et al., 2002] is shown in Fig-3.8. In the left picture the two black contra weights are visible along the vertical rod whilst the (faintly visible) plexi-glass scale model is at the lower side. This scale model is enlarged in the right picture. In this pendulum with its horizontal axis, no springs are required but the angle dependent gravitational acceleration has to be taken into account in the Euler-Lagrange equations of the damper liquid motion.

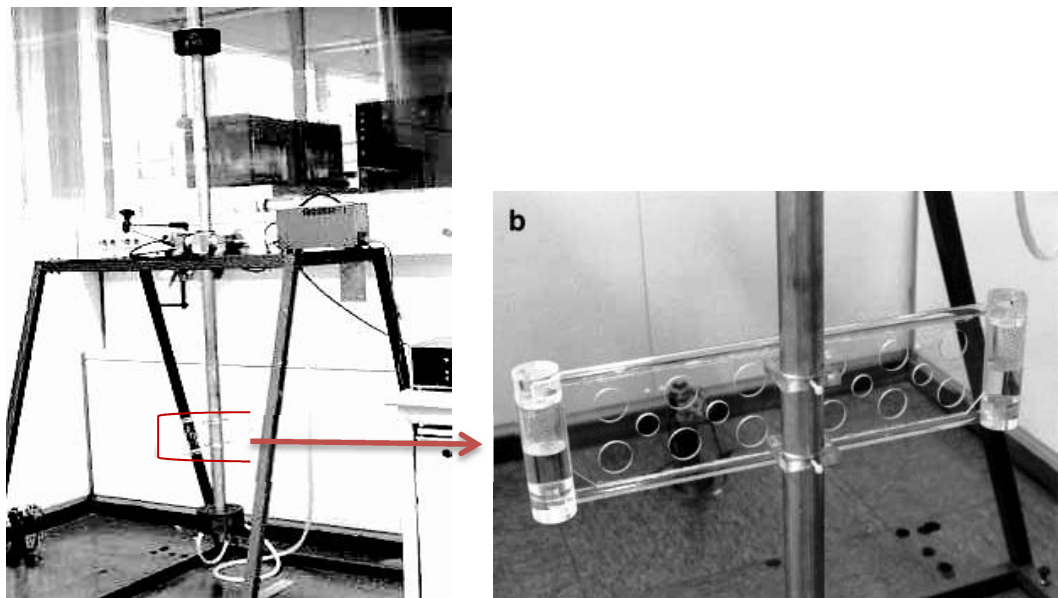


Fig-3.8 The vertical pendulum for ND performance verification used by [Häusler and Eidel, 2001].

3.3.2 Horizontal Pendulum

The setup of the Fokker ND performance measurement setup is shown in Fig-3.9 and 3.10. The right zoomed-in pictures of Fig-3.9 show the central air-bearing hub, the oscillation springs and the ND attachment part at the end of the mounting arm. The equipment was located in the 80s and 90s at the (Fokker) Dutch Space facilities and nowadays at Aeronamic B.V. One of the two wire-suspended arms is recognized, as well as the two oscillation springs which provide the harmonic driving torque. For stiffness and stability reasons a steal test-arm with square intersection and length $R_a = 2$ m was chosen. This limits torsion and linear arm oscillations down to $< 1\%$ relative accelerations of the ND liquid oscillation to be tested. The digital angle read-out which is an optical encoder and the computer system are integrated to monitor the oscillation angle with 2.75 arcsec resolution.

The S/C nutation is simulated by the oscillatory movement about the vertical rotation axis. The desired pendulum time is provided by two adjustable springs and/or additional

masses. The horizontal pendulum with vertical axis uses the gravitational 1-g force to scale (“replace”) the flight centrifugal acceleration.

The damping performance at very small angles is analyzed after automatic recording and processing of the normalized damping versus the angular amplitude. The latter is given by $R\Phi(t)$ over the specified amplitude range, where R is the mounting arm length and $\Phi(t)$ the momentary air-bearing oscillation angle.

The NDs oscillate in the horizontal (iso-gravitational) plane. Visible in Fig-3.9 are the skew suspension wires, a single ND arm and the oscillation springs. The NDs are not attached.

In Fig-3.10 the layout in the horizontal iso-gravity plane is shown in more detail with two FY2 NDs mounted horizontally on the air-bearing arms. The bended tubes are in the vertical plane forcing the endpot damping liquid levels to follow the 1-g directive.

Tuned damping performance evidence is initially gathered by PTM (Performance Test Models) scale tests. In a later project phase this is done in addition by the Qualification Model (QM) and Flight Model (FM) air-bearing performance tests.

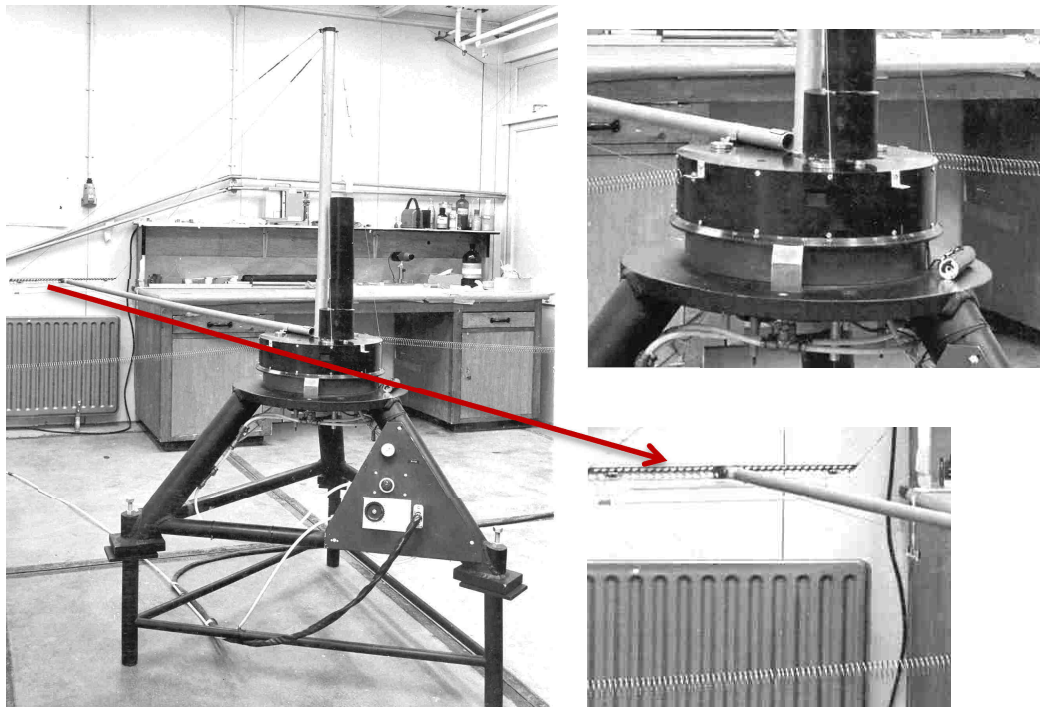


Fig-3.9 The air-bearing setup for the ND damping performance tests at Dutch Space in 1990. The red arrow indicates the support rail for the ND which is not attached.

The air-bearing arm length R and Moment-Of-Inertia (MOI) I_0 are independent of scaling rules. On basis of measurement accuracy trade-offs, the adjustable arm length for the FY-2 ND was taken $R = 2000 \pm 5$ mm whilst the total MOI equals $199.1 \text{ kg} \cdot \text{m}^2$ with two dummy models DMs (=‘dummies’) or $190\text{--}200 \text{ kg} \cdot \text{m}^2$ with two PTMs. The difference is attributed to the ‘free’ sloshing motion of the damping liquid in the end pots. For other ND projects specific choices and trade-offs are made on the arm lengths and the required stability as imposed by the ND test plan. For the Cluster ND this is explored in Chapter 7 and for the FY2 ND in Chapter 4.

The exponential damping time constant τ_i is found using single logarithmic plots of the amplitude $R\Phi(t)$ recorded over a time range $\Delta t = t_e - t_0$ using 4 to 5 logarithmic units, i.e., $\ln[\Phi(t_0)/\Phi(t_e)] = 4$ to 5 with

$$R_a\Phi(t) = R_a\Phi_0 e^{-t/\tau_i}. \quad (3.1)$$

The time test range is related to the required nutation angle range prescribed by the specific ND project requirements. The ranges are scaled by Eqn. (2.104). By shifting the extra weights on the test arm the oscillation frequency can be varied. The ND damping time constant τ_{ND} is obtained by

$$\frac{1}{\tau_{ND}} = \frac{1}{\tau_1} - \frac{1}{\tau_2} \quad (3.2)$$

with τ_1 the test damping time constant using a PTM, QM or FM and τ_2 the test damping time constant using a dummy model (DM). The time constant τ_2 refers to the same test but with the PTM, QM and FMs replaced by dummy models. These DMs have the same mass and geometry; contain no liquid but additional mass to compensate for this. This enables the separation of the liquid damping performance from the friction of the air-bearing and air resistance. The reduced time constant τ_{ND} approximates the time constant of the nutation liquid damping only. The influence of the test room air-environmental damping and air-bearing friction are therefore eliminated in best terms by applying Eqn. (3.2). The exponential time constant related to the damping rate as test parameter is:

$$\frac{1}{\tau_{test}} = \frac{R_a^2 \Omega^2}{I_{tot}} \left(\frac{P}{a_0^2} \right)_{test} \quad (3.3)$$

with $I_{tot} = I_0 + 2I_{ND}$ the total inertia about the vertical air-bearing axis, I_0 the test arm MOI including resonance tuning weights and I_{ND} the test ND thus the PTM, DM, QM or FM.

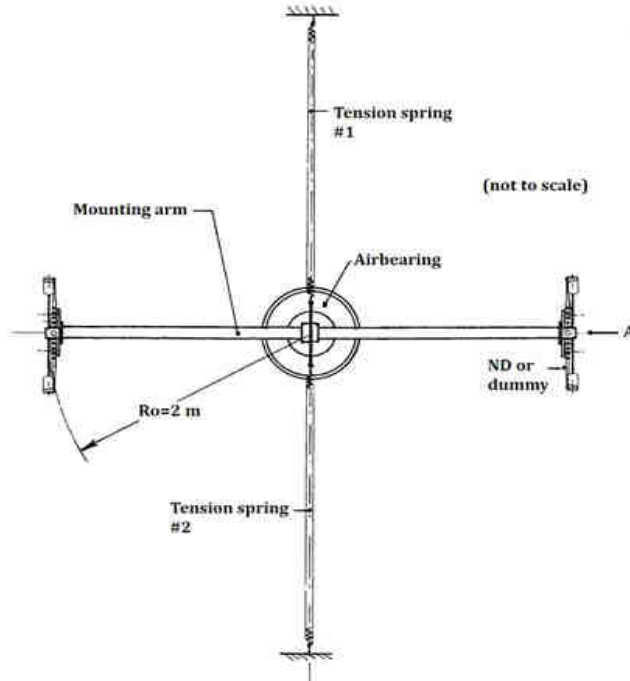


Fig-3.10 FY2 ND air-bearing test arrangement (schematic) in the horizontal 1-g iso-gravity plane.

Eqn. (3.3) enables the determination of the time dependent $P(t)/a_o^2$ value which gets constant only in the laminar small angle oscillation range. It is the air-bearing equivalent of Eqn. (2.26) up to (2.28). The exponential damping time constant τ_{test} depends on the air-bearing radius, its MOI and the damping rate of the test model (PTM, QM, FM and DM). Finally by scaling the 1-g damping rate towards its space value and using Eqn. (2.105), the performance of the FM as function of the inertia ratio λ is found. As basic rule five λ values on basis of Eqn. (2.103) are taken as minimum number to define a proper performance check of the FM design. A series of precautions are taken to obtain optimal test conditions and accurate results:

- The total MOI of the air bearing including the test-setup and the NDs (or DMs) is measured
- The oscillation arms generate airflows. This effect is reduced by doing the same measurements with DMs and applying Eqn. (3.2). Additional disturbance effects, possibly caused by people walking around or accidental (random) ventilation flows, are avoided. It was proposed by the author to do tests with aerodynamic (ellipsoidal encapsulation) profiles attached to the end of the arms around the attached NDs to limit and control the additional airflows even further
- NDs are leveled using a theodolite within ± 10 arcsec
- The air-bearing feet are adjusted up to the level where the end of the arms are within 20 arcsec variation over the full 360° of angular range at 5 PSI air-bearing operational pressure
- The moving damper liquid exerts a torsional moment on the mounting arms. To limit vibrations the torsional material stiffness G [Nm/rad] of the test arms is chosen to limit torsional accelerations down to 1% of the maximum tangential value. The effects were quantified using the generic Eqn. (2.65). The G value is verified by applying a zero and a well-defined torsional moment on one end of the mounting arm. Theodolite measurements are made with a mirror at the end of the arm
- The same kind of engineering arguments hold for the trade-off on the effective test arm length which is driven by a $< 1\%$ relative magnitude of the centrifugal to nutation acceleration
- The centrifugal flight acceleration field is curved whilst the terrestrial 1-g field is straight. This implies a curved FM and a straight PTM. However in general the FM NDs are chosen straight as well as the PTMs. The only exception is the FY-2 FM ND which was bent as a strict requirement from the Chinese customer. The effect on the damping performance is negligible. To prove this, consider a straight ND in a curved acceleration gravity field. It is clear that the acceleration decreases in the left part of the liquid tube is compensated by an equal increase in the right part. The same argument holds for a curved ND in a straight 1-g terrestrial gravity field.

3.4 EQUATOR-S and COS-B Data Analysis

3.4.1 Design Data

Table-3.2 contains the main S/C and ND design data. In the last rows the relative ND liquid mass and the factor k_0 from Eqn. (2.67) is given. The factor k_0 accounts in the RHP-1 model for the effective relative amount of damping liquid mass and was introduced by [Häusler et al., 2002]. The relative amount of COS-B liquid mass, with requirement $m/M \ll 1$ as prerequisite of a quasi-rigid S/C configuration, is about one third of the EQUATOR-S value whilst the k_0 factor is comparable. The 5" extreme nutation angle for COS-B and the less than 0.5" per orbit drift requirement follow from the X-ray science experiment requirements given by [Willmore, 1970].

Table-3.2 COS-B [Bongers, 1984] and EQUATOR-S [Häusler et al., 2002] meridian ND design data.

S/C	COS-B	EQUATOR-S
S/C total mass M [kg]	278	216.9 (dry mass)
[source]	[ESA, 2001]	[Enderle et al., 1997]
Spin axis inertia I_{zz} [kg.m ²]	54.53	34.35 ^a to 38 ^b
Spinrate (nom) [rpm]	10±0.1	48 ^a to 50 ^b
BOL inertia ratio λ_o [-]	1.232	1.330
Nutation amplitude [degree]		
• Initial	3.8	3.3
• Final	< 5"	< 1.0 ^c
Temperature [deg C]	(-20 to +30)	+12.7 (nomimal)
Hardware model	FM PTM	FM PTM ^d
Materials liquid / housing	PP1/ Al PP1/ Al	PP1/Al H ₂ O/Plexiglass
ND time constant [sec]		
• Theory (NS, RHP)	see multiple cases in text	38.7 (RHP) 72.3 (RHP)
• FM space / PTM ground test		38 ± 3 (RHP) 72 ± 6
S/C mounting radius [mm]	668	565
Design dimensions <a, b, L, H> mm]	4.0, 20.96, 400, 40	5.0, 23.04, 500, 80
FM/PTM damping liquid	PP1	PP3
FM /PTM ND liquid temperature [°C]	9.9 18-21	12.7 18-21
ND liquid mass m [kg]	0.136	0.291
ND liquid mass ratio m/M [%]	0.049	0.134
RHP k_0 factor [-]	0.473	0.374

^aBooms folded

^bBooms deployed

^cRange taken from Fig-3.5

^dNot flight representative

3.4.2 Applicable Models

Three applicable models have been extensively dealt with in Chapter 2. In the frame of the Verification and Validation (V&V) purposes they are briefly re-summarized here:

- The **first** Hagen-Poiseuille (HP) model considers a fully developed single directional flow which is in general not valid due to the harmonic nutation sweep-up forces in the liquid tube. Only at low S/C spin-rates with consequently low nutation frequencies the model can be used. The previous chapter showed its applicable range which is a special class of the generic Navier-Stokes solution. The HP model explains and quantifies the natural resonance behavior at sweep-up moments of nutation. This phenomenon ("beat-up") was indeed observed during the Ulysses PTM tests as will be shown in chapter 5.
- The **second** RHP-1 model [Häusler et al., 2002] is an adapted version of the HP model based on theory derived by [Truckenbrod, 1986].

- The **third** Fokker Space NS model was derived by solving the Navier Stokes Equation (NSE).
- A **fourth** ND model [Crellin, 1982] used at ESTEC/ESA is also based on the NSE. The model was used beside the Fokker Space NS model in the Ulysses anomaly study in the period November/December 1990. The results agreed seamless though different inertial systems are used.

The Hagen-Poiseuille (HP), its refined version (RHP-1) and Navier-Stokes (NS) models with common NS basis are used to analyze the differences in flight and ground test results.

3.4.3 EQUATOR-S S/C Nutation

The EQUATOR-S ND design was driven by the RHP-1 model from [Häusler and Eidel, 2001] based on [Truckenbrodt, 1968]. It enabled a compliance in the modeling results, air-bearing test results and flight nutation data of the 48 rpm spin-stabilized EQUATOR-S S/C. The RHP-1 model derivation starts from the generic case of communicating vessels with, in addition, an inertia correction factor to account for the moving liquid mass in the dampers. The determination of the flight operational damping time constant is shown in Fig-3.11 with vertically the detected nutation angle and horizontally the elapsed flight time. The RHP time constant model results are in good agreement with EQUATOR-S ground test and in orbit nutation data [Häusler and Eidel, 2002]. The application of the RHP model to the heritage of Dutch Space nutation dampers, however, revealed substantial differences between the RHP-1 and NS models. These will be further analyzed to study the validation range of the diverse models.

In Fig-3.12 the results of RHP-1, NS and HP modeling are shown. First the EQUATOR-S results from [Häusler and Eidel, 2001] and [Häusler et al., 2002] were verified (model calibration) by embedding their RHP-1 model in MathCad® code. Taking their nominal inertia $\lambda_o = 1.33$ maximum damping design case at $\Omega_o = 1.661$ rad/s, with $2b = 46.08$ mm and $2a = 10$ mm as calibration case, yields perfect agreement. The MathCad® models deliver $\tau = 50.330$ s (NS) and 50.332 s (RHP-1) versus 50.33 s from [Häusler and Eidel, 2002].

Flight validation

The final flight design ($2b = 45$ mm, $2a = 9$ mm) value differs slightly with $\tau = 69.3$ s (RHP-1) versus 72.3 s from the [Häusler et al., 2002] RHP-1 model. The flight validation value equals $\tau_{exp} = 72 \pm 6$ s as derived from Fig-3.11 whilst the NS model value, read from Fig-3.12 at the nominal nutation frequency $\Omega_o = 1.661$ rad/s, equals $\tau = 61.3$ s.

In Fig-3.12 the time constant differences between the NS/HP and RHP-1 model predictions at $\lambda_o = 1.33$ are within 15% whilst the flight value is within the range of the NS and HP model.

In the horizontal direction the inertia ratios all show significant off-sets compared to the desired nominal inertia $\lambda_o = 1.33$ which means a mistuned ND resonance condition. The RHP-1 model shows a -3% off-set whilst the NS and HP model show a -5% offset. It is remarkable that the EQUATOR-S ND design data given by [Häusler and Eidel, 2001] and [Häusler et al., 2002] do not reveal an essential picture like Fig-3.12 with the RHP-1 model time constant as a function of either the nutation frequency Ω or the spacecraft inertia λ .

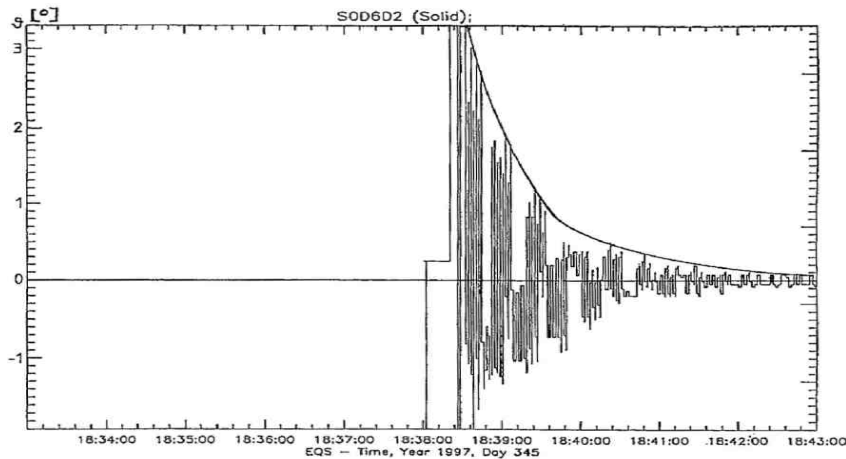


Fig-3.11 Nutation angle attenuation of the EQUATOR-S S/C measured in flight which yields the flight validation value $\tau_{exp} = 72 \pm 6$ s [Häusler and Eidel, 2002].

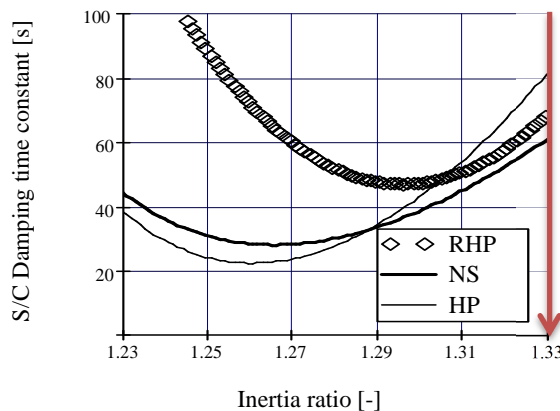


Fig-3.12 EQUATOR-S S/C flight nutation time constant prediction at $T = 12.7$ °C by three ND models with the arrow indicating the desired tuning condition.

Ultimate nutation angle

The EQUATOR-S flight data show a minimum nutation angle < 0.1 deg. No additional test data or test philosophy is given to investigate the ultimate damping angle as was done for the COS-B S/C.

3.4.4 COS-B S/C Nutation

The EOL COS-B S/C flight nutation data were analyzed by [Bongers, 1984]. The COS-B AOCS was equipped with two meridian NDs, shown in Fig-3.13. In the upper picture the liquid and vapor tube, as well as the endpoints are partly disguised by its structural housing. The lower picture shows the A-A cross-section with the liquid tube ($a = 4$ mm) at the bottom.

Nutation experiments were executed during spring 1982 at the S/C EOL cycle. The nutation was induced by thruster firings up to angles of 3.8 degree. The nutation behavior was extracted from the sun sensor telemetry data and analyzed by Fast Fourier Transform (FFT) analysis from the S/C oscillatory behavior, a method described by [Wertz, 2003]. The

ND flight performance complies well with the NS model predictions. The basic uncertainty in the modeling results is caused by inaccuracies in the MOI, i.e. < 2% absolute error, temperature and position angle of the NDs.

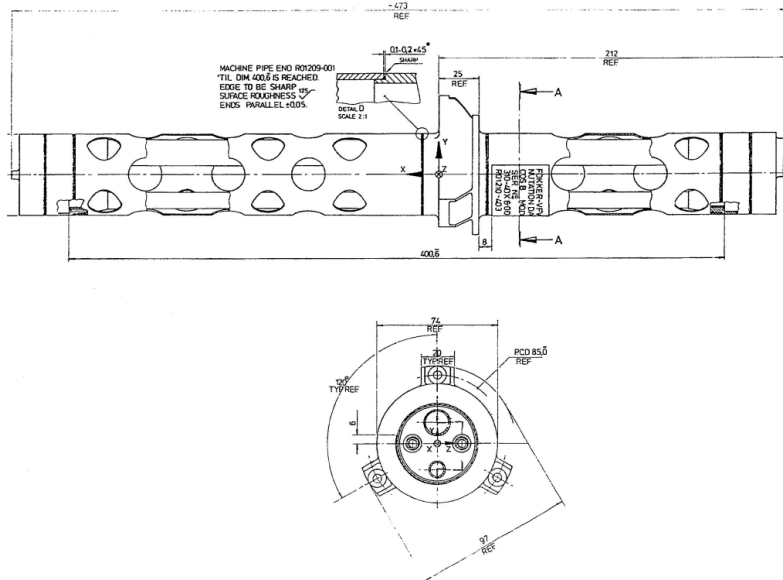


Fig-3.13 Meridian COSB nutation damper built by (Fokker) Dutch Space [FDS, 1992].

Taking these into account the results summarized from [Bongers, 1984] are:

1. The nutation decays exponentially in all cases.
2. No correlation exists between the initial nutation angle and the time constant.
3. The in-orbit time constants, resulting from invoked flight nutation at 9.45 and 17.63 rpm, comply well with the results obtained by NS modeling and air-bearing tests.
4. Air-bearing PTM results comply well at lower spin rates (8 rpm)
5. At the high spin-rates 36.6 and 113.4 rpm the air-bearing predicts less damping so higher time constants.

The Fokker Space models and test setup were improved since the development of the COS-B ND according to [Bongers, 1984] up to the standard used in the design and qualification of the FY2 ND.

Flight validation

The end-of-life (EOL) space nutation experiments [Bongers, 1984] were re-analyzed at the low spin-rate range $\omega_z = 9.45 \pm 0.06$ rpm and at the higher range $\omega_z = 17.63 \pm 0.02$ rpm with inclusion of the RHP-1 model beside the NS and HP model. In Fig-3.14 the HP, RHP-1 and NS modeling results are shown at 9.45 rpm spin-rate with all other parameters nominal defined by Table-3.1 and a ND position angle $\alpha = 40^\circ$.

The NS and HP model show a resonance shift of +5% beyond the specified EOL $\lambda_0 = 1.232$ value whilst the RHP-1 model shows a shift of 9%. Moreover the shape (less bandwidth) of the RHP-1 curve differs. The NS and HP curve almost coincide as expected at low spin-rates.

The result at the EOL value $\lambda_0 = 1.232$ agrees seamless with the space experiment results given, i.e. the flight damping time constant $\tau = 7.0$ min with standard deviation $\sigma = 0.5$. The same shifts hold for the model predictions of the nutation performance at 17.63 rpm spin-rate given in Fig-3.15. The result at $\lambda_0 = 1.232$ matches seamless with the results given by [Bongers, 1984] since the extracted flight damping time constant $\tau = 4.2$ min with standard

deviation $\sigma = 0.3$. In both cases the RHP-1 model and its time constant prediction is far off and does not apply to the COS-B design and its flight performance validation.

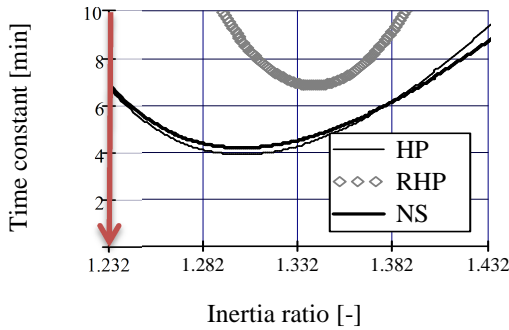


Fig-3.14 The flight COS-B ND damping prediction by the HP, RHP and NS models at 9.45 rpm with the arrow indicating the desired tuning condition.

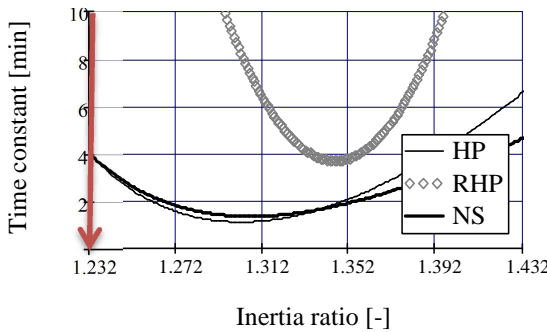


Fig-3.15 COS-B FM damping prediction by the HP, RHP and NS models at 17.63 rpm spin-rate with the arrow indicating the desired tuning condition.

Ultimate nutation angle

The contact angle hysteresis below the required 5" flight nutation angle is not experimentally detectable. Therefore a scaled experiment was executed [Dutch Space heritage] with a glass-water PTM model. The experiments were executed down to air-bearing angular motion levels representative for flight nutation angles $< 0.2^\circ$. Because of the low accuracy, caused by air-bearing turbulence flow phenomena in this range, a large number of repetitive experiments were necessary. The experimental values are valid in the vicinity of the flight spin-rate $\omega_z = 0.661$ rad/s equal to 0.105 Hz in Fig-3.16. The results were re-analyzed and the verified results are given in Fig-3.14. The conclusions are:

- The measured (marked) P/a_o^2 values, determined at 1" and 0.2" equivalent flight nutation angle, do not show a significant difference in damping performance. At these air-bearing amplitudes the typical damping uncertainty is about 30% as will become clear in Chapter 4 in the detailed analysis of the FY-2 PTM ultimate angle test results.
- A resonance shift is not recognized going from the 1" to the 0.2" data cloud. This shows that a second time constant from contact angle hysteresis is absent.

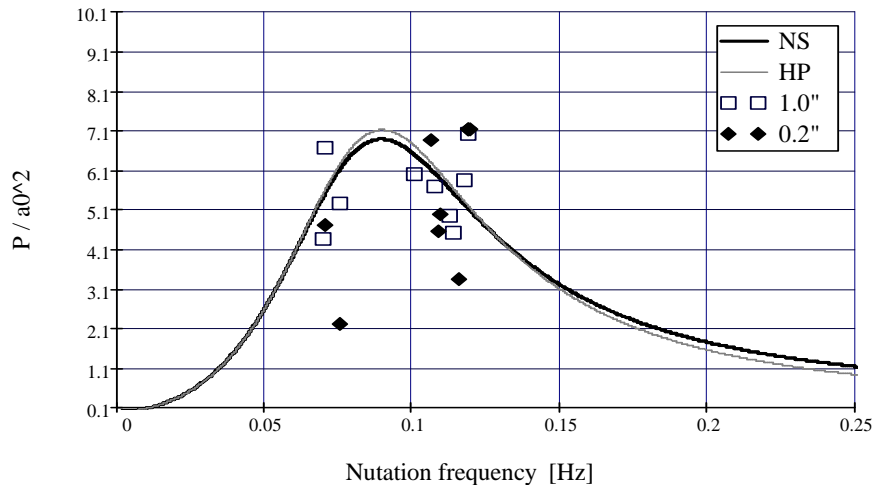


Fig-3.16 Modeling and PTM experiments of the COS-B ND behavior at the extreme small flight nutation angle 1.0'' and 0.2'' in the vicinity of 0.105 Hz ($=0.661$ rad/s) at $T = 7.5$ °C.

3.5 Conclusions

The ND verification and validation data of the following three classes of S/C were investigated:

1. The 5 rpm Ulysses and 15 rpm Cluster S/C flight data mention nominal ND performance but yield no explicit data or in-orbit invoked nutation experiments.
2. The meteorological FY-2 and MSG S/C at 100 rpm yield in-orbit AOCS compliance with the ND S/S design.
3. The EQUATOR-S at 48-50 rpm and COS-B S/C 10 rpm records yield very interesting data. A systematic model comparison was conducted yielding the following results:

The relative amount of COS-B liquid mass, with requirement $m/M \ll 1$ as prerequisite of a quasi-rigid S/C configuration, is about one third of the EQUATOR-S value. The “free liquid” k_0 factor accounting for the applicability of the RHP-1 model is comparable.

The EQUATOR-S RHP-1 (Refined Hagen-Poiseuille model #1) flight damping time constant prediction is within 15% compared to the NS and HP model. Peculiar is the fact that the RHP-1 model which drove the ND design, shows a -3% resonance offset from the design value $\lambda_0 = 1.33$ while the HP and NS model show a -5% offset. The EQUATOR-S ND design data given by [Häusler and Eidel, 2001] and [Häusler et al., 2002] do not reveal an essential picture with the modeled time constant as a function of the S/C inertia ratio λ . The frequency tuning of the ND is not mentioned but only the agreement in damping time constant between the RHP-1 model, air-bearing and flight results at nominal flight conditions. The considerable -3% offset indicates that the mass of the EQUATOR-S ND could have been reduced.

The plexi-glass PTM model of the EQUATOR-S ND has totally different end pot materials, surface treatment (if any) and RMS roughness compared to the Aluminum FM. Despite these differences the PTM tests yield an excellent RHP-1 based agreement with the FM flight and ground damping time constant test results.

The Dutch Space COS-B flight nutation data have been embedded in the HP, RHP-1 and NS model predictions. At the spin-rates 9.45 and 17.63 rpm excellent damping performance agreement was found with the developed HP and NS MathCad® coded models. The RHP-1

model shows an additional resonance off-set of 4% compared to the NS and HP modeling. In both cases the RHP-1 model and its time constant prediction is far off and does not apply to the COS-B design and its flight performance validation.

The COS-B ultimate damping angle tests with the PTM glass model did not reveal a second time constant due to end pot hysteresis phenomena. This is concluded after studying and re-analyzing the results of a high number of repetitive tests at 1.0 and 0.2" ultimate angles in air-bearing tests. An ultimate nutation angle analysis for the EQUATOR-S ND design has not been traced.

It can be concluded that the Fokker Space NS model is the backbone of ND design on basis of its superior V&V status.

4 Stabilizing the FY-2 Spacecraft

I hear and I forget. I see and I remember. I do and I understand.

Confucius

Chinese philosopher & reformer (551 BC - 479 BC)

4.1 Introduction

In this chapter the theory presented in Chapter-2 is applied to the ND design and qualification of the dual-spin stabilized Chinese meteorological *Feng-Yun-2* (FY-2) satellite. The FY-2 S/C, shown in Fig-4.1, was designed and manufactured in the Netherlands in the years 1990-1992 by prime contractor Dutch Space and UCN Aerospace as subcontractor. The customer was the Great Wall Industry China (GWIC) and the Beijing Institute of Control Engineering (BICE). The FY-2 satellite is part of a series still being used. It was employed to monitor the weather conditions during the 2008 Beijing Olympics. The development of the ND fulfills the requirement laid down in the FY-2 Project Technical Specification for a Passive-Liquid-Tube-with-End pots ND [FDS, 1992].

The Chinese FY2 ND customer GWIC (Great Wall Industry China) was the toughest in its kind but this made the FY2 ND project a very interesting one. The 20 years Fokker Space ND design and qualification heritage had to be re-qualified against even more severe requirements compared to the standards of the earlier ESA and NASA programs like COS-B and Ulysses. In fact this meant a knowledge injection which drove the Cluster ND innovation, described in Chapter 6.

The spin-axis of the FY-2 satellite is stabilized within the frame of severe requirements as will be proved by the analysis and test results to follow. First the spacecraft and its mission are summarized [FDS, 1992].

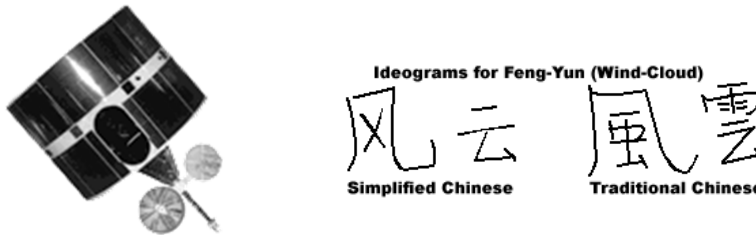


Fig-4.1 Chinese Feng-Yun-2 meteorological S/C (left) and ideogram (right) [FY-2, 2012].

4.2 Spacecraft and Mission Description

China began its geostationary meteorological satellite FY-2 program in 1980. The spacecraft are built by the Shanghai Institute of Satellite Engineering. They are very similar to the Japanese GMS and the GOES-3/7 spin-stabilized satellites, originally built by the Hughes Corporation in the USA. The FY-2 satellites are operated by the China Meteorological Administration (CMA) and the National Meteorological Satellite Center (NMSC). The FY-2 S/C attitude is 100 rpm dual-spin stabilized. The main payload is a Visible and Infrared Spin Scan Radiometer (VISSR) which obtains hourly full-disk images of the Earth, through step action of the scan mirror (comparable to the Meteosat-2 instrument) in three channels. The VIS channel observes and derives the reflectance of clouds and the Earth surface during daylight. The main scan radiometer properties are given in Table-4.1.

Table-4.1 FY2 S/C scan radiometer properties [FY-2, 2012].

Channel	Waveband	Nadir Resolution	Temporal Resolution
VIS	0.55 - 1.05 μm	1.25 x 1.25 km^2	1 hour
Water Vapor	6.2 - 7.6 μm	5 x 5 km^2	1 hour
IR	10.5 - 12.5 μm	5 x 5 km^2	1 hour

The FY-2 S/C series A to H serving the period 1994-2014 is described below:

- The first FY-2 satellite was destroyed on the ground when the rocket blew up during a fueling accident on 2 April 1994, killing 1 person and injuring at least 20.
- FY-2A satellite was successfully launched to 105° East longitude on 10 June 1997 on a CZ-3 booster from Xichang, and began regular service late in 1997. Due to a problem with the S-band antenna on the S/Ct on 8 April 1998, FY-2A ceased transmission of VIS images.
- FY-2B with three years design life time was launched on 25 June 2000. The S/C satellite reached its orbital slot at 105° E longitude over the equator in July. There was a six-month on-orbit checkout of the satellite before it went into full operation. Since November 2003, FY-2B was apparently suffering spin-stabilization problems similar to FY-2A.
- FY-2C was launched on 19 October 2004. The first VIS image was taken on 29 October 2004. It was put into operation in July 2005 at 105° E and moved to storage late in 2009.
- FY-2D was launched on 8 December 2006, and became operational in June 2007 at 86.5° E. It had to form a twin observation system together with the FY-2C. The two

satellites have their own observation tasks, but can replace each other if one of them malfunctions. Each satellite scans the Earth in 30 minutes. They start scanning 15 minutes apart to provide 4 full-earth scans per hour, to support weather forecasting during the 2008 Olympics in Beijing.

- FY-2E was launched on 23 December 2008, and kept in on-orbit storage until it replaces the FY-2C S/C late in 2009.
- FY-2F, FY-2G and FY-2H with 4 years design life are scheduled to be launched in 2010, 2012 and 2014. Each S/C is made operational in the following year.

The following sections deal with the design, qualification and acceptance of the FY-2 NDs.

4.3 FY-2 ND Design

4.3.1 Requirements

The FY-2 ND design requirements are given by Table-4.2 below. The Flight Model (FM) design was driven by the extreme damping requirements at 5 years End-Of-Life (EOL) mission. This made it a new and challenging project with a new customer and at that time a specific culture.

Table 4.2 FY-2 S/C AOCS parameters and requirements defining the ND design boundary conditions.

Item	Description	Nominal	Extreme
τ	Nutation damping time constant [s]	< 30	30
T	Operational temperature [$^{\circ}\text{C}$]	20	-25 to 50
I_{zz}	Inertia figure around Z-axis [kg.m^2]	265	$\pm 12\%$
λ_0	Final (phase C/D) nominal inertia ratio [-]	FM 1.166	1.141 – 1.191
	The QM value equals the phase-A FM value	QM 1.125	1.100 – 1.150
ω_z	S/C spin rate around Z-axis [rpm]	100	$\pm 10\%$
R_0	Distance in XY-COG plane to spin-axis [mm]	900	± 50
Z_0	ND position above COM plane [mm]	600	600-630
θ	Initial nutation angle	1" to 1 $^{\circ}$	1 to 10 $^{\circ}$
	Final nutation angle	< 0.5"	
m	Mass of one damper including brackets [kg]		1.5 + 2%
	Asymmetry in mass of a damper pair.	< 1.5	$\pm 2\%$
f_0	Lowest structural resonance frequency [Hz]	> 200	200
Radiation dose at 5 years EOL [cm $^{-2}$]	Protons (6.8 MeV)		7.0 x 10 11
	Electrons (1.0 MeV)		7.0 x 10 14
	^{60}Co 100% 1.22 MeV β - decay $\tau = 1.650$ (1.5 rad)		1.5 x 10 7

¹ The Cobalt isotope type radiation was not specified, therefore the isotope [HCP, 1980] Co_{27}^{61} with 100% β mono-energetic 1.22 MeV decay and half-live $\tau = 1.650$ hour was taken (accepted by the customer).

The most extreme requirement is the ultimate nutation damping angle $\theta < 0.5''$ at the high nominal 100 rpm spin-rate. Nevertheless, it will be proved in this chapter that the residual nutation angle even exceeds the minimum of 0.5" (=1/7200 degree). The evidence was obtained during the qualification program by analysis and experiments on end-pot liquid phenomena to be dealt in this chapter.

4.3.2 Functional Design

In Table-4.2 the driving requirements for the design of the two equatorial NDs are given. The key ND design parameter, the S/C inertia ratio, was updated once beyond the earlier specified contingency. The required redesign could be made by only enlarging the fluid radius from 3 to 3.8 mm and adapting the support bracket. This is seen in the fourth and

fifth row of Table-4.2 where the λ_0 value for the QM (Qualification Model) is the initial phase-A FM value. The QM was kept the same in phase-C/D and equals the phase-A FM.

The NS model was used to obtain the nominal damper design $\langle a, b, h, L \rangle$ which covers the requirements in best systems engineering sense, i.e.

1. Anticipation to specification changes in later project phases
2. Parameter sensitivity and tolerance-analysis
3. Manufacturability
4. Interface with the S/C
5. Structural design.

The FY2 NDs were offered to and accepted by the Chinese customer on basis of the COSB and Ulysses ND heritage. Meanwhile the design of the Ulysses NDs was re-investigated in the frame of the ESA study of the Ulysses AOCS nutation anomaly in November 1990. As a result the Ulysses ND design was re-validated on basis of the old design data. The re-calibration of the model with the old experimental data made clear that the in- and exit flow lengths contribute considerably to the effective length. A deeper search in the Fokker Space ND records [FDS, 1992] made clear that the effective length $L_{eff} = L + \alpha \cdot 2b$ was taken as a practical rule with $0.5 < \alpha < 1$ and compliant with Eqn. (2.109). This means that the physical tube length L is enlarged with a fraction of the endpot diameter to L_{eff} as input parameter in the model. The initial FY2 ND design on its turn was biased by the Ulysses ND design process and its lessons learned. Although the writer had some doubts on the effectiveness of this rule of thumb, in a high-tech industrial environment there is little time for additional experiments and thorough scientific research. The extended exploration in this chapter, however, will deliver insights for a refined methodology to estimate the effective length.

At the early design phase the pragmatic rule given by Eqn. (2.109) was applied nominally with $\alpha = 0.75$ yielding the initial parameters $\langle a, b, h, L_{eff} \rangle = \langle 3, 40, 40, 520 \rangle$. This comprises a physical tube length $L = 460$ mm and an effective damping model length $L_{eff} = 520$ mm.

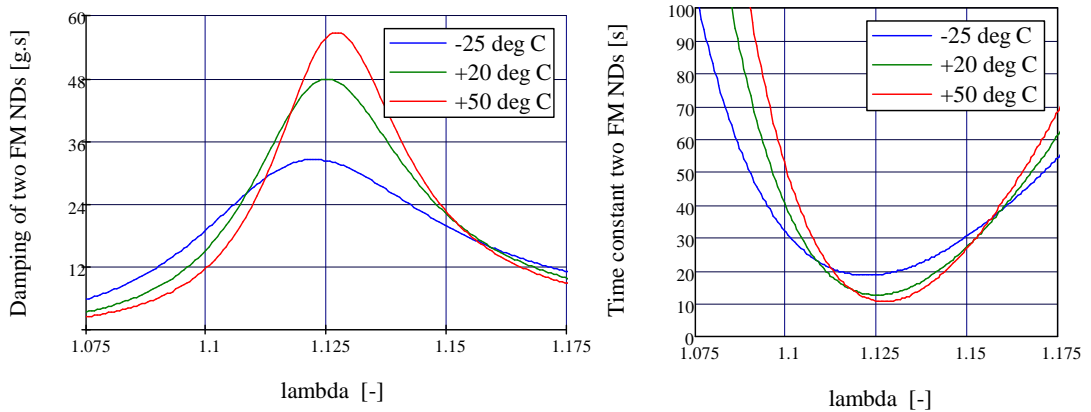


Fig-4.2 Damping performance of **two** FM FY-2 NDs (left) tuned at $\lambda = 1.125$ for the initial phase-A design. The right curve shows the time constant for a pair of NDs. The tuned model tube length equals $L_{eff} = 515$ mm as part of the ND geometry parameter set $\langle a, b, h, L_{eff} \rangle = \langle 3, 40, 40, 515 \rangle$ and temperature range $T = -25, 20$ and 50 °C. All other parameters are nominal.

Starting with the time constant and frequency tuning, Fig-4.2 shows the compliance with the phase-A S/C inertia ratio with $L_{eff} = 515$ mm close to the initial estimate 520 mm. The left picture shows the damping performance given by Eqn. (2.83) of two flight model NDs in the range $\lambda = 1.125 \pm 0.125$. The right picture shows the resulting time constant given by Eqn. (2.27). Additional analysis proved that the nominal time constant of two FM NDs was

11 s being well compliant with the < 30 s requirement. The same holds for the mass and I/F requirements.

In Fig-4.3 the stepwise implementation of the (initial) phase-A FM ND design is shown. The left picture illustrates the CAD model dimensions. The right picture shows the subsequent step towards the implementation of the COSB and Ulysses build standard. The rectangular endpoint cross-section has a size πb^2 equal to the value of the CAD model.

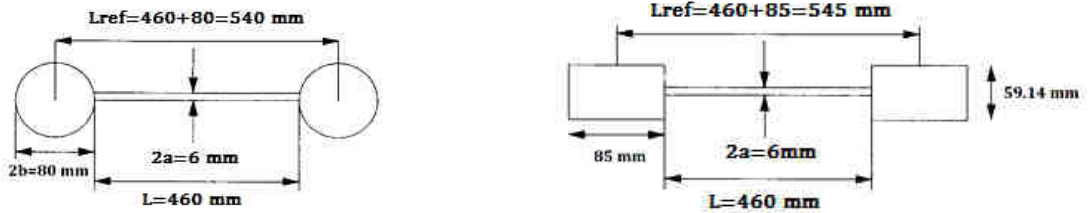


Fig-4.3 First step in the implementation of the *initial* FM ND design from CAD model to build standard with reference length L_{ref} for production purposes only. The left picture shows the model top view with circular endpoints. The right picture shows realistic endpoints with rectangular size but the same cross-sectional area. In this design the additional model damping length was initially taken as a half long side of the rectangular endpoint on both sides.

After the initial definition of the FM geometry and fluid type supported by modeling, the Performance Test Model (PTM) was defined by scaling and successively built and tested. Several calibration steps, however, were necessary to come up to a compliant design. The results of the first PTM experiment (to be studied in section 4.3) followed by model analysis showed that the design had to be re-tuned by a 55 mm tube length-growth. It became clear that $L_{eff} \cong L$ for the FY-2 ND design with drastical deviation from the conservative rule implied by the Ulysses ND heritage. The implementation is shown in Fig-4.4 to Fig-4.5. The latter shows the phase-A hardware design of the FM ND including a support bracket to push the lowest nodal frequency beyond the required > 200 Hz limit to 214 Hz.

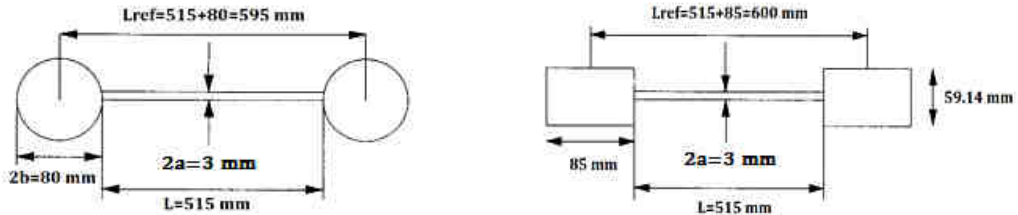


Fig-4.4 Second step in the implementation of the phase-A FM ND design from CAD model to build standard *after* the first PTM experiments based on the design in Fig-4.3. A liquid tube length-growth of 55 mm is implemented. The left picture shows the model top view with circular endpoints. The right picture shows the realistic endpoints with rectangular size but the same cross-section area.

The phase-A design was overruled a year later by the phase C/D design which was driven by a considerable change in the S/C inertia parameters given in Table-4.2. The final ND design is given by Table-4.3 and shown in Fig-4.6 to 4.7. The differences with the phase-A design are the enlarged tube radius from 3.0 to 3.8 mm and the refined support bracket design.

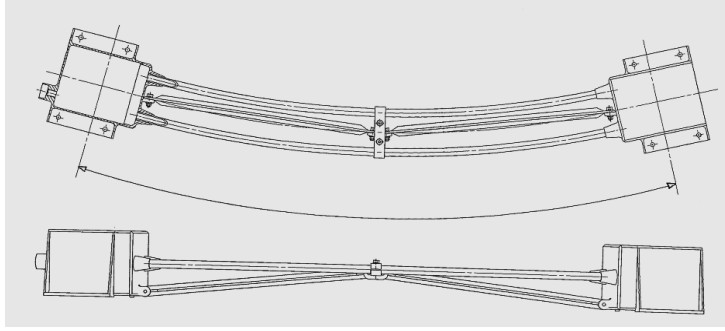


Fig-4.5 The **initial** phase-A FY2 FM curved ND design $\langle a, b, h, L_{eff} \rangle = \langle 3 \text{ mm}, 40 \text{ mm}, 40 \text{ mm}, 515 \text{ mm} \rangle$ after a liquid tube length-growth of 55 mm on basis of the 1st PTM calibration tests. The upper picture shows the equatorial X-Y view whilst the lower one shows the meridian X-Z side view.

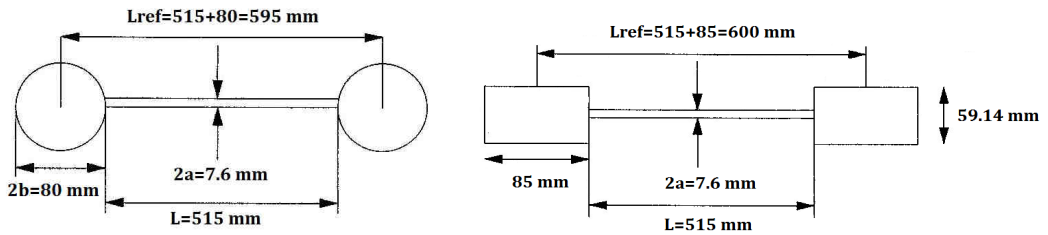


Fig-4.6 Stepwise implementation of the phase C/D final FM ND design from CAD model to build standard. The tube radius was enlarged from $a = 3.0 \text{ mm}$ (phase-A) to $a = 3.8 \text{ mm}$ (phase C/D).

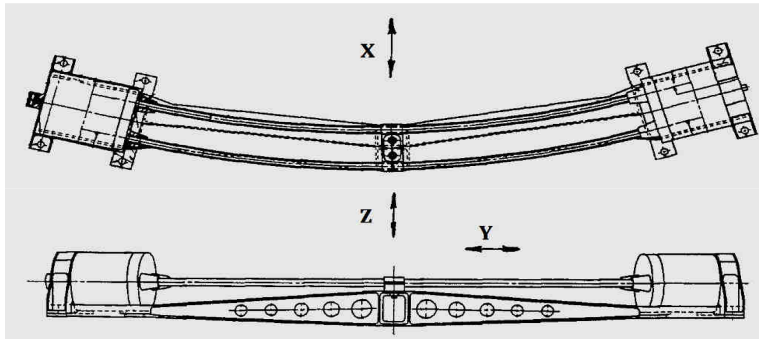


Fig-4.7 Final design with adapted support bracket, liquid tube radius $a = 3.8 \text{ mm}$ and $L_{ref} = 600 \text{ mm}$. The adapted support bracket provides the ND as a mechanical system with a higher natural frequency.

Table-4.3 The nominal FY-2 FM ND design parameters at 20 °C. The only FM geometrical change, marked bold, is the liquid tube radius. The the QM/DM model values are given within brackets.

Item	Description	Value
a	Liquid and vapor tube radius (fase-A value)	3.8 (3.0) mm
b	Endpot radius	40 mm
h	Inner endpot height with equilibrium fluid level at $h/2$	40 mm
L_{ref}	Distance between the endpot middles	600 mm
L_{eff}	Eeffective damping length	515 mm
Liquid	Fluoro-Carbon with commercial name Flutec	PP1
τ	Exponential damping time constant of two dampers	6.5 (11) s
P/a_0^2	Nominal damping rate of two FM dampers (CAD value)	94.0 (47.6) g·s

4.3.3 Structural Design

The strength- and stiffness analysis of the ND is covered by [FDS, 1992] as well as the reliability. The analysis of the latter is analogous to the one to be dealt for the Cluster ND in Chapter 6.

Space qualified Aluminum alloy is used as material for all parts of the dampers. The endpot interconnections are electron beam welded as part of the UCN-Aerospace subcontractor workmanship. The dampers are configured with suitable brackets for the specified attachment to the satellite platform. A rough calculation showed that the lowest eigen-frequency based on the original support bracket, would not meet the predicted value of 214 Hz of the phase-A design. Therefore the first support bracket design, shown in Fig-4.5, was adapted to increase the lowest nodal frequency again beyond the required > 200 Hz. The revised structural design including the support bracket is shown in Fig-4.7. The total mass of a single damper complies with the requirement within an asymmetry of mass between two dampers of 2%.

This section made clear that the final design had to be recursively defined by multiple modeling and testing with PTMs (Performance Test Models). This was new in the sense that prior customers accepted a resonance frequency offset < 2% at specification compliant damping performance, time constant and bandwidth over the required temperature range. For the FY-2 ND design two PTM calibration steps were necessary to tune the design within an offset < 0.5%. Before the essential design iteration can be dealt with in more detail the definition of the development models is essential. The procedure to analyze the air-bearing data will be dealt in the following sections. The process of design, qualification and acceptance will be first explored starting with the description of the verification, qualification and flight acceptance philosophy.

4.4 Verification, Qualification and Flight Acceptance

The FM ND design is made using engineering knowledge (heritage) and CAD simulations. The qualification philosophy is slightly differing depending on the requirements of the customer. For the FY-2 ND the following hardware models were used for qualification and flight acceptance:

- Performance Test Models 2 PTMs
- Dummy Test Models 2 DMs
- Qualification Models 1 QM
- Acceptance and Flight Models 2 x 2FMs (one pair as spare).

The PTMs shall validate and calibrate the FM ND design. Initially only one PTM was offered. The need for symmetrical loading of the air-bearing made it necessary to manufacture a second PTM because of its large size and weight. An advantage is the double air-bearing oscillation attenuation, reducing the required test times by 50%. The DMs are meant for basic inspection of materials and manufacturing processes and QM reference. They have the same mass as the QM and the four FMs. Extra performance checks are executed with the QM/DM and the two FM/FM combinations. The QM is identical to the FM but is meant to survive the most severe qualification test program to test model margins. The two FMs are subjected to a less severe test program. This will be defined in more detail further on. Despite the final redesign of the FM due to the phase C/D update in the flight inertia parameters, the original phase-A QM was maintained for the ND qualification. This was part of a cost effective qualification program but implied an extended acceptance philosophy since the QM performance checks in another λ domain deliver additional performance evidence.

4.4.1 Test Plans PTM-DM-QM-FM

The test plans contain the essential data and analysis to define the diverse tests with the FY-2 DM, QM and FM ND models. The validation, qualification and acceptance tests are followed by a design review. The PTM validation test by the preliminary design review (PDR), the qualification test by the qualification test review (QTR) and finally the acceptance test review (ATR). A successful milestone review means the go-ahead for the following phase. The calibration testplan refers to the PTM airbearing test. After the successful PDR and QTR, the final issue of the test plan deals with the update for the FM test plan only.

Tests sequences and environmental conditions

The general requirements of the qualification- and acceptance test conditions are given in Table-4.4 to 4.8. The environmental conditions during transport, storage and integration are controlled to be less severely than those specified by the test conditions. The generic pressure level control tolerances are not a real test driver but large variations may influence the airbearing cleanroom turbulence flows and the ND damping performance slightly.

Table-4.4 Test tolerances in the QM, DM and FM cleanroom tests.

T	Pressure (Pa)		Constant acceleration
±3 °C	$p \geq 130$ $0.13 < p < 130$ $p \leq 0.13$	±10% ±25% ±50%	±10%
Sine vibration amplitude		Random vibration PSD¹	
≤200 Hz	±10%	Overall RMS	±1.5 dB
>200 Hz	±15%	20-500 Hz	±3.0 dB
		500-2000 Hz	±1.5 dB
Frequency			
≤25 Hz	<0.5 Hz		
>25 Hz	±2%		

¹PSD = Power Spectral Density

Thermal tests

The damper is thermally isolated at a pressure $p < 10^{-5}$ Torr. Therefore it can only be heated up by radiative coupling with the Helium shroud at an absolute slope $|dT/dt| \approx 0.3$ °C/min. This is a relative slow process. Two thermo couples are attached to the ND, one on each endpot. Table-4.5 shows the applicable thermal-vacuum cycles of the QM and FM.

Table-4.5 Qualification (Q) and Acceptance (A) thermal-vacuum cycles at pressure $p < 10^{-5}$ Torr.

Test	# of cycles	Thermal cycle
Qualification (Q) FM	3	-35 °C during 12 hours +60 °C during 12 hours
Acceptance (A) QM	1	-25 °C during 12 hours +50 °C during 12 hours

Vibration tests on QM- and FM models

The sine and random vibration tests on the QM and FM models are given in Table-4.6 and 4.7. In Table-4.6 the amplitude below 23 Hz is discontinue as a required notch filter. The continue value would be 9.5 mm whilst the ability to pass the test was predicted in advance by the strength and stiffness analysis [FDS, 1992].

The test arrangement of the X, Y and Z excitation tests on the shaker table is shown in Fig-4.8. The test-items are mounted on the rigid test-adaptor with the accelerometers 1-6 mounted on key positions. Some measure the base input whilst others are placed on the endpoints with micro-accelerometers attached to the tubes. Their weights are included in the measurement and subsequent test analysis.

Table-4.6 Sine vibration tests for the QM and FM.

QM Modal search		FM Resonance search
5-250 Hz	0.3 g	None
Sweep rate along 3 axis	2 Oct/min ¹	None
Harmonic excitation [Hz]		
5-23	11 mm pp	None
23-70	20 g	None
70-250	10 g	None
Sweep rate along 3 axis	1 Oct/min	None

¹ One octave per minute (1 Oct/min) doubles the frequency every minute

Table-4.7 Random vibration tests for the QM and FM

QM		FM	
Random (Hz)	PSD	Random (Hz)	PSD
25-100	+6 dB/Oct	25-100	+6 dB/Oct
100-500	0.3 g ² /Hz	100-500	0.133 g ² /Hz ¹
500-2000	- 6 dB/Oct	500-2000	- 6 dB/Oct
Overall 15.5 g RMS		Overall 10.3 g RMS	
2 mins per axis		2 mins per axis ¹	
Qualification level	0 dB	Acceptance level	-3.5 dB

¹ Relative amplitude factor 1.5² was agreed on the Design Review to be the difference between qualification and acceptance level on basis of standard of ESA and NASA procedures.

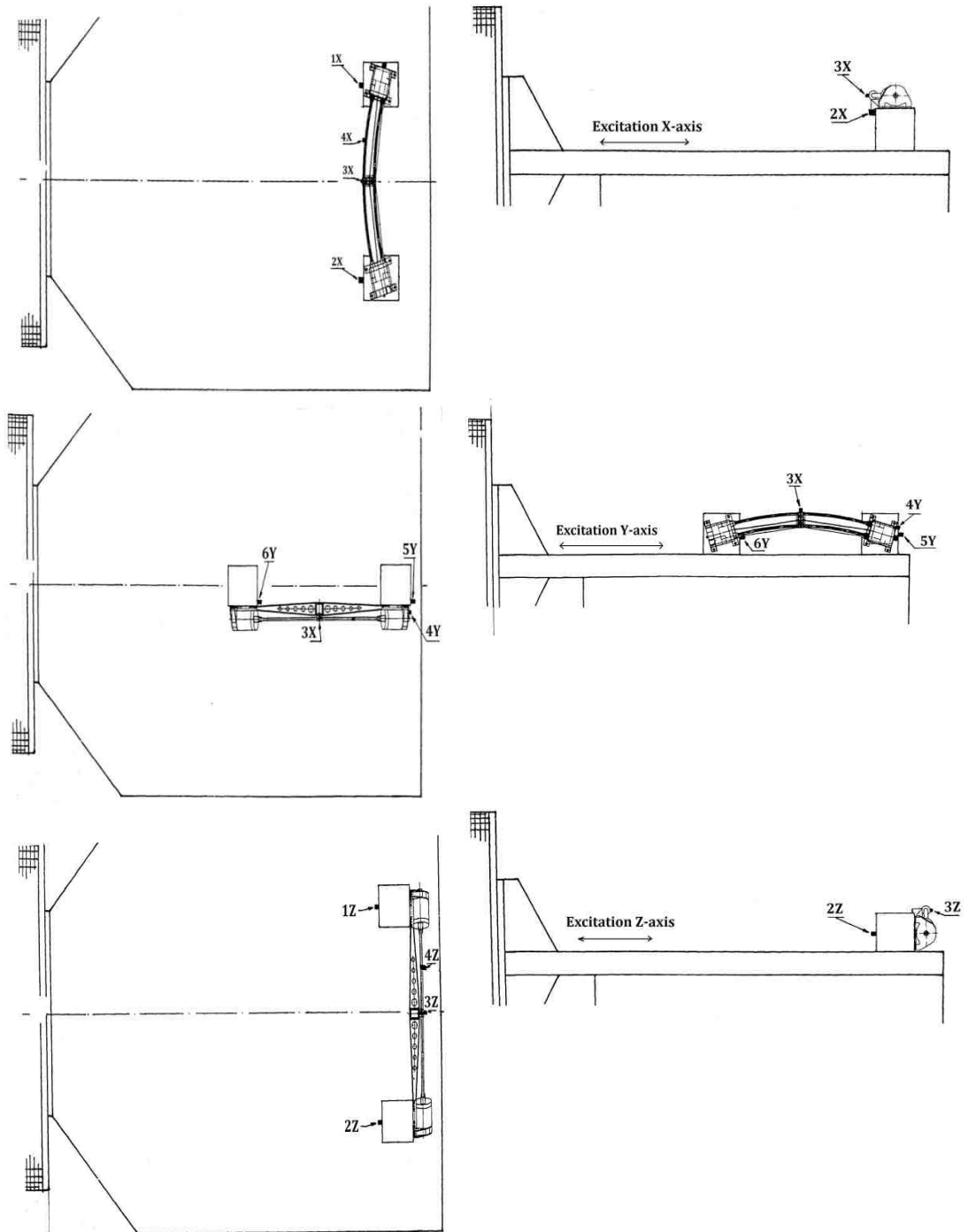


Fig-4.8 Test arrangement of the X (upper row), Y (middle row) and Z (lowest row) excitation tests on the shaker table at Dutch Space, the Netherlands. The FY2 ND and its rigid test adapter are attached. The numbers "iZ" refer to the location of the six accelerometers attached to the ND.

Table-4.8 *Test items and sequence*

		PTM(2)	DM(2)	QM(1)	FM(4)
1	Visual and mechanical status inspection	X	X	X	X
2	Dimensional and weight measurement	X	X	X	X
3	Leakage test	X	X	X	X
4	Airbearing performance checks	X 7-9 frequencies PTM/PTM combi	-	X 3 frequencies QM/DM combi	X 3 frequencies FM/FM combi
5	Sine low level sweep to identify resonance frequencies followed by sine vibrations	-	-	X / Q	-
6	Random vibrations	-	-	X / Q	X / A
7	Thermal cycling in (near) vacuum	-	-	X / Q	X / A
8	Airbearing performance check	-	-	X 1 frequency of item 4	X same
9	Leakage test	X ¹	-	X ²	X ²
10	Dimensional and weight measurement.	X	-	X	X
11	Visual and mechanical inspection.	X	-	X	X

Q Qualification levels specified in Table-4.5 to 4.7

A Acceptance levels specified in Table-4.5 to 4.7

¹ Leakage test by weighting the PTMs before and after test.

² Leakage test requirement of 10^{-9} Torr-liter/s vapor at $< 10^{-6}$ Torr-liter/s ambient pressure.

4.5 PTM Design and Test Matrix

The PTM and its redesigns are the backbone of the recursive design process towards the qualification and acceptance of the FM ND. The consequences of the lessons learnt in this Chapter meant an innovation in the TLD design process. This will be initiated in the following section by the analysis of two recursive series of PTM tests and completed in the following Chapters 5, 6 and 7.

PTM Definition

Using the scaling relations Eqn. (2.100) up to (2.102) the dimensions of the PTM are found. The ND I/F at the R = 900 mm curved iso-centrifugal force line (coaxial with the heart of the liquid tube) is mapped to a straight iso-gravitational force line for the PTM. The model prediction of the PTM dissipation versus the air-bearing oscillation periods enables the validation of the FM ND space performance. First the rationale of the PTM dimensions, given in Fig-4.9, is explained. After this, the key air-bearing test parameters oscillation time, dissipation scaling and angular test range are derived.

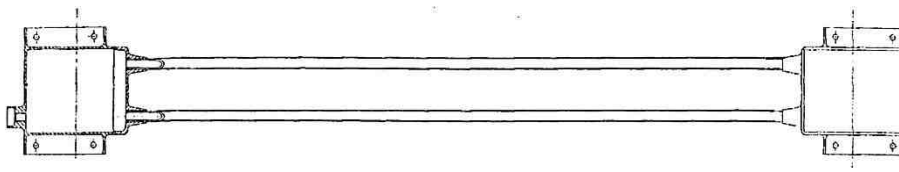


Fig-4.9 First FY2 PTM with $\langle a, b, h, L \rangle = \langle 6.5, 86.7, 86.7, 996.8 \rangle$ mm and $L_{ref} = 1181$ mm.

The same damping fluid for the flight (FM) and test (DM, QM, PTM) models was chosen which means that the density, dynamic viscosity and kinematic viscosity are all the same thus $\rho_r = \mu_r = \nu_r = 1$ in the scaling equations. The scaling theory defines the dimensional scaling factor $L_r = 2.159$ by applying Eqns. (2.101) and (2.102). The physical FM model, however, was scaled up by 2.167 due to aeronautical standard size restrictions. The value 2.167 ($=6.5/3$) was chosen since the closest available PTM liquid tube radius is 6.5 mm. This has no significant influence on the tests but induces a correctable shift of only +0.2 % in the λ direction of the damping curve.

Air-bearing Oscillation Period

The phase-A S/C nutation angle frequency at $\lambda_0 = 1.125$ is $\Omega_0 = (\lambda_0 - 1)\omega_Z = 1.309$ [rad/s]. Subsequently the time scaling Eqn. (2.103) dictates the nominal airbearing angle-frequency $\Omega_0/T_r = 0.281$ [rad/s]. The PTM airbearing nominal oscillation time constant $T_0 = 22.4$ s. The same approach applies for other inertia values in the specified range.

Dissipation Scaling

The dissipation rate scaling M is given by Eqn. (2.105) with $M = \rho_r L_r^3 T_r = L_r^5 = 46.887$ for the PTM. The PTM dissipation performance curve is obtained by scaling the FM curve with M . The test matrix in Table-4.9 comprises the performance checks to be verified on the air-bearing. This table contains the predictions based on NS model simulations. Five test frequencies were selected to obtain a proper comparison between NS model prediction and experiment.

Air-bearing Amplitude and Test Range

The nutation amplitude scaling Eqn. (2.104) defines the angular test range on the air-bearing whilst the λ extremes define the test range in Table-4.9. The PTM air-bearing angle range $90^\circ - 19''$ simulates the FM nutation range 1.2° down to $0.5''$. The range $1.2-10^\circ$ is qualified by similarity with former ND projects.

Table-4.9 Test matrix of the 1st PTM design with phase-A inertia ratio values $\lambda_0 = 1.125$ and $\theta_{nut} = 0.5''$ to 1.0° . The total inertia $I_{total} = I_0 + I_{dampers} = 199.1$ kg·m² at the test arm length $R = 2$ m. The predicted damping values are valid for two NDs.

λ [-]	Ω_{test} [rad/s]	T_{test} [s]	τ_{test} [s]	P/a_0^2 [kg·s]	Φ_{test}
1.1000	0.225	27.9	1525	0.704	40" to 79 ⁰
1.1125	0.253	24.8	556	1.520	29" to 64 ⁰
1.1250 = λ_0	0.281 = Ω_0	22.4 = T_0	300	2.289	27" to 53 ⁰
1.1375	0.309	20.3	328	1.735	22" to 45 ⁰
1.1500	0.337	18.7	444	1.079	20" to 38 ⁰

4.6 PTM Experiments

In the performance calibration test plan [FDS, 1992] two cycles of PTM experiments and the test set-up were defined by combining model predictions and practical constraints. In this section the ND design verifications by the PTM test results are analyzed.

Figure 4.10 shows the PTM test results of the second test cycle at seven different frequencies which are indicated by the airbearing period times $T_a = 18.7, 20.3, 24.8, 22.0, 22.8, 22.4$ and 27.9 s. The tests at $T_a = 22.0$ and 22.8 s were added to the guidelines of the test matrix given in Table-4.9. Some experiments were repeated (1st, 2nd) while others were corrected with dummy model results at other close-by T_a period times. The parameter at the horizontal axis is the product of airbearing arm length R_a times the deflection angle Φ .

Overall damping performance

Fig-4.10 shows the PTM test results in the air-bearing range $0-90^\circ$. The following arguments apply:

1. Linear small angle damper performance since P/a_0^2 gets constant going to the left side of a curve.
2. In the right part of the curves the liquid behavior is turbulent with less damping performance. Regarding Eqn. (2.26) up to (2.27) for the flight time constant and Eqn. (3.3) for the air-bearing both equations remain valid even when $\tau = \tau(\Omega)$ is no longer a constant at the large nutation angles. So when the experimentally determined damping performance is found, the time dependent time "constant" can still be calculated up to about 1.2° . For $\theta_{nut} > 1.2^\circ$ the damping behavior is covered by similarity with other projects. In terms of physics it is clear that there is always damping for any angular range. The time needed from a particular start nutation angle down to a specific angle can be evaluated on basis of analytical/numerical integration of the time varying damping including the turbulent behavior.
3. Air turbulent flows around the air-bearing equipment at angles smaller than about $540''$ disturb the linear damping value significantly. The disturbances are caused by the oscillating movement of the air-bearing itself thus inevitable in an air filled test room. The maximum deviation from the P/a_0^2 mean value is about 23%. The uncontrollable flows around the PTM test equipment cause a quasi-random distribution superposed on the damping performance at very small damping angles. It is therefore reasonable to apply a polynomial regression through the data points. This approach equalizes the air-bearing angle read-out by filtering out the influence of airflows at the residual angles in Figs-4.10.
4. The $740''$ air-bearing angle corresponds to a $10''$ flight angle behavior. This equals 20 times the $0.5''$ limit of flight nutation which is reached for $36''$ air-bearing angle. The air-bearing resolution $2.75''$ provides a test beyond that limit in the absence of air disturbances.
5. The MOI with dummy weights was $199.1 \text{ kg}\cdot\text{m}^2$ whilst with the PTMs a value of $190-200 \text{ kg}\cdot\text{m}^2$ was found by analyzing the variations in the oscillation time period. The variation depends on the air-bearing angle and absolute oscillation frequency. This difference in (momentary) MOI can be explained by regarding the liquid mass in the liquid tube as "free" and by fluid tilt motions in radial direction.

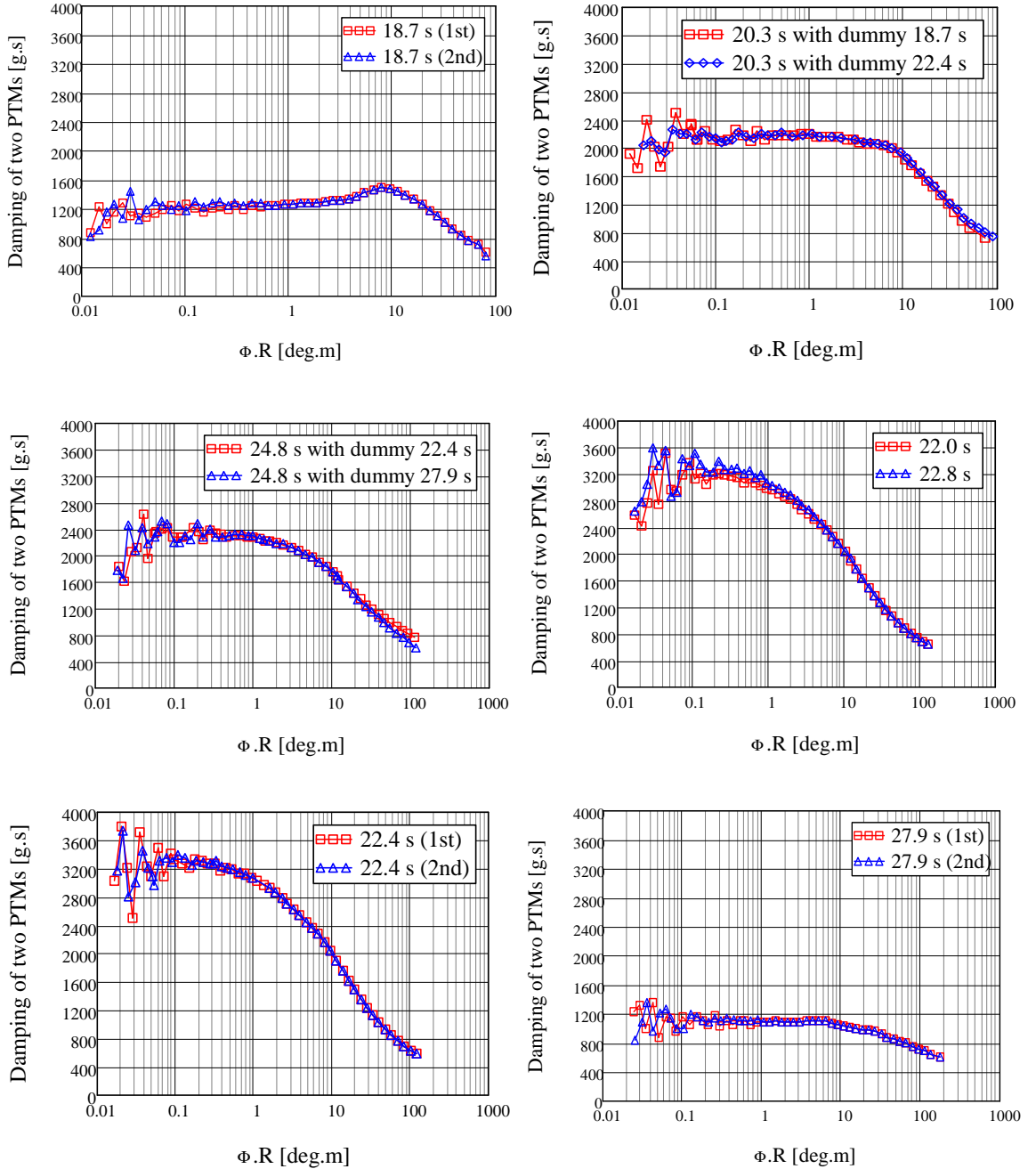


Fig-4.10 The second cycle of PTM experiments at seven airbearing period times $T_a = 18.7, 20.3, 24.8, 22.0, 22.8, 22.4$ and 27.9 s. Some experiments were repeated (1st, 2nd) while others were corrected with dummy model results at other close-by period times. The parameter at the horizontal axis comprises the product of airbearing arm length (R_a) times the deflection angle (Φ).

Tuned performance

The definition of laminar behavior at small angles can be specified by sampling the curves in Fig-4.10 at fixed air-bearing angles. The sampling at 36" with $Re = 65$, shown in Fig-4.11, complies with the ultimate required 0.5" flight nutation angle and coincides with the 0.02 vertical grid lines across the damping curves in Fig-4.10. The LSS results, given in Fig-4.11, show that linear damping is obtained below about 900" where $Re = 1615$ whilst the ND tuning already appears below about 6.25° .

Beyond the 0.5" flight nutation angle limit

The large Bond number $Bo = 400$ at 0.5" on basis of Eqn. (2.89) is the first indicator for the absence of a sticking effect at small angles proving that linear damping is assured in the desired angular nutation range in space. The ultimate conviction is given by the following arguments.

The magnification in the 0-300" angular range of the $T = 20.3$ s curve from Fig-4.10 yields Fig-4.12. The curve proves the linear test damping performance beyond 36" which is the equivalent of the 0.5" flight nutation angle. The $T = 18.7$ s measurement series also passes this ultimate angle. The influence of contact angle hysteresis down to about 20" air-bearing angles is not noticeable. The linear damping performance is preserved at 2.75" resolution and a net (dummy) time constant in the order of 10,000 s. During the tests it became clear that some test series with periods close to the nominal $T_0 = 22.4$ s got too noisy and had to be aborted at about 50".

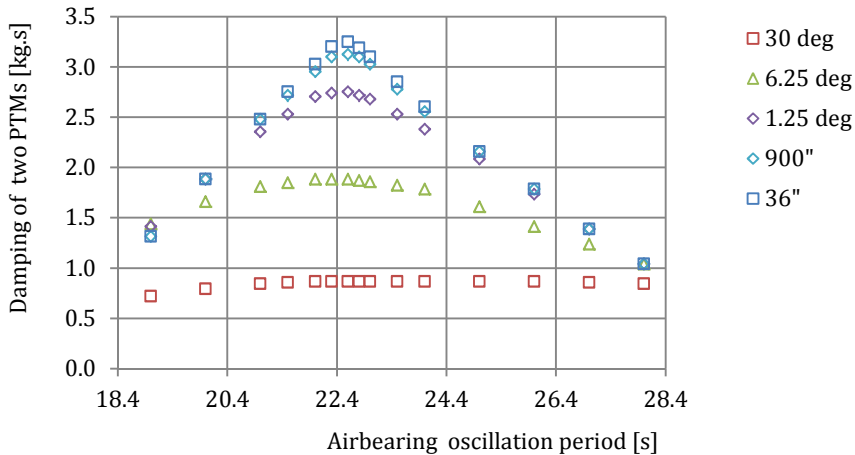


Fig-4.11 PTM performance as a function of the pendulum time sampled at specific oscillation angles.

In Fig-4.11 the resonance period time does not show a shift with the air-bearing oscillation angle down to 36" and this is even valid down to 20" including Fig-4.12. This proves the absence of a second characteristic frequency due sticking of PP1 fluid to the end-pot walls at small angles. The absence of this phenomenon was pragmatically proved by COS-B contact-angle measurements and the subsequent application of fluid dynamics theory in Chapter 2.

The adapted Eqn. (2.87) from [Hong, 1987] applicable to Hagen-Poiseuille (HP) flows and the angular scaling Eqn. (2.104) yield the ultimate reachable air-bearing angle 34". The 36" (0.5" flight) FY2 specification value was probably driven by this (Chinese) source. The HP parabolic velocity profile, however, does not apply in the FY2 ND operational spin range where the NS solution applies.

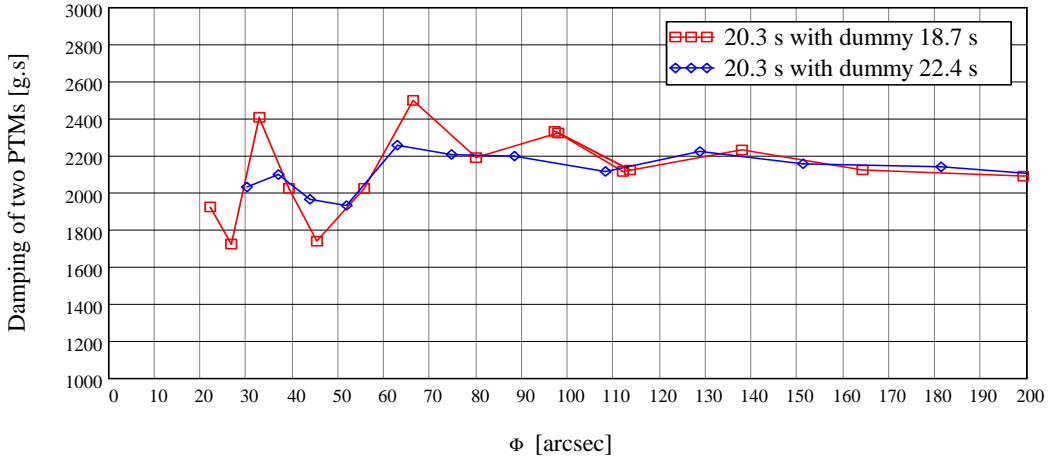


Fig-4.12 The ultimate PTM damping performance beyond the 0.5'' flight nutation angle limit.

The following analysis was not made in the past. Regard the air flow induced by mainly the ND end-pot drag area hb and take the velocity V of this enforced flow equal to the tip velocity of the air-bearing arm $V = \Omega_{test} R_a$ as a first order estimate. This case offers some grip on the calibration of the air flow dissipation as will be made clear. The air-bearing angle amplitude $\Phi(t) = \Phi_0 \sin \Omega t$ yields the liquid acceleration amplitude $a_0 = R_a \Phi_0 \Omega^2$ with instantaneous angle denoted by $\Phi_i = \Phi(t_i)$. The instantaneous damping variation at $R_a \Phi_i$ is derived from Fig-4.10 at the small angle side by

$$\Delta \left(\frac{P}{a_0^2} \right)_i = \left(\frac{P}{a_0^2} \right)_i - \overline{\left(\frac{P}{a_0^2} \right)} = \left(\frac{P}{a_0^2} \right)_i - \frac{1}{N+1} \sum_{i=0}^N \left(\frac{P}{a_0^2} \right)_i. \quad (4.1)$$

The linear or RSS averaged dissipation fluctuation exerted on the four end-pots can be estimated by

$$\frac{1}{N+1} \sum_{i=0}^N \left(\frac{\Delta P}{a_0^2} \right)_i \sim \frac{2bhC_D \frac{1}{2} \rho V^2 V}{a_0^2} \sim \Omega^3 \quad \text{and/or} \quad \sqrt{\frac{1}{N+1} \sum_{i=0}^N \left(\frac{\Delta P}{a_0^2} \right)_i^2} \sim \Omega^3 \quad (4.2)$$

The drag coefficient C_D in Eqn. (4.2) can be minimized by the following measures:

1. Adding an aerodynamic ellipsoidal cone assembly around each PTM (QM, DM, FM)
2. De-pressurizing the test environment
3. Reducing the effective drag area of the air-bearing support assembly.

The implementation of these recommendations will decrease the damping fluctuations and extend the low angular test range. This enables an investigation of the ultimate ND performance related to the meniscus hysteresis as dealt in section 2.10.

The test damping fluctuation defined by Eqn. (4.1) and Eqn. (4.2) was used to calibrate the test results by Ω^3 and yields Fig-4.13. The test range is characterized by the transition to turbulent airflow behavior. This is validated by the Reynold number Re using Eqn. (2.33) at kinematic air viscosity $\nu_{air} = 1.53 \times 10^{-5} \text{ [m}^2/\text{s]}$, test room temperature $T = 23^\circ \text{ C}$, test arm length $R_a = 2 \text{ m}$, $T_{test} = 22.4 \text{ s}$ and effective end PTM endpot size (see Fig-4.9 with $h = b = 86.7 \text{ mm}$) yielding

$$Re = \frac{VL}{\nu} = \frac{\Omega_{test} R_a \sqrt{h^2 + (2b)^2}}{\nu_{air}} \sim 5000 \text{ to } 6000. \quad (4.3)$$

The calibration offers evidence that the air-bearing performance is limited by turbulent airflows solely.

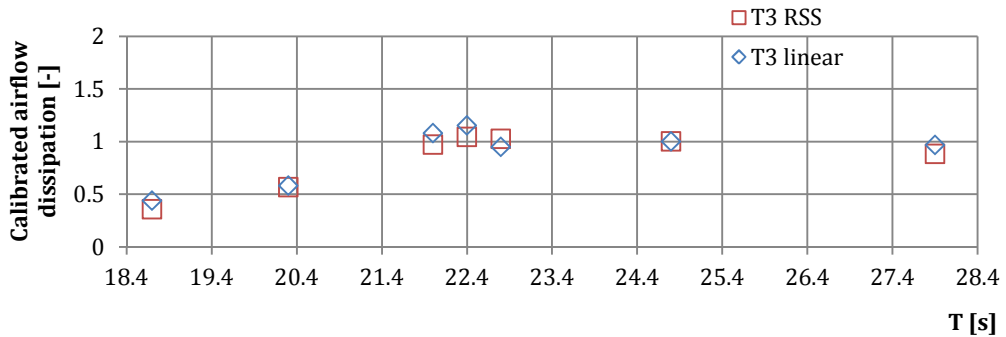


Fig-4.13 First order calibration of Linear (T3 linear) and RSS (T3 RSS) averaged $\Delta(P/a_0^2)$ air-bearing air flow dissipation at small angles in the range $0 - 500$ arcs. T3 refers to a triple point average.

The customer (in 1992) did not see this analysis (in 2012) but asked for an air-bearing independent proof to support the conclusion that end-pot hysteresis phenomena would not disturb the tuned performance down to the $0.5''$ ultimate nutation angle. Therefore the membrane action of the end-pot liquid meniscus in case of contact angle hysteresis was considered as described in Chapter 2. It was concluded that the hysteresis effect is small if the angle θ_e and consequently θ_r and θ_a are close to 90° . This was verified by a dedicated experiment with PP1 and H_2O (for cross-reference checks) droplets on an Aluminum plate as described in Chapter 2.

Earlier a visual assessment (shown to the customer) was made to study manually imposed to-and-fro movements in the endpot levels of the transparent (H_2O filled) COS-B glass PTM. This revealed (Fig-2.20) $\theta_e \approx 10^\circ$ whilst the advancing versus receding contact angle difference $\Delta\theta = \text{abs}(\theta_r - \theta_a) \approx 2^\circ$. In addition FY-2 ND modeling yields Table-4.10 and by taking the numbers of the last row and applying Eqn. (2.89), the inflight number $Bo = 400$ results. This proves that end-pot “sticking” can be neglected using the Fluoro-Carbon liquid PP1 since its surface tension is about 30 times smaller compared to the H_2O value. However, the pragmatic approach and COS-B PTM experimental proof given by Fig-3.16 as well as the absence of the phenomenon in a series of ND projects did not convince the customer. They kept worrying about the validation of the ultimate damping requirement at $0.5''$. Therefore the impact of the selected end-pot material was discussed, i.e.

1. The choice of specific Al materials
2. The surface RMS roughness amplitude (RA)
3. Influence of material (finishing) treatment
4. Scale of surface inhomogeneity.

Table-4.10 End-pot liquid level variations and Reynold numbers in the residual FM ND damping range.

Nutation angle θ	Reynolds number Re	Endpot level Δh
1.0°	39354	24.024 mm
$0.5''$	6	4 μm

Eqn. (2.94) shows (as for PP1) that a large contact angle θ_e and small surface tension γ_0 minimizes in best possible sense the contact angle hysteresis. The impact of surface roughness and surface inhomogeneity is described by Eqn. (2.90) and Eqn. (2.91). These issues, however, do not offer an explanation for a possible contact angle hysteresis. The

ultimate proof was an independent measurement of the real contact angle performed by the subcontractor UCN Aerospace. Therefore an Aluminum sample type AIR 9050 <AlMg5> was taken from the batch of the FY-2 NDs and equally surface treated. According to the material treatment prescriptions, the sample was treated with Alodine 1200 during 2 minutes at 20° C and rinsed with water. The contact-angle of a droplet was photographed laying on the flat sample surface. Both a PP1 and a water droplet (for reference) were imaged. The pictures were taken with use of a stereo-microscope and a CCD camera and hereafter studied with an optical light microscope to measure the contact angles. The microscopic RMS value of the Roughness Amplitude (RA) was < 0.8 μm and the realistic ND macroscopic value ≈ 3.2μm. The microscopic contact angle is the true contact angle between solid and liquid whilst the macroscopic contact angle measured in experiments is the ‘phenomenological’ contact angle. The latter determines the meniscus profile. The results of the test are given in Table-4.11. The measured PP1 contact angle of 8.5° is close to the initially assessed 10° value for the COSB glass PTM (though H₂O filled and not PP1).

Table-4.11 Contact angle measurements of droplets of water H₂O and PP1 on an Aluminum plate.

	Measured contact angle [deg] $90 - \theta_e$	Measured droplet height h	Sticking height h by theory and measured at θ_e	Capillary end-pot height H_c by theory and measured at θ_e	Surface tension at 20° C [N/m] γ_0	Density at 20° C [kg/m ³] ρ	Kinematic viscosity *10 ⁻⁶ [m ² /s] ν
Hg	150 ¹	NA ²	3.7 mm	26.6 μm	0.487	13610	1.142
H ₂ O	45.0±0.5	1.2±0.2 mm	2.1±0.1 mm	263±2 μm	0.375	998.2	1.004
PP1	8.5±0.5	190±20 μm	130±10 μm	5.2±0.3 μm	0.012	1682	0.420

¹Hg was added to the table for comparison. The literature values given by e.g. [HCP, 1980] are almost independent of the surface medium since Hg is strongly cohesive. ²NA= Not Applicable

The instantaneous θ response in the end pot wall sticking height $h = h(\theta)$ obtained by the θ differentiation of Eqn. (2.92) yields

$$\Delta\theta = \frac{2\Delta h}{h} \frac{\sin\theta - 1}{\cos\theta} \quad (4.4)$$

and by applying the ultimate $\Delta h = 4 \mu\text{m}$ (from Table-4.10) and $\theta_e = 8.5^\circ$ (from Table-4.11), a $\Delta\theta = 2^\circ$ contact angle variation results. This variation happens to comply with the visually estimated (COS-B, H₂O) meniscus hysteresis $\Delta\theta = \theta_a - \theta_r \approx 2^\circ$ being only a soft indicator of end-pot limited FY-2 ND performance.

4.7 Recursive PTM Tuning

PTM small-angle test results

The first PTM (length scale factor 2.167) test results are given by the square markers in Fig-4.14. These are small angle test results as given in Fig-4.10 acquired by Least Sum Square (LSS) regression. The test results in Fig-4.14 (left) show an unacceptable -5% offset from the required nominal air-bearing oscillation period $T_a = 22.4 \text{ s}$ which is compliant to the phase-A inertia ratio $\lambda_0 = 1.125$. After reduction of the model length $L_{eff} = 520 \text{ mm}$ to the real physical tube length in the range $L = 460 \text{ to } 470 \text{ mm}$, the measurement results do agree with the modeled ones. This showed that Eqn. (2.109) applies with a much smaller value of α as indicated by the wet thumb rule from the earlier COS-B and Ulysses ND designs.

The effect of the length reduction is made clear going from the left to the right picture in Fig-4.14 where the cleanroom room temperature range $T = 20 \text{ to } 22.5^\circ\text{C}$ and the tilt factor

given by Eqn. (2.108) are included. Due to the reduction of the tube length and the amount of liquid mass, the modeled damping performance reduces about 10%. The renewed design is tuned to the experimental values.

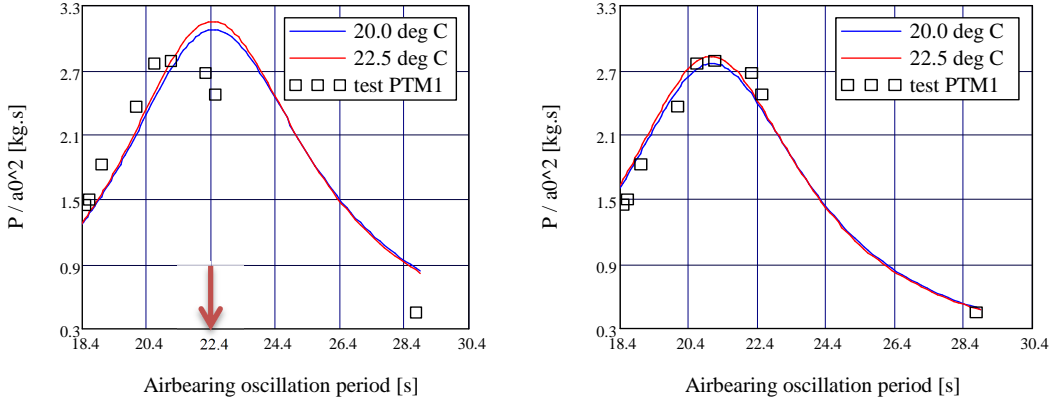


Fig-4.14 First PTM calibration experiment and model results with FM model length $L_{eff} = 520$ mm (left curve) and $n=2$ tilt correction compliant with Eqn. (2.108). The test results show an unacceptable -5% offset from the required nominal air-bearing oscillation period $T_a = 22.4$ s (indicated by the red arrow). The right curve shows the retuned physical model length $L_{eff} = L = 460$ mm.

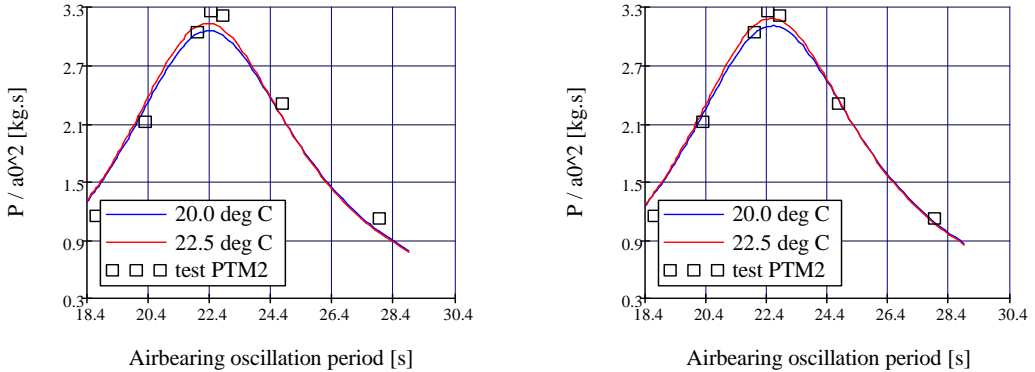


Fig-4.15 The second PTM calibration experiment [square markers] and sensitivity analysis of the final design. The left fit is at $L_{eff} = L = 515$ mm FM length and the right one at $L_{eff} = 525$ mm, both with tilt $n=2$ correction compliant with Eqn. (2.108).

The consequence of this design re-analysis is the necessity of a length-growth to re-tune to $T_a = 22.4$ s. It appears that the rule of thumb from the Ulysses ND design heritage, given by Eqn. (2.109) with $\alpha=0.75$, is not applicable. The reason may be the huge difference in the liquid tube radius being 3 mm of the FY2 FM ND and 8 mm of the Ulysses FM ND since Eqn. (2.46) implies that the liquid tube in- and exit flow lengths are a factor 2.5 larger at the same Reynolds number.

The retuned design was made taking these PTM lessons learned into account by consequently defining the length $L_{eff} = L$ in the model. This yielded the optimized length 515 mm well-tuned within 1% from $T_a=22.4$ s. Fig-4.15 shows the sensitivity analysis for this final design and its validation by the second PTM calibration experiment in the range $L = 515$ -525 mm. Fig-4.11 complies to Fig-4.15 but the test markers in Fig-4.15 signify the LSS average at the ultimate test angles whilst Fig-4.11 comprises the results from single

cross-sections at particular test angles. Fig-4.11 indicates a 1% mistune in frequency which is hardly recognized in Fig-4.15 and therefore it was decided to take the design effective length as the physical length with $L_{eff} = L = 515$ mm. The successive implementation steps up to the FM hardware status were already shown in Fig-4.3 and Fig-4.4. This meant the implementation of a 55 mm (from $L_{ref} = 545$ to 600) length-growth in the DM/QM/FM design and consequently a growth of 119 mm ($= 2.167 \times 55$) for the PTM reference length to 1295 mm. This redesign provided the go-ahead and design release at the PDR for the qualification and acceptance phase.

The recursive calibration approach was extended with an extra parameter n (described in section 2.12 by Eqn. (2.108) to deal with the fits on basis of a variable length and tilt to implement these lessons learned. This approach was applied in the Cluster ND program [van Bakel, 1993] as well. In this methodology the PTM calibration experiments are repeated and the design fine-tuned up to the level required by the specific program requirements. This means that α and n are defined accurately enough only after convergent iteration.

4.8 Final FM ND Design

Once the second PTM calibration was successful the last (secondary) FM design was frozen. The following items cover the main requirements in the design change from phase-A to phase C/D. The final FM ND design model results based on the C/D phase inertia ratio $\lambda_0 = 1.166$ are shown in Fig-4.16 and Fig-4.17.

Tuning

The 32.3% change in the S/C nominal inertia ratio could be met according Eqn. (2.110) with a change of only the liquid tube inner radius from 3.0 mm to 3.8 mm. A tuned design within 0.5% results with 50% improvement in damping performance. The nominal design damping time constant reduces to about 6.5 s and even for the most extreme case its value of 12 s stays below the required 30 s as illustrated in Fig-4.17.

Mass

The mass increase of less than 40 g indicated an estimated mass < 1.48 kg which still fulfills the requirement of less than 1.5 kg per damper (excluding bolts and nuts at the end-pot interfaces).

Structural

Neither the tube length nor the mechanical I/F had to be changed. A first order calculation, however, showed that the lowest eigen-frequency would decrease below the predicted value of 214 Hz of the early phase-A QM/DM design with $a = 3.0$ mm. This necessitated the upgrade of the support bracket shown in Figs-4.5 and 4.7. The report dealing with the structural analysis is given as part of [FDS, 1992].

4.9 Qualification and Acceptance Tests

The two requested additional QM/DM ($\lambda_0 = 1.125$) and FM/FM ($\lambda_0 = 1.166$) ND pair performance checks on the 1-g air-bearing are driven by the scaling essentials given in Chapter 2.11. The damping liquid PP1 applies for all models so $\rho_r = \mu_r = \nu_r = 1$ whilst the length scale factor $L_r = 1$ for the QM/DM/FM model.

The following sequence defines the FM test matrix given in Table-4.10:

1. Inertia scaling by Eqn. (2.101) with $n = L_r^3 = 1$ yields the fictional spacecraft spin-rate $\omega_z = 3.30193$ rad/s.

2. Time scaling by Eqn. (2.103) once more yields $T_r = 1$ which dictates the air-bearing frequency to be equal to the fictional S/C nutation angle frequency.
3. For the FM ND this means $\Omega_{airbearing} = \Omega_{fictional} = (\lambda_0 - 1)\omega_Z = 0.54812 \text{ rad/s}$ so $T_0 = 11.46 \text{ s}$.
4. For the QM and DM ND with $\lambda_0 = 1.125$ this means $T_0 = 15.22 \text{ s}$.
5. Three test-frequencies were selected to enable a proper comparison between model and experiment.
6. Angle amplitude scaling Eqn. (2.104) applies.
7. Dissipation scaling Eqn. (2.105) dictates $M = \rho_r L_r^3 T_r = 1$.

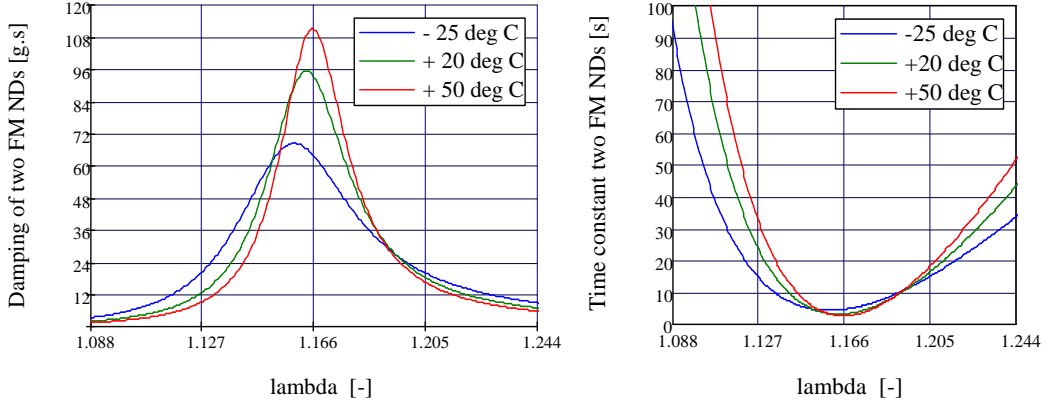


Fig-4.16 The final FM design. Damping of a single FM FY-2 ND tuned at the phase-C/D nominal inertia $\lambda_0 = 1.166$. The new liquid tube radius $a = 3.8 \text{ mm}$ applies with all other parameters nominal.

The final predictions for the damping time constant will differ from Table-4.12 because:

- The final weight of a QM or FM is determined afterwards
- The position of the frequency adjustment weights influences the inertia value.

Furthermore there are practical reasons for limiting the air-bearing oscillation range. The maximum measuring interval $4\tau_{\max} < 1 \text{ hour}$ was chosen for the following practical reasons:

- The FM test of the ultimate laminar behavior is sufficient by four decades. A range of many decades into the turbulent region was already tested during the PTM performance experiments.
- The air-bearing experiments have to be performed over a limited angular range due to the curved damper geometry. The vapor tube shall not be filled with liquid since it cannot return in the end-pots and will otherwise influence the damping behavior and disturb its tuning. A special centrifugal arrangement was made to push out the liquid from the vapor tube without heating into the end-pots.

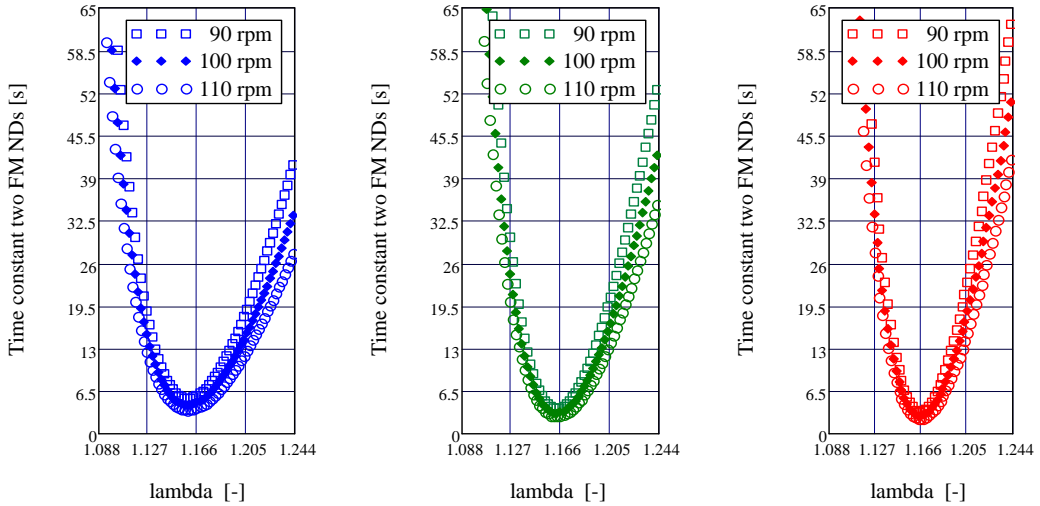


Fig-4.17 Final $\lambda_0 = 1.166$ FM design case with the damping time constant as a function of the inertia ratio at the spin rates of 90, 100 and 110 rpm (top, middle and bottom curve) and temperature range $T = -25, +20$ and $+50$ °C as parameter (left, middle, right picture).

Table-4.12 Test prediction matrix of the FM performance checks including the contribution of two dampers. The total inertia ratio was estimated to be $I_{tot} = 90$ [kg·m²].

λ [-]	Ω_{test} [rad/s]	P/a_0^2 [g.s]	τ_{test} [s]	T_{test} [s]	Φ_{test} at $R = 2$ m
1.173	0.571	115.1	600 ^a	11.0	7.4" – 14.9 ⁰
1.158	0.523	140.0	588 ^a	12.0	8.7" – 17.4 ⁰
1.141	0.466	115.0	901 ^a	13.5	10.6" – 21.2 ⁰

^aThe angular test range $\theta_{flight} = 0.5''$ -10 corresponds to a time interval of $8.9\tau_{test}$ on the air-bearing.

The tests of the QM and FM NDs are governed by their test plan, released, reviewed and approved in advance. The FM and QM test results summary of the performance, vibration and thermal vacuum tests are given in [FDS, 1992]. The QM and the 4 FM NDs survived the qualification and acceptance tests without any problems. All tests (performance, thermal vacuum, vibration) were successful. The test results proved compliance with the full scope of flight acceptance criteria. Following the PTM/DM/QM/FM test sequence of Table-4.8, the following results and comments apply:

Items 1, 2, 10 and 11- Visual and mechanical status inspection, dimensions and mass

The visual and mechanical status and geometry is compliant to the design and build standards. The mass of the FM NDs fulfilled the requirement $M < 1.5$ kg within the pair asymmetry demand of $< 2\%$.

Items 3 and 9 – Leakage tests

The tests are compliant to the leakage test requirement $< 10^{-9}$ Torr-liter/s vapor at $< 10^{-6}$ Torr-liter/s ambient and performed according to the test standards of Fokker (Dutch) Space.

Items 4 and 8 – Performance checks

A 3rd calibration (an extended performance check in addition to the 1st and 2nd PTM calibrations) was executed with the QM/DM combination using nine measurement frequencies. This is shown in Fig-4.18 where the cleanroom temperature range 22 to 24 °C is indicated to cover the measured temperature 23 ± 1 °C. The pictures include the

calibration factor $n = 1.3$ given by Eqn. (2.108). The damping curves in the right picture are tuned (LSS) to the test values by adding 15 mm effective length up to $L_{eff} = 530$ mm in the model. This accounts for the 3% mistuned condition with respect to the required nominal airbearing period $T_a = 15.22$ s which complies with $\lambda_0 = 1.125$.

A 4th extended FM/FM ND pair performance check, using six instead of the three proposed air-bearing test periods, is given in Fig-4.19. The damping curves in the right picture are tuned towards the test values by a calibration factor $n = 0.8$ and adding 35 mm effective damping length up to $L_{eff} = 550$ mm. This accounts for the 6% mistuned condition with respect to the required nominal airbearing period $T_a = 11.46$ s and $\lambda_0 = 1.166$.

The off-sets can be understood by taking the in- and outlet flow from the liquid-tube into account. Moreover Fig-4.11 shows that the frequency tuning settles itself already in the degree range. The QM Reynolds number at $\theta = 0.5^\circ$ is about 7 (result from CAD model) which yields at 1-g an additional length of about 5 mm using Boussinesq's Eqn. (2.46).

In an early phase of the FY2 ND project the statement was already made (by the author) that the ND bandwidth and temperature range as well as the limitations of the test equipment and environment have to be taken into account to specify the test resolution. This argument convinced the customer after all.

The final FM design gained more than a factor two in damping performance and about 10% in the resonance quality factor $Q = \omega_0/\Delta\omega_0$ compared to the initial phase-A (QM) design. This meant a comfortable margin although the mass grew to the very edge of its allowed value. This performance gain is recognized by comparing the QM versus FM performance test results in Fig-4.18 and Fig-4.19 though at length scaling $L_r = 1$ and $\omega_z = 3.302$ rad/s as fictional flight spin-rate. On basis of the PTM, QM and FM tests results the physical length of the FM could have been reduced with at least 15 mm on basis of Eqn. (2.46). The QM and FM off-sets in tuning at $L_r = 1$ were acceptable due to the factor two over-compliance, the given explanation and the fact that the well-tuned PTM calibration towards the flight spin-rate $\omega_z = 10.472$ rad/s was the accepted key driver and primary verification of the FM design.

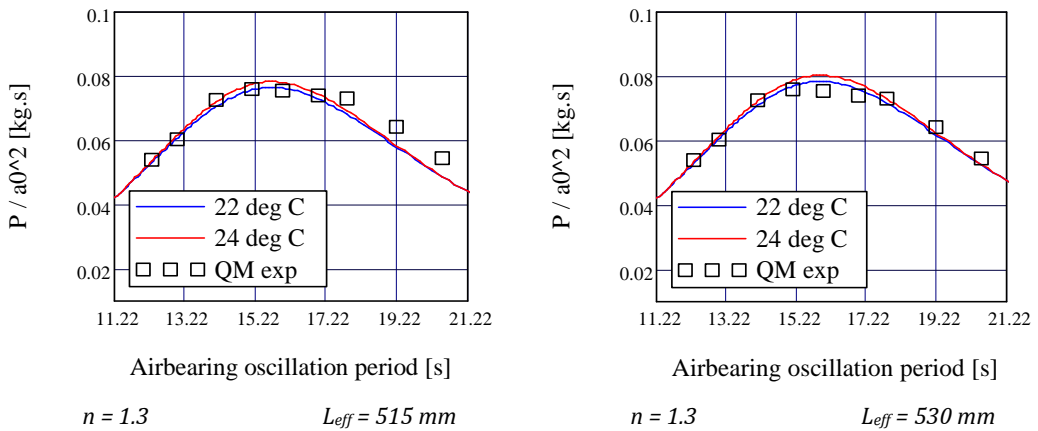


Fig-4.18 Third calibration experiment and simulation of the air-bearing test with the FY2 QM/DM ND pair. The length $L_{eff} = 530$ mm accounts for the 3% mistuned condition with respect to $T_0 = 15.22$ s.

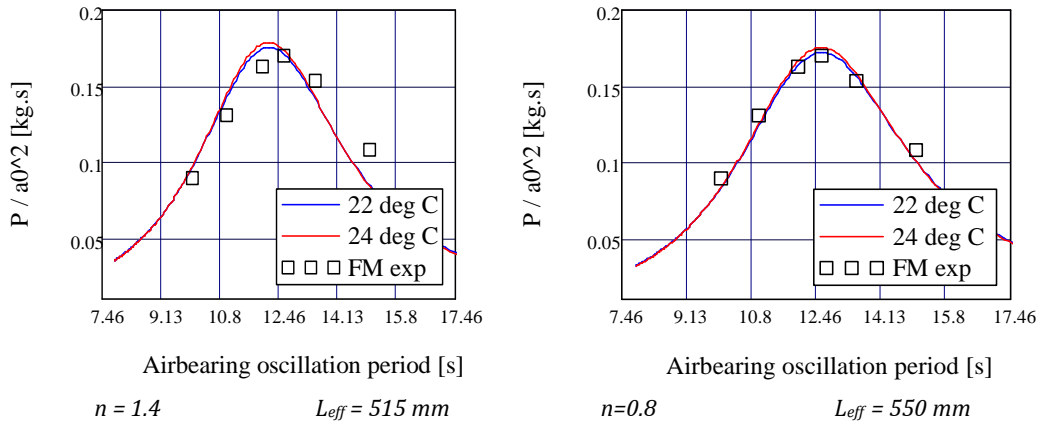


Fig-4.19 Performance acceptance test of a FM ND pair and simulation of the air-bearing test. The increased length $L_{eff} = 550$ mm accounts for the 6% mistuned condition with respect to $T_0 = 11.46$ s.

Items 5 and 6- Sine resonance sweep, sine vibrations and random vibrations

The revised structural design (final FM) including the support bracket is shown in Figure 4.7. The support bracket was upgraded compared to its original phase-A design to increase the lowest resonance frequency once again above the 200 Hz. The original acceptance random vibrations specification in the test plan was overruled on request of the customer. One FM NUDA was subjected to a qualification sine vibration test program. The lowest resonance frequency was found to be within the range 220-230 Hz well beyond the requirement > 200 Hz. The test results are given in [FDS, 1992].

Item 7-Thermal cycling

The required temperature profile could not be approximated at the slopes. The radiative coupling between the shroud and the ND is low due to the fact that the damper is not a black absorber. The thermal vacuum chamber control equipment was regulated to follow the required profile as good as possible. The requirement $|dT/dt| > 1$ °C/min could not be reached and was restricted to ≈ 0.3 °C/min. Only a black painted damper could provide a steeper warming-up slope but its relative large mass and heat capacity is another obstacle. Even when the shroud upper temperature could be set on e.g. 1000 °C the lower value is basically restricted to about -180 °C so an unequal slope would be obtained. The FM models survived the qualification and acceptance thermal vacuum tests without any problems.

The qualification and acceptance tests were all successfully. The only proof left was the radiation compliance which was completed by the radiation analysis in the following section. This analysis with in addition the ND flight heritage was finally accepted by the Chinese customer as satisfactory proof to close this final issue.

4.10 Radiation Analysis

The ND ability to survive the EOL radiation dose [FDS, 1990] was assured by similarity with former ND projects (see Table-1.1 and 1.2). The Aluminum parts including the support brackets and the interfaces offer sufficient radiation shielding. This was roughly assessed for various missions and radiation doses in the past and validated by flight heritage. This argument covered the radiation qualification of missions like Ulysses and Cluster, both ESA missions. During the FY-2 ND Design Review in March 1990 it was shown that for most other ND projects an Al wall thickness of 1 mm and the liquid PP1 were used (see Table-1.1). This was initially not accepted by the customer but only after delivery of an additional document dealing with the FY-2 ND radiation analysis. The updated analysis, proving that the amount of liquid dissociation is acceptable in terms of internal structural load and damping performance, is given here. The related ND structural stability is assured by the strength and stiffness analysis, the reliability and the design heritage [FDS, 1992]. To analyze the impact of a worst case dissociation of the damping liquid due to the specified radiation, first the chemical properties of the Fluoro-Carbons PP1 and PP3 will be examined.

Damping Liquid Constitution

The chemical formulae for the major constituent of the damping fluid PP1 and PP3 are given in Table-4.13. (Per)fluoro-carbons are organo-fluorine compounds that contain strong carbon-fluorine bonds. Fluoroalkanes, that contain only single bonds, are more chemically and thermally stable than alkanes. Fluoroalkanes can serve as oil and water-repellant fluoropolymers, solvents, liquid breathing research agents, powerful greenhouse gases and (nutation) damper liquids [Lemal, 2004].

Table 4.13 *Properties of Fluoro-Carbon damping liquids.*

Flutec type	Chemical name		Structure formula
PP1	Perfluoro-n-hexane	C ₆ F ₁₄	CF ₃ -CF ₂ -CF ₂ -CF ₂ -CF ₂ -CF ₃
PP3	Perfluoro 1-4 di-methyl cyclohexane	C ₈ F ₁₆	CF ₃ -CF ₂ -CF ₂ -CF ₂ -CF ₂ -CF ₂ -CF ₂ -CF ₃

Typical physical properties of fluorocarbon liquids are:

1. Colorless
2. High molecular weight and density more than twice that of water.
3. Low intermolecular forces yield low viscosities compared to other liquids with similar boiling points.
4. Low surface tension, heat of vaporization and refractive indices
5. Very low solubility in water and vice versa, only ~10 ppm.

Stability and Reactivity

Saturated fluoro-carbons with only single bonds are very stable because of the strength and nature of the strongest bond in organic chemistry: The carbon-fluorine bond. When fluoro-carbons are unsaturated, they are less stable and more reactive than fluoro-alkanes, or comparable hydrocarbons, due to the electronegativity of fluorine. Comparing the structural formulas of PP1 and PP3 provides:

- A molecule PP1 contains five Carbon chain bonds and PP3 eight
- The chemical bonds are the same but the PP3 C chain is closed (cyclo-hexane).

A radiation energy equivalent of 100 eV causes the destruction of 8 molecules PP3 [FDS, 1992] equivalent to 12.5 eV/molecule. In another source [HCP, 1980] the chemical bond strengths in C-F and C-C s are released to be < 4.34 eV per bond yielding a worst case equivalent of 4.34 eV/molecule. This would mean that all available radiation energy is used in most optimal sense to destroy as many single molecules (PP1, PP3) as possible which is

most unlikely. Though there are no PP1 data [FDS, 1992] available, it is a reasonable approach to apply the PP3 number of 12.5 eV / molecule as well.

Radiation Dose and Shielding

Aluminum is a common metal used in nuclear physics experiments being inert to nuclear reactions. Proton radiation is absorbed in a thin film on the surface but electron radiation is more penetrative. Electrons of 1 MeV do penetrate through an Al shielding of 1 mm whereas protons of at least 13 MeV are required to do the same. An accurate dose calculation at a specific point on the S/C is a complex analysis, requiring an exact determination of proton and electron fluxes, the directional distribution, energy spectrum and the dimensions and material type of the shielding around the point in question. Normally it is enough to assess the dose and apply a safety margin to compensate for the dose uncertainty and the degradation threshold of the material. In the following analysis this approach is followed. Moreover the quantization of the energy (particle type) has to be taken into account since this determines the penetration capability through the ND Al shielding. Therefore the specific energy of the specified particles is considered. The Al shielding accounts for attenuation of the solar wind e^- or radioisotope β^- radiation which are both electrons by the intensity equation

$$I(x) = I_0 \cdot e^{-\mu x} \quad (4.5)$$

with

$x = \rho d$	Mass effective cross-section with $[x] = \text{g/mm}^2$
d	Shielding wall thickness [mm]
$\mu = 17.0 \cdot E^{-1.43}$	Energy dependent absorption factor with $[\mu] = \text{mm}^2/\text{g}$ [HCP, 1981]
E	Energetic value of the emitted electrons or beta particles.

The liquid tube wall thickness $d = 1.0$ mm whilst for the end-pot $d = 1.5$ mm. The ND external surface is considered to be half exposed to impinging radiation. This is a realistic assumption since extra shielding is present at the ND rear side and by the support bracket and its attachments. These are shown in the mechanical drawings [FDS, 1992] and in Fig-4.7. The radiation dose is specified in Table-4.2.

Liquid Dissociation and Performance Degradation

The radiation induced deterioration of the liquid may produce stable gaseous compounds. These may obstruct the ND performance up to non-compliance. A worst case analysis was made to assess this effect considering a simple (cylinder) ND geometry presentation. The end-pots outer surfaces take 94.4% and contain 95.2% of the total PP1 liquid amount. The first important conclusion is that the proton dose can be disregarded since protons with an energy of 6.8 MeV cannot penetrate into a ND with 1 mm wall thickness. The energy of the Cobalt 1.22 MeV β^- and 1 MeV e^- is attenuated differently as given by Eqn. (4.5) and elaborated in Table-4.14.

Table-4.14 Penetration potential of electrons at different wall thicknesses and energies.

Wall thickness [mm]	Electron energy [MeV]	Penetrated amount [%]
1.0	1.0	1.02
1.5	1.0	0.10
1.0	1.22	2.92
1.5	1.22	0.50

Overall ND shielding

Electron energy [MeV]	Total energy dose [eV]	Net penetration dose [eV]
1.0	7.03×10^{23}	1.8432×10^{22}
1.22	1.35×10^{23}	0.0128×10^{22}
		1.8560×10^{22} total

Dissociation Level

The total PP1 (C_6F_{14}) mass in a FY2 ND is 514 gram which equals 9.158×10^{23} molecules. Considering the total dose of 1.856021×10^{22} eV, this yields the destruction of 8/100 times (see discussion on stability and reactivity) this number of molecules: 1.484816×10^{21} . This is 0.162 % of the amount of PP1 molecules in a single FY-2 ND and equal to about 0.55 g.

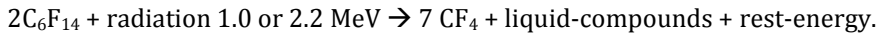
Physical Effects of Flutec PP1 Dissociation

Due to the Flutec PP1 irradiation degradation the following physical effects apply:

1. Internal pressure variation in the end-pots and vapor tube.
2. Impact on the strength and stiffness analysis.
3. Functional performance effects.
4. Chemical effects.

Internal Pressure Variation

The NDs are hermetically closed by electron beam welding. The internal pressure will increase when the PP1 molecules degrade on irradiation into stable CF_4 gas molecules. A worst case analysis for this over-pressure is obtained as an upper limit considering that two mole C_6F_{14} molecules degrade into 7 mole stable inert CF_4 gas molecules and other liquid compounds which do not affect the internal gas pressure. The chemical equation is



Assuming that the CF_4 molecules behave like an ideal gas the state equation of an ideal gas can be applied for the increase of the internal pressure. Its contribution can be linearly added according the superposition of independent partial pressures (Law of Dalton).

$$\sum_i p_i V = \sum_i n_i RT \quad (4.6)$$

with

p	(Partial) pressure [N/m ²]
V	Volume of one end-pot and one vapor tube [m ³]
n_i	Amount of ideal gas type i [mole]
R	Gas constant [8.3 J/mole/K]
T	Temperature [K].

The analysis of the maximum pressure in the ND end-pots due to the EOL radiation dose and the extreme temperature condition $T=50^\circ\text{C}$ is summarized in Table-4.15.

Table 4.15 Maximum pressures in the FY-2 ND due to the specified EOL conditions.

Compound	Calculation	(partial) pressure [Bar]
PP1 damp	read from Flutec PP1 datasheets	0.75842
Helium gas	ideal gas law Eqn. (4.6)	1.10239
CF4 gas	ideal gas law Eqn. (4.6)	0.76635
	Total pressure	2.62716

Impact on the strength/stiffness analysis

The maximum allowable pressure in the weakest spot of the end-pots, the bulkhead, is defined by the margin of safety (MS) by

$$MS = \sigma_{0.2} / \sigma_{VM} - 1 > 0.25 \quad (4.7)$$

with

$\sigma_{0.2}$	typical 0.2% offset strain
σ_{VM}	the Von-Mises (VM) maximum tension.

The von Mises (VM) tension is related to the maximum distortion strain energy [von Mises, 1913]. The margin of safety (MS) and the VM maximum tension σ_{VM} was calculated with

respect to a net internal pressure of 2.03 bar against AM0 (Air Mass zero) conditions outside the damper. Beyond this value Eqn. (4.7) gives 14.75 % margin. This equals 0.3 bar which was not regarded to be enough. For the extreme radiation case (worse case conditions) more details were incorporated in the analysis [FDS, 1992]. The end-pot bulkhead strength- and stiffness model was refined by modeling the real geometry with rounded edges whilst the bulkhead was modeled with plate-bending elements. As a result the following adapted equation to define the MS is taken

$$MS = \sigma_B / \sigma_{VM} - 1 > 0.25. \quad (4.8)$$

The ultimate stress in the analysis was taken to be the ultimate (Break down) strength σ_B . The maximum VM stresses for two bulkhead construction cases were calculated [FDS, 1992] at a pressure difference of 1 bar:

- a) Simply supported along its edges $\sigma_{VM} = 5.8 \times 10^7 \text{ N/m}^2$
- b) Simply clamped along its edges $\sigma_{VM} = 3.0 \times 10^7 \text{ N/m}^2$.

Applying $\sigma_B = 27.5 \times 10^7 \text{ N/m}^2$ for Al 5056 [FDS, 1992] and taking worst case a) with $MS = 0.25$ the ultimate allowable total gas pressure difference inside/outside the end-pot is 3.793 bar. The positive margin left is still $3.793 - 2.627 = 1.166$ bar. This proves that the overpressure due to the CF4 gas contribution (as a result of the radiation degradation of the PP1 liquid) is far from lethal for the ND with respect to its strength and stiffness.

Chemical effects

Fluoro-carbons are generally very stable [O' Hagan, 2008] but PP1 degrades on irradiation. No indications are found in [HCF, 1980] for a possible reaction of fluoro-carbons and Aluminium. Even Magnesium which is a much higher reactive metal, reacts slowly with fluoro-carbons at 700 °C. Therefore the chemical compatibility is guaranteed on basis of the negligible amount of PP1 liquid which is dissociated due to the EOL specified amounts of radiation.

Performance change

Flutec PP1 degrades on irradiation into CF4 (stable, inert gas), high molecular weight polymers and other low molecular species. Therefore the following effects possibly causing a ND performance change by end-pot wall hysteresis shall be evaluated:

- Fluid level displacement.
- Change of the internal geometry by high molecular mass polymers deposited as a film on surfaces.
- A viscosity change due to the formation of lower- and higher molecular mass species.

The destruction level of only 0.16% was assumed to be negligible, not necessitating additional radiation experiments. This vision was agreed by the Chinese customer on basis of the given analysis and the Dutch nutation damper space track record. The latter was supported by the fact that the root cause of the Ulysses nutation anomaly was assessed to be outside the performance scope of the Fokker Space NDs. The following Chapter 5 will deal with this analysis.

4.11 Verification and Validation

Damping performance and time constant

The FY-2 ND design is interesting because of the S/C high operational spin-rate $\omega_z = 100$ rpm. The sophisticated MSG 100 rpm S/C and its ND design were briefly dealt with for comparison in Chapter 3. In the 100 rpm range only the NS solution is applicable as made clear in Fig-4.20. The first picture shows the velocity profile in the liquid tube at $t = 0$ with $Re = 1373$. The strong effect of reverse layers was already shown in Fig-2.16. The right picture shows the huge differences in the predicted damping performance by the three models HP, RHP-1 and NS. The deviation in resonance frequency is 2.2% for the RHP-1 versus the NS model.

Fig-4.21 shows the behavior at the fictional spin-rate $\omega_z = 10$ rpm which is 10% of the operational value. As expected the first picture (mind the X-scale which is 20X magnified compared to Fig-4.20) shows a Poiseuille velocity profile without reverse layers. The second picture proves that the predictions of the damping behavior of the three models at the low Reynolds value $Re = 47$ agree within 20% but the RHP-1 result is again mistuned. The NS and HP model agree reasonably well but the RHP-1 model resonance frequency deviates significantly (in the order of +3%). The RHP-1 model predicts less damping and consequently about 30% higher time constants.

The conclusion was already given in Chapter 3 that the NS model is the superior backbone of TLD and ND design. The fact the NS solution allows for reverse layers overrules the necessity of the factor k_0 in the RHP-1 model. The extreme reverse flow in Fig-4.22 at the highest operational FY-2 ND temperature is typical for the added value of the NS model.

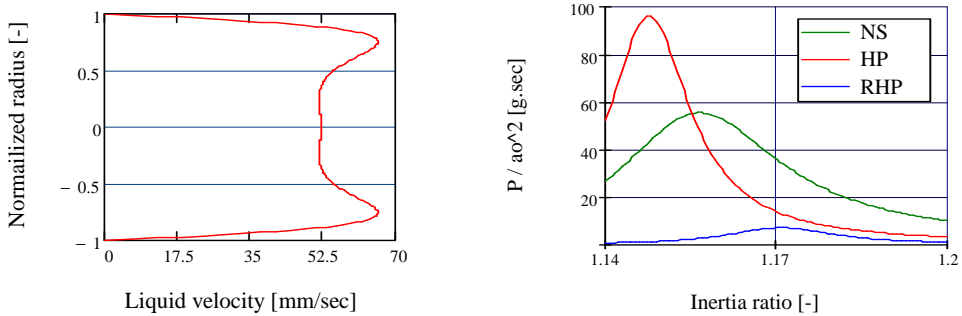


Fig- 4.20 FY-2 S/C nom operation at **100 rpm** modeled by NS, HP and RHP-1 at $Re = 1373$

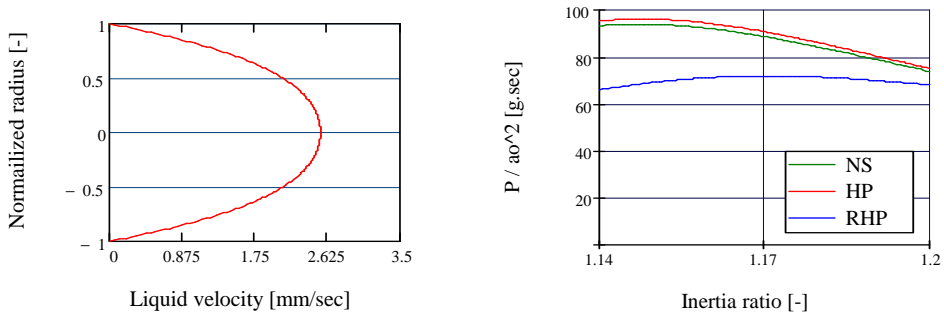


Fig- 4.21 FY-2 S/C nom operation at **the fictive 10 rpm** modeled by NS, HP and RHP-1.

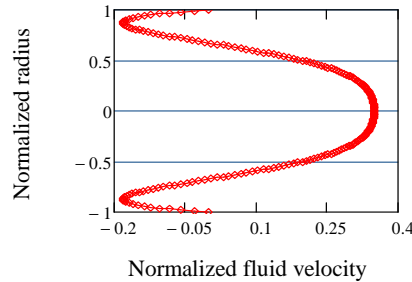


Fig-4.22 Extreme reverse flow layers in the FY2 ND at $t = T/4$, $T = 50^\circ\text{C}$ and other parameters nominal.

Unfortunately no hard flight data can be obtained from the Chinese BICE and GWIC institutes. Digging in the Chinese scientific literature (with support of Chinese colleagues) delivered the following indirect evidence:

- The automatic image navigation algorithm for the FY2 S/C is given by [Lu et al., 2008]. The FY2 image navigation accuracy approaches 5 km in the sub-satellite point and acquires images through the cooperation of ground and space segments. The coherent technique developed and used by the US GOES served as an example. The GOES, however, has a hardware (H/W) approach whilst the FY2 approach is based mainly on software (S/W). As an example: The scanning radiometer changes the moments of inertia (MOI) of the S/C causing small changes in the spin-rate and consequently part of the image is scanned slower than the top or bottom parts. This is corrected for by S/W conversion to identical angular intervals. The effects of long term S/C attitude and roll misalignment are also (aimed to be) corrected. The solar light pressure on an asymmetrical S/C like Meteosat causes a net torque and thereby precession and nutation as shown by [Sorensen, 1997]. As a consequence the monthly instabilities of the FY2 spin-axis are shown in Fig-4.23 with a linear trend easy to calibrate. The impact of the performance of the H/W, i.e. the ADCS with the passive NDs, is not mentioned.

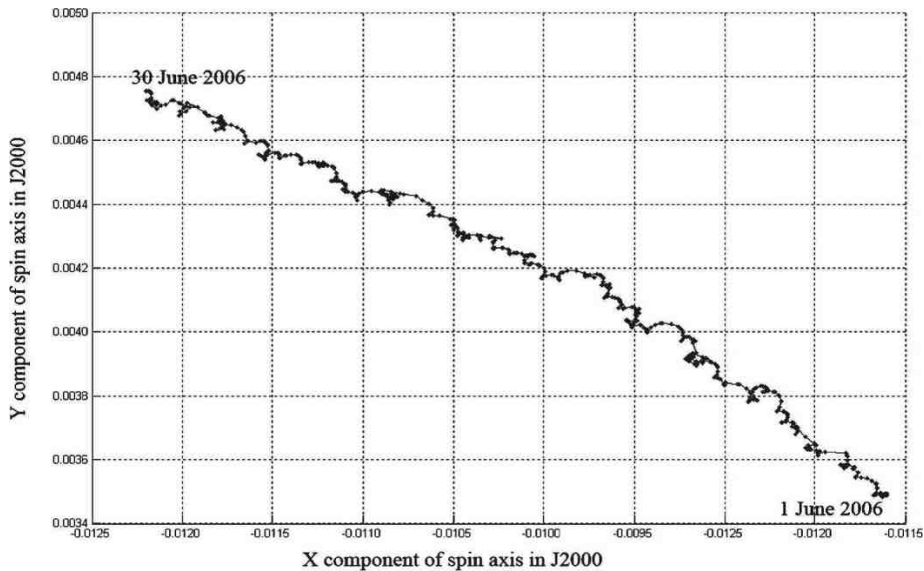


Fig-4.23 Inflight X and Y component of the FY2C S/C spin-axis projections in the O-X-Y plane during the period 01-06-2006 to 30-06-2006 showing long term instabilities [Lu et al., 2008].

- The nominal flight FY2 S/C nutation performance is dealt with by [Wang, 2005]. The author mentions that the observed in-orbit effect of the FY2 S/C attitude dynamics on the directional stability of the spin-axis. The FOV of the radiometer (registration precision) meets the design requirement $\theta < 3.5 \mu\text{rad}$. The original $2.4 \mu\text{rad}$ ($0.5''$) ND design requirement (see Table-4.2) was obviously a major part of the FY-2 spin-axis stability budget. The spacecraft nutation induced by the North-South scan movement of the radiometer meets the stability requirement of $< 3.5 \mu\text{rad}$ on a 0.6 s short timescale. This item was considered in more detail in Chapter 3 which dealt with the sophisticated MSG S/C.

4.12 Conclusions

The FY-2 liquid-in-tube ND design is another derivative of the equatorial damper family, qualified and delivered by Fokker (Dutch) Space for the Ulysses (former ISPM) and ISEE-B satellites. This chapter dealt with the performance verification and qualification of the FY2 ND design. In the early 90s the FY2 ND was the most challenging ND design ever because of the severe residual damping angle requirement $\theta < 0.5''$ ($2.4 \mu\text{rad}$). The overall compliance with the specifications was shown.

The extended test program and the demanding questions from the Chinese customer (GWIC) have led to refined insights in the recursive calibration method and the ultimate damping performance. The recursive calibration approach was extended with an extra parameter n (see section 2.12) and applied in the Cluster ND program [van Bakel, 1993]. The PTM calibration experiments were repeated and the design fine-tuned up to the level required by the specific program requirements.

At a certain nutation level there will be a contact angle variation in equilibrium with the meniscus hysteresis. This potential 'blocking' issue was investigated experimentally, supported by multiple refined analysis of the FY-2 ND PTM air-bearing experiments, but did not show up. Moreover a dedicated liquid drop experiment was executed yielding independent evidence of the superior PP1 contact angle wetting condition.

The extreme limiting air-bearing angles were analyzed. The calibration of air-flow fluctuations on basis of a simple model offered evidence that the air-bearing performance is limited by airflows solely.

An extended radiation analysis was given to show in addition to the ND heritage given in Chapter 1. The analysis made clear that the FY2 ND will survive the accumulated radiation doses towards its End-Of-Life (EOL) performance with sufficient margin.

The overall analysis shows that, though on the limit of the test equipment potentials, the $0.5''$ flight nutation angle requirement is met. In the end the customer accepted the given multiple evidence.

The extended refined tuning analysis using all PTM, QM and FM performance test data delivered valuable results. These support the validation of a new method to estimate the effective damping length more accurately than on basis of the old 10% rule given in section 2.12. This important result will be elaborated in Chapter 8 after inclusion of the test analysis results of the Ulysses and Cluster NDs in the following chapters.

5 Ulysses Spacecraft: Feedback from Space

Necessity, who is the mother of invention.

Plato, *The Republic*

Greek author & philosopher in Athens

(427 BC - 347 BC)

5.1 Introduction

The Ulysses ND project started in 1979 at Fokker Space BV as part of the Ulysses solar probe mission and was called International Solar-Polar Mission (ISPM) at that time. The Ulysses S/C, shown in Fig-5.1, is powered by a radio-isotope thermo-electric generator (RTG) and spin-stabilized at a rate of 5 RPM with its high-gain antenna (HGA) pointing continuously to the Earth. The two 35 m wire booms are coaxial with the S/C X-axis, the rigid radial boom coincides with the +Y-axis and the axial boom with the -Z-axis. The 1.65 m diameter HGA serves both the X-Band downlink and the S-Band uplink. Near-continuous data storage and transmission throughout the mission is a key scientific requirement. Since continuous coverage by ground stations is impossible for a long-duration mission, data are stored on-board and replayed, interleaved with real-time data, during periods of coverage. The nominal tracking coverage is 8 h out of 24 h [Wenzel et al., 1992].

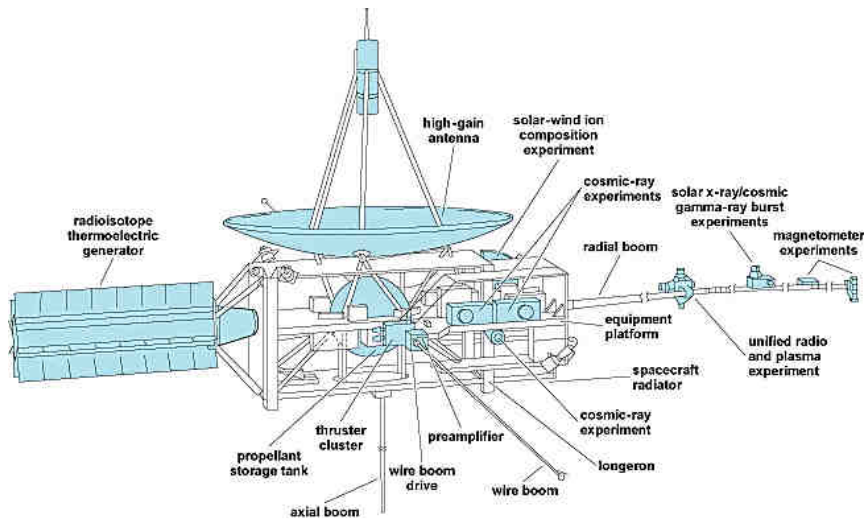


Fig-5.1 The 5 RPM spin-stabilized Ulysses S/C to study the sun from solar polar latitudes. The +Z axis is the vertical, the +Y axis coincides with the rigid radial boom whilst the +X axis coincides with the wire boom. The wire booms are not drawn to scale [ESA, 2012].

The Ulysses orbiter S/C was a joint project between NASA and the European Space Agency (ESA). It was launched the 6th of October 1990 via the Space Shuttle with an Inertial Upper Stage (IUS) and Payload Assist Module (PAM). It encountered Jupiter early in 1992 for a gravity assist to achieve a trajectory at nearly perpendicular angles to the ecliptic plane. While within Jupiter's vicinities for its gravity assist, it made significant observations of the Jovian system. Ulysses carries fields and particles instruments. Since its launch, the Ulysses S/C was successful in active operations until March 2008. At that time the S/C completed its third set of passes of the Sun's polar regions [ESA, 2012].

The author was involved at ESTEC in the early discussions on the Ulysses nutation anomaly which appeared shortly after the deployment of the axial boom in November 1990. This phenomenon endangered the science mission since the Earth downlink (D/L) was obstructed by the wobbling S/C and its High Gain Antenna (HGA). The maximum tolerable off-set being defined by the S/C pointing and link budget. It was therefore of ultimate company importance that an early blame, that the three Fokker NDs did not perform nominally, was rapidly proven to be based on prejudice instead of fact. This chapter will provide solid proof that the NDs did perform as designed and specified. The Ulysses in-orbit analysis and the experience from the FY-2 ND project given in Chapter 4 led to an innovative Cluster ND concept to be dealt with in Chapter 7.

An essential part of the analysis covered in this chapter, is driven by the performance requirements of extendible booms and antennas on a S/C. Refined thermo-mechanical engineering and analysis for deployable booms were already elaborated in the 60s for the Alouette I and II S/C, shown in Fig-5.2 below [Mar and Garrett, 1969]. At that time the application of long extendible ionospheric sounding antennas was a novelty making Alouette-I (launch September 29, 1962) a trendsetter and Canada the third space nation after the US and Russia.

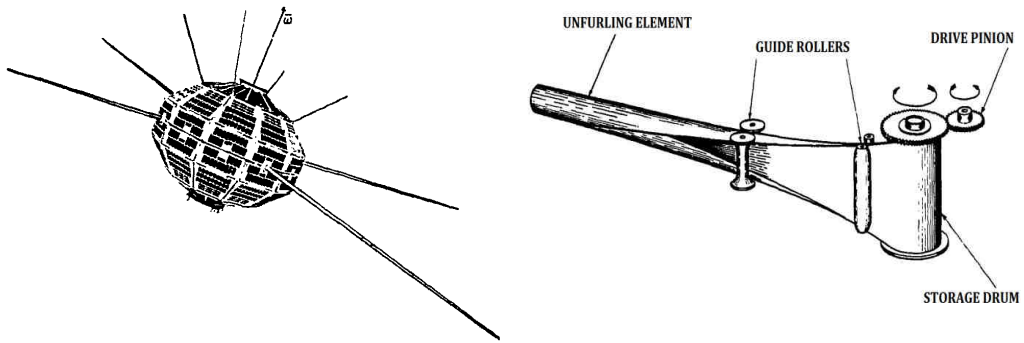


Fig-5.2 *Alouette-I S/C (1960s) and mechanical antenna principle STEM (Storable Extendible Member). STEM is the trade name of the manufacturer SPAR Aerospace of Canada [Mar and Garrett, 1969].*

The combination of the Alouette I-II S/C very high spin-rate $\omega_z = 120\text{--}157$ rpm with long tip-to-tip sounder antenna lengths of 45.7–73.2 m opened the engineering horizon of flexible S/C body engineering. The Alouette-I thin-walled antenna material was a preformed flat strip of spring (blue) steel on a drum but became Beryllium Copper (BeCu) for the Alouette-II. This boom design named STEM (Storable Extendible Member), became the basic antenna design for a long series of magneto-spheric and iono-spheric science missions equipped with extendible booms since that time. The impact of thermal stress and photon pressure from the sun had to be investigated since the impact of solar heating was not well understood in the 1960s.

In the 1970s, a nutation anomaly comparable to the Ulysses case in the 1990s, occurred with the Small Scientific S/C Explorer-45 (or S^3 launched November 15, 1971) shown in Fig-5.3. The mission was to study the Earth's magneto-sphere. The spin-stabilized S/C, with a launch mass of approximately 52 kg, was placed in a highly elliptical orbit of 272 km x 18,149 km at 3.2° inclination.

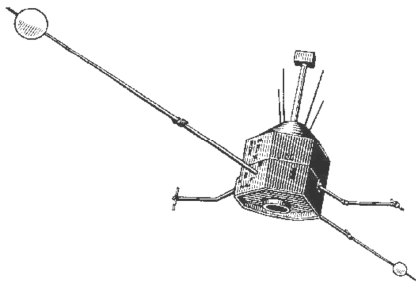


Figure 5.3
The S^3 spacecraft in the 1970s [Hoffman, 2007]

Solar “pumped” nutation appeared despite the fact that the radial booms were relatively stiff. This gave hard indications in an early phase of the Ulysses AOCS anomaly that the root cause of the Ulysses AOCS anomaly was the same [Hoffman, 2007], i.e.

- A magnetic experiment on the S^3 S/C required a radial boom to be isolated from the S/C as a result of the magnetic cleanliness requirement. The booms were designed very stiff compared with the regular tape booms of e.g. the OGO-4 S/C at that time. Nevertheless once in orbit, after deployment of these radial booms, the S^3 S/C suffered with nutation. The boom bending was determined to be a function of the Sun angle whilst its variation comprised a nutation frequency component. The sun obviously provided the energy to enable the S/C nutation instability when illuminated by the sun to its cold state in the shadow of the S/C.

- The thermal time constant of the boom is the time required to achieve a maximum deflection of the boom when lit, or alternately when it returns to its 'cold', unlit state. In case the thermal time constant equals zero no solar induced nutation can be added to the system because it would be in phase with the motion relative to the Sun. The other logical extreme, the 'infinite' time constant, would be a one-time deflection of the boom, not contributing to nutation. For other time constants there will be bending and phase shift components at spin and nutation frequency. The nutation can be regarded to be a structural resonance of the spinning S/C.
- Mass bending at nutation frequency induces or damps nutation. In the case of S³ it drove nutation. If the spin-axis is near the sun line, maximum bending occurs but with zero components at nutation frequency. This case was clear when S3's spin-axis was moved closer to the sun line, with near full sunlight on each boom. With the sun nearly normal to these booms, small angular variation at nutation frequency did not result in any significant component of thermal bending at nutation frequency. The nutation disappeared. If the time constant is such that there is some mass motion and phase shift at nutation frequency, there will be impact on nutation. The phenomenon is not restricted to the booms. Any mass motion at nutation frequency that has the potential to move on a S/C at nutation frequency can affect nutation either stabilizing or destabilizing the S/C in the end.

These arguments from the 80s are confirmed by [Presti and Goulding, 2006] to be applicable for the Ulysses S/C nutation anomaly as well.

5.2 Mission Operations

The Ulysses project initially comprised two S/C to be flown with a Jupiter gravity assist. Fig-5.4 shows the heliocentric orbit with a high inclination relative to the ecliptic. NASA canceled their spacecraft for budgetary reasons but ESA went ahead. The solar probe Ulysses made the first-ever measurements of the Sun from a polar orbit. On the way to its solar polar orbit, it made a close fly-by of Jupiter and did observations of the solar system's largest planet [Hoffman, 2007].

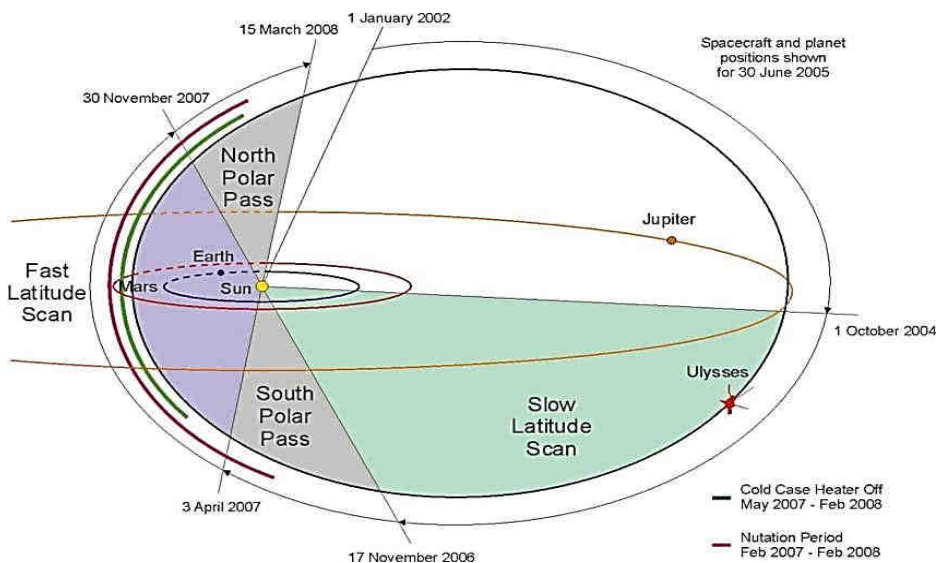


Fig-5.4 The Ulysses S/C heliocentric orbit with high inclination relative to the ecliptic and a Jupiter gravity assist [Presti and Goulding, 2006].

The Ulysses S/C, shown in Fig-5.1, 5.4 and 5.5, used a Jupiter swing-by in February 1992. It passed over the rotational south pole of the Sun at mid-1994 at 2 AU, and the north-pole in mid-1995.

5.3 Ulysses AOCS Anomaly and its Control

Before dealing in more detail with the Ulysses nutation anomaly, the mass and inertia configuration and the AOCS S/S including the Conscan S/S are studied. Sources are [Crellin, 1990], [Hawkyard, 1990], [Kuiper, 1990], [Wenzel et al., 1992], [Marrirodriga et al., 1993], [Chan et al., 2004] and [Presti and Goulding, 2006].

Mass and inertia configuration

The S/C mass and inertia properties were design driven by the requirements for the launch and deployed boom configuration to enable the pointing of the HGA towards Earth. The spin-axis of the launch configuration was the geometric center line. The theoretical Z spin-axis (see Fig-5.5) in deployed configuration is aligned with the electrical axis of the HGA.

Attitude and Orbit Control Subsystem (AOCS)

The primary operational functions of the AOCS are to maintain the S/C spin-axis Earth-pointing and to control the spin-rate. The routine attitude maneuver schedule is driven primarily by the Earth drift rate (relative to the spacecraft) and the maximum allowable Earth off-pointing. The link margin determines the maximum allowable Earth off-pointing which varies from 0.3° to 1.2° depending on Earth range and downlink data rate [Chan et al., 2004]. Additional operational functions are dictated by trajectory control requirements, nutation damping, and by the measurement of the attitude for scientific reasons.

Closed Loop AOCS control by Conscan

The angle between the spacecraft spin axis and the Earth is measured and controlled by the AOCS conical scanning system (Conscan). The spin-rate, its phase and the solar-aspect-angle (SAA) is determined from redundant Sun sensors. The Sun-sensor outputs are processed in the onboard data-handling (OBDH) subsystem to provide the spin reference pulse and the spin segment clock. These signals and the Sun-sensor data are used in the AOCS electronics to determine the S/C spin-rate and SAA for the purpose of closed loop on-board control, failure detection and recovery. Hydrazine thrusters are actuated either by telecommand or autonomously. These are fed from a single tank, mounted at the launch center of gravity [COG], and arranged in two blocks of four thrusters each, providing complete redundancy. The Conscan system is enabled by the fact that the High Gain Antenna (HGA) bore sight is mounted with a small offset from the spin axis.

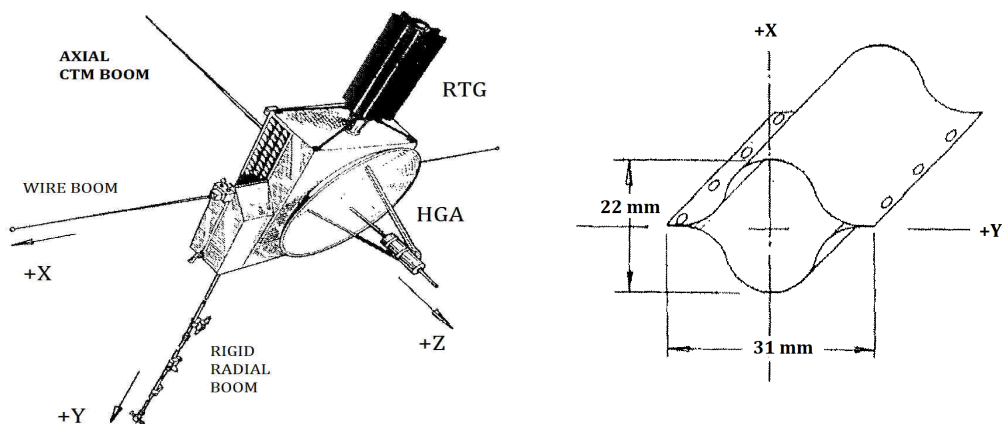


Figure 5.5 The Ulysses S/C and an axial boom segment [Marrirodriga et al, 1993]

This means that in case the spacecraft rotates, the uplink signal strength appears to vary sinusoidal. The amplitude and phase of this signal can be used to derive the magnitude and direction of the Earth off-pointing. The Conscan system can also operate in a closed-loop mode, where Earth off pointing phase and magnitude information is used to time axial thruster firings such that the off pointing is kept at acceptably low levels.

Another AOCS operation is the periodic precession maneuver for correction of the apparent Earth drift with respect to the spin-axis. These can be performed in closed loop on-board or in open loop via time-tagged command.

The AOCS also includes failure-mode-detection and protection functions which result in fail-safe operation and a re-acquisition capability in both automatic and ground-initiated recovery sequences.

The S/C carries three equatorial ND dampers [produced by Fokker Space] containing a fluid (Flutec PP1). The viscous motion in the ND liquid tubes dissipates the nutation energy. In the operational spin-rate range the nominal damping time constant for nutation cone angles from 2.0 to 0.02 degree is less than one hour.

AOCS anomaly

A significant AOCS problem was the nutation-like motion, which built on the 4th November 1990, up to 2.3° full cone angle (peak-to-peak) within 6 hours. This happened shortly after the deployment of the 7.5-meter axial radio wave experiment antenna. The nutation grew exponentially ($\tau = 84$ minutes) during the first two hours. Over the course of the following 11 days it reached a maximum of 6°.

A segment of the Beryllium-Copper alloy CTM (Collapsible Tube Mast) of this axial boom is shown in the righthand picture of Fig-5.5. The CTM geometry is shaped by two 50 micron sheets joined together by a series of 1 mm diameter spot welds. Due to the manufacturing process and storage, the boom is not quite straight after deployment [Marrirrodiga et al, 1993].

Investigation of the anomaly (December 1990) concluded that at certain SAA and solar ranges, the axial boom would flex due to differential solar heating as the S/C spins. The effect of this boom flexing is made worse by free play at the boom root and the efficient transmission of the boom motion to the spacecraft body at the boom deployment motor. Furthermore the passive NDs were not tuned for this kind of nutation behavior [Marrirrodiga et al, 1993]. If this nutation was left uncontrolled, it would have threatened both the quality of the science data and the health and safety of the spacecraft itself. The HGA off-pointing (Fig-5.6) from the Earth caused by the nutation would require the downlink data rate to be reduced which in turn would result in lower science data return. The flexing of the boom might result in its failure due to fatigue and this could cause in its turn structural damage to the rest of the S/C body [Chan et al., 2004].

After months (November and December 1990) of analysis and engineering model tests, the nutation disturbance proved to be driven by asymmetric solar heating (solar “pumping”) by partial illumination of the axial boom as the spacecraft spun [Hoffman, 2007]. The time sequence of the individual phases of forced nutation anomalies, shown in Figs-5.7 and 5.8, is well predictable by the Nutation Forcing Function (NFF) given by [Presti and Goulding, 2006]. In Eqn. (5.1) the effective radius of the S/C is referred to as r_{SC} and the length of the axial boom as L_{AB} whilst HR is the heliocentric range. For this S/C, the geometrical ratio equals $L_{AB}/r_{SC} = 5$.

$$NFF = \frac{1 - \frac{1}{L_{AB}/r_{SC}} \tan(SAA)}{HR^2} \quad (5.1)$$

Figures 5.6 up to 5.8 from [Presti and Goulding, 2006] and [Chan, 2004] visualize the complex S/C nutation dynamics, the applicability of Eqn. (5.1) and the effective Conical Scanning (CONSCAN) system operation. Conscan is a commonly used system by Deep Space Network (DSN) antennas to allow adaptive tracking of a target whose position is not precisely known.

Dedicated operational measures utilizing the on-board Conscan system were developed to suppress the motion. The nutation was successfully (closed-loop mode) controlled at acceptable levels by successive thruster firing to realign the S/C spin-axis with the Earth vector within a pre-selectable dead-band of 0.12° or 0.23° . In Fig-5.8 the half dead-band cone $0.12^\circ/2 = 0.06^\circ$ is recognized at the CONSCAN OFF level. The solid line represents the model results and the other spiky line the in-orbit measured performance. In order to exploit the damping provided by Conscan, continuous ground station coverage was needed. As a result, the ESA ground station in Kourou was upgraded to augment the DSN (Deep Space Network) during periods of a potential nutation since the DSN has only one station in the southern hemisphere.

The quasi-nutation was of a temporary nature and damped out once the boom was permanently in the shadow of the S/C body. As to be expected from the analysis the nutation did resume during the high-latitude phase of the mission. Although the anomaly is now completely understood, the details of the early anomaly analysis on ND level, dated November 1990, are dealt in the following parts of this chapter. Looking backward the involvement in the first anomaly discussions offered a unique opportunity for data analysis. The exploration generated an innovative idea applicable to the passive ADCS control of spinning S/C. The idea was applied in the Cluster S/C and will be developed in its full extent in Chapter 7.

The ND performance, as potential contributor to the Ulysses nutation anomaly, was part of the root cause analysis during the early mission phase in November 1990. The results are reported by [Crellin, 1990], [Hawkyard, 1990] and [Kuiper, 1990]. The ND triplet could not tackle the anomaly for several reasons to follow. The following sections will deal retrospectively with the ND design, its qualification recovery, re-calibrated damping performance and potential anomaly related performance items.

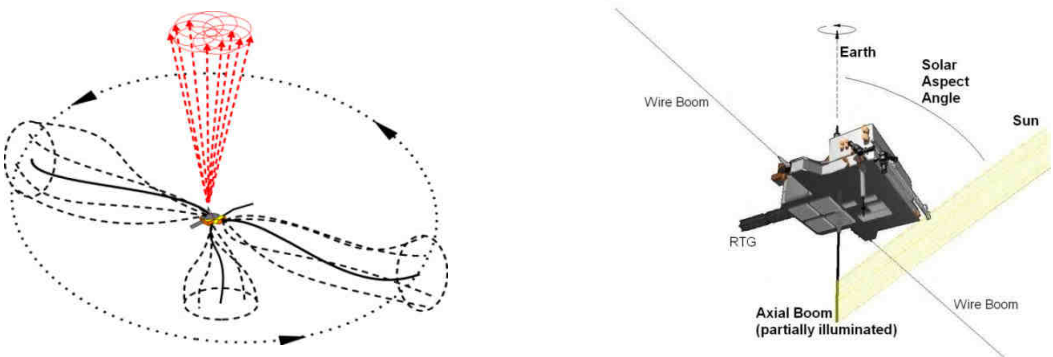


Fig-5.6 Ulysses S/C nutation induced body dynamics, the HGA pointing consequence (red) and the partial axial boom illumination (right) [Presti and Goulding, 2006].

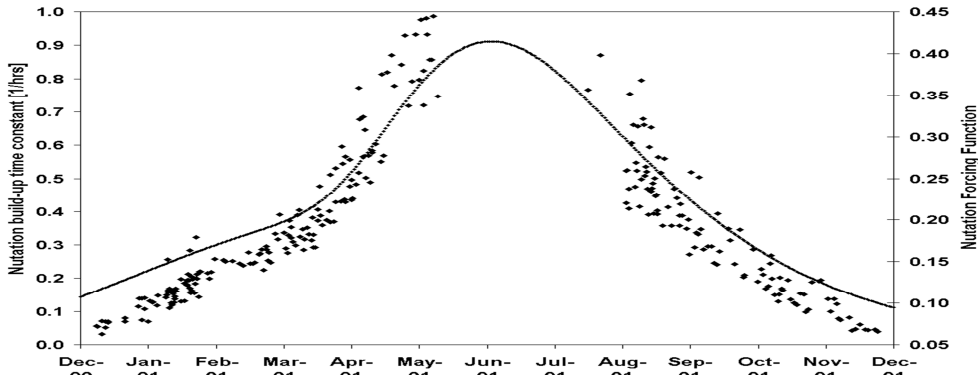


Fig-5.7 In-orbit measurements of the anomaly in the nutation, as compared to its NFF prediction by Eqn. (5.1) [Presti and Goulding, 2006].

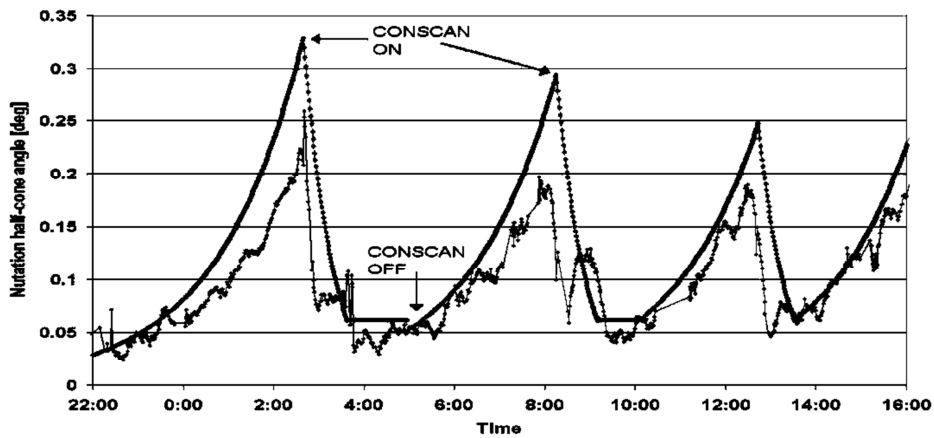


Fig-5.8 Ulysses in orbit nutation and CONSCAN operation. The solid line represents the model results and the other the in-orbit measured performance [Presti and Goulding, 2006].

5.4 Early Nutation Anomaly Investigation

The early root-cause investigation of the nutation anomaly in November 1990 comprised the damping performance of the Fokker Space NDs. Parts of the discussion (joined by the author) at ESTEC are found in [Kuiper, 1990], [Crellin, 1990] and [Hawkyard, 1990]. It was agreed that the period from 4 December to the end of 1990 S/C operations would be used to focus on “solar pumping” effects.

The ND performance was studied at the spin-rate range 5, 6 and 7 rpm since in an early stage it was suggested that an increased spin-rate, invoking a stronger ND performance, could attenuate the S/C nutation. The author started with a ND re-calibration followed by an investigation of the following ND performance related items:

1. ND design recovery and recalibration
2. Transient ND flow phenomena
3. Effective ND bandwidth
4. Antenna deployments and invoked nutation instabilities
5. In orbit analysis and the impact of increased ND performance using a S/C spin-up.

These items will be studied in the subsequent sections 5.4.1 to 5.4.5 to follow. The in orbit S/C nutation behaviour was partly derived from orbit Doppler data analysis. This will be

dealt in section 5.4.5 whilst the results there are evaluated using the impact of the studied ND properties in this section.

5.4.1 ND Design Recovery and Recalibration

Part of the early in-orbit analysis of the Ulysses AOCs behaviour during November 1990 was the recovery and validation of the original ND 1981 design data. The ND design driving requirements from the main specifications are given in Table-5.1 and the derived ND design data in Table-5.2. The required damping time constant (< 120 min) from the Ulysses ADCS subsystem specification had to be fulfilled with two out of the three NDs.

Table 5.1 *Ulysses S/C parameters and requirements to define the ND design boundary-conditions.*

Symbol	Description	Nominal value	Extreme
τ	Nutation damping time constant [min] of two NDs	< 120	120
T	Temperature [deg C]	7.5	-20 to 40
I_{zz}	Inertia figure around Z-axis [kg.m ²]	519.54	$\pm 10\%$
λ_0	Nominal inertia ratio [-]	1.7632	$\pm 10\%$
ω_z	S/C spin rate around Z-axis [rpm]	5	$\pm 10\%$
R_0	Distance in XY-COG plane to spin-axis [mm]	860	
Z_0	Position of the two dampers above COG plane [mm]	326	
θ	Initial to final nutation angle [deg]	2°	$< 0.02^\circ$

Table 5.2 *Ulysses flight model ND nominal design dimensions.*

Symbol	Description	Value
a	Liquid and vapor tube radius [mm]	8
b	Endpot radius [mm]	26.5
h	Inner endpot height [mm]	40
L_{ref}	Distance between the endpot middles [mm]	230
L	Length of liquid tube [mm]	220
$PP1$	Fuoro-Carbon damping liquid (Flutec PP1)	
τ	CAD model damping time constant of a single FM [min]	38.5
T	Operational temperatures min, nom, max [°C]	-20.0, 7.5, 40.0
P/a_0^2	Nominal model damping rate of a single FM ND with RSS fit to 7.5 °C flight conditions from PTM data [kg·s]	0.445
m	Total mass of one damper including brackets [kg]	0.56
M	S/C dry mass 333.5 kg with 33.5 kg propellant [kg]	367
m/M	Relative damper mass (liquid of three dampers)	$< 0.46\%$

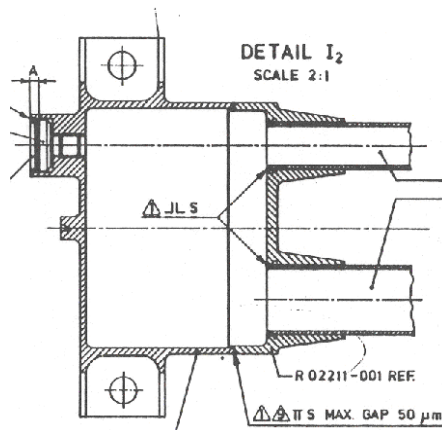


Fig-5.9 Mechanical drawing showing the end-pot details of the Ulysses ND. The upper tube is the vapor tube whilst the lower one with the largest diameter ($a = 8$ mm) is the liquid tube. The inner height of the end-pot equals h and the fill height is $h/2$ [courtesy Dutch Space].

Mechanical S/C layout

In Fig-5.9 the mechanical end-pot construction of the equatorial Ulysses ND is shown. The three NDs, integrated in their S/C platform positions, are shown in Fig-5.10. The NDs are mounted in the equatorial S/C plane at $Z_0 = 326$ mm above the Centre-Of-Mass (COM) plane at $\alpha = 69^\circ, 90^\circ$ and 111° with respect to the +X-axis. Mind the off-set from the launch to the flight COM indicated by the red arrow.

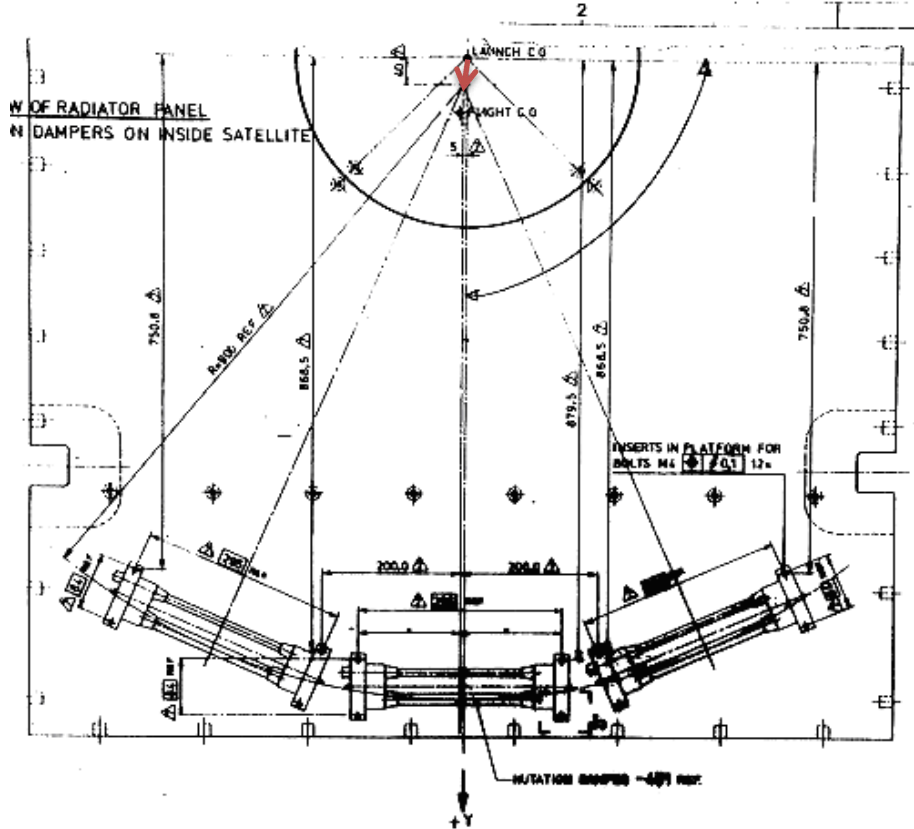


Fig-5.10 Ulysses NDs in the equatorial S/C plane at $Z_0 = +326$ mm. The NDs are located at $\alpha = 69^\circ, 90^\circ$ and 111° with respect to the +X-axis. The +Y-axis points vertically downwards [courtesy Dutch Space].

Recovery by modelling

A re-calibration of the Ulysses FM ND performance was executed in November 1990. The original 1981 PTM test results were scaled to the spin-rate 5 rpm and $T = 7.5$ °C flight conditions (square points in Fig-5.11). From a modelling point of view the following factors have to be taken into account:

- The tilt factor Eqn. (2.108)
- The liquid tube in- and exit flows given by Eqn. (2.109) whilst the value of α has to be found by a recursive cycle of PTM testing and modeling as shown in Chapter 4.
- The first order estimate $\alpha = 6.5\%$ (Boussinesq's value) was taken. The NS modeling of the tube liquid flow (see Chapter 2) at the nutation angle $\theta_{\text{nut}} = 1.2^\circ \leq 2^\circ$ requirement yields $Re \approx 1000$. Scaling this number to the required $\theta_{\text{nut}} = 0.02^\circ$ (Table 5.1) implicates an additional length of about 15 mm.

The results are shown in Fig-5.11 with three options as a stepwise approach to the best experimental Least Squares Sum (LSS) fit:

1. The original CAD design with $L = 220$ mm with +0.6% frequency off-set
2. A length upgrade from $L_{eff} = 220$ to 226 mm to tweak the ND optimum damping performance with the required S/C inertia ratio $\lambda_0 = 1.7632$.
3. RSS length fit to PTM data yields $L_{eff} = 234$ mm.

The model values agree with the given LSS fit of the PTM experimental results. Although the additional effective tube length was roughly estimated at $\theta_{nut} = 0.02^\circ$ the results and conclusions from Chapter 4 (end of section 4.6) are (post factum) applicable and validate this approach. This empirical knowledge, however, was developed after the period of the Ulysses anomaly analysis during the FY2 ND project, to be dealt with in Chapter 4. The validation of this approach, based on the latest insights from fluid mechanics theory [2012], is dealt with in Chapter 8 as an overall result of this thesis.

The test results correspond to a -0.7% off-set in frequency tuning (compared to the original CAD data) which is an acceptable (customer agreed) design tuning margin within 1%. The model results were confirmed by an independent model at ESA/ESTEC [Crellin, 1990]. The agreed re-calibration of the Ulysses ND damping performance was part of the basic assessments of the early anomaly analysis.

Dissipation rate from three dampers

The fine-tuned model damping rate is shown in Fig-5.11. In addition the MathCad® model simulation of the ND performance at the nutation angle $\theta \leq 1.143^\circ \approx 1/50$ rad and Reynolds number $Re = 1663$ yields a fluid level variation $\Delta h = \pm 12$ mm in the end-pots. Using Eqn. (2.13) the nutation X amplitude becomes

$$A_x \approx \frac{1}{50} \omega_z \lambda_x.$$

The Ulysses NDs are located at $\alpha = 69^\circ, 90^\circ$ and 111° with respect to the X-axis (see Fig-5.10). The damping time constants at the angles $\alpha = 69^\circ$ and 111° deviate only about 1 min from the value at 90° as can be seen in Fig-5.12. Therefore the error by taking $\alpha = 90^\circ$ for the three dampers is negligible.

The nutation acceleration vector in the liquid tube with the three liquid dampers mounted in the equatorial plane positions $\mathbf{X}_0 = (0, Y_0, Z_0)$ and $\mathbf{X}_{1,2} = (\pm X_0, Y_0, Z_0)$ is given by Eqn. (2.21) and the damping time constant by Eqn. (2.26).

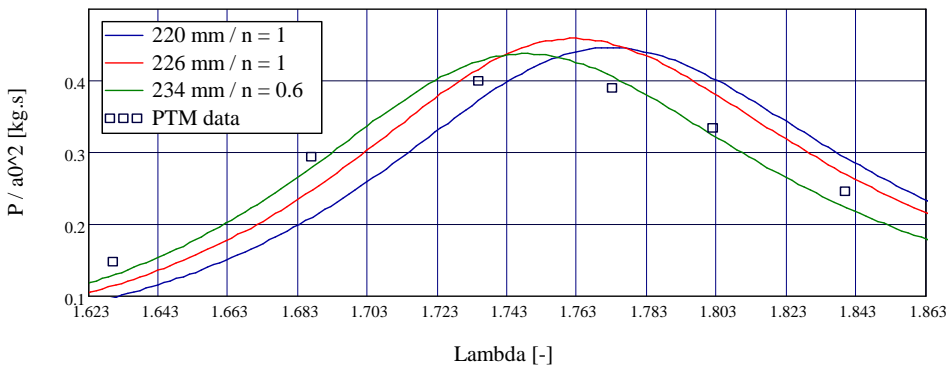


Fig-5.11 The calibrated single Ulysses FM ND damping performance at 7.5 °C (top) showing a fine-tuned design within -0.7% offset from the nominal design $\lambda_0 = 1.7632$.

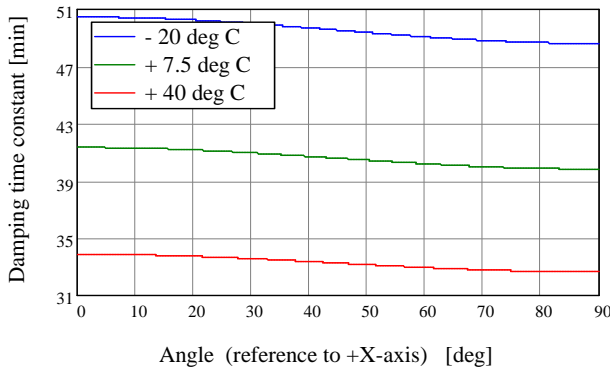


Fig-5.12 Ulysses ND time constant for one ND at variable angle. Upper curve $T = -20^\circ\text{C}$, middle (nominal operational temperature) $T = +7.5^\circ\text{C}$ and lower (max) curve $T = +40^\circ\text{C}$.

Finally, using the nutation energy dissipation Eqn. (2.24) of the asymmetrical S/C Ulysses, applicable numbers and the exponential damping time constant τ from model simulations, the simultaneous dissipation in the ND triplet is obtained and given in Table-5.3. The typical amounts of ND dissipation $< 20 \mu\text{W}$ were input to the thermo-mechanical system analysis of the Ulysses S/C axial boom behaviour by [Marrirrodiga et al, 1993].

Table-5.3 Maximum Ulysses S/C nutation dissipation rate P_{\max} at $\theta_{\text{nut}} \leq 1.143^\circ$ of the three equatorial NDs at $\alpha = 69, 90$ and 111 degree (with respect to the +X-axis) in the equatorial $Z_0 = +326$ mm plane.

Temperature [deg C]	Time constant [sec]	$P_{\max} [\mu\text{W}]$
-20	1132	-12.2
+20	903	-15.3
+40	722	-19.1

5.4.2 Transient ND Flow Phenomena

In Chapter-2 (section 2.7.1) the HP theory was derived to describe the forced and natural resonance behavior of a ND. Transients (sweep-up phenomena) were indeed observed during the Ulysses PTM tests in the 80s. These are significantly present due to the relative large FM liquid tube radius $a = 8$ mm which results in a considerable transient damping time constant according to Eqn. (2.57).

Table-5.4 shows the time constants of the nominal nutation cycle, the transient time constants for PP1, PP3 and PP9, the required damping time constant and the RSS predicted value from the previous section. The PP3 and PP9 time constants do not apply to the design but are given for comparison.

Table-5.4 Typical nutation related time constants of the Ulysses S/C.

Time constant	Type	Comment	Value
T_0	S/C nominal nutation cycle time [s]	FM time constant	15.8
τ_1	FM inrush time constant [s]	PP1	50.8
τ_3	Same [s]	PP3 (not applied)	18.9
τ_9	Same [s]	PP9 (not applied)	5.8
τ_{req}	Required S/C ND time constant [min]	Two out of three NDs	< 120.0
τ_{CAD}	Predicted damping time constant [min]	Two out of three NDs	19.3

Figure 5.13 shows the flight transients in the Ulysses FM ND during an arbitrary chosen $\theta_{\text{nut}} = 0.5^\circ$ nutation angle start-up at the S/C spin-rate range $\omega_z = 5, 6$ and 7 rpm. This range

is applicable to the required range anomaly mission required) This angle equals 25 times the required minimum 0.02° . The left-hand pictures show the PP1 liquid amplitude $s(t)$ in the liquid tube whilst the right-hand pictures shows the related changes in (absolute) kinetic energy dE_a/dt in the liquid tube in time [s].

The FM ND resonance and damped frequencies are $\omega_\theta = 0.3828$ rad/s and $\omega_p = 0.3820$ rad/s as given by Eqn. (2.58) and (2.62). In general the liquid transient does not obstruct the ND behavior but may play a role in inducing cross-couplings to oscillations of other flexible S/C parts.

Therefore the transient, its energy content and frequency has to be included in an inventory table of potential nutation anomaly invokers. Transients are clearly visible in the first minutes at an energy magnitude of about $2 \mu\text{W}$. Accounting for both the ND triplet and a $\theta_{\text{nut}} = 5^\circ$ (a factor 30) the resulting $60 \mu\text{W}$ is still a negligible amount but exceeds trifold the earlier assessed maximum dissipation.

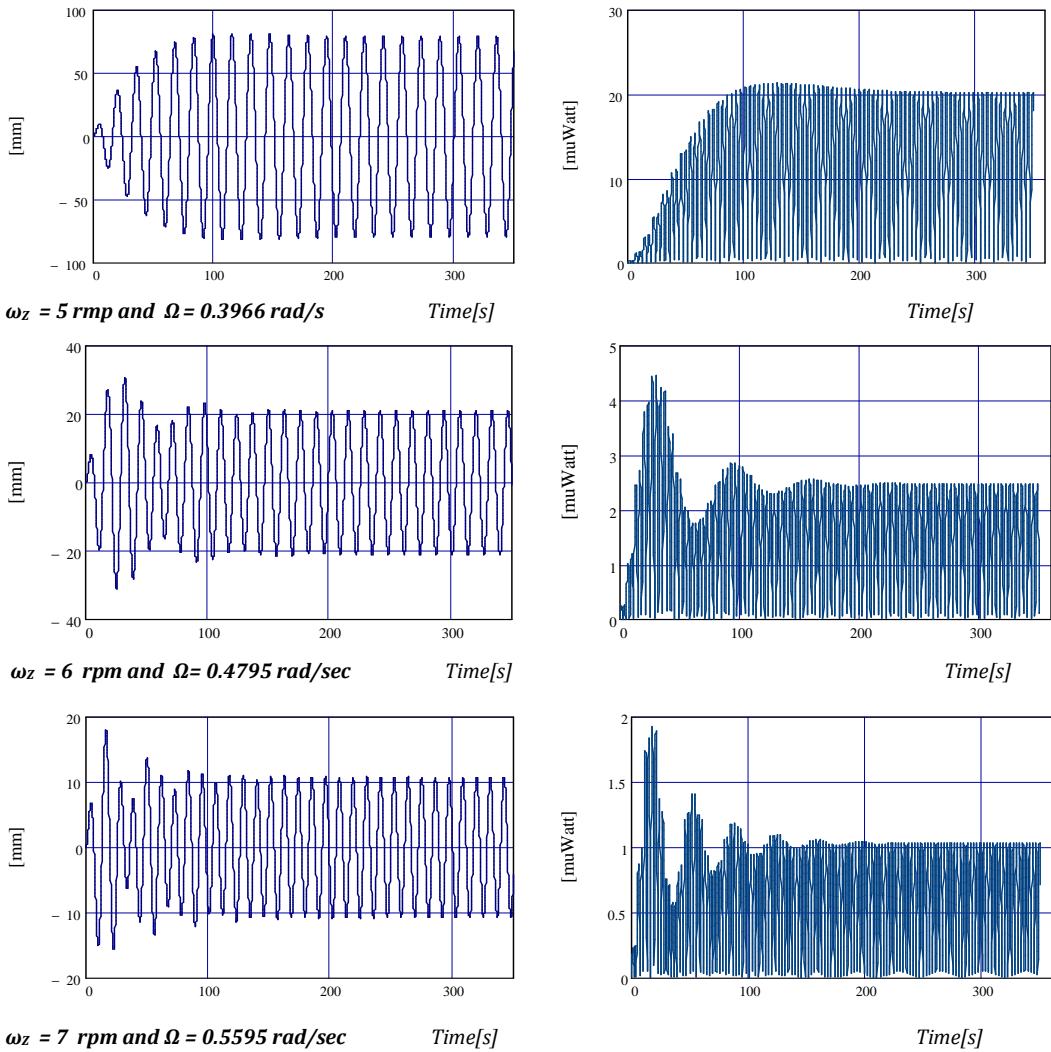


Fig-5.13 Ulysses FM ND damping liquid transients at $\omega_z = 5, 6$ and 7 rpm and $\theta_{\text{nut}} = 0.5^\circ$.

5.4.3 Enlarged ND Bandwidth

A ND transient is in principle easily suppressed by choosing a more viscous liquid. This design freedom is clearly present since Table-5.4 reveals a factor six over-compliance in the damping time constant: 19.3 min versus the required maximum of 120 min. Therefore, this comfortable margin could have been used (post factum) to enlarge the bandwidth of the damping curve. The impact of such a change is studied for completion of the ND performance analysis. Fig-5.14 shows a stepwise change of the damping fluids PP1 (top), PP3 (middle) and PP9 (bottom). In principle such a change enables a limited suppression of other (unaddressed) anomaly contributors as well. The added bandwidth is an interesting design feature regarding the Ulysses S/C nutation and was therefore studied *post factum*. Looking at the FWHM bandwidth, the resonance peak position and the liquid properties it is concluded at the operational temperature $T = 7.5^\circ\text{C}$ that:

1. PP3 yields 100% bandwidth gain, 60% acceptable damping performance loss and 9% increase in liquid mass. The kinematic viscosity and density of PP2 and PP3 are comparable and therefore the same holds for PP2
2. Applying PP9 serves no purpose. The strong decrease in damping performance is accompanied by a highly dispersive temperature tuning.

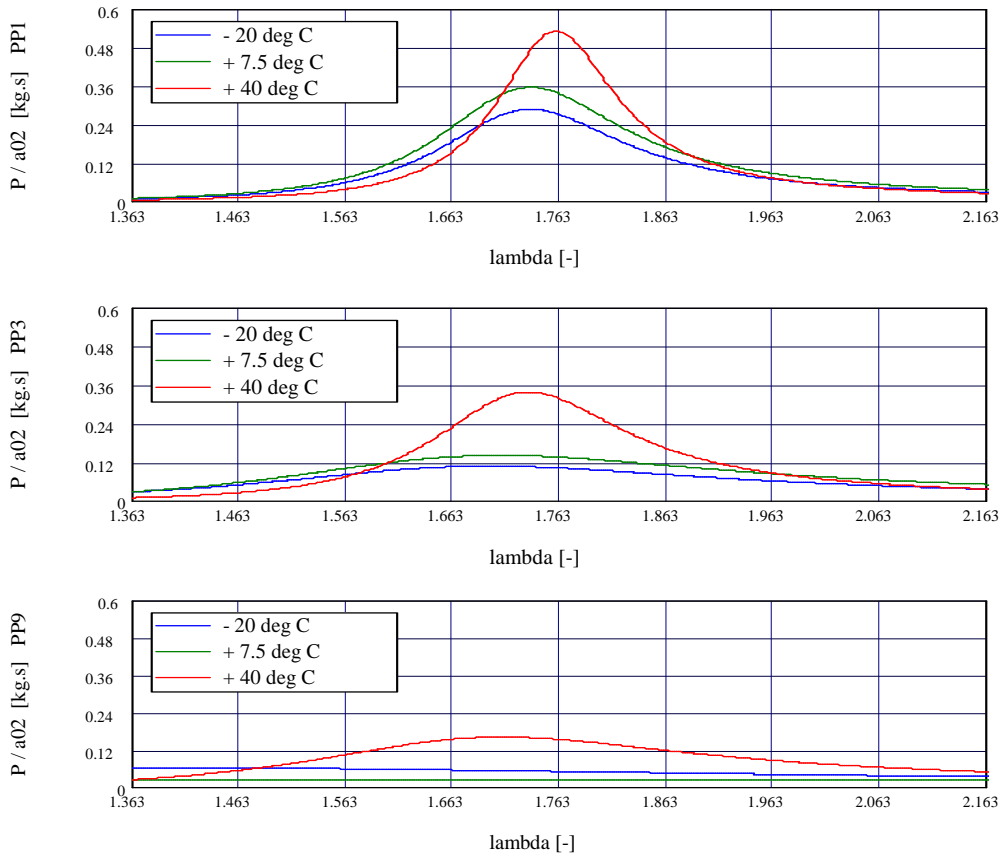


Fig-5.14 Damping liquid change - PP1 (top) to PP3 (middle) or PP9 (bottom) - as a model study (post factum) in a single Ulysses ND. All curves refer to the calibrated case i.e. the green curve in Fig-5.11.

5.4.4 Antenna Deployments and Invoked Nutation Instabilities

This section deals with a survey of the effects of deployments on the varying nutation as part of the anomaly inventory. In Table 5.4 the mass and inertia data during all successive deployment phase are given. From these data the Ulysses S/C normalized inertia values λ_x , λ_y and λ_o are determined and shown in Fig-5.15.

The design driving case is given in the first column of the Principal Moments of Inertia in Table 5.5. The last column contains the ESTEC case dated 29-11-1990. This refers to an additional requested nutation analysis case during the early in-orbit nutation anomaly analysis in November 1990.

The crucial last axial boom deployment phase is given by the stowed (Case 5) to deployed (Case 6) transition. The resulting nutation instability can be analyzed by exploring Eqn. (2.12) which defines the nutation angle as the angle between the nominal spin Z-axis and the angular momentum vector. Its approximation for a symmetrical S/C is given by Eqn. (2.13). The elaboration of the cycle average after normalization to the nutation angle θ_0 is given by

$$\frac{\theta(t)}{\theta_0} = \frac{\Omega}{2\pi} \int_0^{2\pi/\Omega} dt \sqrt{1 + \frac{\lambda_x - \lambda_y}{\lambda_y - 1} \cos^2 \Omega t} \quad \text{with} \quad \theta_0 = \frac{A_x}{\omega_z \lambda_x} \quad (5.2)$$

The relative nutation amplitude ratio A_y/A_x is given by Eqn. (2.8). Even for the highly asymmetric Ulysses configuration Eqn. (2.13) is valid. This is made visible with use of Eqn. (5.2) in Fig-5.16 where the two extreme inertia cases 5 and 6 from Table-5.5 and 5.6 are shown.

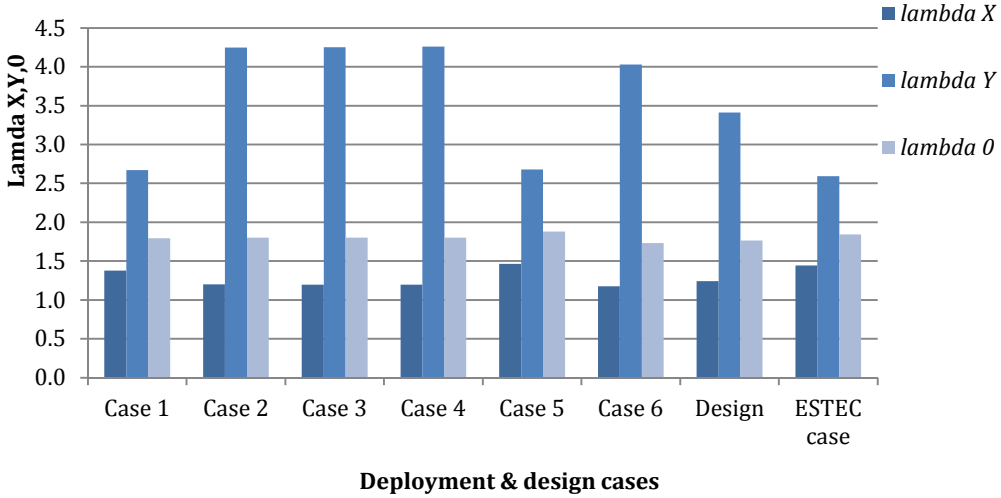


Fig-5.15 The Ulysses S/C relative inertia values λ_x , λ_y and λ_o during its successive deployment phases. The boundary conditions for the ND design (Design) were defined by the average over the cases 1-6.

Table-5.5 The Ulysses I_{xx} , I_{yy} and I_{zz} inertia and mass data during diverse deployment phases The boundary conditions for the ND design are given by the BOL to EOL cases 1-6 given below. The ESTEC case #7 (29-11-1990) refers to an extra requested case for analysis during the early in-orbit anomaly [courtesy Dutch Space]. The most pronounced feature (bold indicated) is the change in the value of the moment of inertia when the axial boom is deployed (case 6 versus case 5).

Project Ulysses derived from Dornier GmbH data (dated 30-07-1990)								
	Case 1	Case 2	Case 3	Case 4	Case 5	Case 6	Case 7	
Cover	Closed	Closed	Open	Open	Open	Open		
Radial Boom	Stowed	Deployed	Deployed	Deployed	Deployed	Deployed		
Axial Boom	Stowed	Stowed	Stowed	Stowed	Stowed	Deployed		
Wire Booms	Stowed	Stowed	Stowed	Stowed	Deployed	Stowed		
Propellant left	33.49 kg	33.49 kg	33.49 kg	11.20 kg	11.20 kg	11.20 kg		
S/C mass incl. 4.485 kg for balance								
	366.67	366.67	366.54	344.24	344.24	344.24		
COG of S/C [m]								
X	0.0000	0.0105	0.0110	0.0117	0.0117	0.0117		
Y	0.0000	0.0690	0.0733	0.0733	0.0733	0.0733		
Z	0.4335	0.4335	0.4340	0.4340	0.4340	0.4319		
Principal Moments of Inertia [kg·m ²]								
	Design case	Case 1	Case 2	Case 3	Case 4	Case 5	Case 6	Case 7
I _{xx}	418.48	215.59	365.89	365.89	365.44	365.71	371.95	372.00
I _{yy}	152.26	113.22	103.25	103.07	102.79	199.61	108.63	207.00
I _{zz}	519.54	302.22	438.56	438.40	437.83	534.98	437.83	537.00
λ _x	1.2415	1.3763	1.1986	1.1982	1.1981	1.4629	1.1771	1.4435
λ _y	3.4122	2.6693	4.2476	4.2534	4.2595	2.6801	4.0305	2.5942
λ _θ	1.7632	1.7926	1.8031	1.8029	1.8035	1.8818	1.7326	1.8409
Direction of Principal Axes [deg]								
A11	1.08148	02.3966	02.4025	02.3995	03.8002	02.3995		
A12	91.0814	92.3966	92.4020	92.3991	93.8002	92.3990		
A13	90.0000	89.9861	89.9494	89.9525	89.9794	89.9525		
A21	88.1186	87.6034	87.5980	87.6009	86.1998	87.6010		
A22	01.0814	02.3966	02.4020	02.3991	03.8002	02.3991		
A23	90.0000	89.9976	89.9974	90.0033	90.0030	90.0032		
A31	90.0000	90.0140	90.0506	90.0473	90.0204	90.0474		
A32	90.0000	90.0018	90.0005	89.9948	89.9956	89.9948		
A33	00.0000	0.01410	0.05060	0.04760	0.02080	0.04760		
Nutation to Spin Frequency Ratio (NSFR) [-]								
	0.7632	0.7926	0.8031	0.8029	0.8035	0.8819	0.7326	

Table-5.6 Nutation parameters for the stowed and deployed axial boom phases.

	λ [-]	NSFR ¹ [-]	Ω [rad/s]	T [s]	T _θ [s]	A _y /A _x [-]	$\bar{\theta}/\theta_{max}$ [-]
Case 5 Axial boom stowed	1.8818	0.8818	0.462	13.608	6.804	0.962	0.781
Case 6 Axial boom deployed	1.7326	0.7326	0.384	16.379	8.189	0.828	0.680

¹Nutation to Spin Frequency Ratio (NSFR) [-]

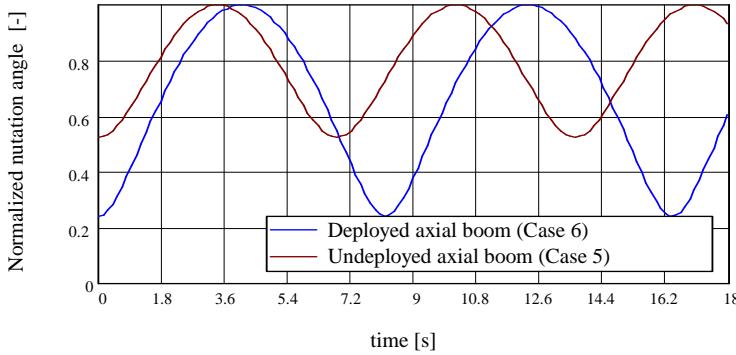


Fig-5.16 Nutation transient modeling of the Ulysses S/C by axial boom deployment case 5 to 6.

5.4.5 In-orbit S/C Data Analysis

In the following section the deployed axial boom (case-6) is regarded at the start of the anomaly. The primary sources are [Crellin, 1990], [Hawkyard, 1990] and [Kuiper, 1990]. The nutation frequency is modified by the inertia ratio (case-5 to 7) or a spin-rate change. The inertia ratio change during the axial boom deployment yields a nutation rate change

$$\frac{\Delta\Omega}{\Omega} = \frac{\Delta\lambda}{\lambda-1} + \frac{\Delta\omega_z}{\omega_z}. \quad (5.3)$$

At fixed spin-rate this change equals -8% whilst at an AOCS spin-rate change from 5 to 7 rpm 40% is added. This was typically the spin-rate try-out range considered in the early anomaly study. Fig-5.17 shows the performance of a single Ulysses FM ND at these spin-rates and operational temperature $T_0 = 7.5$ °C. On basis of the data gathered in Table-5.5 and 5.6, the nominal inertia ratio $\lambda_0 = 1.8819$ before axial boom deployment and $\lambda_0 = 1.7326$ right after are taken into account. The observed Ulysses nutation frequency after deployment, however, was consequently higher than the predicted theoretical values. This was concluded from the results of the Doppler frequency analysis, in the $\omega_z = 0.524$ rad/s (5 rpm) vicinity, as illustrated in Fig-5.18. The observed $\lambda_0 = 1.7453$, after axial boom deployment, is obtained by a LSS fit and consequently the difference with the Case-5 prediction value equals $\Delta\lambda = 0.127$.

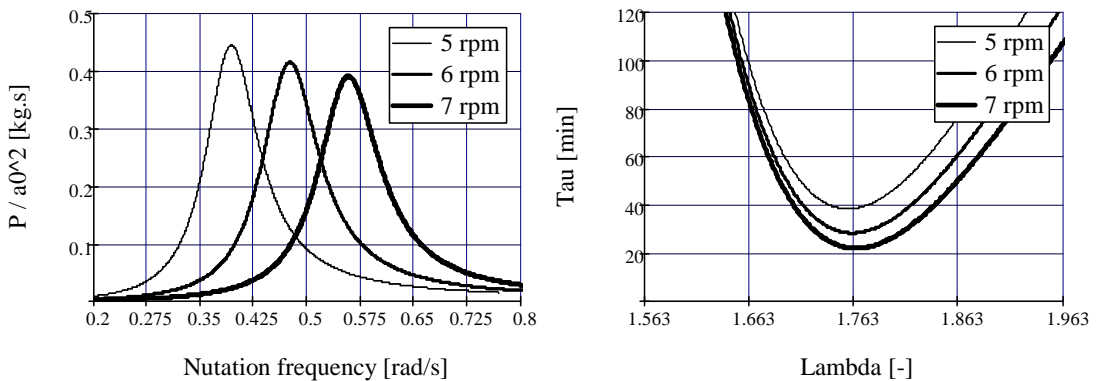


Fig-5.17 Damping of a single Ulysses ND at spin-rates 5, 6 and 7 rpm with $T_0 = 7.5$ °C. The left figure shows the damping performance and the right one the damping time constant.

In December 1990 it became clear that the difference was caused by the dead space at the root of the axial boom. This was a result of the Ulysses S/C engineering model survey and mechanical analysis.

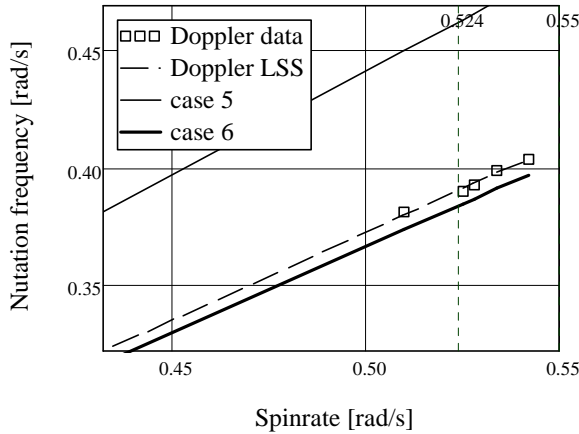


Fig-5.18 In-orbit data for the Ulysses S/C nutation rate derived from Doppler data (squares) after deployment of the axial boom. The Ulysses S/C nutation rate in the $\omega_z = 5$ rpm (0.524 rad/sec) spin-rate vicinity is regarded. Comparison with modeling results shows: The theory predicts the straight lines at $\lambda = 1.8819$ (case 5) and $\lambda = 1.7326$ (case 6) whilst LSS on Doppler Data delivers $\lambda = 1.7453$. The marks are derived from S/C Doppler data (squares) after axial boom deployment at varying S/C spin-rate after [Crellin 1990].

From the curves in Fig-5.17 the maximum damping rates were derived. These results, obtained from a model calibration to the PTM values in Fig-5.11, are found in column two of Table-5.7. In addition Eqn. (2.26) shows that the single ND time constant can be rewritten and simplified into

$$\tau = \frac{k}{\omega_z^2} \left(\frac{P}{a_0^2} \right)^{-1}.$$

Analysis showed that the Ω dependence in the range 5 to 7 rpm is well approximated by $\Omega^{-1.7}$ as shown in Table-5.7 with single ND time constant $\tau_5 = 38.5$ min at 5 rpm.

Table-5.7 Modeling the nutation trend of the Ulysses S/C at increasing spin-rate.

ω_z [rpm]	P/a_0^2 [kg.s]	τ / τ_5	Trend $\sim \Omega^{-1.7}$
5.0	0.445	1	1
6.0	0.415	0.734	0.733
7.0	0.391	0.570	0.564

This result was compared to the thermal pumping effect (driven by the asymmetric solar heating of the axial boom) which is proportional to the spin rate according to [Marrirrodiga et al, 1993] and [Hoffman, 2007]. It was concluded that the net effect of a spin-rate increase (as a cure) in the order $\Omega^{-0.7}$ is very small and this was indeed observed from the flight data as well. The conclusion by [Crellin, 1990] was that an increase of the S/C spin-rate could only be one of the smaller means to reduce the nutation from 5 to 1 degree minimum nutation required for proper X-band operation.

During December 1990 S/C operations were conducted to categorize the solar pumping effects. Fokker Space (the author of this thesis) only played a minor role in the whole anomaly analysis. On-ground measurements and operations using the S/C engineering model helped to study and identify the artefacts of the axial boom behaviour. The results

from the space Doppler frequency analysis in the X and S-band were not conclusive for the existence of axial boom-vibration modes and stiffness issues related to the nutation anomaly. A spin-up could help in identifying the S/C system characteristics and to be conclusive on the cause of the nutation anomaly. Therefore a range 5.0 (step 0.1) to 5.5 rpm with caution was proposed allowing an emergency spin-down command. Ground engineering model data and modal analysis indicated that a spin-mode of 5.4 rpm should be avoided since the first two axial boom modes are then exact multiples of this spin-frequency. In addition of other effects able to reduce the nutation oscillation to less than 3.0 degree, a test of the damping effect by use of the CONSCAN system in a closed loop was considered [Hawkyard, 1990]. This approach finally made the anomaly fully controllable as already explained at the start of this Chapter.

5.5 Conclusions

A moving solar shadow (“solar pumping”) on the axial boom combined with mechanical artefacts, can act as an effective “finger flick” on the virtual rotation axis of a spinning S/C. This effect can be enough to create a considerable amount of nutation as was already known since the 1960s [NASA, 1969]. Unfortunately this was again observed 21 years later, during the early flight analysis of the anomalous Ulysses S/C AOCS behaviour in November 1990. The ND part of the Ulysses anomaly investigation delivered the following insights.

ND performance justification

A source [NASA-1, 2012] suggested that the build-up of the Ulysses nutation-like behaviour was due to the combination of solar heating and under-performance of the NDs. Four hard evidential arguments prove the opposite and justify the original Ulysses ND design:

- The detailed analysis of flight data and the simulation of the ND performance (including its artefacts) as given in this chapter exclude under-performance
- The ND design complies with the specification to damp nutation solely within its limited bandwidth. Table-5.3 even shows a factor six over-compliance i.e. $38.5/2 = 19.3$ versus the specified 120 min
- The conclusions from ND verification and validation exploration (Chapter-3) prove, especially at low spin-rates like the 5 rpm of Ulysses, that model and experiment comply well
- The Ulysses S/C AOCS operated normally for about a month (before axial boom deployment) with proper passive ND operation [Hoffman, 2007].

Lessons learned anno 2012

The thermal mathematical analysis of the Ulysses flexible axial boom behaviour and its impact on the S/C AOCS is nowadays well understood and dealt with in articles like [Marrirrodrga et al, 1993] and [Gulick and Thornton, 1995]. The lessons learned during four decades are nowadays recognized in the system design of e.g. the THEMIS S/C and its complex multiple boom antenna constellation using multi-body dynamics simulation [Auslander et al, 2008]. This mission will be part of the extensive Cluster damper design trade-offs as described in Chapter 7.

Innovation

The given reflections led the author to the idea in December 1990 to apply the Cluster S/C NDs for the attenuation of the coupled wire boom antenna oscillation modes as well. The design principle proposed by fax to the prime BAe/Dornier and ESA [Kuiper, 1990], was eventually accepted by ESA to be used in the Cluster mission. The phase-A design and its successful implementation is dealt with in the following Chapter 7.

6 Spacecraft with Extended Wire-Booms: A New Challenge

6.1 *Introduction*

The material of the previous chapters did create the gateway to the design of a passive multi-mode viscous damper to be incorporated in the Cluster ADCS. The Cluster S/C is shown in Fig-6.1. After an introduction of the Cluster mission in section 6.2 and the Bepi-Colombo, RBSP, DICE, THEMIS and FAST missions in section 6.3, the design features of wire boom sensors are dealt with in the sections 6.4 to 6.7. The remainder of the chapter will confine towards the Cluster ADCS. In addition the system engineering arguments are explored to support a S/C design with multiple wire boom antennas. Since the launch of the Cluster S/C this field of design and engineering became mature. On basis of the gathered insights the additional design drivers of the Cluster liquid dampers will be dealt.

The design of the Cluster wobble dampers (the ND being a dedicated case) provides the reduction of both nutation and wire boom antenna oscillation modes. The S/C wire boom dynamics relates to the orbital motion, self-spinning, coupled boom oscillations, boom vibrations, translation, precession and nutation about the equilibrium position. Boom vibrations are insignificant compared to the pendulum type coupled hub-boom oscillations. Solar radiation-induced oscillations and bending of wire booms are insignificant for thin wires [Lai and Bhavnani, 1975]. The stability problems addressed so far (i.e. the Ulysses case) refer to the impact of the relatively thick and stiff axial booms.

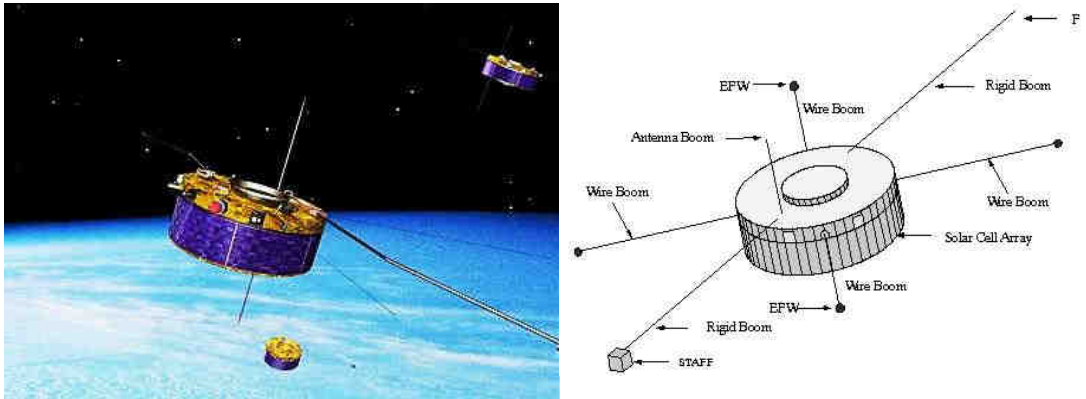


Fig-6.1 The four Cluster S/C flying in formation between 19000 and 119000 km above the Earth. The individual S/C is equipped with a set of four 41-meter booms with a small instrument at each end. The other indicated instruments are the Field Gate Magnetometer (FGM), the Electric Field and Wave sensor (EFW) and the Spatio Temporal Analysis Field Fluctuation (STAFF) three-axis search coil magnetometer to measure magnetic fluctuations [ESA, 2012].

The Cluster S/C antenna morphology, shown in Fig-6.1, has some similarity with the Ulysses S/C configuration. As a result the lessons learned from the Ulysses in-flight nutation anomaly induced the innovative design for the Cluster NDs. The author, being the ND consultant of UCN Aerospace, initiated the idea to combine the damping of nutation and antenna oscillation modes by dedicated liquid dampers. It popped up in the mind, on the 12th of December 1990, flying back from Bristol after the presentation and discussions of the phase-A Cluster ND proposal to the prime British Aerospace (BAe). After some back-of-the-envelope calculations and analysis based on the results from [Lai and Bhavnani, 1975] the principle proved to be healthy. The idea was proposed by fax [Kuiper, 1990] to the primes and ESA. The design and its current status will be presented in this chapter, 20 years after its launch. At first ESA mentioned the idea “an improper use of NDs” but eventually it was accepted and incorporated in the Cluster S/C ADCS design. The extended ND principle, however, had to be explored in terms of S/C stability constraints, deployment scenarios and refinements of the air-bearing tests. It is a serious scientific restriction that the material is not traceable in the publication domains nowadays until (this PhD thesis in) 2012 or otherwise accessible due to non-disclosure arguments as given by [Kermans, 2009] and [de Kraker, 2009]. Nevertheless the enlarged scope of the ND performance was fully explored and analyzed being the main topic of this chapter.

6.2 Cluster Mission

The ESA Cluster mission consists of four (named Salsa, Samba, Tango and Rumba) identical S/C spinning at 15 rpm that initially flew in a tetrahedral formation in an elliptical polar orbit with apogee at 119 000 km and perigee at 19 000 km altitude. The S/C configuration is shown Fig-6.1. With time, the orbit has evolved, and the perigee was April 2011 around 3 000 km above Earth. To benefit from the S/C formation, the distance between the satellites has to be closely monitored. The most of the S/C mass consists of propellant for maneuvering. A mass of 600 kilograms (half the launch weight) of each Cluster S/C was taken up by propellant required for the complicated maneuvers employed to position the spacecraft into the correct orbit. The mission studies the interaction between the solar wind and the Earth’s magnetosphere in 3D. There are 12 instruments on every spacecraft and one of them is the Electric Field and Wave instrument (EFW), which was built by a

consortium led by The Swedish Institute of Space Physics. Fokker (Dutch) Space was responsible for the thermal subsystem and the early phase-A study of the NDs.

Two launches took place on 16 July and 19 August 2000 by Russian Soyuz rockets at Baikonur, Kazakhstan. The two pairs Cluster S/C were initially placed in an elliptical orbit whose height varied from 200 to 18000 km above the Earth. The two S/C of each launch were then released one after the other and used their on-board propulsion systems to reach the final operational orbit. The first Cluster S/C were destroyed when the Ariane-5 rocket exploded during its maiden launch on 4 June 1996. Three new Cluster S/C had to be built while the fourth was constructed out of spare parts. These were launched four years later. Cluster was the first space project ever to have built a true series production. After the second launch on 9 August 2000 and proper injection of the pairs of S/C, the Cluster mission was back on track. Due to its success the mission has been extended several times and at the moment it is planned to continue until the end of 2014. This was possible since the orbit injections were at once successful so enough propellant was left [ESA, 2012].

Using identical instruments simultaneously, three-dimensional and time-varying phenomena can be studied. The four-point, relatively closely spaced measurements with identical instruments have already yielded unparalleled views of space plasma processes in key regions of the magnetosphere and in the near-Earth, upstream solar wind. On 24 January 2001, the formation flew at an approximate altitude of 105,000 km, in tetrahedron formation. Each S/C was separated from the others by a distance of about 600 km. At that time the formation encountered a shock wave that kept breaking and reforming and were predicted only in theory 20 years earlier.

Each of the S/C is equipped with a set of four 44 m Electric Field Wave (EFW) instrument booms with a small Electro-Magnetic (EM) information-collecting instrument at each end. The mission critical booms, looking like long tethered wires, are designed to gather information about the Earth magnetosphere. The EFW booms were allowed to creep out of their individual S/C at a snail pace of 1 cm/s. The configuration of four booms per S/C is preferred because it meant the best resolution and scientific data acquisition possible. Each S/C only needs one pair to successfully collect the magnetosphere data [ESA, 2012].

6.3 Wire Boom Sensor Designs

A number of prominent magneto-spheric planetary missions equipped with EFW instruments will be briefly dealt with to show the high compliance in wire boom design based on a common heritage. On basis of the acquired knowledge the study will confine to the design of the passive liquid damper subsystem of the Cluster ADCS in the sections to follow.

A planetary magnetosphere can be observed and analyzed by using dedicated sensors. These are usually spinning S/C equipped with long wire boom pairs to enable measurements and successive validation of ambient electro-magnetic field models. The extended wire boom is flexible with a typical mass of 0.15 kg (Cluster 44 m boom length) carrying a mass of about 0.25 kg at the tip end. The Spin Plane Boom (SPB) single wire release mechanism and the wire boom assembly of the THEMIS S/C are shown in Fig-6.2. A detailed description of the comparable THEMIS and FAST axial and radial wire boom systems is given by [Auslander et al., 2008] and [Pankow et al., 2001]. The active sensor part is composed of an aluminum sphere and a 3 m stainless steel fine wire with diameter $d = 0.25$ mm attached to the pre-amplifier inside the usher.

The wire pair deployment is controlled by ground operations. The S/C hub spin in the range 5 to 20 rpm enables the wire boom to extend, obtain a stable orientation and to support accurate measurements.

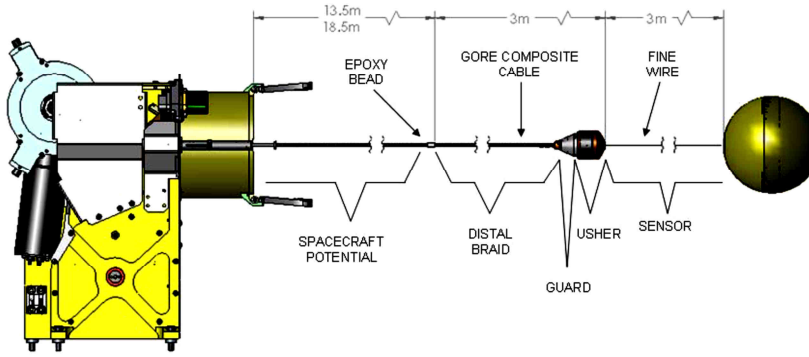


Fig-6.2 Spin Plane Boom (SPB) release mechanism of the THEMIS S/C [Pankow et al., 2001].

In the sensor booms an electric field is induced as a result of the S/C rotation and its movement through the ambient electro-magnetic field. The principle of the double probe direct potential measurement is shown In Fig-6.3 for two wire pairs in the Viking, Cluster and Polar mission [Vogt, 2007]. The induced electrical potential difference $\Delta V = V_1 - V_2$ between the end tip sensors of a deployed boom pair at distance d follows from the Maxwell equation [Jackson, 1998]

$$\frac{V_1 - V_2}{|d|} = (\mathbf{E} + \mathbf{v} \times \mathbf{B}) \cdot \mathbf{d} \quad (6.1)$$

with V_1 and V_2 the voltage (potential) at the end tip sensor 1 and 2, \mathbf{v} the orbital velocity of the sensor relative to the planetary (Earth) ambient magnetic field vector \mathbf{B} and the planetary (Earth) ambient electric field vector \mathbf{E} whilst $\mathbf{d} = \mathbf{r}_1 - \mathbf{r}_2$ the connection vector between the probes at the end-tips.

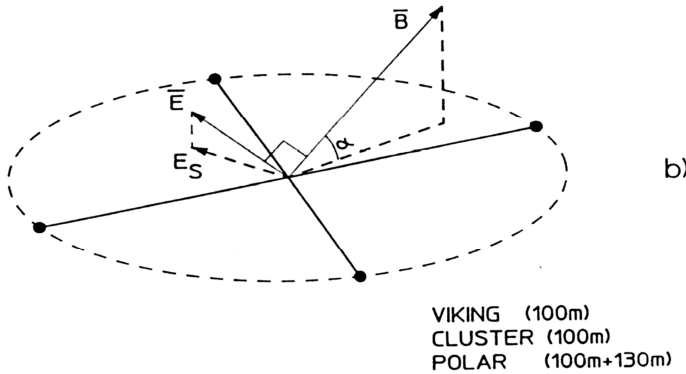


Fig-6.3 Double probe E-field measurement by a wire boom antenna pair on a spinning hub S/C (Viking, Cluster and Polar) with rough order of magnitude of the tip-to-tip wire booms distance [Vogt, 2007].

A number of key magneto-spheric missions going backwards in time will now be dealt with. The first one out of the series THEMIS, FAST, Bepi-Colombo, DICE, Radiation Belt Storm Probe (RBSP), Cluster, is the Bepi-Colombo Mercury mission whilst the other five are Earth missions.

6.4 Mission Data

Bepi-Colombo [launch 2015]

The Bepi-Colombo Cornerstone to Mercury is the next milestone of the ESA Horizon 2000+ scientific program plan devoted to the study of the planets of the Solar System. The instruments to study the interplanetary fields and particles are incorporated in the Mercury Magneto-spheric Orbiter (MMO). The MMO, a small sub-satellite shown in Fig-6.4, is attached to the sidewall of the Mercury Planetary Orbiter S/C and will be ejected once arrived at Mercury. Its radio and plasma wave instrument (RPW) measures three magnetic and one electric components of the wave field. It is composed of three search coils mounted on a boom and one 60-m long dipole antenna. The antenna deployment as well as the azimuthal scan of the sensors is facilitated by the MMO spin-stabilisation. The time characteristics of the centrifugal deployment are the deployment time of less than 75 min and speed of less than 10 mm/s. The same speed applies for the Cluster wire boom deployment.

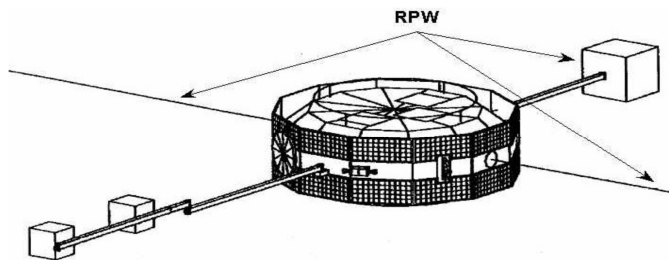


Fig-6.4 15 RPM Mercury Magneto-spheric Orbiter (MMO) and its radio and plasma wave instrument (RPW) with only two of the four 15 m wire boom antennas made visible [González Lodoso et al., 2001].

The primary structure of the MMO is an octagonal prism, measuring 1.8 m between opposing faces and with an overall height of 0.9 m. Its total mass will be around 275 kg with 45 kg accounting for the instruments. A circular central core carries the separation interface at one end and supports the pylon for the high-gain antenna at the other. The MMO will be spin stabilized, with a rotation rate of 15 RPM and a spin-axis almost perpendicular to the orbital plane of Mercury around the Sun. This choice of spin axis ensures that the top and bottom of the spacecraft are never Sun-pointed, and enables Earth-pointing of the high-gain antenna with only one degree of freedom mechanism. The centrifugal effect of the spin will enable the deployment of four 15-metre-long wire antennas for electric field and radio wave measurements. The orbiter will also be equipped with two five-metre-long masts to provide a suitable environment for magnetic field measurements, clear of the influence of the spacecraft structure and electrical equipment. The MMO will travel around Mercury in a polar orbit with a period of approximately 9.3 hours, a perihermion (periapsis) of 400 km and an apohermion (apoapsis) of 11 824 km [González Lodoso et al., 2001].

RBSP [launch August 2012]

The two Radiation Belt Storm Probe (RBSP) S/C spin-stabilized at 5 RPM, shown in Fig-6.5, will operate entirely within the radiation belts throughout their mission. The probes carry a number of instruments (suites) to support five experiments that will address the mission's science objectives. The John-Hopkins Applied Physics Laboratory (JPL) will build and operate the twin RBSP spacecraft for NASA's Living With a Star program. The RBSP Electric Field and Waves Suite (EFW) will study the electric fields in near-Earth space that energize radiation particles and modify the structure of the inner magnetosphere. The EFW investigation consists of a set of four spin-plane electric field (E-field) antennae and a set of

two spin-axis stacer (tubular, extendable) booms. The RBSP S/C will have nearly identical eccentric orbits covering the entire radiation belt region whilst the two S/C lap each other several times over the course of the mission. The RBSP in situ measurements discriminate between spatial and temporal effects, and compare the effects of various proposed mechanisms for charged particle acceleration and loss. The single EFW wire boom antenna length equals 38.02 m whilst the wire pair width (tip-to-tip) equals 77.964 m [McGee et al., 2009].

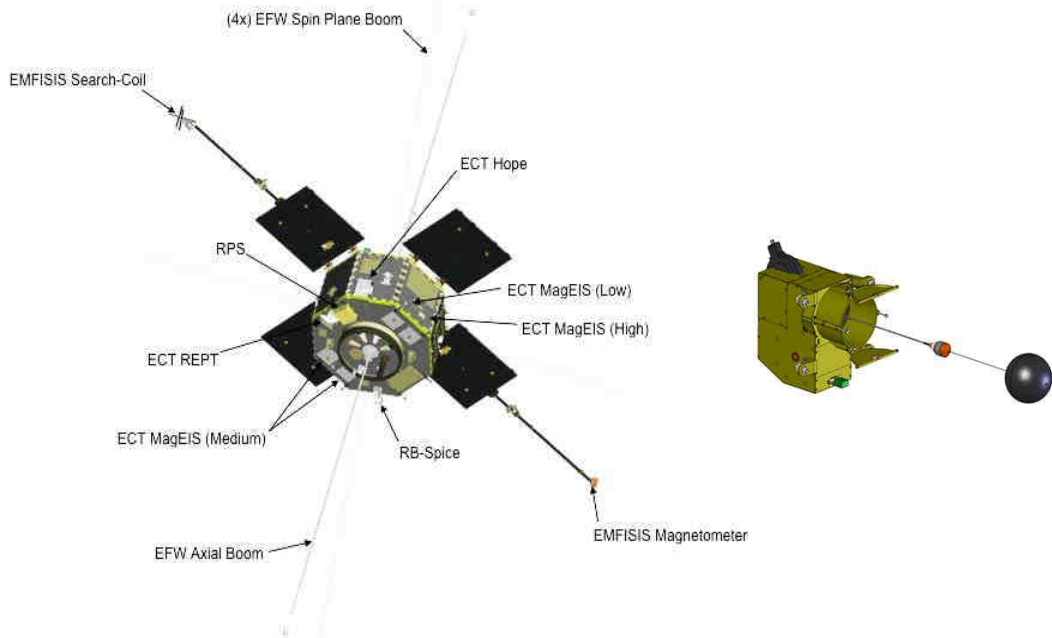


Fig-6.5 The RBSP S/C in nominal flight configuration with the EFW spin-plane, Energetic particle, Composition, and Thermal Plasma (ECT), Magnetic Electron Ion Spectrometer (MagEIS) and Electric and Magnetic Field Instrument Suite and Integrated Science (EMFISIS) instruments [McGee et al., 2009].

DICE [2011]

The Dynamic Ionospheric Cubesat Experiment (DICE), shown in Fig-6.6, was launched the 28 October 2011. The DICE was developed at the Space Dynamics Laboratory (Utah State University) and is now mapping geomagnetic Storm Enhanced Density (SED) plasma bulge and plume formations in Earth's ionosphere. The mission consists of two identical 1.5U (10 cm x 10 cm x 15 cm) CubeSats deployed simultaneously from a single P-POD (NASA's Poly Picosatellite Orbital Deployer) into the same orbit. After launch, the S/C formed a mini-constellation, one S/C trailing within 200 kilometers of the other. The two 12 RPM spinning S/C measure plasma density and electric fields to determine the how and why of variations in ionospheric plasma density that affect the performance of communications, surveillance, and navigation systems on earth and in space. Each S/C carries an electric field probe, two Langmuir probes, and science-grade magnetometer. These instruments perform co-located measurements of plasma density and the electric field to trace the formation and evolutions of SEDs. The electric field probe consists of four 10 m wire booms shown (shown shortened) at the edges at the top of the cubesats. The Langmuir probes measure in-situ ionospheric plasma densities and electric field probes to measure DC and AC electric fields.

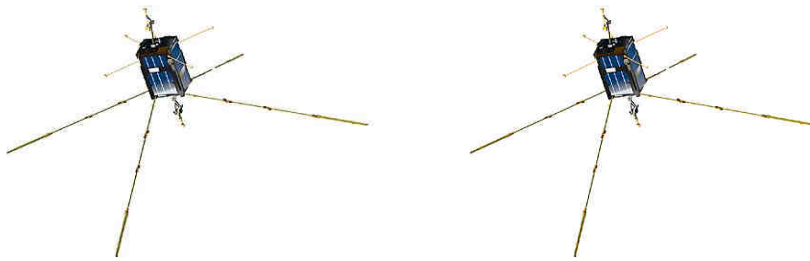


Fig-6.6 The two identical DICE spacecraft forming a mini-constellation [Stromberg, 2011].

The measurements provide accurate identification of storm-time features, such as the SED bulge and plume, together with simultaneous, co-located electric field measurements, which have previously been lacking. Over time, the satellites will separate relative to each other due to differences in the ejection velocity. The use of two identical satellites permits the de-convolution of spatial and temporal ambiguities in the observations of the ionosphere from a moving platform [Stromberg, 2011].

THEMIS [launch 2007]

The “Time History of Events and Macro-scale Interactions during Substorms” (THEMIS) microsatellite constellation is another example out of this S/C class. The 20 RPM THEMIS S/C, shown in Fig-6.7, was launched by a Delta II, 7925 heavy, on February 17, 2007. The University of California Berkeley Space Sciences Laboratory (UCBSSL) provided the S/C appendages. The S/C systems engineering comprised the design, development, testing and orbital deployment of the following radial and axial boom systems: the 1 and 2 m carbon fibre composite magnetometer booms, the 40 and 50 m tip to tip orthogonal spin-plane wire boom pairs and the 6.3 m dipole stiff axial booms. The probe dry mass is 77 kg with a wet mass of 126 kg and comprises 49 kg propellant. The spin-axis orientation knowledge is less than 1° at a control of less than 3° and spin phase knowledge of less than 0.1° with ground based attitude determination [Auslander et al., 2008].

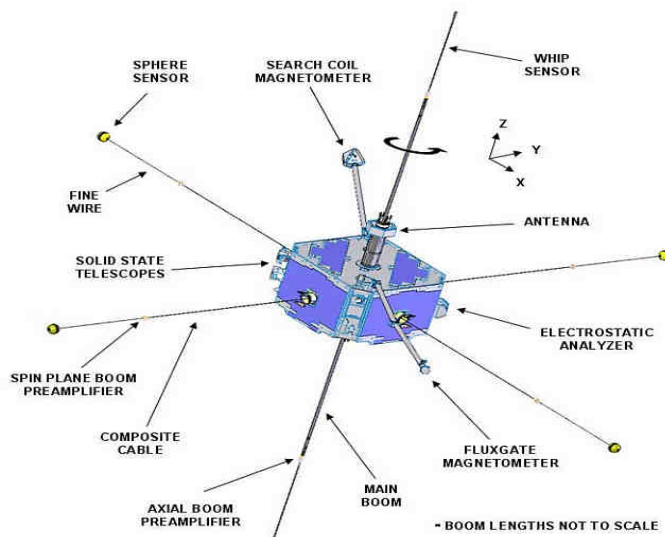


Fig-6.7 The THEMIS S/C in orbit with deployed booms configuration [Auslander et al., 2008].

FAST [launch 1996]

The NASA Fast Auroral SnapshoT (FAST) S/C, shown in Fig-6.8, studies the Earth magnetosphere. The 12 RPM spin stabilized spacecraft was designed to carry out in situ measurements of acceleration physics and related plasma processes associated with the Earth's aurora.

FAST was launched on August 21, 1996 into a high inclination (83°) elliptical orbit with apogee and perigee altitudes of 4175 km and 350 km, respectively. The EFW instrument was designed to deploy ten spherical sensors, two each on four 28 m long radial wire booms and one each on two axial stacers. The spheres on the wire booms are located 28 m and 23 m from the spacecraft. The axial spheres are separated by 8 m tip-to-tip. Each sphere houses a preamplifier circuit. Unfortunately, one of the wire booms did not deploy properly. However, this did not preclude gathering vector electric fields by the FAST spacecraft. Finally to get some insight in a typical ADCS system in this field, the FAST S/C is explored as dealt with by [Pfaff et al., 2001].

Attitude Control System

The Attitude Control System (ACS) provides autonomous spin and precession control following separation from the launch vehicle, to control S/C spin and precession during the normal mode operations to meet the science imposed attitude requirements, and to maintain a spin-rate and spin-axis attitude consistent with the power and thermal requirements. The FAST ACS has to maintain the S/C attitude as a simple spinner with at approximately 12 rpm. Pointing requirements are met by utilizing a complement of sensors, torquers and standard electronics. Spin-rate and spin-axis orientation are maintained using two magnetic torquer coils. Either one spinning sun sensor, one horizon crossing indicator, or the spacecraft magnetometer can be used to measure the actual spin period. In addition to the active control elements, a fluid ring damper provides passive nutation control. The ACS provides closed-loop spin-rate control. Spin-axis precession is performed open loop and is closed via ground commands. The near orbit-normal spinner uses electromagnets to keep up with the daily orbit precession and to perform sun angle avoidance maneuvers to maintain the sun angle to less than 60° , if necessary.

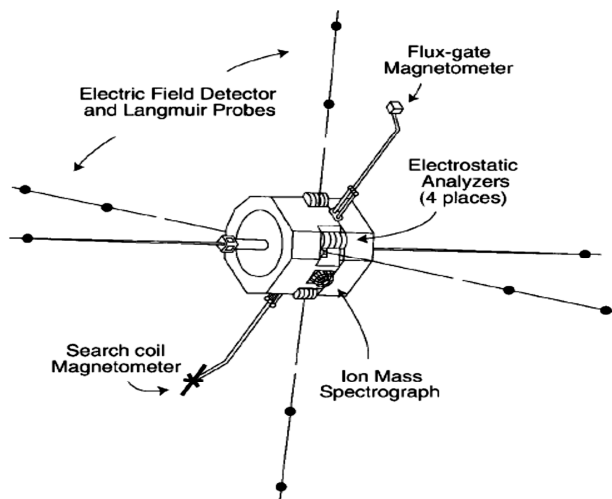


Fig-6.8 FAST S/C in nominal flight configuration (one EFW boom did not fully deploy)[Pfaff et al., 2001].

Attitude Knowledge

The FAST attitude knowledge consists of two elements: spin axis pointing and spin phase. Spin-axis pointing is verified by orbit differences between model and observed magnetic field results. The nominal accuracy using actual FAST data is typically 0.1° , although this is a factor of two worse on orbits around torque coil operations. The spin-phase error is much less than 0.1° in sunlight (Sun-sensor determined), but jitter of this order is present when FAST is in eclipse (where the equivalent sun-phase is determined from using nadir-phase information). There are frequent phase skips at eclipse entry and exit. Therefore, although the spin period may be reasonably accurate in eclipse, the absolute phase reconstruction can have problems.

Structure

The FAST primary structure is constructed of aluminum and includes a single deck on which the instruments and electronic boxes are mounted. Two magnetometer booms are located 180° relative to each other in the spin plane, which are stowed along the spin-axis for launch. In addition, there are two axial stacer electric field booms and four radial, equally spaced, EFW booms that are deployed after launch. Placing all of the instruments and main spacecraft components on a single deck whose plane includes the spin plane electric field wire booms and deployed magnetometer booms is an important design feature of the FAST spacecraft. Such a single plane design, together with the placement of the instruments at the furthest edges of this plane, optimizes the S/C moment of inertia such that the S/C is thus able to support the longest possible spin-axis electric field booms [Pankow et al., 2001]. The S/C structural design provides a shape optimized for power and a Moment-Of-Inertia (MOI) optimized to support the longest possible EFW booms.

6.5 Wire Boom Oscillation Modes

After the previous introduction of spinning S/C with magneto-spherical missions, the theory of passive ADCS of such S/C equipped with wire boom sensors will be dealt with. The S/C attitude sensors deliver ADCS data like the average S/C velocity but do not account for the imposed oscillations and off-sets (in-plane and out-of-plane) in the orientations of the booms. In exceptional cases unequal lengths within a pair may occur due to deployment failures or individual slow-downs. These are dealt with by [Lai and Smiddy, 1979] but are not regarded here. The same holds for the negligible effects of aerodynamics at the typical S/C altitudes of magneto-spherical missions.

The treatise of the spinning S/C dynamics (including the wire booms) by Laplace transform analysis, facilitates a straight forward solution of the linearized set of equations of motion. As a result the transient modal response analysis of the system yields principle insight into the systems dynamics and its damping properties. The large Cluster hub-to-tip mass ratio supports the negligence of hub translations (X, Y) in the analysis. On its turn the large tip-to-boom mass ratio in the range 15 - 30% yields uncoupled and coupled equations characterized by:

- **Uncoupled mode** - All booms perform in a correlated mode such that the sum of their angular momenta is zero. The individual boom angular momentum is fully uncoupled from the S/C hub.
- **Coupled mode** - All boom movements, i.e. their angular deviations $\varphi_i(t)$, are in phase with each other. In this case the hub angular momentum intermediates in the overall in-plane angular momentum coupling.

In addition this allows for a distinction of oscillation modes, i.e.

- **In-plane modes** - The in-plane system dynamics, shown in Fig-6.9, of a spinning hub with two wire-boom pairs comprises seven degrees of freedom: the S/C hub spin-rate,

two (X, Y) translations and the angular deviations $\varphi_i(t)$ of each wire boom orthogonal from its normal radial direction. In Fig-6.9 the in-plane coupled EA1 (Equatorial Asymmetric) oscillation mode is recognized as the joint coupled oscillation of all wire booms in phase with the hub oscillating in the opposite direction at 180° phase lag.

- **Out-of-plane modes** - These modes, shown in Fig-6.10, also comprise seven degrees of freedom with four non-trivial modes so the pure rotation and translation modes are excluded. The characteristic resonance frequencies are the coupled modes and the uncoupled Saddle and Jelly-Fish modes. In Fig-6.10 the two basic out-of-plane MA (Meridian Asymmetric) modes can be recognized. The first is the oscillation around the Y-axis and the other the oscillation around the X-axis. In both cases the pair of wirebooms in the normal plane is coupled to the oscillation around the Y or X hub axis. The key angles are the out-of-plane wire boom oscillation angle ψ_i and the meridian hub oscillation angle θ_M .

Most authors, e.g. [McGee et al., 2009], confine to the basic symmetrical coupled or uncoupled cases and refer to the full spectral Fourier solution of the non-linear Euler-Lagrange (EL) equations only as additional proof. In the definition of the Cluster liquid damper requirements to follow all modes refer to equal boom lengths with negligible in-plane mode coupling. The EA and MA modes are the drivers in the design of the extended Cluster ND and will be explored in more depth in the following sections.

The feasibility of the analytic solutions has to comply seamless with the recognition of engineering insights. As a consequence realistic assumptions are made like: no deployment or retraction, equal boom lengths and the validity of the harmonic linear approximation. The booms are supposed to move by wire bending at the hub anchor locations $r=R_0$ from the spin-axis. In addition the S/C dynamics analysis requires knowledge of the inertia and engineering material properties of the interacting S/C appendages.

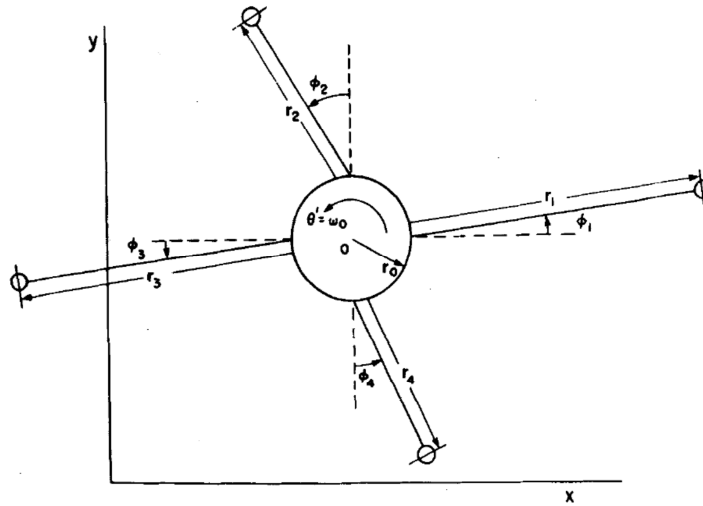


Fig-6.9 In-plane EA wire boom oscillation modes of two wire boom pairs attached to their S/C hub anchor position ($\varphi_i \doteq$ boom (i) deflection angle, $m \doteq$ effective tip-end mass, $R_i \doteq$ deployed radius at anchor radius $r=R_0$ and $\theta_E \doteq$ hub rotation angle) [Lai and Smiddy, 1979].

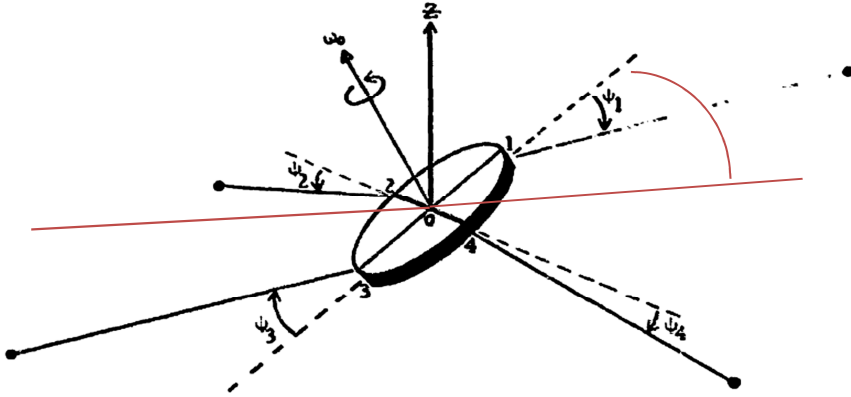


Fig-6.10 Out-of-plane wire boom geometry at its hub hinge attachment point [Lai and Bhavnani, 1975]. The added red-lined angle is the hub oscillation about the (indicated 2-4) θ_1 axis.

6.6 Stability Considerations

Radial wire booms support the spin stabilization by an increase of the S/C stability margin but on the other hand the resonant (un)coupled antenna modes oppose this. The axial booms shall be limited in length because they decrease the stability margin by the increase of the transverse moment of inertia. A disadvantage of flexible wire booms are their susceptibility to transient motions and oscillations provoked by S/C attitude control manoeuvres. The induced pendulum movements depend on the

- Wire root or hinge attachment radius from the spin-axis called exit or anchor point
- Friction (Coulomb) mechanisms at the root
- Internal damping within the boom
- Hub incorporated multi-mode liquid damping [this thesis].

The deployed wire boom plane location is preferably close to the spacecraft Z-axis Center-Of-Mass (COM). This minimizes a spin-axis tilt caused by wire boom mass moment asymmetries. The axial booms have to be rigid to avoid elastic instability [Lai and Bhavnani, 1975]. At systems engineering level a spin-axis alignment budget has to be maintained. A number of uncertainties like the deployed boom straightness and the alignment of balance fixtures influence the alignment of the spin axis with the S/C geometric axis. A linear error (uncertainty) budget is far too conservative. The random clocking of uncertainties with respect to the spin-axis leads to half the Root Sum Square (RSS) of the inertia residuals. The regular NASA requirement for the minimum S/C stability margin is $\lambda - 1 = 4\%$ with λ the inertia ratio. This value is based on uncertainties of mass moment measurements. For the THEMIS S/C the sensitivity analysis of the spin axis alignment did indicate a practical stability minimum of 8–10%. The S/C spin-axis probe stability margin equals 16–25% depending on the remaining propellant whilst the Cluster value is 95% (phase-A) down to 75% (phase-B) and the RBSP value 40%. The THEMIS S/C regular in-orbit deployment sequence was magnetometer booms followed by radial wire booms and axial booms [Auslander, 2008].

The EFW probes create a coupled multi-body system whilst the spin-rate and deployment state (boom lengths) change the resonant modes. The application of thruster pulses may also invoke natural oscillations. A stability analysis can be supported by analytical calculations e.g. by Simulink® simulations which provide efficient estimators of operational constraints to support mission planning. Simulink® is an environment for multi-domain simulation and Model-Based Design for dynamic and embedded systems. The identification of operational constraints can provide means to avoid the interaction of thruster pulsing

and spin-rate with resonant frequencies. A boom length growth with reduction of the wire density decreases its stiffness. On the other hand a spin-induced boom flexing amplifies the 'effective' boom second mass moment [Meirovitch and Calico, 1972]. On basis of analysis the resonance frequency of a THESIS S/C wire boom (anchored at one side) was chosen four times the spin-rate to maximize its length [Auslander, 2008]. The propellant mass behavior was modeled as a slug mass 3D pendulum. Reference is made to [Pankow, 2001] who uses analytical results from [Lai and Bhavnani, 1975] once more.

6.7 Wire Boom Cable Composition

Tests of the hub hinge attachment behavior are crucial to be able to model the overall dynamics. The coupling and interaction of the wire booms with the S/C hub are driven by the wire material parameters internal cable damping k_0 [$\text{kg}\cdot\text{m}^2/\text{s}$] and stiffness S_0 [$\text{kg}\cdot\text{m}^2/\text{s}^2$]. They result from dedicated tests with the specific cable design. The following cable design composition data cover 40 years EFW instrument engineering development:

- **At the dawn: the 1970s.** The S3-2 S/C (Small Secondary Satellites) was launched in the 70s as piggy back payloads on a number of KH-9 military reconnaissance launches. The wire boom is composed of Raychem Triax Cable EPD-1763, Kynar insulated with diameter $d = 20$ mm and density $\rho = 9.45$ mg/m. Precise pendulum experiments in air (with drag correction) yield $k_0 = 0.001$ $\text{kg}\cdot\text{m}^2/\text{s}$ and $S_0 = 0.04$ $\text{kg}\cdot\text{m}^2/\text{s}^2$ [Lai and Bhavnani, 1975].
- **The state-of-the-art.** [Pankow et al., 2001] and [Auslander et al., 2008] release the wire boom design heritage data of the RBSP, THEMIS and FAST S/C. The RBSP cable type is given by the Gore RCN8411 specification, i.e. AWG36 (7/44) SPC, Polyimide insulation with diameter $d = 1.24$ mm and density $\rho = 34.2$ mg/m. The EFW RBSP Technical Note [RBSP-2, 2009] deals with a series of thermo-mechanical experiments comprising pendulum tests in vacuum. It can be derived that $k_0 = 0.001547$ $\text{kg}\cdot\text{m}^2/\text{s}$.

The salient properties of the RBSP cable design compared to the S3-2 cable design are its small diameter, a 50% higher internal damping factor at a tri-fold higher wire density. The other RBSP tests included mechanical tensile strength, coefficient of thermal expansion (CTE) and cable straightness but no stiffness data are given.

The overall effectiveness of the cable is determined by the on-orbit characteristics of the EFW instrument design. The most apparent thermal impact is a change in length when the S/C enters and emerges from an eclipse. The terrestrial CTE test was compared with on-orbit data and revealed during a 28 minute RBSP S/C eclipse a slight increase in spin-rate. This results from the lower wire boom temperature inducing a contraction of the boom cables and consequently the S/C MOI decrease. It was verified by on-orbit S/C eclipse data with the spin plane booms in a stowed configuration that the upsets from other RBSP S/C appendages is negligible. A dedicated enhancement in the cable construction can further decrease the CTE and minimize the effect on spin rate and science measurements.

Cable boom damping may be related to the anelastic flexure at the hub attachments. The bending (moment) is greatest at the root attachment point and decays rapidly with distance. The damping can be partly a combination of dry friction and hysteretic behavior. The dry friction is due to small relative motions between the cable components whilst hysteretic damping is due to a slight anelasticity of the composite materials. These two types of damping are usually assumed to be reasonably independent of the excitation frequency.

The pendulum damping as shown from terrestrial test and flight performance might be nonlinear since the wire tension can have some influence. Therefore the damping tests shall be performed as similar as possible to flight conditions. The cable straightness test

determines the sensitivity of the radial positioning of the spin plane boom sensor. The cable behaves anelastically for small bending loads because of the complexity of construction and interaction between cable constituents.

6.8 Multi-mode Analysis

The Euler-Lagrange (EL) equations to describe the S/C dynamics of a central hub with attached wire boom pairs were originally derived by [Lai and Bhavnani, 1975] and [Longman and Fedor, 1976]. They use a rigorous mathematical analysis including the deployment and retraction of wire booms. The analytical natural frequencies and vibration modes resulting from the 2nd order linear differential equations can be found by decoupling the EL equations of motion.

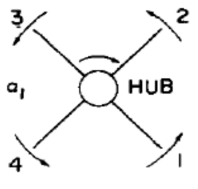
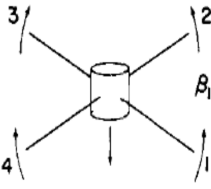
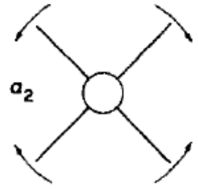
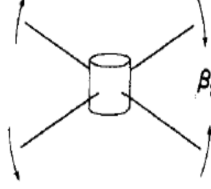
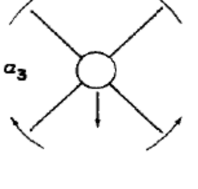
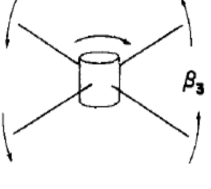
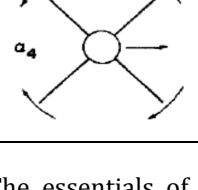
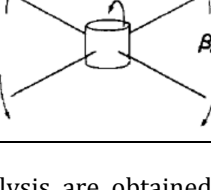
The S/C spin, however, implies at forehand that particular modes are gyroscopically coupled. The combination of mathematical completeness and this physical intuition is obtained by introducing a priori the eight natural sinusoidal vibration modes shown in Table-6.1 [Longman and Fedor, 1974]. This inclines the EL equations by using the following change of variables

$$\begin{aligned}
 \alpha_1 &= \frac{1}{4}(\varphi_1 + \varphi_2 + \varphi_3 + \varphi_4) & \beta_1 &= \frac{1}{4}(\psi_1 + \psi_2 + \psi_3 + \psi_4) \\
 \alpha_2 &= \frac{1}{4}(\varphi_1 - \varphi_2 + \varphi_3 - \varphi_4) & \beta_2 &= \frac{1}{4}(\psi_1 - \psi_2 + \psi_3 - \psi_4) \\
 \alpha_3 &= \frac{1}{4}(\varphi_1 + \varphi_2 - \varphi_3 - \varphi_4) & \beta_3 &= \frac{1}{4}(\psi_1 + \psi_2 - \psi_3 - \psi_4) \\
 \alpha_4 &= \frac{1}{4}(-\varphi_1 + \varphi_2 + \varphi_3 - \varphi_4) & \beta_4 &= \frac{1}{4}(-\psi_1 + \psi_2 + \psi_3 - \psi_4).
 \end{aligned} \tag{6.2}$$

The variable φ_i (Fig-6.9) is the angle in the equatorial S/C plane whilst the angle ψ_i (Fig-6.10) is defined by the normal meridian plane from each wire boom attachment point (hinge) to the tip mass in. The indices refer to one of the four booms out of two pairs ($i = 1$ to 4). The linearized EL equations define the analytical solutions of the oscillation modes given in Table-6.1. The oscillation modes for equal boom lengths are visualized after [Longman and Fedor, 1976] and [Auslander et al., 2008]. The limiting cases consider a negligible wire boom mass compared to the tip mass. The out-of-plane frequencies are determined for negligible interaction with the in-plane modes.

The modes couple with the rotation and translation α_1 and β_1 (EA1 and MS1) equations, but do not interfere with other modes. The modes α_2 and β_2 (EA2 and MS2) are independent of other mode variables. The modes α_3 and α_4 are gyroscopically coupled whilst β_3 and β_4 are coupled with the hub precession and nutation. The critical Cluster modes are the asymmetric ones, i.e., the in-plane equatorial EA modes and the out-of-plane meridian MA modes, since only these cause the S/C main body Z-axis to oscillate. The spin-normalized frequencies are found either by solving the EL equations for these modes or they are specified towards the subcontractor of the liquid damper S/S. The latter applies to the Cluster design since the $\lambda_{EA} = 1 + \Omega_{EA}/\omega_Z$ and $\lambda_{MA} = 1 + \Omega_{MA}/\omega_Z$ values were specified with ω_Z the spin-rate and Ω the specific mode angle frequency.

Table-6.1 Wire boom oscillation modes after with causes indicated bold [Longman and Fedor, 1975] and [Auslander et al., 2008].

Equatorial in-plane mode		Meridian out-of-plane mode	
	α1 or EA1 hub coupled rotation. Equatorial anti-symmetric coupled modes EA1 and EA2 These coupled twist modes are excited by a:		β1 or MS1 Jelly-Fish mode Meridian symmetric uncoupled modes MS1 and MS2 induced by:
	spin-up or shadows casted over the wire booms. α2 or EA2 no hub rotation.		spin-axis thrust while no changes in the Z-axis direction are induced. β2 or MS2 Saddle mode
	α3 or ES1 Equatorial Symmetric uncoupled ES1 and ES2 modes induced by:		β3 or MA1 Meridian anti-symmetric coupled modes MA1 and MA2 caused by:
	in-plane flexibilities from aerodynamic drag, translation or wire pair deployment. α4 or ES2		S/C re-pointing operations which do induce Z-axis direction changes. β4 or MA2

The essentials of the wire boom mode analysis are obtained by an exploration of the principle derivations from [Lai and Bhavnani, 1975]. These are based on two sets of the Euler-Lagrange with equations with Lagrangian $G(t) = E(t) - V(t)$ holding for the in-plane and out-of-plane modes shown in Fig-6.9 and Fig-6.10:

In-plane modes (EA1, EA2)

$$\frac{d}{dt} \frac{\partial G_i}{\partial \dot{\theta}_i} - \frac{\partial G_i}{\partial \theta_i} = - \sum_{j=1}^N \kappa_{ij} \frac{d\theta_j}{dt} \quad \frac{d}{dt} \frac{\partial G_i}{\partial \dot{\varphi}_i} - \frac{\partial G_i}{\partial \varphi_i} = - \sum_{j=1}^N \kappa_{ij} \frac{d\varphi_j}{dt} - S\varphi_i \quad (6.3)$$

Out-of-plane modes (N, MA1, MA2, Jelly Fish, Saddle, etc.)

$$\frac{d}{dt} \frac{\partial G_i}{\partial \dot{\theta}_i} - \frac{\partial G_i}{\partial \theta_i} = - \sum_{j=1}^N \kappa_{ij} \frac{d\theta_j}{dt} \quad \frac{d}{dt} \frac{\partial G_i}{\partial \dot{\psi}_i} - \frac{\partial G_i}{\partial \psi_i} = - \sum_{j=1}^N \kappa_{ij} \frac{d\psi_j}{dt} - S\psi_i. \quad (6.4)$$

The parameter θ_i refers in the in-plane case to the equatorial (oscillation around the Z axis) hub angle θ_E (Fig-6.9). In the normal meridian plane (oscillation around the X or Y axis) this angle is called θ_M (see Fig-6.10).

The stiffness factor $S_i = S$ is taken equal for all booms and accounts for the wire boom inelasticity. The damping factors κ_{ij} refer to external (e.g. atmospheric drag) or wire boom

damping types like Coulomb, hysteretic and viscous damping. These parameters differ from the earlier defined wire material parameters internal cable damping k_o [kg·m²/s] and stiffness S_o [kg·m²/s²] by a Moment-Of-Inertia (MOI) normalization as given in Eqn. (6.10) and (6.13). A way to treat all damping types in the viscous format of Eqn. (6.3) and (6.4) is given by [McGee et al., 2009].

To obtain key physical insights in the nature of wire boom deployment, [Lai and Smiddy, 1979] employ the classical mechanics of [Goldstein et al., 1980] to deal with in-plane $Z = 0$ boom deployments and retraction without S/C hub translation on basis of a 2nd order linear differential equation. This equation results from the analytical combination of the hub θ -Lagrangian with the wire boom(s) φ -Lagrangian using Eqn. (6.3) and (6.4). The model describes the uncoupled mode with all booms out of phase ($N = 1$) or the coupled mode with all booms in phase with $N = 2$ (one pair) or $N = 4$ (two pairs). This basic case is explored here to assess the advantages of applying a refined wobble liquid damper design as passive part of the Cluster S/C ADCS.

The equatorial solution

With respect to the following sections, the in-plane wire boom off-set angle φ is indicated in Fig-6.9 whilst Ω is a generalized oscillation and refers no longer to nutation only. A constant centrifugal actuator force term $f(t)$ is applied as a step function during an instant τ as part of a snail pace release of the wire boom from the S/C hub attachment exit point. The differential equation which describes the boom EA1 oscillation results straight from Eqn. (6.3) yielding

$$\frac{d^2\varphi}{dt^2} + 2\kappa_{EA1} \frac{d\varphi}{dt} + \Omega_{EA1}^2 \varphi = f(t). \quad (6.5)$$

The term $f(t)$ is constant during $0 < t < \tau$ and 0 once $t > \tau$ as seen from Eqn. (6.10) and (6.13). This condition is valid at small boom length variations at the following constraint

$$\tau \frac{dr}{dt} \ll r. \quad (6.6)$$

At a typical deployment pace of 1 cm/s which means $\tau \ll 6$ mins at $r = 3.6$ m and $\tau \ll 1$ hour at $r = 36$ m.

The solution of Eqn. (6.3) was already given in Chapter 2 as part of the determination of the Hagen-Poiseuille (HP) damping in a ND with κ being the liquid damping factor. This equation is solved [Lai and Smiddy, 1979] by applying the Laplace transform yielding the hub oscillation mode Ω and damping factor κ given by Eqns. (6.9) to (6.14). The general uncoupled case yields

$$\frac{\Omega}{\omega_z} = \sqrt{\frac{(m_t + \frac{1}{2}\rho r)rR_0 + S_o/\omega_z^2}{m_t r^2 + \frac{1}{3}\rho r^3}} \quad (6.7)$$

$$\kappa = \frac{(m_t + \frac{1}{2}\rho r)r \frac{dr}{dt} + \frac{k_0}{2}}{m_t r^2 + \frac{1}{3}\rho r^3} \quad (6.8)$$

whilst in case of a negligible wire density with $\rho = 0$, this reduces to

$$\frac{\Omega}{\omega_z} = \sqrt{\frac{R_0}{r} + \frac{S_0/\omega_z^2}{m_t r^2}} \quad (6.9)$$

$$\kappa = \frac{1}{r} \frac{dr}{dt} + \frac{k_0}{2m_t r^2} \text{ during } 0 < t < \tau \text{ whilst } \kappa = \frac{k_0}{2m_t r^2} \text{ when } t > \tau \quad (6.10)$$

$$f(r, t) = -2\omega_z \frac{1}{r} \frac{dr}{dt} \frac{I_z}{I_T} \text{ during } 0 < t < \tau \text{ and } 0 \text{ otherwise.} \quad (6.11)$$

In the case of a coupled EA1 mode, the following is obtained

$$\frac{\Omega_{EA}}{\omega_z} = \sqrt{\frac{R_0}{r} + \frac{S_0/\omega_z^2}{m_t r^2}} \sqrt{\frac{I_T}{I_z}} \quad (6.12)$$

$$\kappa = \frac{1}{r} \frac{dr}{dt} + \frac{k_0}{2m_t r^2} \frac{I_T}{I_z} \text{ during } 0 < t < \tau \text{ whilst } \kappa = \frac{k_0}{2m_t r^2} \frac{I_T}{I_z} \text{ when } t > \tau \quad (6.13)$$

$$f(r, t) = -2\omega_z \frac{1}{r} \frac{dr}{dt} \text{ during } 0 < t < \tau \text{ and } 0 \text{ otherwise} \quad (6.14)$$

with m_t [kg] the effective tip mass of a single wire boom with zero wire density ρ [kg/m³], R_0 [m] the S/C hub radius, r [m] the wire boom deployment radius from its hinge position ending at R_1 [m] and the total in-plane inertia $I_T = I_z + N \cdot m_t (R_0 + R_1)^2$ in case of a single wire boom ($N = 1$), a pair ($N = 2$) or two pairs ($N = 4$). In the Cluster S/C geometry the radial values are $R_0 = 1.45$ m and $R_1 = 42.5$ m.

The analysis of the solutions resulting from Eqn. (6.3) and (6.4) yield the deployment fundamentals from [Lai and Bhavnani, 1975] given below. The first three bullets follow from the conservation of angular momentum.

- The S/C hub spin slows down at boom deployment and speeds up during retraction.
- In an uncoupled mode the hub spin is steady with booms oscillating completely out-of-phase.
- The uncoupled mode frequency is the lowest frequency in any S/C boom configuration.
- In the coupled mode the hub spin rate oscillates with a frequency identical to that of the booms which are oscillating in phase.
- A retraction is less stable since $dr/dt < 0$ reverses the sign of the damping factor κ .
- Damping at a typical constant low deployment rate is mainly noticeable at short boom lengths since κ is proportional to $1/r^2$ and solely due to the property of the wire material used for the booms.
- The deployment force $f(t)$ is proportional to $1/r$ at small booms lengths.
- At large (critical) damping values κ no oscillation occurs and $\varphi(t)$ decays exponentially.
- The amplitude $\varphi(t > \tau)$ after a deployment (or retraction) is a function of $\varphi(t = \tau)$ and $d\varphi(t = \tau)/dt$.
- The presence of translation implies the existence of an uncoupled mode, and gives somewhat higher frequencies than if translation is ignored.
- The coupled mode frequency is larger than the uncoupled frequency because of the higher level energy hub interaction.
- The coupled mode with symmetrical boom lengths lacks translation.
- Out-of-plane frequencies are consistently higher than in-plane frequencies because the tip masses operate in a normal rather than in a radial field.
- In-plane mode frequencies are generally lower than the spin frequency ω_z unless $R < R_0$

- Out-of-plane modes frequencies are higher than the spin frequency ω_z .
- Beat phenomena appear in modes with translational hub oscillation causing fine spectral line splitting.
- If all booms deploy or retract simultaneous, the coupled mode is excited because symmetry allows no way to distinguish one boom from another forcing the booms to move together in a coherent pattern.
- If some but not all booms are deployed or retracted, generally both uncoupled and coupled modes emerge. Booms being deployed lag behind in phase relative to those undeployed or retracted.
- Uncoupled modes are usually favored due to their lower frequency and energy level.
- In the absence of an external force, the COM of the isolated hub system is initially at rest and does not translate. If initially at $t = 0$ the COM of mass and hub center coincide, then final translational displacement ($t \gg \tau$) must oscillate around the COM, i.e., the initial hub center ($X = 0, Y = 0$).
- If initially ($t = 0$) the COM does not coincide with the hub center (in some cases where booms are initially deflected), then although the translational displacement ($t \gg \tau$) still oscillates around the center of mass, it does not oscillate about the initial hub center.

The Meridian Solution

The differential equation which describes the pure meridian (MA) I_x and I_y out-of-plane boom oscillations, shown in Fig-6.10 resembles Eqn. (6.5) since

$$\frac{d^2\psi}{dt^2} + 2\kappa \frac{d\psi}{dt} + \Omega^2\psi = f(t). \quad (6.15)$$

The damping parameter κ and resonance frequency Ω value, however, are significantly different due to the different rotation axes with I_x and I_y inertia values. The out-of-plane wire boom oscillation angle ψ_i and the meridian hub oscillation angle θ_M add up to $\psi_{1,3} + \theta_M$ in the meridian YZ plane and to $\psi_{2,4} + \theta_M$ in the XZ plane. This is seen in Fig-6.10 where the Z-axis is spatially fixed and the X and Y axis are co-rotating about the Z-axis.

Taking $f(t) = 0$ after deployment and applying additional derivations using [Lai and Bhavnani, 1975] yields the following MA1 differential equation at root hinge 1 and 3 coupled to the hub oscillation around the X-axis

$$\frac{d^2\psi_{1,3}}{dt^2} + 2\kappa_{MA1} \frac{d\psi_{1,3}}{dt} + \Omega_{MA1}^2\psi_{1,3} = 0. \quad (6.16)$$

The MA2 differential equation at root hinge 2 and 4 coupled to the hub oscillation around the Y-axis becomes

$$\frac{d^2\psi_{2,4}}{dt^2} + 2\kappa_{MA2} \frac{d\psi_{2,4}}{dt} + \Omega_{MA2}^2\psi_{2,4} = 0. \quad (6.17)$$

A zero wire density approximation yields the single wire boom inertia $I_B = m_t(r + R_0)^2$ whilst

$$(\lambda_{MA1,2} - 1)^2 = \left(\frac{\Omega_{MA1,2}}{\omega_z} \right)^2 = \left(1 + \frac{R_0}{r} \right) \left(1 + 2 \frac{I_B}{I_{x,y}} \right) \quad (6.18)$$

comprises the angular frequencies of the coupled modes MA1,2. In addition the main analytical wire boom modes Ω are derived from [Lai and Bhavanani, 1975], [Lai and Smiddy, 1979], [Auslander, 2008] and [McGee, 2009] and harmonized in a format using the spin normalized $\Omega/\omega_z = \lambda - 1$ and hub mass M yielding

$$(\lambda_1 - 1)^2 = \frac{R_0}{r} \quad \text{uncoupled single wire boom mode} \quad (6.19)$$

$$(\lambda_{EA1} - 1)^2 = \frac{R_0 I_T}{r I_Z} \quad \text{equatorial anti-symmetric mode EA1} \quad (6.20)$$

$$(\lambda_{MS1} - 1)^2 = \left(1 + \frac{R_0}{r}\right) \left(1 + \frac{4m_t}{M}\right) \quad \text{meridian symmetric 'Jelly Fish' MS1 mode} \quad (6.21)$$

$$(\lambda_{MS} - 1)^2 = \frac{I_T}{I_T - I_Z} \quad \text{Jelly Fish MS mode [Auslander, 2008]} \quad (6.22)$$

$$(\lambda_{MS2} - 1)^2 = \left(1 + \frac{R_0}{r}\right) \quad \text{Saddle mode MS2.} \quad (6.23)$$

The full-blown solutions of the non-linear Euler-Lagrange (EL) Eqn. (6.3) and (6.4) yield slight differences with the analytical values given by Eqn. (6.18) to (6.23) from the linearized dynamical equations. This was shown by [Lai and Bhavanani, 1975], [Lai and Smiddy, 1979], [Auslander, 2008] and [McGee, 2009]. The latter deals with the actual wire boom dynamics of the NASA Radiation Belt Storm Probes (RBSP) dual S/C mission with planned launch in 2012. The Cluster and RBSP wire boom configuration designs are comparable but the RBSP S/C $\lambda_0 = 1.406$ inertia configuration differs significantly from the Cluster $\lambda_0 = 1.951 \pm 10\%$ (initial phase-A) to 1.75 (phase B) values.

RBSP stability model

The remarkable RBSP modal analysis by [McGee et al., 2009] deals specifically with the RBSP S/C stability but applies to the general class of spin stabilized S/C with multiple flexible wire booms as well. As usual a linear dynamics analysis of out-of-plane modes is used to estimate the modes of the natural S/C system response. The effects of various damping mechanisms (viscous ring dampers, Coulomb friction, hysteretic damping) on these modes, and the dynamic response of the system to various S/C manoeuvres is considered. Nine out-of-plane performance parameters are combined in a vector by

$$\mathbf{x} = (z, \omega_x, \omega_y, \psi_1, \psi_2, \psi_3, \psi_4, k_1, k_2)^T. \quad (6.24)$$

Though this format does not uniquely representing the inertial status of the system, the approach circumvents a complication in the linear analysis by effectively excluding the use of Euler angles or quaternions. The parameter z is the hub COM displacement normal to the spin plane and the k parameters refer to the viscous damping of two orthogonally positioned ring nutation dampers. The out-of-plane modes comply well with the results obtained independently from the full non-linear dynamics in a separate paper [Kemp et al., 2009]. In Fig-6.11 these modes are shown: Beside the well-known Jelly-Fish and Saddle modes (1, 2) three more complicated coupled gyroscopic MA modes (3, 4 and 5) appear.

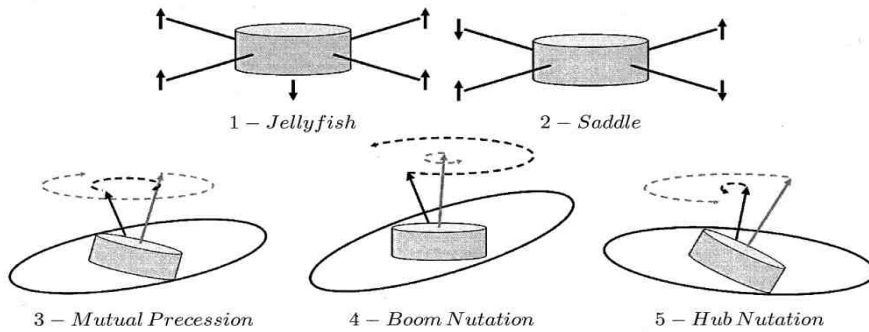


Fig-6.11 The five normal wire boom MA modes identified in the modal analysis of [McGee et al., 2009].

In the visualization of the four booms, coplanar and 90° out of phase with each other, they are regarded as a coplanar solid mass ring around the central hub. The ends of the unit vector normal to the boom plane and the hub Z-axis unit vector are tracing out circles in inertial space around the constant system constant angular momentum H with frequencies

$$\Omega_{I3} = \Omega_3 - \omega_z \quad (6.25)$$

$$\Omega_{I4,5} = \Omega_{4,5} + \omega_z \quad (6.26)$$

where the first index I refers to the inertial space system. These angular frequencies are crucial regarding the signal strength of the communications up and downlink to the Earth. The resonance frequencies $\Omega_{3,4,5}$ and eigenvectors (modal shapes) are obtained as usual from the system matrix $\mathbf{A}(s)$ by the equation

$$\det[\mathbf{A}(s)] = 0 \quad (6.27)$$

with $s = j\omega$ as the Laplace variable. The 9 x 9 system matrix \mathbf{A} components and parameters are given by [McGee et al., 2009]. The authors state that the three $\Omega_{3,4,5}$ modes were not properly identified in the past by [Longman and Fedor, 1976] and [Lai and Bhavnani, 1975]. The rigorous full non-linear dynamics approach described in [Lai and Bhavnani, 1975], however, does not exclude these modes. The merit of the approach and visualization by [McGee et al., 2009] is the combination of intuition and physics insight in the analysis and visualization of the out-of-plane mode shapes.

The outcome of the undamped case proves to be weakly sensitive to the inclusion of any damping type with respect to vibration frequencies and mode shapes. The two applied RBSP ring NDs are mentioned to be only effective in damping mode 5 which is close to hub nutation [McGee et al., 2009]. It is, however, not mentioned whether the RBSP ring dampers were tuned for multiple modes. The implementation of the multi-mode damping of the Fokker liquid dampers follows a different approach. This will be made clear in the following sections which deal explicitly with the Cluster damper design. In section 7.8 the RBSP model will be used to compare the wire boom dynamics of the RBSP S/C with the Cluster S/C design. At the end of Chapter 7 in section 7.13, a full review of the relevant parts of the [McGee et al., 2009] article will be given which emphasizes the actual application strength of the proposed [Kuiper, 1990] multi-mode Fokker liquid damper and its implementation approach.

6.9 Conclusions

In this Chapter the following was achieved:

- A series of stabilized spinning S/C, since the 70s of the previous century up to 2012, were reviewed and show the potentials of broadband liquid dampers
- The generic theory of wire boom oscillations, gyroscopically coupled to the hub spin and nutation modes, was explored using a new parameterization
- The RBSP stability model was introduced.

This serves as the basis of the following Chapter 7 which deals with the design and systems engineering of broadband liquid dampers for passive ADCS control of spinning S/C.

7 Multi-mode Liquid Damper for the Cluster ADCS

The real voyage of discovery consists not in seeking new landscapes but in having new eyes.

Marcel Proust

French novelist (1871 - 1922)

7.1 Introduction

The gathered insights given in the previous chapters did enable the design of the extended Cluster (wobble) damper in the early 90s. At first the author realized that in general the Fokker ND damper reliability strongly exceeds its requirement. The only thinkable disaster is the very unlikely double weld failure, i.e., one in each damper. The over-compliance in reliability initiated the thoughts of an extended use of liquid dampers in flexible space structures. Therefore the sequence of topics in the remainder of this chapter will be:

- Proof of the extreme reliability, i.e., single point of failure (SPF) and reliability
- Trade-off towards a multi-mode damper design
- Redundancy and enlarged bandwidth
- Design methodology
- Tuning sensitivity of the final design
- Performance test model (PTM) experiments.

7.2 Trade-off towards a Multi-mode Damper Design

The previous section showed that the ND reliability and SPF status are a comfortable issue. This provoked the idea for the following thoughts. Taking the redundancy as a strict requirement, one may consider the deliberate use of different geometrical damper shapes. Such a design option has the potential to attenuate both nutations as well as wire boom modes. An initial design option was the extended ND design expressed in Fig-7.1. The two liquid tubes impose a different resonance frequency whereas their damping characteristics results in a first order merge. This suggests that even more than two liquid tubes may be applied. The Euler-Lagrange (EL) theory given in Chapter-2 is applicable to deal with this option. The EL analysis, however, has to take into account the coupled behaviour of the multiple liquid tubes which depends on the intermediate distance of the liquid tube axes, endpot size, liquid tube radii and in and out flow phenomena. In addition dedicated experiments are required to qualify this new design. The same conclusion was valid in the feasibility study of the Fokker F-100 stabilo wing tail dampers, an aeronautical design exercise [Kuiper, 1992]. The design deviates too much from the qualification heritage of the earlier Fokker NDs. Therefore the following practical option was proposed by the author: *Stick to the classical design but use a redundant pair of NDs which are not identical.*

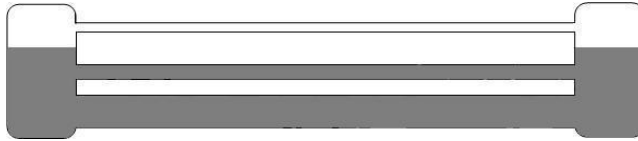


Fig-7.1 The damper design option with two liquid tubes which provide damping at two different resonance frequencies. The overall damping characteristics result to 1st order by the merge of the individual ones.

7.3 Redundancy and Enlarged Bandwidth

Due to the inherent enlarged bandwidths in the combined design an unforeseen disturbance or slight incomppliance can be much better tackled. A prerequisite however is that enough damping mass is allowed and claimed in the S/C mass budget allocations as part of the overall S/C system engineering.

The robustness of the combined damper design has to comply with multiple excitations. This can be assessed by modelling on basis of the applicable theory in section 2.9. A sensitivity analysis has to be executed by taking (worst case) four frequency samples out of the four different required bands (see Fig-7.21). The study of the resulting damping time evolution on basis of these model input variables enables the validation of the multi-excitation performance.

The redundancy now refers to the attenuation of the nutation and antenna modes. The non-identical pair can be incorporated in the S/C by one of the following damper combinations: Meridian-Equatorial, Meridian-Meridian or Equatorial-Equatorial. The parameters a , b , L and R_m are free to tune the Cluster EA or MA damper with the required frequency Ω on basis of Eqn. (2.106). The S/C mounting of the two fully defined phase-A equatorial dampers with equal $L = 278$ mm is shown in Fig-7.2. The right side shows snapshots at a 2.5 magnification to visualize the differences in the EA and MA liquid tube and end-pot diameters. The MA damper dimensions are $a = 14$ mm and $b = 38.2$ mm whilst the EA dimensions are $a = 7$ mm and $b = 48.6$ mm. In reality the dampers are slightly curved to be coaxial with the liquid tube mounting radius as shown in Fig-7.3 for the final EA and MA flight models (FM).

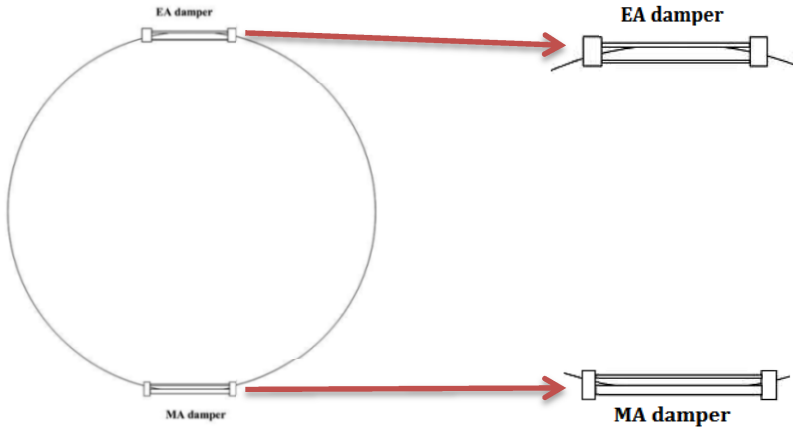


Fig-7.2 Cluster EA (upper mounting position) and MA (lower position) liquid dampers mounted in the equatorial $Z = 300$ mm plane at $R = 900$ mm.



Fig-7.3 The final Cluster MA (bottom) and EA (top) equatorial FM dampers [courtesy Aeronamic B.V.].

7.4 Design Implementation

The phase-A design requirements of the Cluster damper design are summarized in Table-7.1. Once the combined damping proposal [Kuiper, 1991] was accepted, the EA and MA antenna modes in addition to the nutation N mode were specified [van Bakel, 1993]:

$\lambda_{EA} = 1.40$	Equatorial Anti-symmetric (EA) antenna mode
$\lambda_0 = 1.951-1.75$	Nutation mode (N) from phase-A up to phase-B
$\lambda_{MA} = 2.05$	Meridian Anti-symmetric (MA) antenna mode.

The design options, related engineering boundary conditions and implementation will be step-wise unfurled. The phase-A data comply with an effective tip mass m_t of about 0.2 kg and agree with design data from later missions with comparable wire boom designs like the RBSP [McGee, 2009], Bepi-Colombo [Gonzalez et al., 2001], Themis [Auslander et al., 2008] and Fast [Pankow et al., 2001]. The single wire boom inertia I_B complies with an effective wire boom density of 0.9 g/m (homogeneous boom with 42.5 m length) which is close to the S3-2 value of 9.45 mg/m.

Table-7.1 specifies the phase-A value $\lambda_{EA1} = 1.40$ which is compliant with Eqn. (6.20). The specified $\lambda_{MA} = 2.05$ value (MA_{spec}) does not agree with the analytic values of the pure high order MA1 and MA2 modes in Table-6.4. The origin of this value is not traceable but MA_{spec} complies with the so-called gyroscopic boom nutation mode #4 from [McGee et al., 2009] which was dealt with in section 6.7 and visualized in Fig-6.11.

In section 7.8 an in-depth comparison of the analytic mode values, modal analysis using the RBSP model from [McGee et al., 2009] and the phase-A to phase-B changes will be given. The treatment will first confine to the early (1990) implementation arguments of the hybrid EA-N-MA liquid damper design as passive part of the Cluster ADCS.

Table-7.1 Cluster S/C phase-A requirements and ND design boundary-conditions (1991).

Item	Description	Nominal value	Extremes
τ	Nutation damping time constant [hr]	< 10	10
T	Temperature [$^{\circ}\text{C}$]	20	-20 to 40
I_{xx}	Inertia around X-axis [kg.m^2]	210.0	$\pm 10\%$
I_{yy}	Inertia around Y-axis [kg.m^2]	240.0	$\pm 10\%$
I_{zz}	Inertia around Z-axis [kg.m^2]	439.0	
λ_0	Nominal nutation mode N phase-A (phase-B)	1.951 (1.75)	$\pm 10\%$
λ_{EA}	Equatorial Anti-symmetric mode EA	1.40 (-)	
λ_{MA}	Meridian Anti-symmetric mode MA	2.05 (-)	
M	BOL S/C mass [kg]	1200	
	EOL S/C without propellant mass [kg]	550	
ω_z	S/C spin rate around Z-axis [rpm]	15	$\pm 10\%$
R_0	Distance in XY-COG plane to spin-axis [mm]	900	± 50
Z_0	Position of the two dampers above COG plane [mm]	300-500	
θ	Initial nutation angle		6.0°
	Final nutation angle		$< 0.05^{\circ}$
m	Total damper mass (EA and MA) with brackets [kg]	< 3	3
m/M	Mass fraction of ND BOL - EOL	0.25-0.55%	< 0.55%

Table-7.2 Basic Cluster analytical wire boom oscillation modes using Eqns. (6.19) to (6.23).

N	Single boom	Equatorial Coupled	Meridian JF ¹	Meridian JF ²	Meridian SM	Meridian X-axis ³	Meridian Y-axis ³
λ_N	λ_1	λ_{EA1}	λ_{MS1}	λ_{MS1a}	λ_{MS2}	λ_{MA1}	λ_{MA2}
1.75 - 1.951	1.185	1.40	2.018	2.127	2.017	3.461	3.358

JF=Jelly-Fish N=Nutation SM=Saddle Mode

¹[Lai and Bhavnani, 1975] and ²[Auslander, 2008]

³ Rotation about lateral inertia axis indicated in Fig-6.10

7.5 Early Assessments

The early phase-A proposal of the extended liquid damper concept required a validity analysis to prove its soundness [Kuiper, 1991]. As a result the synergic action of the EA and MA mode damper, tuned to comply with the Cluster requirements in Table-7.1, is given in Fig-7.4. The horizontal axis shows the frequency ratio $\Omega/\omega_z = \lambda - 1$ [-] and the vertical axis the combined EA and MA damping performance P/a_0^2 [kg.s]. The result is an early (“first shot”) design based on the choice of the PP1 damping liquid. The type of liquid (practically PP1 or PP3) and the possibility to fill each damper with a different liquid leaves some design freedom both in damping level and tuned frequency. The broadband performance modelling is exposed in Figs-7.4 and 7.5 and uses either PP1 or PP3 in both dampers. The proposed PP1 performance tests from Fig-7.4 were left in Fig-7.5 to signify the differences. The use of PP3 instead of PP1 shifts the tuned MA frequency ratio from 1.08 to 1.05 and decreases the MA damping slightly. At the MA side is seen that the use of PP3 broadens the bandwidth further whilst the performance gets more dispersive with temperature. Both phenomena make the design even more robust whilst small length changes enable the (re)shift of its center. The early feasibility modeling took an additional effective length $2a_{EA}$ or $2a_{MA}$ into account compliant with Eqn. (2.109). This is an educated guess at the start of the recursive design process. In this design case, the implementation

and tuning arguments of section 2.12 apply beyond the scope of nutation. The in-plane EA and out-of-plane MA modes are gyroscopically coupled to the hub nutation. This enables the functionality of equatorially mounted dampers to support damping even in the case of the out-of-plane modes.

The N mode damping value of about 0.016 kg·s in Figs-7.4 and 7.5 equals four times the minimum value 0.004 kg·s based on the required < 10 hr time constant (see Table-7.1) and the application of Eqn. (2.26). This means that the maximum nutation time-constant τ_N is about 2.5 hr over the full operational temperature range firmly within its specification.

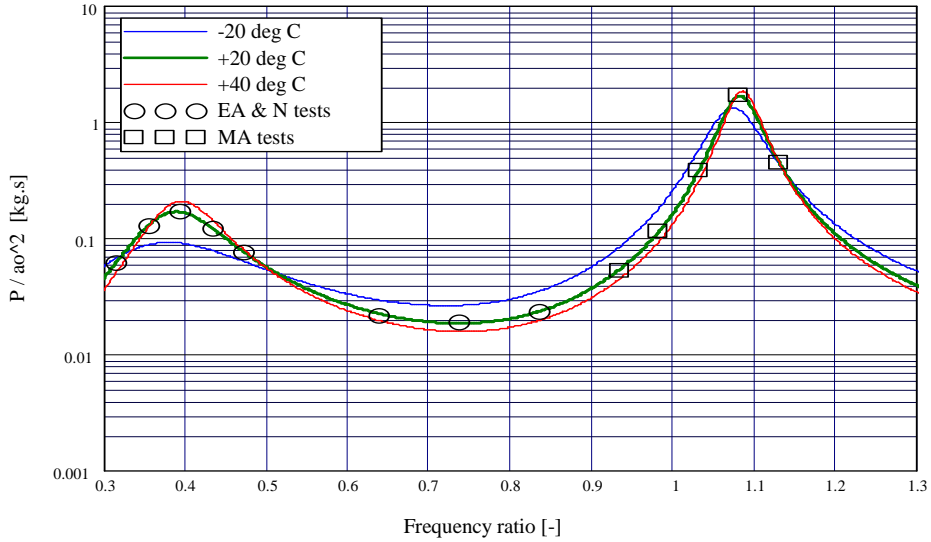


Fig-7.4 Phase-A/B design tuning and proposed performance tests of the Cluster dampers with $\lambda_{EA} = 1.40$, $\lambda_N = 1.951/1.75$ and $\lambda_{MA} = 2.08$ as validation of the proposed design [Kuiper, 1990].

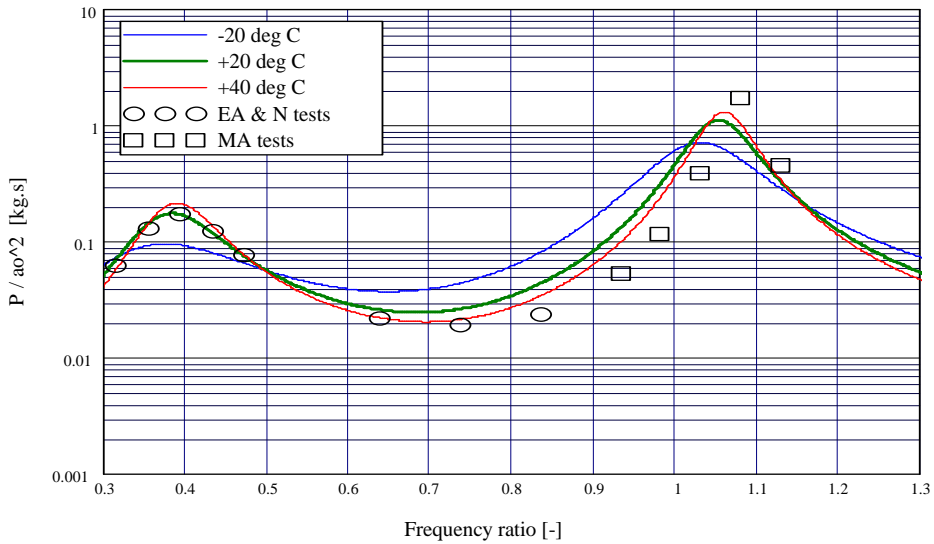


Fig-7.5 Concept validation with PP3 as damping liquid. The proposed PP1 performance tests from Fig-7.3 were left as markers to signify the MA frequency ratio shift towards 1.05 and the slight decrease of MA damping.

7.6 Recursive Bottom-up Approach

The imposed modes (derived from higher level SE trade-offs) require a multi-mode design methodology. In case of the Cluster damper the drivers are the broadband EA, N and MA requirements. The EA-mode damping is obviously driven by the requirement to control the S/C spin-phase error. The MA damping rate is determined by the required time-constant of the spin-axis stability recovery after re-pointing operations (see Table-6.1). The large required damping of the broadband MA mode (see Figs-7.4 and 7.5) is obviously a necessity given by the fact that the equatorial dampers attenuate the multi MA modes via partial gyroscopic coupling only [McGee, 2008].

The following design flow yields a bottom-up approach as first sequence in a recursive damper optimization process:

1. Apply the SE rules of section 2.13 to start the design based on nominal requirements.
2. Maximize the (I/F restricted) effective damping length L_{eff} to minimize the mass of both dampers and maximize the damping. The ND mass is mainly determined by the applied liquid (PP1 or PP3 as a rule).
3. Choose the EA and MA mounting radius $R_m = R_0$ or compliant to a specified radial liquid tube position.
4. Tune the radii a_{EA} and b_{EA} with half the allocated mass budget and frequency Ω_{EA} using Eqn. (2.59) so

$$\left(\frac{\Omega_{EA}}{\omega_Z}\right)^2 = \frac{2R_m}{L} \left(\frac{a_{EA}}{b_{EA}}\right)^2. \quad (7.1)$$

The a_{EA} size determines the remnant EA1 in-plane wire oscillation amplitude via direct hub viscous damping. The time averaged damping rate \bar{P}/a_0^2 is proportional to $L a_{AE}^4$ (holds at small a_{AE} where the HP model is valid) and determines the damping time constant. The other input parameters are: S/C inertia parameters, required performance time constant, temperature range, liquid viscosity, liquid density, wire density, wire stiffness and wire boom composition.

5. Choose the height of the endpot level h_0 such that no liquid overflow via the vapor tube can occur at the maximum (initial) nutation angle (e.g. 6° for the Cluster S/C).
6. Apply Eqn. (2.59) once more to the specified “MA” mode ($= MA_{spec}$), i.e.,

$$\left(\frac{\Omega_{MA}}{\omega_Z}\right)^2 = \frac{2R_m}{L} \left(\frac{a_{MA}}{b_{MA}}\right)^2. \quad (7.2)$$

It is seen that two parameter are left at a specified Ω_{MA} value. Choose $b_{MA} = b_{EA}$ as an initial guess and solve Eqn. (7.2) for the MA radius a_{MA} .

7. Determine the endpot level height $h_0/2$ and the total mass of the damper.
8. Verify the compliance with the N mode damping requirement being a natural cause after the steps 1 to 6.
9. Check the overall specification compliance of the dissipation rate P/a_0^2 and the derived time constants by modeling the damping performance in the full operational range. In case of an incompliance or intermediate specification changes by S/C design maturation the recursive cycling starts. At this point mass budget or mounting radius changes may be required.
10. Verify the design by PTM tests.

The given recursive bottom-up design approach will be extended by a top-down model in section 7.8. The results from a full Cluster dynamics model implemented in MathCad® will be presented. The model is based on the RBSP S/C system modeling of [McGee et al., 2009]. The model calibration outcome shows a full compliance with the RBSP S/C results. This

system model will prove to be a sound tool to analyze the (SE top-down) causes of the Cluster mode changes. In combination with the described recursive bottom-up approach this results in a solid scientifically founded SE design approach for broadband liquid damper designs.

7.7 Implementation of the Multi-mode Damping Principle

The following liquid damper implementation analysis is made partly in retrospective sense and based on the S3-2, RBSP, FAST and THEMIS S/C cable data and where possible the applied Cluster parameters. The Cluster hub radius $R_0 = 1.45$ m and the full deployment wire length $R = 42.5$ m apply. The internal wire damping factor is $k_0 = 0.001$ kg.m²/sec from S3-2 S/C data. A homogeneous wire boom is taken in the analysis. In reality the Cluster and other wire boom cables are composed of different length parts. Diverse sensitivity trade-offs, however, taking length and material property variations into account, show that the results hardly change. This is shown in Fig-7.6 and 7.7 which result using the Eqns. (6.9) up to (6.13). Fig-7.6 (right picture) shows the effect of a varying wire density on the uncoupled wire boom oscillation period in the applicable range from S3-2 (9.45 mg/m) to RBSP S/C (34.2 mg/m) at the fully deployed 42.5 m Cluster wire boom length. The left picture shows the Cluster S/C wire boom damping time constant τ as a function of the deployed length.

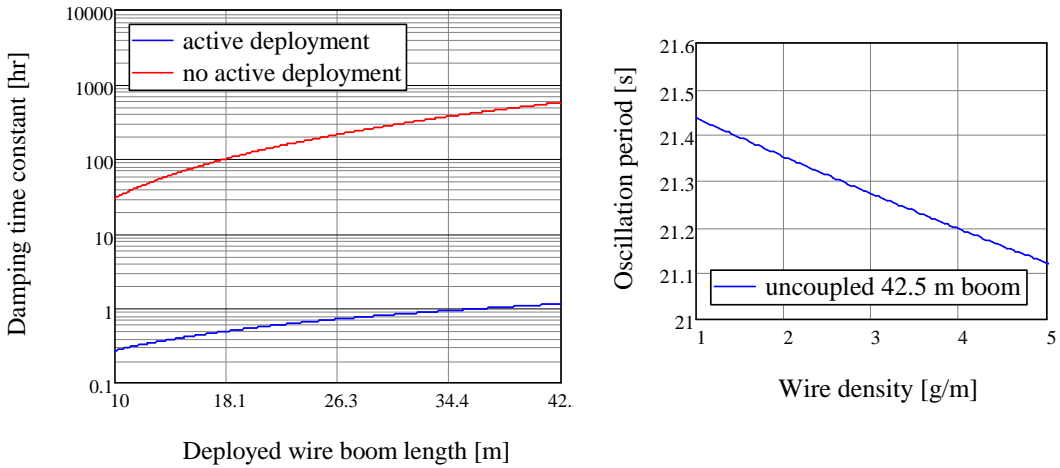


Fig-7.6 Cluster S/C internal wire boom damping time constant as function of the deployed length (left). Uncoupled wire boom oscillation period T as function of wire density at a full deployed boom (right).

EA1 Mode Damping

In Fig-7.7 the EA1 frequency ratio (left) and oscillation period T (right) at increasing wire boom length are shown. The impact of the wire mass shows only a change of 2% in the oscillation period magnitude going from S3-2 (9.45 mg/m) to RBSP (34.2 mg/m) values.

The Eqns. (6.3) to (6.6) do not include the impact of a liquid damper mounted inside the hub. In this case, looking at Eqn. (2.56), $s = R_m \theta_E$ holds with R_m being the equatorial mounting radius of the liquid damper and θ_E the hub rotation angle in the equatorial $Z = 0$ plane. The additional viscous damping factor given by Eqn. (2.66) in Chapter 2 yields in the equatorial and meridian format

$$\kappa_{EA} = \frac{4v_{EA}}{a_{EA}^2} \quad \text{and} \quad \kappa_{MA} = \frac{4v_{MA}}{a_{MA}^2}. \quad (7.3)$$

At first the pure hub EA1 oscillation is regarded on basis of Eqn. (6.3).

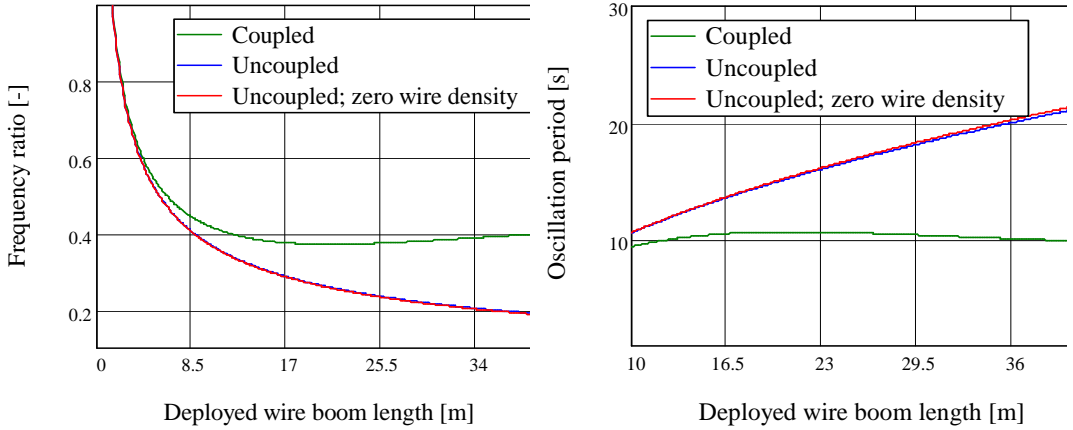


Fig-7.7 EA1 frequency ratio (left) and oscillation period (right) at increasing wire boom length.

The EA1 in-plane perturbation of the regular hub spin is damped by a Fokker liquid damper design optimized at the frequency Ω_{EA} so

$$\frac{d^2\theta_E}{dt^2} + 2\kappa_{EA1}\frac{d\theta_E}{dt} + \Omega_{EA1}^2\theta_E = 0. \quad (7.4)$$

The independent hub liquid damper attenuates the wire boom EA1 oscillations indirectly since the coupled EA1 amplitudes of the hub and wire boom(s) are related by the factor $-4mr(r + R_0)/I_T$ (hub/boom). The time constant equation results from Eqn. (2.28) with $F_e(\alpha, \lambda_x, \lambda_y) = 1$ and complies with Eqn. (3.3). Therefore the maximum value in full deployed configuration in the $\Omega = \Omega_{EA}$ vicinity becomes

$$\tau_{EA,max} = \frac{I_T}{R_m^2\Omega^2} \left(\frac{P}{a_0^2} \right)_{av}^{-1}. \quad (7.5)$$

This means that the in-plane ultimate EA1 wire boom amplitude has become a design variable with the damper mounting radius R_m (deviating from the hub radius) as additional input design parameter. The effective EA1 damping and time constant as a function of the frequency ratio are plotted in Fig-7.8.

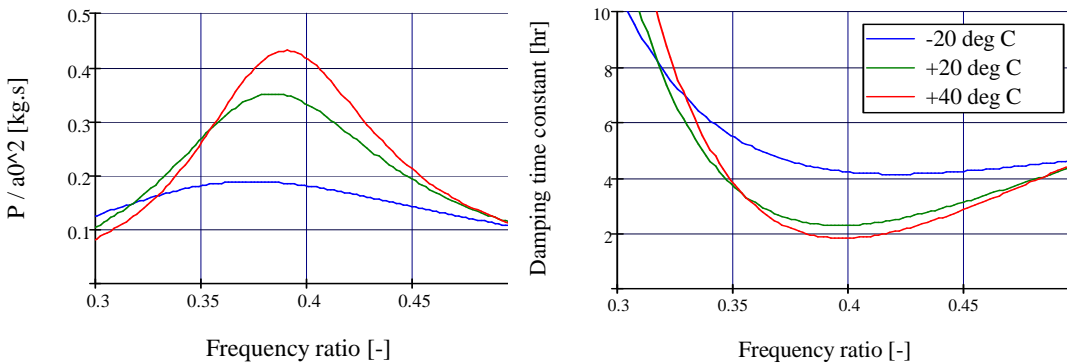


Fig-7.8 Cluster phase-A EA mode damping (left) and damping time constant (right) of two EA dampers filled with PP3 whilst $a = 7$ mm, $L = 278$ mm, $b = 48.6$ mm and $R_m = 1.37$ m.

The design values from [van Bakel, 1993] were applied with the optimized mounting radius $R_m = 1.37$ m. The time constant is in the order of 2 to 4 hr over the full operational temperature range. This value is in balance with the earlier determined 2.5 hr value of the nutation damping time constant (see last part section 7.5).

Wire Boom Deployment and Damping of EA1 Oscillations

Once the basics of wire boom deployment and its damping by liquid dampers have been dealt with, the flight representative EA1 deployment case is studied. An arbitrary wire boom design with Cluster length (42.5 m) and RBSP parameters is regarded, i.e., $\rho = 34.2 \text{ mg/m}$ and $k_0 = 0.001547 \text{ kg}\cdot\text{m}^2/\text{s}$. The deployment starts at $t = 0$ as a step function with a constant 1 cm/s rate and stops at $t = 20 \text{ min}$ or $t = 20.6 \text{ min}$ for reasons to be made clear. Two cases are considered, at $r = 4 \text{ m}$ and $r = 40 \text{ m}$, to study the impact of the deployed radius on the residual EA1 deflection angle Φ of the wire boom. Figs-7.9 up to 7.13 show the analysis results at $r = 4 \text{ m}$ whilst Figs-7.14 up to 7.18 contain the results at $r = 40 \text{ m}$.

In Fig-7.9 the internal wire boom damping at $r = 4 \text{ m}$, given by Eqns. (6.10) and (6.13), shows that the coupled case ($6.1 \times 10^{-5} \text{ s}^{-1}$) damping is comparable to the uncoupled case ($5.8 \times 10^{-5} \text{ s}^{-1}$). The damping at $r = 40 \text{ m}$, in Fig-7.14, is much smaller whilst the difference between the coupled ($2.6 \times 10^{-6} \text{ s}^{-1}$) and the uncoupled ($5.8 \times 10^{-7} \text{ s}^{-1}$) case is getting significant. The effect of only internal wire boom damping on the uncoupled mode is seen in Figs-7.10 and 7.12 (red) after deployment. The EA1 oscillation attenuates with damping time constant $\tau = 1/\kappa = 5 \text{ hr}$ at $r = 4 \text{ m}$ whilst at $r = 40 \text{ m}$ this value becomes 500 hr.

Figures 7.11 and 7.13 (blue) clearly visualize the impact of the liquid damper during and after deployment in addition to the internal wire boom damping. The prerequisite is, however, that the wire booms keep following the EA1 damping rate of the hub through the energy exchange of the coupled mode. At small angular deflections, however, diverse material artifacts and anelastic flexure at the hub anchor positions may pop up as dealt with in section 6.6. The combined action will anyhow attenuate the EA1 mode further though its damping rate is hard to quantify. Only dedicated engineering tests can clarify this issue.

The initial angular off-set is linearly dependent to the change in inertia caused by the 1 cm/s deployment rate. The maximum amplitude of the wire boom right after the deployment stop, limits (initially) the EFW instrument science performance beside the wire straightness issue. The EA1 damper, however, attenuates this residual angle at a time constant of about 2.5 hours. The result proves to be insensitive to a 10-fold increase in the model wire stiffness.

An interesting feature is the fact that the EA1 oscillation phase at the moment of the deployment stop determines the amplitude of the wire boom oscillation right afterwards. This can be clearly seen by comparing the $t = 20 \text{ min}$ and optimized $t = 20.6 \text{ min}$ cases. Figure 7.18 shows that the residual deflection angles right after the deployment stop can be made $0.03^\circ (=108'')$ depending on the critical timing of the stop.

In addition to the critical timing of the deployment stop another optimized deployment sequence approach was found. The proposed deployment strategy by [Ivchenko et al., 2007] is shown in Fig-6.29, i.e.

- The upper three pictures show with time, for a stepwise induced constant deployment rate with sudden stop at $t = 60 \text{ s}$, the normalized deployment length r/R , boom deflection φ and hub spin-rate respectively.
- The lower three pictures show the same sequence but a different deployment strategy to control the wire boom amplitude: At $t = 60 \text{ s}$ the deployment rate is reduced by 50% during a half cycle before it stops.

In the latter case the remnant coupled oscillations in the hub and wire booms disappear almost completely at the expense of 4% more deployment length (compare the 1st and 4th picture of Fig-7.19). The implementation of a proper timing sequence, however, is not easy and straightforward since it will require additional deployment sensors and control electronics. No implementation data have been found.

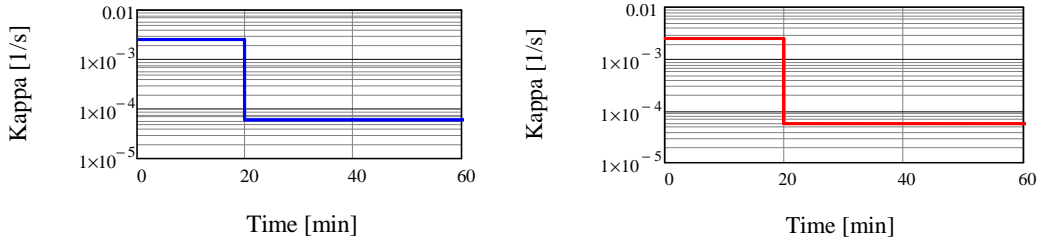


Fig-7.9 Internal wire boom damping of the coupled (left) and uncoupled EA1 mode (right) during and after deployment at $r = 4$ m. The RBSP wire boom parameters $\rho = 34.2$ mg/m and $k_0 = 0.001547$ kgm²/s are applied.

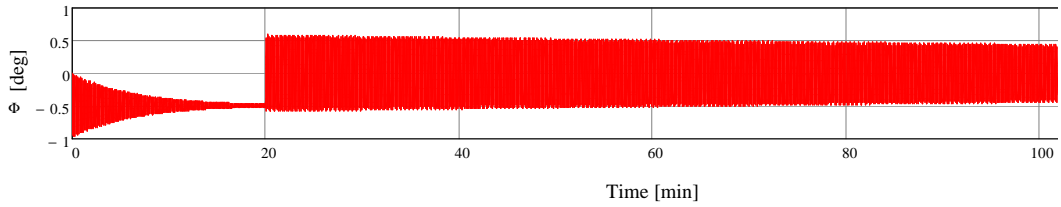


Fig-7.10 Attenuation of the uncoupled mode at $r = 4$ m. The wire boom deployment starts at $t = 0$ min and stops at $t = 20$ min.

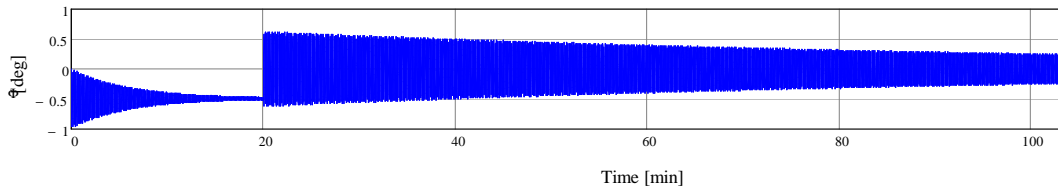


Fig-7.11 Attenuation of the coupled EA1 mode at $r = 4$ m using the tuned EA1 liquid damper. The wire boom deployment starts at $t = 0$ and stops at $t = 20$ min.

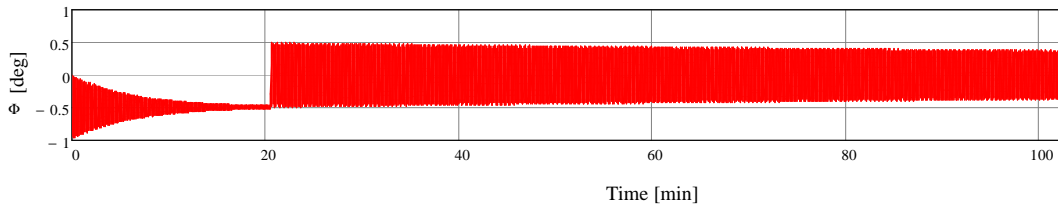


Fig-7.12 Attenuation of the uncoupled mode at $r = 4$ m. The wire boom deployment starts at $t = 0$ min and stops at $t = 20.6$ min

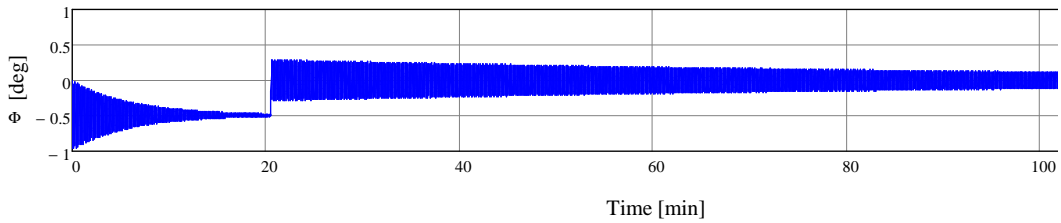


Fig-7.13 Attenuation of the coupled EA1 mode at $r = 4$ m using an EA1 tuned liquid damper. The wire boom deployment starts at $t = 0$ and stops at $t = 20.6$ min.

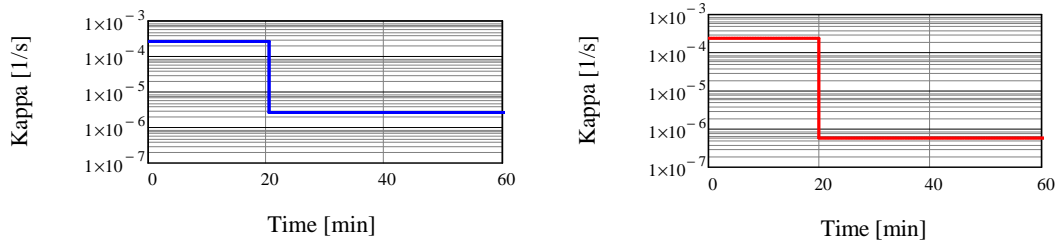


Fig-7.14 Internal wire boom damping of the coupled (left) and uncoupled EA1 mode (right) during and after deployment at $r = 40$ m. The RBSP wire boom parameters $\rho = 34.2$ mg/m and $k_0 = 0.001547$ kgm²/s are applied.

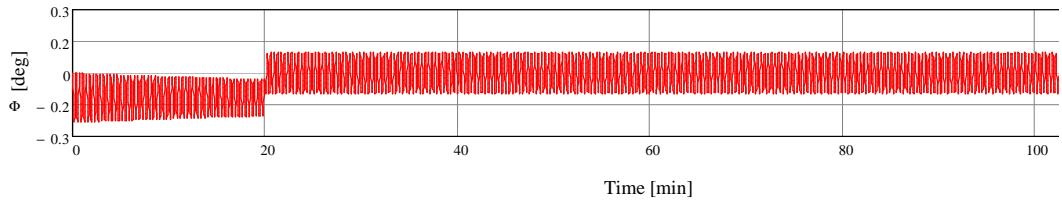


Fig-7.15 Attenuation of the uncoupled mode at $r = 40$ m. The wire boom deployment starts at $t = 0$ min and stops at $t = 20$ min.

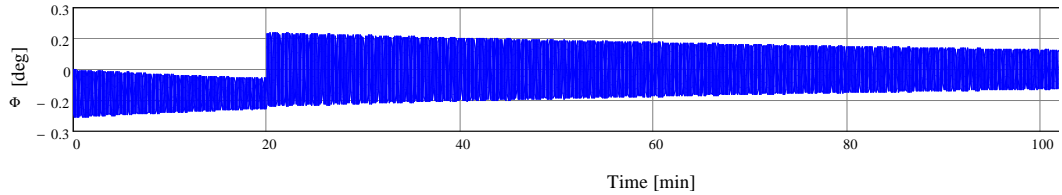


Fig-7.16 Attenuation of the coupled EA1 mode at $r = 40$ m using the tuned EA1 liquid damper. The wire boom deployment starts at $t = 0$ and stops at $t = 20$ min.

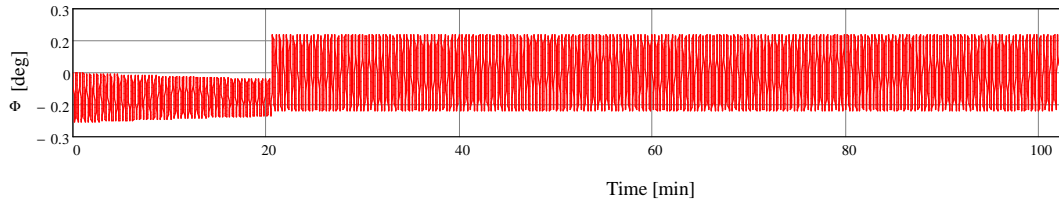


Fig-7.17 Attenuation of the uncoupled mode at $r = 40$ m. The wire boom deployment starts at $t = 0$ min and stops at $t = 20.6$ min

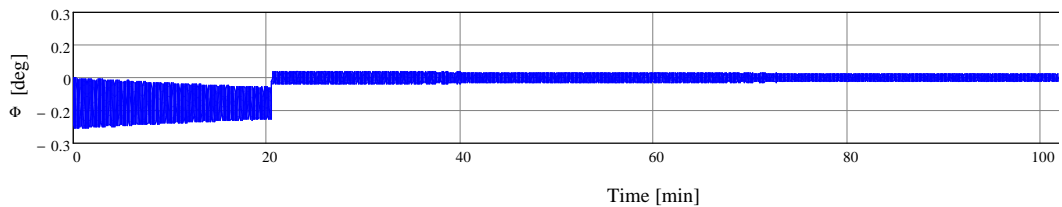


Fig-7.18 Attenuation of the coupled EA1 mode at $r = 40$ m using an EA1 tuned liquid damper. The wire boom deployment starts at $t = 0$ and stops at $t = 20.6$ min.

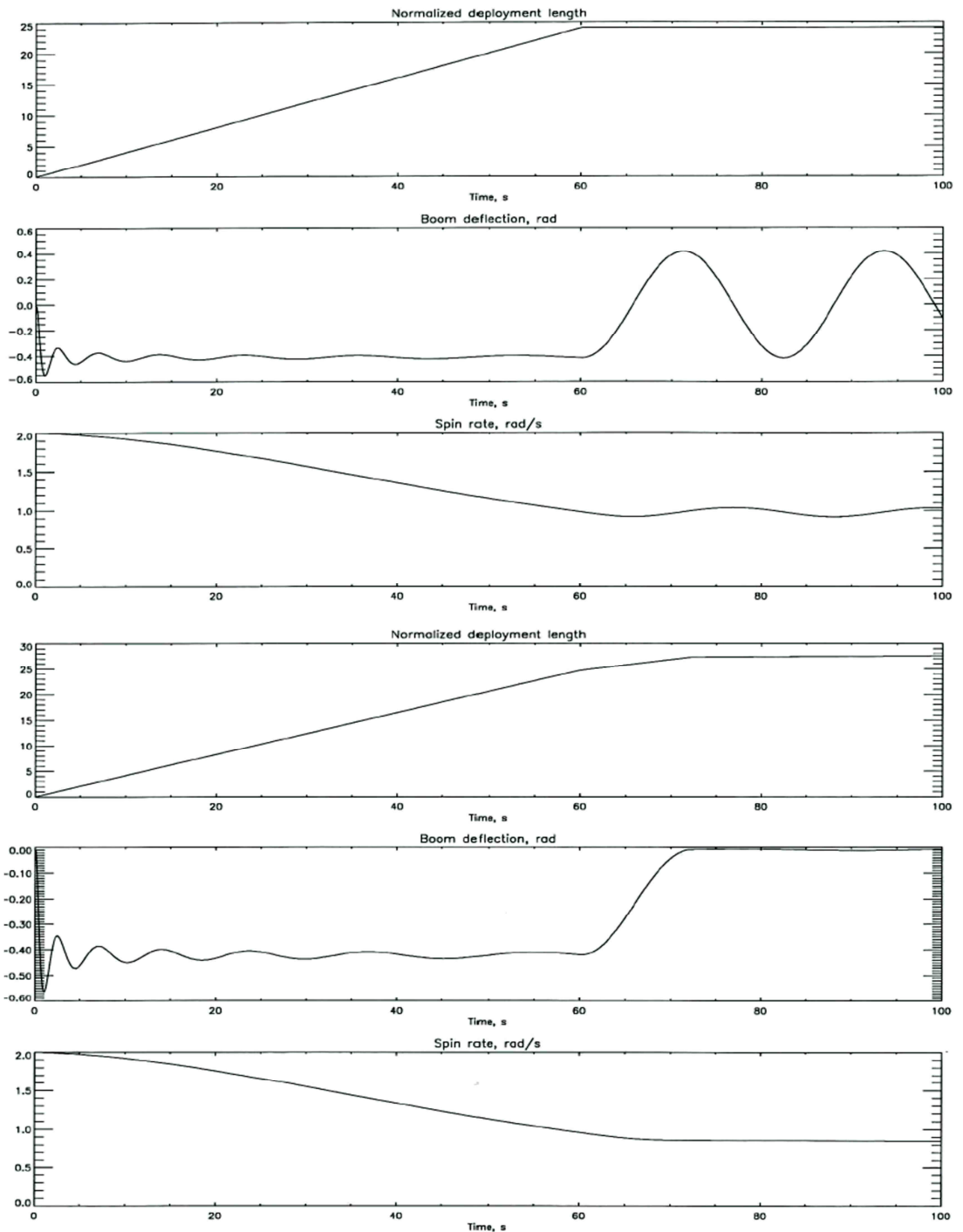


Fig-7.19 A deployment strategy to control the wire boom damping effectively. The upper three pictures show with time, after a stepwise induced constant deployment rate with a sudden stop at $t = 60$ s, the normalized deployment length r/R , the boom deflection φ and the hub spin-rate respectively. The lower three pictures show the same sequence with a different deployment strategy to control the wire boom amplitude: At $t = 60$ the deployment rate is first reduced by about 50% during a half cycle before it is stopped [Ivchenko et al., 2007].

MA Mode Damping

A complete optimization approach is obtained by applying Eqns. (6.16) to (6.18) yielding the I_x and I_y hub rotations with normal modes $\Psi = (\Psi_1, \Psi_2, \Psi_3, \Psi_4)^T$ as well. This enables the tuning of a_{MA} to comply with in principle the same residual deflection as the EA in-plane mode. The MA variant of Eqn. (7.5) in the $\Omega_{MA1,2}$ frequency vicinity using meridian dampers becomes

$$\tau_{MA,max} = \frac{I_{x,y} + 2I_B}{Z_0^2 \Omega^2} \left(\frac{P}{a_0^2} \right)^{-1}_{av} \quad (7.6)$$

The results of the pure MA analysis on basis of Eqn. (7.6) using the MA damper data from [Bakel, 1993] are shown in Fig-7.20. The enlarged MA dissipation function $P/a_0^2 \sim \lambda a_{MA}^4$ (compared to the EA mode) results from the large $a_{MA} = 2a_{EA} = 14$ mm liquid tube radius and proves to be tuned to the specified $\lambda_{MA} = 2.05$. The result is a broadband damper performance covering the full λ range from 2.02 to 2.1 with a factor 3 to 4 smaller time constants (faster) compared to the EA and N mode damping time. The analysis, however, does not cover the non-pure MA modes #3, 4 and 5 from Fig-6.11 whilst these modes are the essential specified MA modes.

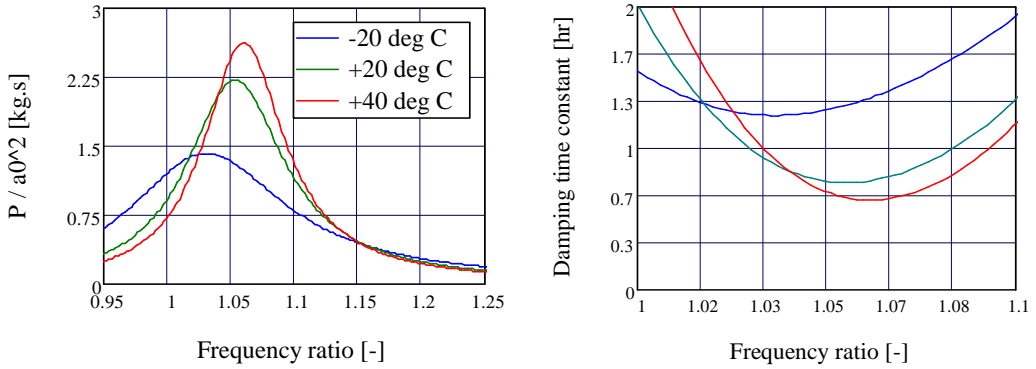


Fig-7.20 Cluster phase-A MA mode damping (left) and damping time constant of two MA dampers filled with PP3 whilst $a = 14$ mm, $L = 278$ mm, $b = 38.2$ and $Z_0 = 500$ mm.

The given analysis, however, shows the considerable bandwidth of the Cluster MA damper design with the potential to tackle these modes indirectly via gyroscopic coupling. To make this ability more explicit the full dynamics Cluster model duplicated from [McGee, 2009] is regarded in the following section. This model is able to determine the exact frequency ratios related to the I_x and I_y hub rotations since the compliant ω_x and ω_y angular velocities are part of its output. This closes the full design cycle and its required methodology.

7.8 Spacecraft Stability Analysis

The progression in 30 years of passive damping research and development is well reflected by the stability analysis of the RBSP S/C [McGee, 2009] and the results from this PhD thesis. The key elements of the RBSP mathematical physics approach were incorporated in a MathCad® model in order to compare the dynamics and stability of the RBSP and Cluster S/C. The modal and stability analysis is based on solving the 9×9 matrix singularity Eqn. (6.27) yielding the modal shapes, i.e., the λ values, their null space and the $\mathbf{x} = (z, \omega_x, \omega_y, \psi_1, \psi_2, \psi_3, \psi_4, k_1, k_2)^T$ eigenvectors. The mass of the RBSP ring dampers was derived from the inertia values yielding $m_d = 0.186$ kg. The results are given in Table-7.3 up to 7.5 where both S/C are symmetrized in inertia compliant to the equation

$$\sqrt{(\lambda_x - 1)(\lambda_y - 1)} = \frac{I_z}{I_{eq}} - 1. \quad (7.7)$$

An important conclusion from [McGee et al., 2009] is the fact that the analysis with four equal booms, no damping and symmetrized inertia is very close to the real cases with damping as used in the study of S/C manoeuvres like axial thrusts and repointing.

The RBSP stability analysis and its model was introduced at the end of section 6.7. The replicated model enables the Cluster S/C root sensitivity analysis using Eqn. (6.27) and the input from Table-7.3. This made clear that the resonance peaks of the Cluster wire boom configuration, based on the $Q = \omega/\Delta\omega$ factor, are very sharp compared to the RBSP S/C configuration. This can be explained since the Cluster spin stability safety margin $MS = 95.1\%$ (see Table-7.3) is more than twice the RBSP 40.6% value. This indicates that Cluster S/C is much more stable whilst the S/C operates at the trifold higher spin-rate 15 RPM compared with the RBSP S/C.

In Table-7.4 it is seen that the [McGee et al., 2009] RBSP results comply seamless with the replicated model results. Only the Ω_i/ω_z values are explicitly compared since the other vector components are exactly the same. The imaginary ψ_i mode shapes, shown in Fig-6.11, refer to the fact that the variables are out of phase with one another due to gyroscopic coupling. On basis of this solid calibration the undamped modal shapes are given for the Cluster S/C in phase-A at $\lambda_{eq} = 1.951$ in the last four rows of Table-7.5.

Table-7.3 Input parameters of the wire boom dynamics model using Cluster values and RBSP data from [McGee et al., 2009].

Parameter	S/C	Cluster	RBSP
$I_{eq} (I_x)$	Inertia around X-axis [kg.m ²]	225.0 (210)	349.7 (412.5)
$I_{eq} (I_y)$	Inertia around Y-axis [kg.m ²]	225.0 (240)	349.7 (264.6)
I_z	Inertia around Z-axis [kg.m ²]	439.0	491.7
$MS = \lambda_{eq} - 1$	Spin stability margin of safety MS [-]	95.1%	40.6%
M	S/C hub mass [kg]	550 (EOL) 1200 (BOL)	511.8
R_0	Wire boom attachment radius [m]	1.45	0.962
R_1	Wire boom length [m]	42.55	38.02
m_t	Effective sensor tip mass [kg]	0.231	0.231
m_d	Viscous damper mass [kg]	1.5	0.186
ω_z	S/C spin-rate [rpm]	15	5
θ_b	Boom mounting offset angle [deg]	0	0

Table-7.4 Undamped **RBSP S/C** modal shapes calibration towards [McGee et al., 2009].

Mode #	1	2	3	4	5
Ω_i/ω_z [-]	1.0135	1.0126	1.0473	1.0131	0.4403
MathCad model	1.01349	1.01257	1.04739	1.01312	0.44040
λ_i [-]	2.0135	2.0126	2.0473	2.0131	1.4403
z [m]	-0.069	0	0	0	0
ω_x [rad/s]	0	0	0.018i	0.043i	0.759i
ω_y [rad/s]	0	0	-0.018	0.043	0.759
ψ_1 [rad]	1	1	1	-1	-1
ψ_2 [rad]	1	-1	i	i	i
ψ_3 [rad]	1	1	-1	1	1
ψ_4 [rad]	1	-1	-i	-i	-i

Table-7.5 The undamped **Cluster S/C** modal shapes (phase-A data with $\lambda_{eq} = 1.951$) using the duplicated RBSP model in MathCad.

Mode #	1	2	3	4	5
Ω_i/ω_z [-]	1.0178 ^a 1.0173 ^b	1.0169	1.0825	1.0497	0.9839
λ_i [-]	2.0178 ^a 2.0173 ^b	2.0169	2.0825	2.0497	1.9839
z [m]	-0.071 ^a -0.033 ^b	0	0	0	0
ω_x [rad/s]	0	0	0.037i	-0.373i	6.24i
ω_y [rad/s]	0	0	-0.037	-0.373	6.24
ψ_1 [rad]	1	1	1	-1	-1
ψ_2 [rad]	1	-1	i	i	i
ψ_3 [rad]	1	1	-1	1	1
ψ_4 [rad]	1	-1	-i	-i	-i

^a Spacecraft total M=550 kg at EOL ^bM=1200 kg at BOL

Comparing the results in Tables-7.4 and 7.5 makes clear that:

- The RBSP MA mode #5 angular velocity $\omega_x = 0.759$ [rad/s] is close to pure hub nutation since Eqns. (2.4) and (2.13) yield $\omega_x = \theta_{nut}\lambda_{eq}\omega_z = 0.736$ rad/s at $\theta_{nut} = 1$ rad. The spin-rate normalized value $\omega_x/\omega_z = 1.45$ whilst for comparison the pure RBSP MA1 mode $\Omega_{MA1}/\omega_z = 3.084$.
- The Cluster pure hub nutation, however, yields $\omega_x = \theta_{nut}\lambda_{eq}\omega_z = 3.065$ rad/s at $\theta_{nut} = 1$ rad which is about half the MA mode #5 value of 6.24. The reason must be that the highly stable Cluster S/C configuration with its tri-fold spin-rate is forced in a high MA #5 oscillation mode. The value $\omega_x/\omega_z = 3.973$ is in the order of the pure MA_{1,2} modes (3.461 and 3.358) given Table-7.2.
- The S/C mass change from 1200 kg BOL to 550 kg EOL has only some impact on the Jelly-Fish mode #1.

Analysis of the Cluster Phase-A and B Modal Specifications

The Cluster phase-A ADCS modal specification is given by the upper part of Fig-7.22 whilst the lower part contains the analytical spectrum given by Eqns. (6.18) to (6.23) and Table-7.2. Up to now the analysis confined to the phase-A Cluster S/C specification but will now be directed towards phase-B. The phase-B frequency ratio specification in Fig-7.21 was taken from [van Bakel, 1993] and shows four specified bandwidths. These cover a

spectral range of oscillation modes centered about the specified EA (1.4), N (1.75) and MA (2.08) modes. The rationale of the fourth bandwidth (close to the N mode) at the frequency ratio 0.79 ± 0.03 is not traceable or accessible (non-disclosed) as confirmed by [Kermans, 2008] and [de Kraker, 2008]. The indicated bandwidths are probably accounting for EA, N and MA variations by:

- BOL versus EOL inertia changes caused by the reduction of the amount of propellant
- Engineering issues like uncertainties, contingencies and tolerances
- Inclusion of spectral modes from the full non-linear EL solution or MS modes
- Other modes resulting from the radial magnetometers or axial antennas
- Derived additional modes from the diverse boom engineering tests
- Contingency modes anticipating for an implementation later in the project phase.

The required phase-B design, as specified by Fig-7.21, proves to be close to the early phase-A design trade-offs indicated in Figs-7.4 and 7.5. The worst case damping curve (as requirements envelope) in Fig-7.21 gets very close to Fig-7.5 using PP3 at -20°C in both dampers. The phase-B EA1 (0.4) and N (0.75) modes are recognized straight away but the MA modes (frequency ratios) $\lambda - 1 = 1.05$ in phase-A and 0.79 and 1.08 in phase-B must have been derived from higher level Cluster S/C ADCS system engineering trade-offs. These can be facilitated by a complete non-linear Euler-Lagrange (EL) model of the S/C dynamics.

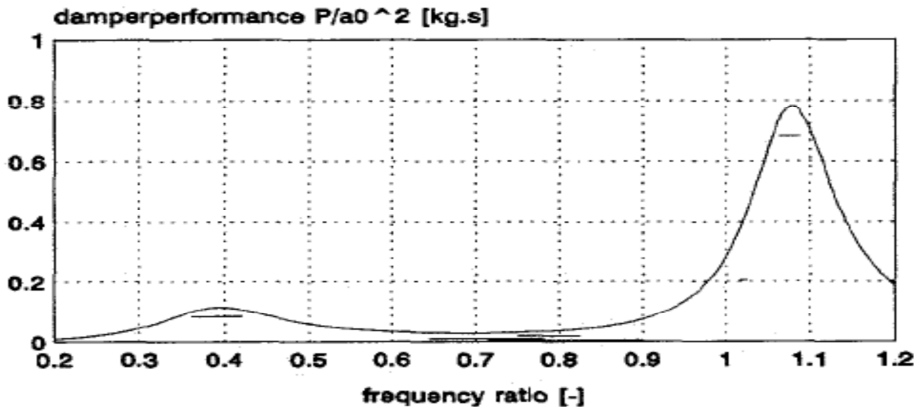


Fig-7.21 Visualization of the phase-B damping requirements [van Bakel 1993].

Such a system dynamics model, e.g. based on [Lai and Bhavnani, 1975], can generate the full spectrum of oscillation modes including the impact of S/C engineering maturation, operational constraints, contingencies and BOL to EOL mass variations. The replicated RBSP model [McGee et al., 2009] facilitates such an approach as well and reveals explicitly the coupled MA modes. This is clear looking at the key Fig-7.23 which resulted after applying the replicated and calibrated RBSP stability model to the Cluster phase-A and phase-B inertia values. The following results are extracted by comparing the histograms in Fig-7.22 (upper) and 7.23:

- Identified modes MA_{#1}, MA_{#2} and MA_{#3} are not present in the phase-A specification
- Phase-A mode MA_{#4} is fully compliant with the specified phase-A value $\lambda_{MA} = 2.05$
- Phase-A mode MA_{#5} = 1.984 is close to the phase-A specified nutation value $\lambda_0 = 1.951$
- Phase-B mode MA_{#4} update 2.022 is not given by the specification in Fig-7.21
- Phase-B mode MA_{#5} update 1.815 is within the specified 0.79 ± 0.03 in Fig-7.21.

The MA_{#5} = 1.815 value deviates from the specified pure hub nutation mode $\lambda_0 = 1.75$ in phase-B (see Table-7.1) which is traceable within the specified broad bandwidth 0.72 ± 0.06 in Fig-7.21. Though the MA_{#5} mode change is imposed by the change in the rigid hub inertia

ratio from $\lambda_o = 1.951$ to 1.75, it is not necessarily the same. The reason is that the three MA modes (#3, #4 and #5), depicted in Fig-6.11, describe gyroscopically coupled modes between the solid ring of wire boom masses and the hub itself. The application of the RBSP model to the Cluster ND specification would, therefore, have led to different requirements.

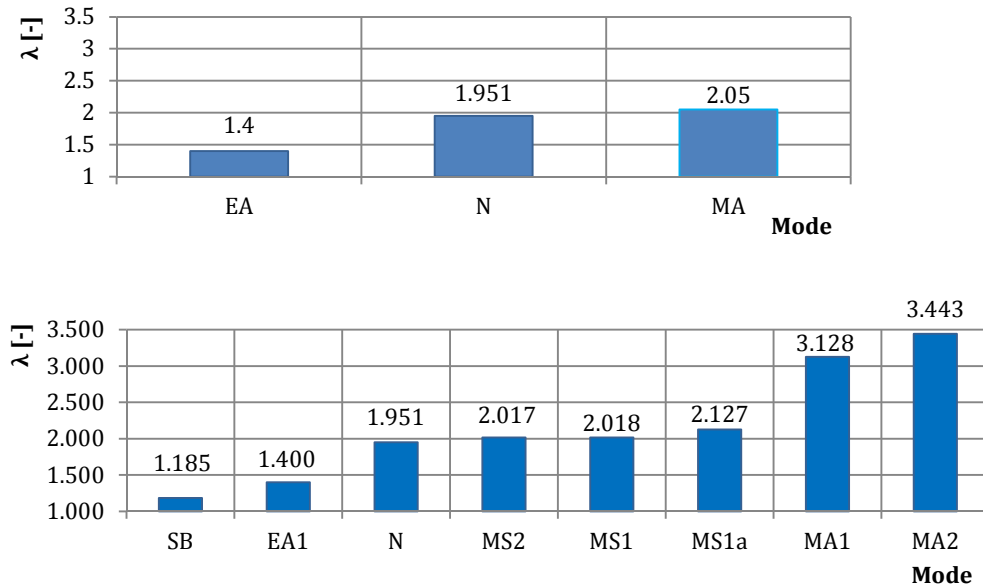


Fig-7.22 Cluster ADCS phase-A modal specification and spectrum from Eqns. (6.18)-(6.23).

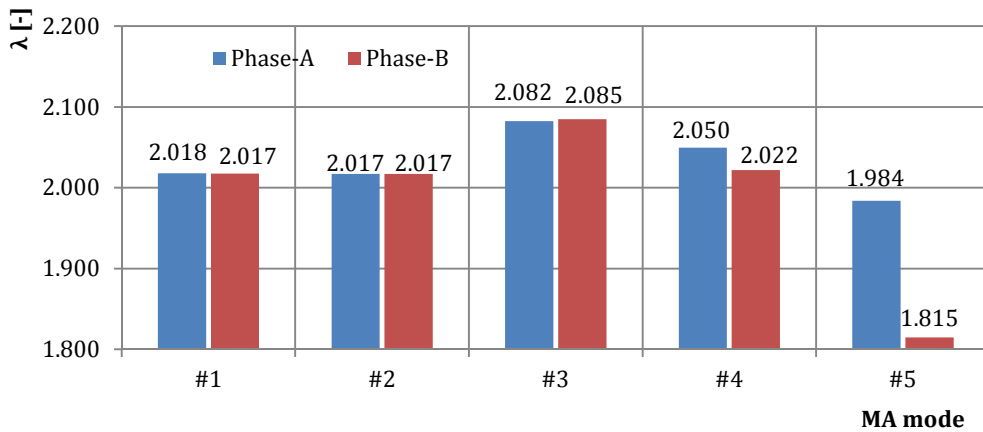


Fig-7.23 Cluster S/C dynamics: MA modes changes from phase-A to B on basis of the MathCad® model.

7.9 Bandwidth Considerations and Design Options

In principle the required damping rates of all modes can be derived from the specified time constants and the full EL treatise or the replicated RBSP model. The soundness of the latter model was used for the Cluster phase-A/B analysis in the previous section. We will now give some more consideration towards the bandwidth and damper system choice as part of the bottom-up system engineering yielding additional design options.

The choice of two liquid dampers enables the exponential attenuation of the two most bothersome asymmetric modes (EA1 and MA) and the N mode by their combination. A logical choice in case of the Cluster damper design could have been:

1. Take the extremes EA1 (1.4) and MA#3 (2.08)
2. Tune the two dampers to these modes
3. Implement additional MA bandwidth to cover additional modes.

The overall damping performance can be simulated by the multiple excitation (multi-mode) theory derived in section 2.9. The contents of [van Bakel, 1993] shows that such an approach was indeed followed but not disclosed [de Kraker, 2008].

A number of other damping options exist as will be made clear by the following arguments. At first the Fokker “tube-with-endpots” liquid damper was primarily meant to attenuate nutation by viscous dissipation. The latter is initiated by the nutation acceleration amplitude $a_{0,N}$ on basis of Eqn. (2.21) by

$$a_{0,N} = \theta_N \omega_z^2 Z_0 (\lambda^2 - 2\lambda + 2\lambda_x). \quad (7.8)$$

The MA modes can be tackled by their ω_{x0} (or ω_{y0}) value obtained from the RBSP stability model and given in Table-7.5. These amplitudes define the magnitudes of the accelerations $a_{0,i}$ in the liquid tube whilst Ω_i has to be used in Eqn. (7.6).

Consider an equatorially mounted MA mode damper at $Z = Z_0$ above the COM plane. The time derivative of the mode i angular velocity $\omega_{x,i} = -\omega_{x0} \sin \Omega_i t$ (or) $\omega_{y,i} = \omega_{y0} \cos \Omega_i t$ yields an acceleration for viscous dissipation

$$a_{0,i} = \omega_{x,i} Z_0 \Omega_i = \omega_{x,i} Z_0 (\lambda_i - 1) \omega_z.$$

In addition a straightness correction for the equatorial mounting of the damper is required so finally

$$a_{0,i} = \omega_{x,i} Z_0 \frac{\sin \alpha}{\alpha} (\lambda_i - 1) \omega_z. \quad (7.9)$$

The angle $2\alpha = \text{atan}(L/Z_0)$ accounts for the geometrical deviations from the iso-centrifugal circle. Finally Eqn. (2.86) enables the study of the simultaneous use of an arbitrary number of modes by the analysis of the time development of the dissipation function $P(t)/a_0^2$. This closes the recursive development circle of a bottom-up system engineering design tuned to high level ADCS SE trade-offs.

The choice of a meridian MA damper (mounted parallel to the Z-axis) and an equatorial EA damper both mounted in the XY plane could also be an effective choice. In that case Eqn. (7.5) applies to both dampers using either I_T for the EA mode or $I_x + 2 \cdot I_B$ (or I_y) for the MA mode. It is also possible to use two meridian dampers in the $Z = 0$ COM plane. Another choice could be to dampen the highest order MA1 and MA2 modes from Table-6.4 since these represent the high frequency disturbances in the S/C spin-axis inertial stabilization. The given considerations show the existence of multiple design options.

In the following sections the tuning sensitivity, extended PTM tests, Cluster flight validation and final conclusions will be dealt with.

7.10 Tuning Sensitivity of the Final Design

An additional strong advantage of the proposed broadband approach is found in minimizing the tuning sensitivity of the final FM ND design. The mass- and inertia figures of the Cluster S/C were suffering with rather large margins and uncertainty in the initial design phase-A (early 1991). At the start of a S/C development project this issue is very important in terms of development risk mitigation for the ADCS subcontractors. The Cluster nominal inertia value was $\lambda_0 = 1.948 \pm 10\%$ in the early phase-A, later 1.951 and finally 1.75 in phase-B. Taking the extreme $\lambda = 1.948 - 10\% = 1.75$ at nominal spin-rate this implies a change of $\pm 21\%$ in the nutation frequency since Eqn. (2.110) dictates

$$\frac{\Delta\Omega_0}{\Omega_0} = \frac{\Delta a}{a} = \frac{\lambda_0}{\lambda_0 - 1} \frac{\Delta\lambda_0}{\lambda_0} = -20.6\% \quad (7.10)$$

This equation expresses that only a change in the tube radius is chosen to comply with an extreme phase-C/D change in the S/C inertia ratio. In general this change has to be overcome by a new proper combination of the parameter set $\langle a, b, h, L \rangle$ which in its turn means a considerable change of the design dimensions, interfaces and physical (thermal, mechanical) properties and, at last but not at least, the project control. The proposed ND combination will be less vulnerable to this design change necessity. The changes are recognized in the early phase-A design driving parameters given in Table-7.1, the ND parameters in section 7.4 and the traceable FM EA and MA parameters [van Bakel, 1993] in Table-7.6. The mounting radius was obviously used as a tuning parameter since it differs for the EA and MA dampers and the original value of 900 mm.

Table-7.6 FM and PTM phase-A and final EA and MA Cluster damper data [van Bakel, 1993].

Liquid damper model		FM				PTM	
		EA	final	MA	final	EA	MA
R_m	Mounting radius [mm]	1370	1410	1370	1422	-	-
a	Fluid tube radius [mm]	7.0	6.4	14.0	14.0	5.0	10.0
b	End-pot radius [mm]	48.6	44.2	38.2	36.8	34.7	27.3
h_o	Distance fluid tube axis to end-pot level [mm]	7.0	13.8	22.5	35.6	5.0	16.1
L	Fluid tube length [mm]	278.0	278.0	278.0	278.0	199.0	199.0
m	Estimated mass [kg]	1.2	-	1.8	-	2.3	2.5
	Flutec type	PP3	-	PP3	-	PP3	PP3
τ_r	Transient damping time constant [min]	39.8	-	159	-	20.3	81.3
T_r	Time constant of transient response [s] using a 1% remnant response criterion.	183.0	-	730	-	93.0	374.0

7.11 PTM Experiments

The combined damper action has to attenuate three modes. This means that both dampers have to be tested simultaneously. The aim of the damping performance tests is to measure the dissipation function P/a_0^2 versus the excitation angle θ and frequency ratio λ .

The existing FY-2 air-bearing set-up at the Dutch Space facilities (see Chapter 3 and 4) complied with the EA1- and N-mode. However for the MA mode, a dedicated change in the test rig inertia I and test arm-length R was required as shown in Table-7.7.

Table-7.7 Test rig inertia and airbearing arm length to test the EA1, N and MA modes.

Mode	Test range	R_a [m]	I [kg·m ²]
EA1	$0.32 \leq \lambda - 1 \leq 0.48$	2	70
N	$0.65 \leq \lambda - 1 \leq 0.85$	2	70
MA	$1.00 \leq \lambda - 1 \leq 1.20$	0.8	300

The resulting test matrices are given in Tables-7.8 and 7.9. Table-7.8 shows the N- and EA1-mode PTM test matrix and Table-7.9 the MA-mode matrix. All parameter values are obtained by applying the scaling relations from section 2.11 in Chapter 2. The 1st column contains the EA1 (Table-7.9) and MA (Table-7.9) frequency ratios to be tested, the 2nd the airbearing period, the 3rd the transient response time (1% criterion), the 4th the total test time, the 5th and 6th the airbearing angular test range and the 7th the predicted (scaled) damping performance.

The steady state response of the dampers has to be measured and distinguished strictly from the transient responses. This means that the measuring time has to be long enough to extinct the transients. Taking a 1% criterion Table-7.9 (first row $\tau = 1971$ s) shows that the long term transient response of the MA damper is the limiting factor.

Table-7.8 Test matrix of the N- and EA-mode PTM experiments with $R=2$ meter and $I=70$ kg·m²

$\lambda_0 - 1$ [-]	T_{airb} [s]	τ [s]	T_{test} hr:min:s	Φ_{max} deg	Φ_{min} arcsec	P/a_0^2 [g·s]
0.32	6.38	1036	1:33:54	0.521	8.172	17.40
0.36	5.67	388	0:35:11	0.411	6.444	36.67
0.40	5.10	218	0:19:44	0.333	5.220	52.94
0.44	4.64	233	0:21:07	0.273	4.320	40.91
0.48	4.25	313	0:28:20	0.232	3.636	25.61
0.65	3.14	560	0:59:33	2.300	13.932	7.81
0.75	2.72	455	0:48:23	1.720	10.440	7.22
0.85	2.40	239	0:25:27	1.340	8.136	10.68

The testing was quite challenging. This was already the case for the FY-2 damper but was even more severe for the combined Cluster PTM triple test action. Refined analysis [van Bakel, 1993] was made at UCN-Aerospace combined with special air-bearing experiments at Fokker Space [Webber, 1991] to investigate air-bearing side effects. Dedicated engineering effort was invested in the setup and dimensioning of the air-bearing PTM experiment as was done for the FY-2 ND described in Chapter 4. This was necessary to avoid test arm cross-over effects and non-flight relevant test artefacts (anomalies) in damper performance caused by the following items:

- Linear- and torsion stiffness modes control by design of the air-bearing test-arm
- Taking the coupled equations of motion of damper and the test-rig into account
- Regarding transient (sloshing) effects from the two different nutation dampers
- Refined differential choices of the MOI and the arm-length R of the test-bearing
- Analysis of transition to turbulence flows based on the Reynolds number Re
- Study of tube liquid tube in- and out flow effects.

The damping behaviour at large nutation accelerations is for a significant part caused by the transient damper behaviour according to [van Bakel, 1993] and [Webber, 1991]. It was shown [van Bakel, 1993] that the energy exchange between the test rotor and the NDs impacts the damping performance at off-resonance frequencies.

Table-7.9 Test matrix of the MA-mode PTM experiments with $R=0.8$ meter and $I=300$ kg·m²

$\lambda_0 - 1$ [-]	T_{airb} [s]	τ [s]	T_{test} hr:min:s	Φ_{max} deg	Φ_{min} arcsec	P/a_0^2 [g·s]
0.95	2.15	1971	2:41:01	0.566	14.904	27.80
1.00	2.04	817	1:06:46	0.501	13.428	60.49
1.05	1.94	263	0:21:30	0.455	12.204	170.29
1.10	1.86	141	0:11:33	0.414	11.088	288.98
1.15	1.77	299	0:24:26	0.379	10.152	124.93

7.12 Normal Operation

The qualification test program was successfully closed at UCN-Aerospace nowadays named Aeronamic Aircraft Subsystems. The H/W was shipped and mounted into the Cluster S/C in 1993. The passive liquid damper performs within nominal performance since the launch in August 2000 up to now [ESA, 2012].

The Cluster S/C is described by [Credland and Lehn, 1993]. They mention the passive liquid NDs to be part of the Cluster ADCS and to enhance the damping characteristics of the S/C body.

A smooth deployment of the Electric Field Wave (EFW) instrument wire antennas within nominal nutation prediction is described by [Dow et al., 2004]. This source deals with the Cluster II part of the mission and the nutation performance derived from telemetry data of all four S/C, i.e.

- A nominal initial attitude and rapid nutation damping in the range 0.5° down to 0.1° .
- The estimated nutation levels during the rigid boom deployments were small compared to the maximum 6 degree value from the Cluster user manual [ESA, 2012] and damper specification in Table-7.1. The results (three booms per S/C given only) are summarized in Table-7.10. The explanation is that for the Cluster II S/C more propellant was left onboard compared to the Cluster I S/C resulting in an improved damper to S/C mass ratio.

Table-7.10 Maximum nutation levels during the Cluster-II rigid boom deployment [Dow et al., 2004].

S/C	-Y boom [deg]	+Y boom [deg]	-X boom [deg]
1	1.1	1.7	1.5
2	1.1	0.7	0.2
3	1.1	0.5	0.8
4	1.2	1.9	1.3

Spin-rate Changes

The EFW instrument comprises four wire boom units, each containing about 42.5 m of wire to be deployed by motors in each unit, shown in Fig-7.25. The length of the wire boom deployment is monitored by two independent means:

1. A potentiometer giving an analog measurement of the boom length contained in the S/C telemetry.
2. A "click counter" giving a digital measurement of the boom length. This value is also used by the EFW flight onboard data handling (OBDH) system to control the deployment. The click counter is just a switch going on and off once during each half revolution of a measurement wheel which is driven by the cable.

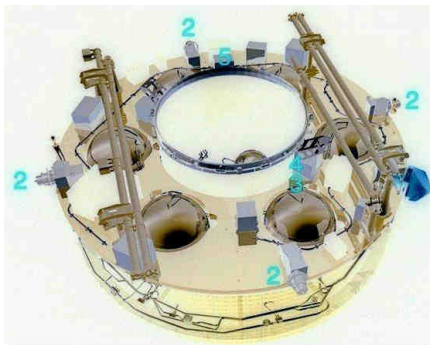


Fig-7.25 The four EFW instruments (2) mounted on the Cluster S/C (left) and before mounting (right).

The boom lengths agreed with the reduction in S/C spin-rate and potentiometer readings. The processing of data from [ESA, 2012] yields Fig-7.26. This figure illustrates the stepwise spin-rate change during the EFW instrument wire boom pair deployment per S/C (booms 1+2 simultaneously followed by 3+4). For all four S/C named Rumba, Salsa, Samba and Tango the deployment cases are shown. For the Rumba S/C the deployment had a deviation (boom 1 and 2 deployed after each other) but also successful sequence. During the intervals 5 to 6, 8 to 9 and 11 to 12 (Rumba 5 to 6, 9 to 10 and 12 to 13) a spin-up is executed.

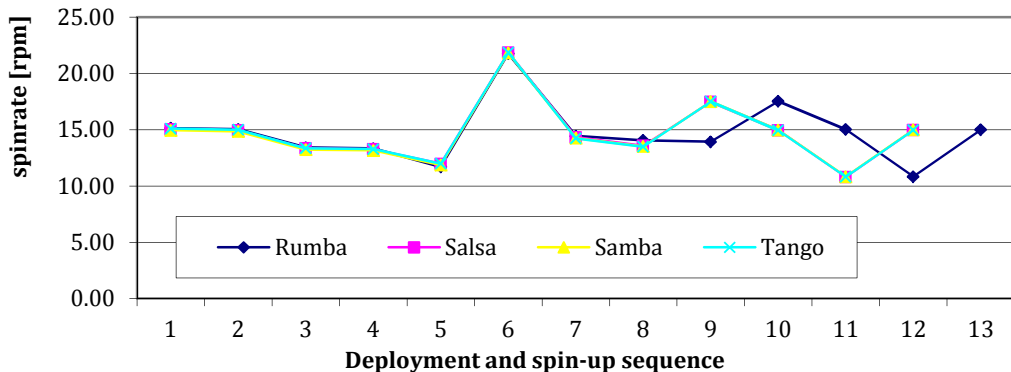


Fig-7.26 Spin-rate changes after deployment per S/C of the pairs 1+2 followed by 3+4 in successive steps. During the sequences 5 to 6, 8 to 9 and 11 to 12 (for Rumba 5 to 6, 9 to 10 and 12 to 13) a spin-up is executed.

7.13 Summary and Conclusions

This chapter dealt with the early design phase of the broadband Cluster liquid dampers in 1991 and the developments in liquid damper design up to 2012. The field of passive ADCS is still in development whilst the art of EFW instrument design has become mature.

The following was achieved in this chapter:

- The design space of multiple liquid dampers was investigated showing refined and extended damping potentials to be incorporated in the passive ADCS subsystem of a spinning S/C
- A recursive bottom-up design versus top-down methodology was developed to attenuate EA, N and MA oscillation modes
- Bandwidth considerations were given which prove the potential to extend the applicability of the combined liquid damper designs even further
- The tuning sensitivity of the final design was studied
- The severe requirements of testing a multi-mode liquid damper were studied to determine the derived requirements for the airbearing test setup.
- Finally the Cluster flight evidence was explored which showed evidence of the successful passive operation firmly within the original requirements.

The goal of the treatise was to develop both quantitative and qualitative bottom-up and top-down design methodologies using the available scientific literature from the past. The Cluster research in the frame of this thesis could not be fully released from the high-tech space industry due to non-disclosure restrictions. The disclosed results re-validated the potentials of the proposed Cluster damper system concept which gave a sound basis in phase-A to push the application of an extended liquid damper design in the Cluster ADCS. The concept development in the later phases B up to C/D within the industry was beyond

the scope of the author since the activities were transferred from Dutch Space to UCN Aerospace in the early 90s after the release of the phase-A design. Nevertheless the design was fully explored using the latest models of spinning S/C dynamics. The following review of the RBSP article [McGee, 2009], taking the analysis and results of this thesis into account, reflects the actual status [2012] of passive multi-mode damper designs:

- It is concluded that the internal wire boom damping itself is able to attenuate all modes. However, a time constant range is not given. The RBSP spin plane boom cable damping parameters in support of the GNC boom dynamics modeling efforts [RBSP-1, 2009] are characterized by a boom settling to less than 0.5° within 8-12 hours post-repointing. The Cluster analysis depicts a much better condition since the Cluster wire boom (remnant oscillation) amplitude can be damped after full deployment starting at less than 0.2° with a time constant less than 2.5 hour. In case of an optimized phase timing of the deployment stop even a start at 0.03° is possible disregarding boom material and boom anchor position artifacts.
- A suggestion is made that some additional boom damping between the S/C body and the wire booms is required to tackle all modes effectively. A comparable solution based on a hinge pendulum damper concept on the Galileo S/C, confined to nutation only, was already suggested and worked out analytically by [Eke et al., 1989].
- In the early 70s ring dampers, pendulum dampers and liquid dampers with-tube-and-endpots (the NDs in this thesis) were studied in full mathematical detail. A trade-off on the use of these dampers was given by [Ancher et al., 1977]. The annular and pendulum ND designs suffer both with considerable angular off-sets of about 2-3 rad and significant inrush time constants of about 40 min which are not accounted for in the RBSP model. The tube-with-endpots Fokker ND design as applied in the Cluster ADCS lacks this artefact.
- The conclusion that only the RBSP hub nutation mode is damped effectively does not comply with the dedicated design outcome of the multi-mode broadband Cluster liquid damper system which is based on the well tuneable tube-with-endpots Fokker design. The broadband Fokker Cluster system damper does provide optimally tuned damping to both the normal (out-of-plane) modes (EA, MA) via gyroscopic coupling and the nutation mode (N).
- RBSP flight data is not yet available but only nutation related Cluster data to validate the modelled normal mode damping results. The excellent ND performance of the Cluster ADCS reported by [Dow et al., 2004] serves as an indirect but incomplete prove of the hybrid liquid damper design.
- An impression of the accuracy of future RBSP ADCS data is given by [Srinivasam et al., 2012]. The RBSP spin-axis estimation methodology using RF Doppler, is validated by in-orbit data from the Interstellar Boundary Explorer (IBEX) S/C. As a result, the flight spin-rate accuracy determination of the RBPS spacecraft will be better than 50 ppm.

The refined liquid damper system concept contributes to the success of the Cluster mission and especially its ADCS performance. On the other hand, it is hard to trace and validate the designed multi-mode performance itself. It would be of great scientific value to obtain dedicated ADCS flight data. The excellent nutation damping performance of the Cluster S/C ADCS, comfortably within the specification values, was traceable and worked out. This proves indirectly the specification compliant broadband performance of the combined (EA1, N and MA mode) liquid damper concept.

The passive Cluster damping control system with in addition the internal wire damping enables the boom deflection limit and its damping time constant to be a design parameter. The highly reliable independent damper subsystem is fully passive and relatively easy to implement in a spinning S/C ADCS.

8 Conclusions and discussion

Simplicity is the ultimate sophistication.

Leonardo da Vinci

*Italian engineer, painter, & sculptor
(1452 - 1519)*

8.1 Introduction

In this thesis, the theory, design, verification and application, and applications of passive liquid dampers have been studied. These dampers are incorporated in the structures of buildings, bridges and ships but also as nutation dampers in windmills and spinning spacecraft. The liquid (nutation) damper class is still wanted due to its broad applicability, extreme reliability, robustness, long life time and its ease of manufacturability. In this chapter the space research results and especially the hybrid multi-mode liquid damper design will be outlined and the future research topics addressed.

8.2 Objectives and Results

The research objectives laid down in section 1.5 have been overall achieved. The specific and detailed conclusions are found at the end of each chapter. The following main conclusions are given whilst the reference between brackets refers to the applicable section.

Methodology

M-1

The cross-fertilization between the space and terrestrial applications of (liquid) dampers was studied and delivered an active broadband liquid damper candidate from shipbuilding engineering. The Tuned Liquid Damper (TLD) concept was investigated as potential active

broadband damper in space applications. The design was overruled as space ADCS candidate for reasons of reliability and complexity. The multi-mode liquid damper design proved to be the best candidate (2.8.5).

M-2

The scope and limitations in the application of NDs was investigated and summarized (1.7).

M-3

The differences between a vertical and horizontal pendulum test setup were investigated. An extensive treatment of the applied Dutch vertical air-bearing pendulum was given including the measurement principle and test limitations (3.3). The results were used in the refined setup of the FY2 (4.2) and the Cluster performance model tests (7.11).

Theory

T-1

A broad introduction was generated in the field of spin-stabilized S/C and passive ADCS systems (2.1). A number of nutation damper models were derived, (re)analyzed and compared (2.4 until 2.8). The Hagen-Poiseuille (HP) model was derived with and without (frictional) endpot effects (2.8.4). It was shown that these endpot effects can be neglected in a regular ND design with $b \gg a$.

The application strength of the NS model was shown by the latest calibration results from literature (2.8.1). Two Navier-Stokes (NS) models (Fokker, ESA) were compared during the Ulysses anomaly study (5.4.1). The results match seamless with the re-derived Fokker NS model (2.8.6).

The HP model is only applicable, at low spin-rates and consequently low nutation frequencies, as limiting case of the NS model. An advanced HP model (RHP-1) was analyzed which was used in the EQUATOR-S ND analysis (2.8.5). The same holds for a second refined HP (RHP-2) model to analyze the performance of a tunable liquid damper (TLD). All models differ on basis of different constraints but were shown to comply.

T-2

The multi-mode damper design requires a model to analyze the effects of multiple excitations in one damper. A time dependent damping equation was derived which accounts for the simultaneous damping effect of multiple modes (2.9). A comparable equation (without derivation) given by [van Bakel, 1993] is based on the prior developed models at Fokker Space in the period 1980-1992 and was used as part of the qualification of the Cluster ND design.

T-3

The limiting nutation angle was investigated using multiple models and sources. The impact of the endpot surface treatment and damping liquid choice was taken into account. Equations to analyze the limiting angle are given and derived to be used in the COSB and FY2 test performance analysis.

The state of the art was explored by an exploration of recent scientific literature in the field of nano-tribology [Bhushan, 2008] and wetting transitions on biomimetic surfaces [Bormashenko, 2010] and showed:

- The need for fundamental knowledge development of adhesion, friction, stiction and wetting
- A broad applicability in the field of micro-electronics, NEMS/MEMS, green technologies, coating technology, joining processes, design of hydrophobic materials, self-cleaning properties, etc
- The general theory of contact angle hysteresis has still not been formulated.

Well defined microscopic surface treatments are the experimental way forward. Refined surface treatment of the endpot materials in combination with dedicated coatings offers a way to reduce the minimum nutation angle and dead band even further (2.10).

T-4

A broad in-depth scientific literature research in the field of fluid dynamics was executed. The laminar and turbulent behavior of the damping liquid was studied for unidirectional and oscillatory tube flows. The flow stability, in and outlet effects in the endpots and effective damping length were investigated (2.8.1 to 2.8.3). This knowledge combined with the extensive analysis of all available damping performance tests resulted in an appropriate methodology to estimate the effective damping length (8.2, SE-2).

T-5

The relevant theory to scale space to terrestrial tests conditions was extracted and adapted from literature in a compliant parameter and equation format (2.11).

Systems Engineering

SE-1

An inventory of boundary conditions was made thinking ahead for production and project cost escalations with risk mitigation as an essential part of system engineering (SE). The release of changing inertia values during a (spinning) S/C development project and the release of flight data require recalibrations of the ND design. As a rule, due to interface restrictions, the mass and thermal-mechanical requirements are fixed and therefore preferably kept within a certain range. Trade-offs between, customer requirements discovery, effective modeling and (ground) testing options have to be made. In the high-tech industry, however, there is little focus on a profound scientifically based bottom-up SE approach though such effort does pay off. It was the quest for this thesis to prove the added value of such an investment. The developed methodologies do contribute to a science based SE approach in the development of multi-mode liquid dampers (2.12 and 2.13).

SE-2

The following key SE issue is dealt with out of the scope of the previous chapters since the results were obtained after an overall analysis of all damping performance tests in the previous chapters combined with the latest results from fluid dynamics theory (2.8.3).

The first step in tuning the damper resonance frequency towards the excitation frequency is achieved by the choice of the design geometry parameters $\langle a, b, h, L \rangle$ and the damping fluid on basis of modeling. This offers a first order guess for the initial design. In addition the fluid mechanics research in Chapter 2 and the compliant performance test analysis in Chapter 4 and 5 make clear that the tuning process of a liquid damper can be accelerated by a proper initial estimate. The methodology will be explained on basis of the test results and modeling summary given in Table-8.1 and Fig-8.1.

Fig-8.1 shows the Trajectories in the (Re_A, Re_R) flow characteristics field of the Ulysses, Cluster and FY-2 FM liquid damper models EA, MA and N. The FY-2 QM and FM 3rd and 4th calibration series at the virtual spin-rate 3.302 rpm finish just above the quasi-steady laminar flow region with the largest $\delta/a \approx 0.3$ ratio (mind that $a = R$ in the figure). On the other side the smallest $\delta/a \approx 0.06$ ratio is found for the Cluster FM MA 15 rpm design in the Stokes laminar flow region.

The tube flow entrance (inlet) length is regarded to be a measure of the effective damping length increase ΔL (as surplus to the physical model length). This assumption is validated by the unidirectional flow equivalent, i.e., the derivation of Eqns. (2.44) and (2.45).

The last column of Table-8.1 contains the ΔL value derived from the recursive FY2 PTM, QM and FM performance tests in Chapter 4 and the Ulysses ND re-calibration in Chapter 5. The Cluster ΔL values for the MA and EA dampers were obtained by applying Eqn. (2.106) to the test data from [van Bakel, 1993].

In addition, the ΔL magnitude proves to become a constant below a certain nutation angle. The evidence of this fact is given by Fig-4.11 which shows that the 100 rpm FY2 ND performance gets tuned at 1.25° already and moves to a constant damping value beyond 0.25° . This value is much larger than the Stokes layer laminar flow region entrance angle $\theta_A = 0.083^\circ$ given in Table-8.1. This table makes also clear that the δ/a ratio of the FY2 ND is relatively high which is caused by the small tube radius $a = 3$ mm (QM) or 3.8 mm (FM). The FY2 ND performance is, therefore, at $Re_A = 8000$ (with nutation angle θ_A) already driven in a quasi-steady-non-oscillatory mode with consequently a very low Re value. This explains that Boussinesq's Eqn. (2.46), normally valid for a single directional flow, applies rather than the Stokes Eqn. (2.50). The Cluster and Ulysses ND cases, however, yield higher Re values and the Stokes Eqn. (2.50) delivers clearly better estimates.

Table-8.1 Educated guesses for the effective length of liquid dampers on basis of ND heritage.

	θ_A [deg]	Re_R [-]	Re_A [-]	Re [-]	δ [mm]	$2 \cdot a$ [mm]	Stokes ΔL_{inlet} [mm]	Bousinesq ΔL_{inlet} [mm]	Calibration ΔL [mm]
Ulysses FM 5 rpm	1.14	51	8071	536	1.1	16.0	11.0	557.9	14-15
Cluster FM EA 15 rpm	0.9	23	8016	169	1.3	12.8	6.2	140.5	12.4
Cluster FM MA 15 rpm	0.492	286	8055	3502	0.8	28.0	22.3	6373.0	33.9
FY-2 FM 100rpm	0.083	60	8032	43	0.5	7.6	0.4	21.0	9-10
FY-2 QM 3.302 rpm	0.104	9	8016	11	1.0	6.0	0.5	4.3	14-15
FY-2 FM 3.302 rpm	0.147	19	8031	27	0.9	7.6	0.7	13.3	30-35

These facts and the research results from section 2.8.3 using Fig-2.14 and Table-8.1, validate the following sequence to estimate the ND effective damping length:

1. In Fig-2.14 the Stokes layer laminar flow region is entered below $Re_A = 8000$. Define the critical nutation transition angle θ_A at $Re_A = 8000$ by a NS sensitivity analysis using Eqn. (2.49) and solve for Re as well. Use Re and discriminate for the typical Re values, i.e. low ($Re < 100$) and high ($Re > 100$)
2. Determine the inlet length by Eqn. (2.50) at high Re value and by Eqn. (2.46) otherwise.
3. Estimate $\Delta L = \chi L_{inlet}$ with χ [-] an educated guess factor based on Table-8.1 taking the heritage of the Ulysses, Cluster and FY2A calibration into account. The following engineering approach to determine the factor χ is reasonable with the FY2 100 RPM case (bold) as exceptional one:
 - $\chi = 0.5$ at low Re and high spin-rate
 - $\chi = 1$ otherwise
4. Choose $\Delta L = \max(2 \cdot a, \chi L_{inlet})$ as non-conservative approach.

This educated guess methodology will effectuate a considerable reduction in test and analysis time since less iterative calibration cycles are needed. Depending on the specific ND requirements this may even yield “first shot (almost) right”.

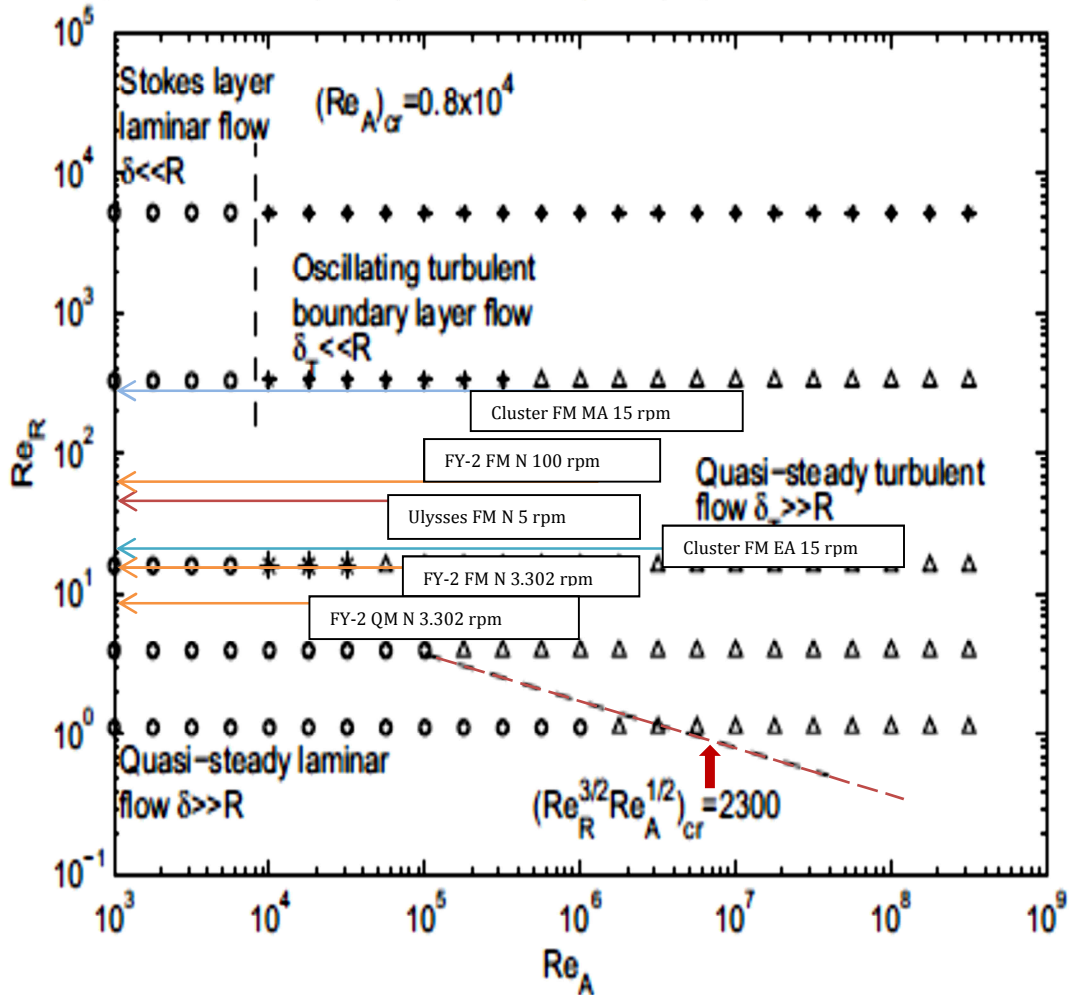


Fig-8.1 Oscillating tube flows using coordinates (Re_A, Re_R) after [Su et al., 2012] with

- : laminar flow
- * : oscillating turbulent boundary flow
- Δ : quasi-steady turbulent flow
- : flow transition lines at the two extremes corresponding to boundary layer flows and quasi-steady viscous flows.

The added colored ND trajectories in the (Re_A, Re_R) flow characteristics field signify the Ulysses, Cluster and FY-2 FM liquid damper models EA, MA and N. The 3rd FY-2 QM and 4th FM calibration series at the virtual spin-rate 3.302 rpm finish just above the quasi-steady laminar flow region with the largest $\delta/a \approx 0.3$ ratio (mind $a = R$ in this figure only). On the upper side the smallest $\delta/a \approx 0.06$ ratio is found for the Cluster FM MA 15 rpm design in the Stokes laminar flow region.

SE-3

The rich amount of FY-2 nutation damper (PTM, QM and FM) test data was thoroughly analysed in full detail. The extended test program and the demanding questions from the Chinese customer (GWIC) have led to refined insights in the recursive calibration method and the ultimate damping performance.

The meniscus hysteresis, as a potential killer of the linear ND performance at extremely small nutation angles, was investigated experimentally (4.2) and theoretically (2.10). The diverse refined analysis methods applied to the PTM air-bearing experiments did not reveal this phenomenon in the (scaled flight) nutation range down to 0.5". An additional PP1 liquid drop experiment was executed yielding independent evidence of the superior low contact angle wetting condition. This result was obtained on basis of the extreme low surface tension in combination with the Aluminum endpot material properties and its finishing. The overall analysis shows that, though on the limit of the test equipment potentials, the 0.5" flight nutation angle requirement is met.

The very small angular range of the air-bearing tests was analyzed. The calibration of the airflow fluctuations by a model offered evidence that the air-bearing performance is limited by airflows solely.

An extended radiation analysis was executed in addition to the ND heritage given in Chapter 1. The results show that the FY2 ND performance will not be obstructed by the accumulated radiation doses towards End-Of-Life with sufficient margin.

The extended refined tuning analysis using PTM, QM and FM performance test data delivered valuable data. The results support the validation of a new method to estimate the effective damping length more accurately than on basis of the old 10% rule given in section 2.12 (8.2, SE-2).

SE-4

The solar heating ('pumping') of a rotating axial boom (though stiff designed) was the root cause of diverse S/C nutation anomalies during the last decennia. The potential anomalies (transients, mistuned performance) of the Ulysses ND were excluded by analysis of the original design files, performance tests and in-orbit Doppler data (5.4).

Verification and Validation**V&V-1**

A series of S/C with verification and validation (V&V) data were selected. The COSB and EQUATOR-S S/C, both equipped with meridian NDs, with relatively abundant available V&V data. Their V&V results (3.4.3 and 3.4.4) were obtained by a systematic comparison of test, flight and triple model results (HP, RHP-1 and NS). On basis of these results, the extended NS model proves to be the backbone of ND design and development. The other selected missions Ulysses, Cluster and MSG equipped with equatorial NDs yield limited flight data but the nominal nutation performance of all three is confirmed (3).

V&V-2

Endpot hysteresis locking phenomena may play a critical role to be reinvestigated for every new design. The COS-B ultimate damping angle tests with the PTM glass model did not reveal a second time constant due to endpot hysteresis phenomena. This is concluded after studying and re-analyzing the results of a high number of repetitive tests at 1.0 and 0.2" at flight nutation angles in air-bearing tests (3.4.4).

The extensive study and analysis of the FY2 PTM experiments (4.2) revealed that the limiting air-bearing angle (20") exceeds the theoretical prediction (34") from [Hong, 1987]. The same holds for the COS-B experiments (3.4.4). The FY2 ultimate nutation angle

performance analysis shows that the flight limit beyond 0.5" (36"on the air-bearing) is just detectable at the air-bearing resolution of 2.75".

The turbulence air-flows in the test environment were modeled. The successive calibration of the PTM performance fluctuations at very small test angles offers evidence that the air-bearing performance is limited by self-induced airflows solely (4.2).

Design

D-1

The following scientific S/C with antenna wire boom morphology were investigated: Bepi-Colombo, Cluster, RBSP, DICE, Themis and FAST. The Electric Field Wave (EFW) instrument, Spin Plane Boom (SPB) release mechanism and ADCS were introduced as the keystones of the wire boom antenna concept. The broad applicability of the multi-mode liquid damper concept was shown (6.1).

D-2

The generic stability theory of wire boom oscillations (gyroscopically) coupled to the hub spin and nutation modes was explored and partly derived using a new parameterization and harmonized equation format (2.9 and 6.5). The results enabled the development of the recursive bottom-up design approach of broadband liquid dampers (7.6 and 7.9).

D-3

An inventory of engineering stability issues was dealt with (6.6) as well as the impact of the wire boom composition (6.7). This made clear where the limits of multi-mode modeling are reached and subtle ("healthy") engineering trade-offs are required.

D-4

The phase-A design trade-offs of the Cluster broadband liquid damper system were studied (7). The ND reliability assessment was made using parameters from the latest welding techniques (1.8). The over-compliance in reliability provoked the thought of an extended multi-mode design. A trade-off between two early concepts is given whilst the superior (Cluster) candidate was evaluated further. This design proved to be sound on basis of a (EA1, N and MA) multi-mode analysis. The passive Cluster damping control system with in addition the internal wire damping enables the boom deflection limit to be a design parameter (7). The highly reliable independent damper subsystem is fully passive and relatively easy to implement in the ADCS of a spinning spacecraft.

D-5

A recursive bottom-up design approach has been developed (7.7) with the in-plane and out-of-plane wire boom deflection angles as additional design parameters. The stepwise EA1 to MA implementation methodology (7.9) enables design freedom to vary the effective bandwidths, time constants and to comply with other damping requirements. These may be nutation (N) or the multiple MA modes derived with the RBSP stability model. This model was replicated in MathCad® and refers to the state-of-the-art in top-down stability modeling (7.8) for spinning S/C with extendable wire booms.

D-6

The optimal deployment strategy on basis of the implementation of the multi-mode damping principle is studied (7.7) and compared from literature. The residual deflection angles right after the deployment stop can be designed down to less than 0.03° depending on the critical timing of the stop. At small angular deflections, however, diverse material artifacts and anelastic flexure at the hub anchor positions pop up (6.6 and 6.7). This means that only dedicated engineering tests can clarify this issue.

A dedicated damping analysis by [Ivchenko et al., 2007] shows that the remnant coupled oscillations in both hub and wire boom can disappear almost completely. The implementation of a proper timing sequence, however, is far from easy and straightforward since it will require additional deployment sensors and control electronics. No implementation or flight data have been found (7.7).

D-7

The Cluster S/C dynamics design was compared with the RBSP S/C by MathCad® implementation of the 9 degrees of freedom model from [McGee et al., 2009]. The RBSP modal analysis results comply seamlessly with the MathCad® RBSP calibration results (7.8). The stability results by the root sensitivity analysis (Eqn.-6.27) of the system matrix shows that the resonance peaks of the Cluster wire boom configuration are very sharp (high Q-factor) compared to the RBSP values. This can be explained since the Cluster spin stability margin, as shown in Table-7.3, is more than twice the RBSP margin. Thus, the Cluster S/C is much more stable and in addition it operates at a trifold higher spin-rate.

The spectral modes of the Cluster phase-A and phase-B ADCS specification have been fully analysed. The specified, analytical and derived values from the RBSP model are compared, analysed and explained.

The RBSP authors state that the internal wire boom damping itself is able to attenuate all modes whilst a boom settling to less than 0.5° is mentioned within 8-12 hr after repointing. The Cluster analysis depicts a much better condition: The wire boom remnant oscillation amplitude right after deployment shows amplitudes down to 0.2 degree with a typical time constant of 2.5 hr. A critical deployment phase stop timing, which is probably not implementation feasible, can even yield a start residual angle of 0.03 degree.

The bottom-up design methodology (7.6) is completed by the top-down approach of the RBSP model. The research results from both methodologies offer a full SE model base to design multi-mode dampers in flexible S/C designs.

The RBSP annular (ring) dampers suffer from considerable angular off-sets in the range 2-3 rad and significant inrush time constants of about 40 min which are not accounted for in the RBSP model. The tube-with-endpots Fokker liquid damper design, applied in the Cluster ADCS, lacks this artefact.

D-8

In the Cluster ADCS the multi-mode liquid damper system is composed by an equatorial EA and MA damper. An equatorial damper choice for the EA1 mode is trivial but less obvious for the MA modes since these are effectively damped via gyroscopic coupling only. Therefore the combined damping action of an equatorial (EA1) and a meridian (multiple MA) damper is studied and shows potentials to function as a broadband liquid damper system (7.9). This design option was not applied up to now [2012].

D-9

An SE approach to deal with changing inertia figures during the phase-A to phase-C/D maturation of the S/C design is given. The tuning sensitivity of the damper design is assessed to enable risk mitigation in an early design phase (7.10).

D-10

The combined damper performance requires dedicated PTM tests with consequently derived additional requirements for the air-bearing test setup. The relevant engineering issues are studied as well as the required changes in the test setup with respect to the refined FY2 ND performance tests (7.10 and 3.3.2).

D-11

The refined liquid damper concept still contributes to its well performing ADCS and to overall success of the Cluster mission. On the other hand it is hard to trace and validate the designed multi-mode performance itself. The availability of dedicated flight data would be of great scientific value.

The excellent nutation damping performance of the Cluster S/C ADCS, comfortably within the specification values, was traceable and analyzed. This fact renders an indirect proof of the overall damper performance.

F-1

See Chapter 8 and 9.

9 Outlook

The achievements of this thesis have been summarized in the previous section. Diverse objectives are extendible towards further refinements in liquid damper design, valorization opportunities and new application scenarios. These topics are dealt in the following sections.

9.1 *Future Research Topics*

The limit of linear nutation angle damping

Refined surface treatment of the endpot materials in combination with dedicated coatings offers a way to reduce the minimum damping angle and dead band even further. Performance test improvements to detect the ultimate damping and hysteresis, however, are required. An exploration of recent scientific literature in the field of nano-tribology and wetting transitions on biomimetic surfaces showed that the general theory of contact angle hysteresis has still not been formulated. Mother Nature, e.g. the perfect hydrophobic behavior of the Lotus flower, shows that defined microscopic surface treatments pave the experimental way forward. The limiting damping performance can be detected with performance test refinements, i.e. the minimization of air-flow fluctuations. Therefore the following suggestions are made to reduce the drag coefficient C_D in Eqn. (4.2)

1. Add an aerodynamic ellipsoidal cone assembly around each PTM, QM, DM and FM
2. De-pressurize the test environment
3. Reduce the effective drag area of the air-bearing support assembly.

The implementation of these recommendations will decrease the damping fluctuations and extend the low angular test range. This may enable an investigation of the ultimate ND performance related to the miniscus hysteresis as dealt in section 2.10. Although, the limiting angle is not known, there is strong evidence that the limits can be extended by further research down to 0.1° or beyond. This value complies with the pointing accuracy of the Hubble Space Telescope.

Combination of an Equatorial and Meridian damper

In section 7.9 the design option to use an equatorial EA and a meridian MA damper to control the in-plane and out-of-plane (normal) wire boom oscillation modes beside nutation is analysed. It is a promising research option to compare it with the Cluster damper design which uses two equatorial dampers.

Superior multi-mode damper

In the RBSP S/C the toroid (annular) orthogonal XZ and YZ NDs suffer with considerable angular off-sets of about 2-3 rad and significant inrush time constants of about 40 min which are not accounted for in the RBSP model. The tube-with-endpots Fokker multi-mode design applied in the Cluster ADCS lacks this artefact. Moreover [McGee et al., 2009] state that only the RBSP hub nutation mode is damped effectively by the two RBSP toroid (annular) dampers. This is not valid for the refined multi-mode broadband Cluster liquid damper system which can be fine-tuned to the desired modes. An explicit study to compare both multi-mode (wobble) damper system designs can show that the Cluster solution is the superior and renders an excellent choice for use in future S/C with wire boom configurations. The availability of dedicated Cluster flight data or data from other comparable missions is therefore of great scientific value.

9.2 Valorization Opportunities

The hybrid multi-mode liquid damper and the derived design methodologies are qualified by their space applications. The given methodologies including the effective damping length determination enable a significant reduction in development and test efforts. The solutions are in principle applicable to any kind of terrestrial structure which requires a tuneable damper. Market research and the allocation of dedicated solutions are an obvious way towards valorization.

9.3 Application Scenarios

The multi-mode damper application is restricted to spinning S/C equipped with a wire boom configuration. The space qualified broadband liquid damper system is an excellent choice for use in future spinning S/C with wire boom configurations. At the moment, these are mainly magneto-spherical missions equipped with Electric Field Wave (EFW) instruments which require long wire lengths in the order of 50 to 100 m. A huge rotating interplanetary S/C like a space docking station with permanent human occupation is just another example of a future application. Space market research and the development of specific applications are a way forward to extend potential applications.

9.4 Final Remarks

The results of this PhD thesis enable the extreme refinement of the given damper concept for any application. The developed concept is an extremely reliable passive closed system which does not contain any control loop or moving parts. It functions in any extreme – temperature, pressure, chemical, electrical or radiation – environment. Terrestrial spin-offs in the engineering fields of refined centrifuges, windmills, shipbuilding and bridge stabilization may offer the best valorisation opportunities in short terms.

Bibliography

- Abramowitz M. and Stegun Irene A., *Handbook of Mathematical Functions* - Dover Publications, Inc. New York, New edition, June 1965
- Agrawal B., *Dynamic Characteristics of Liquid Motion in Partially Filled Tanks of a Spinning Spacecraft*, AIAA Journal of Guidance, Control, and Dynamics, Vol. 16, No. 4, July-August, 1993, pp. 636-640.
- Ancher L.J. , van den Brink H. and Pouw A., *Asymmetric oscillation of a passive nutation damper*, Fokker-VF The Netherlands. Study on passive nutation dampers performed under ESA contract 2318/74 Volume I, II and III (Appendices). Proc. of the CNES-ESA Conf. on 'Attitude Control of Space Vehicles – Technological and dynamical problems associated with the presence of Liquids', ESA SP-129, pp. 179-183, 1977
- Auslander D., et al, *Instrument Boom Mechanisms on the THEMIS Satellites; Magnetometer, Radial Wire and Axial Booms*, Space Sci Rev, 185-211, 2008
- Bakel C. van, *Nutation Damping Theory and Computer Implementation* – UCN & Technical University Eindhoven, WFE document 93.006 – January 1993
- Bakel C. van, *On the behaviour of the tube-with-endpots nutation damper* – UCN & Technical University Eindhoven, WFE document 93.105 – August 1993
- Barkow, B., et al, Various Methods of Controlling the Deployment of a Tethered Satellite, *Journal of Vibration and Control*, 9: 187-208, 2003
- Batchelor G.K. - *An Introduction to Fluid Dynamics* - Cambridge University Press, Chapter 4, 1980
- Bauer H. F. and Eidel W., *Axisymmetric viscous liquid oscillations in a cylindrical container*, *Forsch. Ingenieurwe.* (1997), 189-201, Springer-Verlag 1997
- Bell, J., Walker, W.P., 1966, *Activated and passive controlled fluid tank system for ship stabilization*, SNAME Trans. 74, 150–193.
- Bhushan B., *Nanotribology and nanomechanics in nano/biotechn.*, *Phil. Trans. R. Soc. A* 2008 **366**, 1499-1537
- Bohr N. and Pauli W., photo taken at the opening of the University of Lund, Sweden, 1951 <http://www.fysikbasen.dk/English.php?page=Vis&id=79>
- Bongers E., 2012 Private conversation with Ed Bongers, Head Innovation & Develop., Dutch-Space EADS
- Bongers E., 1984, *In-orbit Experiments on COS-B nutation damper performance*, ESA report TR-R-84-037
- Borghouts A.N., - *Inleiding in de Mechanica* –, Delftse Uitgevers Maatschappij BV, 1974
- Bormashenko E., *Wetting transitions on biometric surfaces*, *Phil. Trans. R. Soc. A* 2010 **368**, 4695-4711
- Boussinesq J., 1891, *Seanc. Acad. Sci.*, Paris **113**, 9, 49.
- Boyd, D. and Kuiper, H., *The Compound Parabolic/elliptic Lightshades: Near-Optimal Shading for Cold Radiators*, SAE Technical Paper 2000-01-2278, 2000, doi:10.4271/2000-01-2278.
- Bryson A.E., *Control of Spacecraft and Aircraft*, 1994, Princeton University Press

- Butikov E., Precession and nutation of a gyroscope, 2006,
<http://www.ifmo.ru.butikov/Applets/gyroscope.html>
- Cadwallader L.C., Selected Component Failures rate values from Fusion Safety Assessment Tasks, Idaho National Engineering and Environmental Lab, Nuclear Eng. Techn. Department, 1998
- Cassie A.B.D., Discussions, Faraday Society, no 3 page 11, 1948
- Chan C.K. et al – Ulysses Attitude and Orbit Operations: 13+ Years of International Cooperation – Space Operations 2004 Montreal 17-21 May, 2004,
<http://www.aiaa.org/Spaceops2004Archive/downloads/ppts>
- Chetty P.R.K. , - *Satellite Technology and its Applications* - , Fairchild Space Company, TPR/TAB books, Blue Ridge Summit- PA, 2nd edition, 1991
- Chobotov Vladimir A. – Spacecraft Attitude Dynamics and Control – Krieger Publishing Company, Chapter 1 Kinematics and Dynamics of Angular Motion and Chapter 2 – Spin Stabilization, 1991
- COS-B S/C mission description <http://sci.esa.int/science-e/www/object/index.cfm?fobjectid=31447>
 and http://www.esa.int/esaSC/120375_index_0_m.html
- COS-B S/C (2), ESA bulletin no2, special August 1975
- Cox Glenn N. and Germando F.J ,*Fluid Mechanics*, New York - D. van Nostrand Comp. Inc, page 184 -191, 1947
- Credland, J. and Lehn, G., The Cluster Spacecraft Journal: Cluster: Mission, Payload and Supporting Activities., Edited by W. R. Burke. , ESA-SP, Vol. 1159, 1993. ISBN: 92-9092-073-4., p.235, 1993
- Crellin E.B., WMM, FAX –ULS/EBC/11 to the ESOC/JPL/GSFC/Dornier/Fokker Space team on Ulysses nutation anomaly, *Nutation Damper performance as a function of spin-rate*, 13-12-1990
- Crellin, E.B., A model of the performance of a fluid-in-tube nutation damper, March 1982, Estec Working Paper 1315
- Crowden J.B., Fax No92927190 from Marconi Space Systems / Aerospatiale Cannes, Nutation Dampers for 2nd generation Meteosat, 22-01-1990
- Dallard, P., et al, *The London Millennium Footbridge*, The Structural Engineer, , Volume 79/No. 22, Pg. 17., with Supplemental Fluid Viscous Dampers,” Technical Report NCEER-92-0032, National Center for Earthquake Engineering Research, Buffalo, NY, November 20, 2001
- Desu B.N., Deb S.K. and Dutta A, *Coupled tuned mass dampers for control of coupled vibrations in asymmetric buildings*, STRUCTURAL CONTROL AND HEALTH MONITORING, Struct. Control Health Monit., Wiley InterScience, **13**:897-916, 2006
- Dow J., Matussi S., Mugalesi Dow R., Schmidt M. and Warhaut M. – *The Implementation of the Cluster II constellation*. – Acta Astronautica Vol. 54, pages 657-669, 2004
- Duckworth R.A., - *Mechanics of Fluids* -, Longman -London and New York, page 154 -179, 1977
- Ebert K. and Reger G., SLOSHING ANALYSIS FOR METEOSAT SECOND GENERATION, Proc. 2nd European Spacecraft Propulsion Conference, ESA SP-398, August 1997.
- Eckmann, D.M. and Grotberg, J.B., *Experiments on transition turbulence in oscillatory pipe flow*, Journal of Fluid Mechanics 322, page 329-350, 1991

- Eke, Fidelis O.; Eke, Estelle M., *Backup nutation damping strategy for the Galileo spacecraft*, 1989 American Control Conference, 8th, Pittsburgh, PA, June 21-23, 1989, Proceedings. Volume 3 (A89-53951 24-63). New York, Institute of Electrical and Electronics Engineers, 1989, p. 2263-2268.
- Enderle W. and Feucht U., Attitude Control Simulation for EQUATOR-S Using Object Oriented Modeling, GSOC DLR Oberpfaffenhofen, Proc. 3rd Int. Conf. on spacecraft GNCS, ESTEC. ESA SP-381, 1997
- ERIKSSON Anders I., KHOTYAINTEV Yuri and LINDQVIST Per-Arne, SPACECRAFT WAKES IN THE SOLAR WIND, *Proc. of the 10th Spacecraft Charging Technology Conference*, June 18.21, 2007
- ESA-1999, ESA BR-153, ISBN 92-9092-634-1, *MSG – The Satellite Development*, November 1999
- ESA-2012, ESA Ulysses and Cluster archive [ESA, 2012]
1. WEC commissioning data - The Cluster Wave Experience Consortium
http://www.plasma.kth.se/cluster/wec_commiss.html
 2. www.esa.int/esaSC/120383_index_0_m.html
 3. www.esa.int/esaSC/SEMYN5T1VED_index_0.html
 4. www.space.com/scienceastronomy/planetearth/cluster_boom_000918.html
 5. <http://sci.esa.int/science-e/www/object/index.cfm?fobjectid=24931>
 6. www.plasma.kth.se/cluster/wec_commiss.html
 7. Cluster Active Archive – User guide to EFW data – 19-05-2008
 8. http://www.cluster.irfu.se/efw/data/EFW_CAA_UG.pdf
 9. sci.esa.int/science-e/www/object/index.cfm?fobjectid=31262
 10. www.esa.int/esapub/sp/sp1259/sp1259web.pdf
 11. Cluster Mission ESA <http://clusterlaunch.esa.int/science>
- Fargie D. and Martin B.W., *Developing laminar flow in a pipe of circular cross-section*, Proc. Roy. Soc. London, A. **321**, 461-476, 1971
- FDS-1992 - Fokker-Dutch-Space FY-2 Nutation Damper project archive. A Non-Disclosure-Agreement (NDA) did not apply to the Chinese GWIC contract. The record list contains faxes, specifications, design and engineering reports and is found some pages after this regular bibliography.
- Fleminga Karl N. and Lydell Bengt O.Y., *Database development and uncertainty treatment for estimating pipe failure rates and rupture frequencies*, Reliability Engineering and System Safety 86 (2004) 227–246, 2004
- Fortescue P., Stark J. and Swinnerd G. - SpaceCraft Systems Engineering -- J. Wiley and Sons, p. 63-77, 2003
- FY2-2012, internet spacecraft archive 2012
- (1) <http://goes.gsfc.nasa.gov/text/geonews.html#FENGYUN2>
 - (2) <http://www.fas.org/spp/guide/china/earth/fy-2.htm>
- Garcia-Perez Raul et al, ESOC / JPL – ARGOS A system to monitor Ulysses nutation and thruster firings from variations of the S/C signal – Proceedings of the International Symposium on Space Dynamics, Toulouse 19-23 June 1995
- Gawad, A.F.A et al., *Roll stabilization by anti-roll passive tanks*, Ocean Engineering 28, pp 457-469, 2001
- Gerrard J. and Hughes M., The flow due to an oscillating piston in a cylindrical tube: a comparison between experiment and a simple entrance flow theory, Journal of Fluid Mechanics 50, 97-106, 1971.

- Ginsberg Jerry H., Georgia Institute of Technology, – Advanced Engineering Dynamics 2nd edition, Cambridge University Press, Chapter 8 – Gyroscopic Effects, 1995
- Goldstein H., *Classical Mechanics*, 2nd edition, Addison-Wesley, pages 107-175, 1980
- González Lodoso, J. F., Echevarria J. J. and Gavira, J. M., Wire boom mechanism for BepiColombo mission to Mercury, Proc. of the 9th European Space Mechanisms and Tribology Symposium, 19-21 September 2001, ESA SP-480, ISBN 92-9092-761-5, 2001, p. 171 - 178
- Grobov V.A., “*Damping nutations of rotating asymmetrical solids*”, UDC 531.38/629.78, Kiev Institute of Civil Engineering, translated from Prikladnaya Mekhanika, Vol.17, No.6, pp. 119-123, 1981
- Gulick, D.W. and Thornton, E. A., - THERMALLY-INDUCED VIBRATIONS OF A SPINNING SPACRAFT BOOM- , Acta Astronautica Vol. 36 No.3, pp. 163-176, 1995
- Härendel G., Torbert R.B. and Höfner H., *The Equator-S mission* , Ann. GeoPhys., 17, 1499-1502, 1999
- Häusler B. and Eidel W., *Ein Flüssigkeitsnutationdämpfer für den Satellit EQUATOR-S* , Forschungsbericht: LRT-WE-9-FB-1, Institut für Luft und Raumfahrttechnik, Universität der Bundeswehr München, Neubiberg, Germany, 2001
- Häusler B., Eidel W. and Stöcker J., *Ein Flüssigkeitsnutationdämpfer für den Satellit EQUATOR-S*, Forschung im Ingenieurwesen, 67, 27-39, 2002
- HCP-1980, Handbook of Chemistry and Physics – 61st edition, CRC Press Inc., 1980-1981
- Harrison J.V., *Analysis of spacecraft nutation dynamics using the drop test method*, Journal of Space Communication and Broadcasting 5 (1987) 265-280
- Hawkyard A. et al., (PRS) FAX – PR/105B/AH/14770/AP - to the SOC/JPL/GSFC/Dornier/Fokker Space team, *Ulysses Dynamic Oscillation/Nutation Anomaly*, ESTEC/ESOC meeting 29-11-90
- Hino, M., Sawamoto, M. and Takasu, S., *Experiments on transition to turbulence in an oscillatory pipe flow*, Journal of Fluid Mechanics 75, page 193-207, 1976
- Hoffman, H.C., *Lessons Learned from Six Decades of Spacecraft Guidance and Control Experiences*, AIAA GN&C Conference and Exhibit, AIAA 2007-6333, 20 - 23 August 2007
- Hong, J.Z., *Residual Nutation Angle of Satellites with Viscous Nutation Dampers*, Acta Astr. , Vol. 15, No. 1, pp. 1-7, 1987
- Hong, J.Z., *Nutation Damping of Spinning Satellites with Viscous Annular Dampers*, Acta Astr., Vol. 19, No. 12, pp. 939-946, 1989
- Hubert C. and Swanson D., *Surface Tension Lockup in the IMAGE Nutation Damper-Anomaly and Recovery*, Hubert Astronautics, Inc., Lockheed Martin Space Systems, 2000.
- Hubert C., *Modeling Completely Filled Viscous Ring Nutation Dampers*, GSFC Technical Report B2027, Hubert Astronautics, Inc., 2002
- Hughes Peter C., *Spacecraft Attitude Dynamics*, Chapter 4 - *Attitude Dynamics of a Rigid Body* and Chapter 5 - *Effect of Internal Energy Dissipation on the Directional Stability of spinning bodies*, John Wiley & S, 1986
- Ibrahim M. and Waqar H., *OSCILLATING FLOW IN CHANNELS WITH A SUDDEN CHANGE IN CROSS SECTION*, Computers Fluids, Vol. 23, No. 1, pp. 211-224, 1994
- Inman Daniel J., *Engineering Vibration*, 2nd edition, Virginia Polytechnic Institute and State University, Prentice-Hall Inc., 2001

- Ivchenko, N., Bylander, L. and, Olson, G., Fast Deployment of Wire Booms without Residual Oscillations, Proc. 18th ESA Symposium on 'European Rocket and Balloon Programmes and Related Research', (ESA SP-647), November 2007
- Jackson J.D., Emeritus, Univ. of California, Berkeley, Classical Electrodynamics, 3rd edition, ISBN: 978-0-471-30932-1, December 1998
- Kassalanati, A., Constantinou, M. 1999, *Experimental Study of Bridge Elastomeric and Other Insolation and Energy Dissipation Systems with Emphasis on Uplift Prevention and High Velocity Near-Source Seismic Excitation*., Technical Report MCEER-99-0004, Multidisciplinary Center for Earthquake Engineering Research, Buffalo, NY., 1999
- Kemp, B.L., McGee, T., and Shankar, U.J., *Analysis of Spinning Spacecraft with Wire Booms, Part-1: Derivation of Nonlinear Dynamics*, AIAA GNC Conference, 2009
- Kermans S., Telephone conversation in 2008 with Sido Kermans: In the 90s development engineer at UCN Aerospace and now staff member at Aeronamics B.V. in Almelo, the Netherlands.
- Knott G.F. and Flower J.O., *Measurement of energy losses in oscillatory flow through a pipe exit*, Applied Ocean Engineering Research, 1980, Vol. 2, No. 4
- Kuiper J.M., Fokker Space Systems B.V., *Ulysses Dynamic Oscillation- I*, Ulys-FO-ND-TFX-01-90, 28-11-1990
- Kuiper J.M., Fokker Space Systems B.V., *Ulysses Dynamic Oscillation- II*, Ulys-FO-NUDA-TFX-02-90, 5-12-1990
- Kuiper J.M., Fokker Space Systems B.V., *Ulysses Dynamic Oscillation-III*, Ulys-FO-NUDA-TFX-01-90, 7-12-1990
- Kuiper J.M., Fokker Space, *Proposal for an innovative combined NUDA design*, Cluster phase-A ND concept laid down by fax to BAe, 8 January 1991, Clus-FO-NUDA-TFX-01-91
- Kuiper J.M., FAX to Fokker Aircraft department FAC F-28/F-100 Schiphol, *Liquid tube damping for the Fokker F-100 stabilo wing (I+II+III)*, dated 26-08-92, 27-08-92 and 8 September 1992
- Kuiper J.M. and van der Heijden R., Electrical hazard analysis during assembly, integration and testing of solar arrays, Delft University of Technology, Chair Space Systems Engineering, Solar Energy 85 (2011) 849-856
- Kraker A. de, 2008, Private conversation with Bram de Kraker, Associate Professor Structural Engineering at the Eindhoven University of Technology
- Lai, S. T. and Bhavnani, K. H., *Dynamics of Satellite Wire-Boom Systems*, AFCRL-TR-75-0220, Journal of Applied Mathematics and Physics (ZAMP), 1975.
- Lai, S. T. and Smiddy M., *Dynamics of Wire Boom Oscillations on a Spinning Satellite Part I, Lagrangian Equation of Motion and Transient Response*, Journal of Applied Mathematics and Physics, Vol. 30, 1979
- Lai, S. T. et al., *Dynamics of Wire Boom Oscillations on a Spinning Satellite Part II, Normal Modes in Spin Plane*, Journal of Appl. Mathematics and Physics, Vol. 30, 1979
- Lancaster J.F., The Physics of welding, International Institute of Welding, Pergamon, 1984
- Lancaster J.F., Handbook of structural welding, Woodhead Publishing, 1997
- Lee, B.S. and Vassalos, D., 1996, *An investigation into the stability effects of anti-roll tanks with flow Obstructions*, Int. Shipbuild. Prog. 43 (433), 70-88.
- Lemal, D.M., Perspective on fluorocarbon chemistry, J. Org. Chem. 69 (1), 2004

- Lewandowski, G., Meissner, E and Milchert, E. , *Special applications of fluorinated organic compounds*, *Journal of Hazard Materials* **136** (3): 385–91, 2006.
- Lindqvist P.A., *Cluster EFW boom deployment status report*, 18-09-2012
- Loitsyanskii L.G., *Mechanics of Liquids and Gases*, page 496 – 509, Pergamon Press, 1966
- Longman R.W. and Fedor J.V., Columbia University, NY, *Dynamics of flexible spinning satellites with radial wire antennas*, , *Acta Astronautica*, Vol. 3, pp. 17-37. Pergamon Press, 1976
- Love J.S. and Tait M.J., *Non-linear multimodal model for tuned liquid dampers of arbitrary tank geometry*, dept. of Civil Engineering McMaster University Canada, *Int. Journal of Non-Linear Mech.* **46**, 1065-1075, 2011
- Lu F., Zhang X. and Xu J., *Image Navigation for the FY2 Geosynchronous Meteorological Satellite*, ©American Meteorological Society, page 1149-1165, July 2008
- Lubbers J., de Vries M. P., Veldman A. E. P. and Verkerke G. J., "Influence of a downstream narrowing on the flow profile in a tube," *J. Biomech.* **39**, 70, 2006
- Luengo, O., *DYNAMIC MODEL OF THE MSG ATTITUDE*, EUMETSAT (GMV consultant), ESA Proceedings., ESASP.548-313L, 2004
- Mar, J. and Garrett, T., *Mechanical Design and Dynamics of the Alouette Spacecraft*, 882 PROC. OF THE IEEE, VOL. 57, NO. 6, JUNE 1969
- Marrirrodiga, C.G., Zeischka J., Boslooper E.C., *Numerical simulation of Ulysses nutation*, Proc. 'Fifth European Space Mechanisms and Tribology Symposium, ESTEC, ESA SP-334, April 1993
- McGee G.T. et al., *(RBSP) Analysis of Spinning S/C with Wire Booms – Part 2: Out-of-Plane Dynamics and Maneuvers*, AIAA GNC conference, 10-13 August, 2009
- Meirovitch L., *Liapunov stability analysis of hybrid dynamical systems with multi-elastic domains*, *Int. Journal of Non-Linear Mechanics*, Vol.7, pp. 425-443, Pergamon Press, 1972
- Meirovitch, L. and Calico, R.E. , *The stability of Motion of Satellites with Flexible Appendages*, NASA CR-1987, 1972
- Mendez P.F. and Eagar T.W., MIT, *New trends in welding in the aeronautic industry*, 2nd Conf. of New Manufacturing Trends, Bilboa, Spain, Nov 19-20, 2002
- Modi V.J., Welt F. and Irani M.B., ON THE SUPPRESSION OF VIBRATIONS USING NUTATION DAMPERS, *Journal of Wind Engineering and Industrial Aerodynamics*, **33** (1990) 273-282
- Mitsui T., Aihara K., Terayama C., Kobayashi H. and Shimomura Y., *Can a spinning egg really jump?*, *Proc. of the Royal Soc. A* **462**, 2897-2905, 2006
- Moaleji, R. and Greig, A.R., *On the development of ship anti-roll tanks*, *Ocean Eng.*, **34**, pp 103-121, 2007
- Muto T and Nakane K., *Unsteady flow in circular tube (velocity distribution of pulsating flow)*, Bulletin in the Japan society of Mechanical Engineering, 1980
- NASA SPACE VEHICLE CRITERIA (GUIDANCE AND CONTROL), *Effects of Structural Flexibility on Spacecraft Control Systems*, NASA SP-8016, 1969
- NASA-2012, NASA Ulysses and Cluster archive [NASA, 2012]
1. www.starbrite.jpl.nasa.gov/pds/viewHostprofile.jsp?INSTRUMENT_HOST_ID=ULY
 2. Ulysses ESA/NASA, <http://www.solarviews.com/eng/ulysses.htm>
 3. Cluster Mission Objective and organization NASA <http://nasataxonomy.jpl.nasa.gov/>

- Nebauer, J.R.A. and Blackburn H.M., STABILITY OF OSCILLATORY AND PULSATILE PIPE FLOW, Department of Mechanical and Aerospace Engineering, Monash University, AUSTRALIA, 7th Int. Conf. on CFD in the Minerals and Process Industries CSIRO, Melbourne, Australia, 9-11 December 2009.
- Norman R.O.L. and Waddington D.J., Modern Organic Chemistry Bell & Hyman publishers, 1972
- O'Hagan, D., *Understanding organofluorine chemistry - An introduction to the C-F bond*, Chem. Soc. Rev. 37 (2): 308-19, 2008.
- Paluszek M., Thomas S., Mueller J. and Bhatta P., *Spacecraft Attitude and Orbit Control*, <http://www.psatellite.com>, Princeton Satellite Systems Inc, ISBN 978-0-9654701-0-0, 1996-2008
- Pankow, D. et al, *Deployment mechanisms on the FAST satellite: magnetometer, radial wire, and axial booms*, Space Sc. Rev 98:93-111, 2001
- Papanastasiou T.C., Georgiou G.C. and Alexandrou A.N., *Viscous Fluid Flow*, page 243-253, CRS Press 1999
- Patience G.S. and Mehrota A.K., *Laminar Start-up Flow in Short Pipe lengths*, The Canadian Journal of Chemical Engineering, Vol. 67, December 1989
- Pfaff R., Carlson C., Watzin J., Everett D. and Gruner T., An overview of the Fast Auroral Snapshot (FAST) satellite, Space Science Reviews **98**: 1-32, 2001
- Prandtl L. and Tietjens O.G., *Applied Hydro- and Aeromechanics*, Dover Publ. Inc., New York - 1934
- Presti D. and Goulding C., *Coping Nutation in Ulysses' Third Orbit - New Challenges and Operational Solutions*, AIAA 2006-5520, 2006
- Prins, M., Kuiper, J. M. and Vieggers, M. P. A., The design of an X-ray microprobe at the SRS Daresbury (UK)
Nuclear Instruments and Methods in Physics Research Section B, Volume 3, Issue 1-3, p. 246-249, 1984
- RBSP-1, EFW Instrument Science Operations Center, *RBSP Critical Design Review report*, University of Minnesota, School of Physics & Astronomy, RBSP EFW **CDR** 2009 9/30-10/1 report, 2009
- RBSP-2, EFW RBSP Technical Note [RBSP_EFW_TN12_V4], 2009
- Reiterer M. and Hochrainer M., *Damping Of Pedestrian-Induced Bridge Vibrations By Tuned Liquid Column Dampers*, PAMM · Proc. Appl. Math. Mech. **4**, 109-110 (2004) / DOI 10.1002/pamm.20041003624 NOV 2004, © 2004 WILEY-VCH Verlag GmbH & Co. KGaA, Weinheim
- Reynolds, R., *Dynamic Modeling of Ring Nutation Dampers*, J. GUIDANCE, VOL.26, NO1, Eng. Notes, 2002
- Ryan R.S., Marshall Space Flight Center (MSFC), Alabama 35812, *A History of Aerospace Problems, Their Solutions, Their Lessons*, September 1996
- Saffman P.G., A model for inhomogeneous turbulent flow, Proc. Of the Royal Society of London, Series A, vol. 317, pp. 417-433, 1970
- Samanta A. and Banerji P., *Structural vibration control using modified liquid dampers*, The IES Journal Part A: Civil & Structural Engineering, Vol. 3, No. 1, February 2010, 14-27

- Sato, Y and Kanki, H, *Simplification of formulas for compression wave and oscillating flow in circular pipe*, Kobe University, Graduate School of Science and Technology, Machine Dynamics Lab. (MA-2), Japan, Journal of Appl. Acoustics, Elsevier Science Direct, 2008
- Schetz Joseph A. and Fuhs Allen E., *Fundamentals of Fluid Mechanics*, John Wiley & Sons, Inc., page 7, 70-72, 485-486, 1999
- Seto M.L. and Modi V.J. - *Control of Fluid-Structure Interaction Instabilities Using Circular Cylindrical Nutation Dampers*, International Journal of Offshore and Polar Engineering. Vol.7, No.3 - September 1997
- Shrinivasan D. K., Heyler G.A. and McGee T., *Spin-axis estimation of the Radiation Belt Storm Probes spacecraft using RF Doppler data*, Acta Astronautica, 73 (2012) 30-37
- Shum K.M. and Xu Y.L., *Multiple tuned liquid column dampers for reducing coupled lateral and torsional vibration of structures*, Eng. Structures 26 (2004), 746-758
- Shyu, K.L. and Kuo, H.C., *Characteristics of a U-type tuned liquid damper and its coupling motion with a structure in frequency domain*, Int. Shipbuild. Progr., 47, no 449, pp. 23-36, 2000
- Sorensen, A.M., *Meteosat log-term spin axis drift and maneuver optimization*, Proc. 12th Int. Symp. on Space Flight Dynamics, ESA SP-403, p215-220, 1997
- Simons J.H., *Fluorine Chemistry*, Vol. I (1950), Academic Press Inc. - New York
- Singh, M.P. et al, *Tuned mass dampers for response control of torsional buildings*, Earthquake Eng. Structural Dynamics ,32:749-769, 2002
- Stromberg E., *DICE CubeSat Mission*, CubeSat Workshop April 20, 2011, Space Dynamics Lab, Utah State University Research Foundation, erik.stromberg@sdl.usu.edu
- Su Y., Davidson J.H. and Kulacki F.A., *Numerical investigation of fluid flow and heat transfer of oscillating pipe flows*, International Journal of Thermal Sciences 54 (2012) 199-208
- Taylor, D.P., *"Damper Retrofit of the London Millennium Footbridge - A Case Study in Biodynamic Design"*, Proceedings of the 73d Shock and Vibration Symposium, 2002
- Truckenbrodt E., *Strömungsmechanik*, Springer, Berlin Heidelberg, NY, 1996
- Truckenbrodt A., Schultysik B. and Mehlretter J.P., *Nutationsdämpfer für den AMPTE-IRM Satelliten: Abschlußbericht*, Technology Consulting Institute for Applied Research GMBH (West Germany), TC-no. 017-Tru-Sch0/sa, 9 Dec. 1982
- Tyc G., and Han, R.P.S., *On the dynamics of spinning tethered space vehicles*, Phil. Trans. Royal Society., London A, 359, 2161-2190, 2001
- UCLA Fusion Science and Techn. Center Archived Technical Reports, APEX Interim Report January 31, 2000
- Vasta, J., Giddings, A., Taplin, A., and Stilwell, J. (1961), Roll stabilization by means of passive tanks, Trans-actions of The Society of Naval Architects and Marine Engineers SNAME, 69, 411-439
- Veldman A.E.P., Gerrits J., Luppens R., Helder J.A. and Vreeburg J.P.B., *The numerical simulation of liquid sloshing on board spacecraft*, Journal of Computational Physics 224(2007) 82-99.
- Vogt J., International University Bremen, Germany, *Solar-Terrestrial Interactions: Instrumentation and Techniques (STIINTE)*, The sixth COSPAR Capacity Building Workshop, Sinaia, Romania, June 4-16, 2007.
- Vreeburg J., *Liquid Dynamics from Spacelab to Sloshsat*, Micro-Gravity, Sci. Techn. 21:11-20, 2009

- Wang G.P., Su X.S. and Zhang Y.X., *Influence of inlet radius on Stokes flow in a circular tube via the Hamiltonian systematic method*, Physics of Fluids 21, 103602 (2009)
- Wang Yu Hua, *Clouds Imaging Technology for the FY-2C Meteorological Satellite*, China Academic Journal Electronic Publishing House, Shanghai Institute of Satellite Engineering, 2005
- Webber, J., *Het meten van de dempingskarakteristiek bij diverse frequenties volgens opgave, alsmede het bepalen van de twee resonantie-frequenties*, FSS Test Result Summary 2382, 1991
- Wenzel, R.N., Ind. Eng. Chem., #28 page 988 (1936); Journal of Colloid Chemistry, #53, p.1466, 1948
- Wenzel, K. P., R.G. Marsden, D.E. Page, and E.J. Smith, *The Ulysses mission*, Astron. Astro-Phys. Suppl. Ser., 92, No. 2, 207-219, Jan. 1992.
- Wertz, James R., *Spacecraft Attitude Determination and Control*, Springer, 73rd ed, 2003
- Wertz, J. R. and Larson W.J., *Space Mission Analysis and Design*, 3rd edition, Space Technology Library, 1999
- Weymiens B., Oremus R., Battrick B. et al, *Meteosat Second Generation*, ESA Publications, ESA BR-153, ISBN 92-9092-634-1, 1999
- Wang G.P., Xu X.S. and Zhang Y.X., *Influence of inlet radius on Stokes flow in a circular tube via the Hamiltonian systematic method*, Journal of Physics of Fluids 21, 103602, 2009
- Willmore A.P., *A PROPOSAL FOR AN X-RAY EXPERIMENT FOR COS-B*, Non-Solar X- and Gamma-Ray Astronomy, 50-53, IAU, 1970
- Womersley J.R., *Method for the calculation of velocity, flow and viscous drag in arteries when the pressure gradient is known*, Journal of Physiology, **127**, 533–563, 1955.
- Wu W. and S. Richard, *The creeping motion in the entry region of a semi-infinite circular cylindrical tube*, Math. Mech.-Engl. Ed. **4**, 833, 1983
- Yamanaka G., Kikura H., Takeda Y. and Aritomi M., *Flow measurement on an oscillating pipe flow near the entrance using the UVP method*, Experiments in Fluids 32 212-220, 2002
- Yang, W.H. and Yih, C.-S., *Stability of time periodic flows in a circular pipe*, J. Fluid Mech., **170**, 497–505, 1977.

Fokker-Dutch-Space FY-2 project archive [FDS, 1992]

Abbreviations

DRDP	Design Review Data Package
SOW	Statement Of Work
QA	Quality Assurance
CWGI	China Great Wall Industry
BICE	Beijing Institute of Control Engineering
RP	Report
PL	Plan
FO	Fokker
TN	Technical Note

1. SOW FY2 Project Statement of work for NuDa FY2-WS-CG-001
2. SPEC FY2 Spec for passive liquid with endpots NuDa FY2-SP-CG-001
3. DRDP Design Report FY2-RP-FO-001
4. Design Report, issue 4, dated 15-01-93, FY2-RP-FO-001
5. DRDP Strength and stiffness analysis FY2-RP-FO-002
6. DRDP Mechanical Drawings FY-DD-FO-001
7. DRDP Specification of damping fluid FY2-SP-FO-001
8. DRDP Performance calibration test plan FY2-PL-FO-004
9. DRDP Test equipment technical description FY2-TN-FO-001
10. DRDP PMP list FY2-LI-FO-001
11. PLAN General Test plan FY2-PL-FO-002
12. DRDP Performance report FY2-RP-FO-003
13. Performance calibration test plan FY2-PL-FO-004
14. Test equipment technical description - FY2-TN-FO-001
15. PTM performance test procedure - FY2-PR-FO-001
16. PTM test report FY2-RP-FO-007
17. Reliability assessment for GWIC-NUDA FY2-RP-FO-006
18. Design Report (Issue 4 - FM update), FY2-RP-FO-001
19. QA plan for CGWIC Nutation Damper - FY2-PL-FO-003
20. Performance report, FY2-RP-FO-003
21. FY2 project technical specification for NUDA CGWIC report
22. DRDP Strength and stiffness analysis FY2-RP-FO-002
23. Radiation analysis for the FY-2 NUDA - FY2-RP-FO-0010
24. Test plan [QM-DM]-FM_ FY2-PL-FO-008
25. Test report QM-DM FY2-RP-FO-009
26. FM and QM test procedure FY2-PR-FO-002
27. Test procedure for the QM and FM performance checks FY2-PR-FO-003
28. CGWI Equipment Technical Spec. for the FY-2 Nutation Damper, 20-01-1989
29. DRDP Specification of damping fluid FY2-SP-FO-001
30. DRDP Test equipment technical description FY2-TN-FO-001
31. FAX FO90/FY2/007-Dated:02-6-90-Subject: Length growth items(I)
32. FAX FO90/FY2/009-Dated:11-7-90-Subject: Length growth items(II)
33. FAX FO90/FY2/005-Dated:10-5-90-Subject: Contact angle & project advance

Authors Background and Motivation

The direction in which education starts a man will determine his future life.

Plato, *The Republic*

Greek author & philosopher in Athens (427 BC - 347 BC)

Background

At the age of 52, after a career of 26 years as a physicist in the high-tech industry (Philips Research 7 years, Fokker/Dutch Space 12 years and ASML 7 years), I joined the chair Space Systems Engineering (SSE) of the Faculty of Aerospace Engineering at the Delft University of Technology in autumn 2008. In the preceding decades I worked in diverse fields of R&D, i.e., Philips (research / development): electron and proton beam optics, X-ray optics, VIS (visible range) system optics, Dutch Space (system analyst / engineer) : passive ADCS, solar array electrical system design, earth observation instruments design, robotics, system engineering and ASML (sr. group leader and system engineer): refined sensors.

During this period up to now I have always been fascinated by (bottom-up system) engineering problems and physics-based end-to-end performance modelling. These offer challenges in the interactive field between mathematical physics and the realization of working hardware within timely delivery and costs constraints, thus reality. In some of these areas I booked very satisfying success in dedicated end-to-end performance modelling implementing the physics tailored to the problem, e.g. [Prins, Kuiper and Vieggers, 1984], [Boyd and Kuiper, 2000] and [Kuiper and van der Heijden, 2011]. Most topics, however, were not appropriate for scientific publishing (though fruitful material still exists) especially in the field of system optics and solar array impedance. The main reason being that in industry there is little focus on publications due to intellectual property restrictions and purely market driven development. Further, there is simply no time to explore certain recurring and therefore costly issues to sufficient scientific depth. On the other hand this is a *contradictio in terminis* since such effort does reimburse. Especially during my Dutch Space years (1989-2001) this was a challenge. As an example: in many solar array interface (SA I/F) discussions with sub and the prime contractors the issue of solar array impedance was a hot topic. There were, however, no appropriate models to describe the dynamic solar array capacitance and static inductance of the power transfer harness. Being fascinated by both problems and sometimes disappointed by the limited system engineering role as a subcontractor, I kept working stubborn on both issues within allowable project margins. The results are two verified and validated models over a series of solar array projects to be published in the coming year. In the end, industry is very content with these articles for obvious reasons.

At Dutch Space, I also worked as a (bottom up) system engineer in space instruments design (Sciamachy, OMI, IASI/ISS). Being involved in the development of system end-to-end models, these tools are a key factor for project success in terms of systems engineering and technical management.

The gathered insights throughout the years are now ingredients in the lectures Systems Engineering and Technical Management (AE3S01 and AE4S01) and Space Instruments Engineering (AE4S880) at the Faculty of Aerospace Engineering at the Delft University of Technology. For the latter I am the principle lecturer since November 2011.

Thesis motivation

After leaving Philips in May 1989 and starting at Fokker Space B.V. (now Dutch Space-EADS) I took over the design leadership of passive Attitude and Orbit Control Systems (ADCS), i.e., nutation dampers (NDs). This took place in a pleasant and constructive corporation with Ed Bongers who is now head innovation at Dutch Space-EADS Astrium. During the period 1989-1991, I was involved in a series of related projects. Starting with the Chinese FY2 nutation damper (ND) design, half a year later (November 1990) I was consulted by ESA/ESTEC to discuss the mission critical Ulysses AOCS nutation anomaly which arose early after launch. After a series of meetings with a trouble shoot core team at ESTEC, it was verified that the triple set of Fokker nutation dampers (NDs) was not the root cause of the nutation anomaly [Hawkyard A., Crellin E., Muench R., Eaton D., ..., Hoffman H., Kuiper H., 1990]. To come that far, I had to dive all over in the Ulysses ND project archives. This was a very interesting challenging period generating new insights which led a year later to the generation of a renewed damping concept for the Cluster NDs. The concept comprised the idea to attenuate effectively both nutation and coupled flexible antenna modes [Kuiper, 1991]. The gathered insights strongly supported the refined design of the complicated FY-2 ND as well. This was a significantly different design due to the extreme requirements. These topics are successively dealt with in Chapter 4 (FY2 ND), 5 (Ulysses anomaly) and 7 (Cluster ND innovative design).

During the same period, I was actively consulted in diverse passive ADCS ND S/C projects like the MESUR (JPL, R. Goddard), the Meteosat-2 and the Cluster ND. The proposal support of the latter, as consultant for UCN-Aerospace at British Aerospace in Bristol December 1991, was successful and the project was acquired. During the flight back to the Netherlands, the idea of combined multiple mode damping arose and was handed over [Kuiper, 1991] to the ADCS prime British Aerospace, the overall prime Dornier GmbH and ESA/ESTEC. After being first rejected by ESA as an abnormal use of NDs, it was finally accepted. The idea was not patented or publicized at that time. Looking backwards, based on my ASML experience, this is strange but comprehensible in the frame of activities of a much smaller company with a different culture and market. Similar ideas popped up in shipbuilding engineering a decade later.

The phase-A design concept was further elaborated by UCN-Aerospace with consultancy and experimental support from Fokker Space. During this period the ND activities and knowledge were sold and transferred to UCN Almelo. Their space division is nowadays part of Aeronamic BV in Almelo, The Netherlands.

Working with different cultures is another fascinating part of space technology. I had many fruitful discussions in that time with a good friend (as his PhD paranimph in 1996) and academic international management specialist Dr. Rene Olie. He is now academic director of the School of International Management at the Erasmus University Rotterdam.

In the 90s I worked parallel in different projects (passive AOCS, SA design) with Russian, Chinese and American project partners combined with regular travels to those countries. Looking backward these were exquisite opportunities in a time period when the world globalization boomed by the collapse of communist regimes and the opening of the People's Republic of China. In this scope, the Chinese FY2 nutation damper project (1989-1991) was the most interesting project during my career and was chosen to be one of the drivers of this PhD work. Since I was involved as design leader in the full span of the FY2 ND project, from early phase A up to phase C/D and customer delivery, the lessons learned are a grateful subject to evaluate the systems engineering heritage.

The European space industry of the 80s and early 90s was driven by comfortable cost plus contracts from ESA. These times are over nowadays since huge spacecraft (S/C) developments are overruled by the potentials of miniaturization and distributed systems developments. These items compose the roadmap of the chair Space Systems Engineering led by Prof. Dr. E. Gill at the Delft University of Technology. This scope enables rapid breadboarding with a more relaxed attitude towards the severe ESA qualification rules from the earlier decades. The development of the liquid NDs described in this thesis typically reflects the severe extended qualification programs in those decades.

Curriculum Vitae

July 24 1956	Born in Zaandam, the Netherlands
1969 - 1975	Sint-Michael College in Zaandijk <ul style="list-style-type: none"> ▪ VWO - Atheneum-B
1975 - 1983	Eindhoven University of Technology <ul style="list-style-type: none"> ▪ MSc Applied Physics
1983 - 1984	Philips Physics Labs / Eindhoven University of Technology <ul style="list-style-type: none"> ▪ X-ray optics design for scientific instruments
1984 - 1987	Philips ELCOMA pre-Development Labs <ul style="list-style-type: none"> ▪ E-beam optics development for high-resolution applications
1987 - 1989	Philips Optics Basic Lab <ul style="list-style-type: none"> ▪ VIS system optics design for LCD projection television
1989 - 2000	Fokker (Dutch) Space <ul style="list-style-type: none"> ▪ Design leader and System Analyst / Engineer of Solar Arrays, passive ADCS, Earth Observation Instruments, Robotics and passive Thermal Coolers ▪ Coaching of MSc Aerospace students High Technical College Amsterdam (BSc education) <ul style="list-style-type: none"> ▪ Lecturer (hobby evening job) ▪ Coaching of BSc students in Electrical Engineering
2001 - 2008	ASML <ul style="list-style-type: none"> ▪ sr. development group leader, sr. system designer of optical sensors and project leader of new sensors Eindhoven University of Technology <ul style="list-style-type: none"> ▪ External advisory board member SAI-DTI¹ institute ▪ Coaching of PDEng² students
2008 - present	Delft University of Technology – Faculty of Aerospace Engineering <ul style="list-style-type: none"> ▪ Staff member chair Space Systems Engineering ▪ Teaching (bottom-up) Systems Engineering ▪ Tutor of Design Synthesis Exercise projects ▪ Principle lecturer Space Instrumentation Engineering ▪ Research topics: miniaturized Cubesat and Nanosat sensors & actuators, space instrumentation development and space based solar power systems.

¹Stan Ackermans - Design and Technology of Instrumentation

²Professional Doctorate in Engineering